NATIONAL ADVISORY COMMITTEE
FOR AERONAUTICS

TECHNICAL NOTE

No. 1742

STABILITY AND CONTROL CHARACTERISTICS AT LOW SPEED OF AN

AIRPLANE MODEL HAVING A 38.7° SWEPTBACK WING WITH

ASPECT RATIO 4.51, TAPER RATIO 0.54, AND

CONVENTIONAL TAIL SURFACES

By Vernard E. Lockwood and James M. Watson

Langley Aeronautical Laboratory
Langley Field, Va.

Washington
December 1948

NATIONAL ADVISORY COMMITTEE FOR AERONAUTICS

TECHNICAL NOTE NO. 1742

STABILITY AND CONTROL CHARACTERISTICS AT LOW SPEED OF AN

AIRPLANE MODEL HAVING A 38.7° SWEPTBACK WING WITH

ASPECT RATIO 4.51, TAPER RATIO 0.54, AND

CONVENTIONAL TAIL SURFACES

By Vernard E. Lockwood and James M. Watson

SUMMARY

A low-speed wind-tunnel investigation was made of a $\frac{1}{4.5}$-scale model
of an airplane having a 38.7° sweptback wing with an aspect ratio of 4.51,
a taper ratio of 0.54, and conventional tail surfaces. The investigation
was conducted with several leading-edge and tail configurations to
determine the low-speed stability and control characteristics. Good
agreement was obtained between values of the lift-curve slope and the
angle of attack for maximum lift obtained experimentally and the calculated
values obtained by using a cosine relationship with lift-curve slopes and
angle of stall of the unswept wing. A leading-edge modification simulating
a circular-arc wing gave a value of 0.51 for the slope of the tail-off
lift curve and a maximum lift coefficient of 0.88 as compared with corre-
sponding values of 0.59 and 1.04 for the plain wing.

In general, the model showed a large margin of static longitudinal
stability about a center of gravity located at 18 percent of the mean
aerodynamic chord. At lift coefficients near the stall, particularly
with the flaps down, there was a decrease of stability and sometimes
instability existed through a small lift-coefficient range, which was
followed thereafter by increased stability at stall. The elevator, how-
ever, was capable of trimming the model at maximum lift. The simulated
circular-arc wing gave a large variation of longitudinal stability with
lift coefficient. The static margin was large at low lift coefficients,
negative at higher lift coefficients and, at maximum lift, was large again.

The effective dihedral of the model increased with lift coefficient
in a manner similar to that obtained with other swept wings and the
variation of effective dihedral with lift coefficient for the wing alone
was in good agreement with the calculated value. A good correlation of
wing-fuselage interference effect on effective dihedral was obtained
between data for the test model and other American and German data. This
model gave low aileron effectiveness for all leading-edge configurations
tested.

INTRODUCTION

The sweptback wing offers a means of increasing the speed of an aircraft to a value approaching the speed of sound by delaying compressibility effects. When the wing is sweptback, however, the aerodynamic characteristics are usually adversely affected in the low-speed range.

The present paper contains the aerodynamic characteristics of a $\frac{1}{4.5}$-scale model of an airplane with a sweptback wing as determined from tests in the Langley 300 MPH 7- by 10-foot tunnel. The usual stability and control tests were made and, in this case, several leading-edge configurations (plain, slotted, and drooped nose) which might be used with a sweptback wing design were investigated. Data with various tail configurations are given. Also included are the results obtained with a simulated circular-arc airfoil section.

A separate investigation was made to determine the flight characteristics of a similar full-scale airplane and to determine whether correlations are possible between wind-tunnel results and flight-test results on sweptback wings. The results of the flight investigation are reported in references 1 and 2.

COEFFICIENTS AND SYMBOLS

The results of the tests are presented as standard NACA coefficients of forces and moments. Rolling-, yawing-, and pitching-moment coefficients are referred to a center of gravity located at 18 percent of the mean aerodynamic chord. (See fig. 1.) The data are referred to the stability axes, which are a system of axes having their origin at the center of gravity and in which the Z-axis is in the plane of symmetry and perpendicular to the relative wind, the X-axis is in the plane of symmetry and perpendicular to the Z-axis, and the Y-axis is perpendicular to the plane of symmetry. The positive directions of the stability axes and of angular displacements of the airplane and control surfaces are shown in figure 2.

The coefficients and symbols are defined as follows:

C_L lift coefficient (Lift/qS)

C_X longitudinal-force coefficient (X/qS)

C_Y lateral-force coefficient (Y/qS)

C_l rolling-moment coefficient (L/qSb)

C_m pitching-moment coefficient ($M/q\bar{S}c$)

C_n yawing-moment coefficient (N/qSb)

$C_{L_{max}}$ maximum lift coefficient obtained for a particular configuration

ΔC_{l_ψ} increment in C_{l_ψ} due to wing–fuselage interference

$$\left(C_{l_{\psi\text{ wing-fuselage combination}}} - C_{l_{\psi\text{ wing alone}}} \right)$$

X longitudinal force along X-axis, pounds

Y lateral force along Y-axis, pounds

Z normal force along Z-axis (Lift = $-Z$), pounds

L rolling moment about X-axis, pound-foot

M pitching moment about Y-axis, pound-foot

N yawing moment about Z-axis, pound-foot

q free-stream dynamic pressure, pounds per square foot $\left(\rho V^2/2 \right)$

q_t effective dynamic pressure at tail, pounds per square foot

S wing area (12.36 sq ft on model)

S_t horizontal tail area (2.29 sq ft on model)

$\bar{c}$ wing mean aerodynamic chord (1.733 ft on model)

C wing chord, feet

b wing span (7.47 ft on model)

V air velocity, feet per second

D propeller diameter (2.574 ft on model)

R Reynolds number

A aspect ratio (b^2/S)

ρ mass density of air, slugs per cubic foot

α angle of attack of root chord line, degrees

α_T angle of attack of thrust line, degrees ($\alpha - 1.20^\circ$)

ψ angle of yaw, degrees

$pb/2V$ wing tip helix angle in roll, radians

l fuselage length, feet

d fuselage diameter, feet

z distance of wing above fuselage center line, feet

ϵ average downwash angle at tail, degrees

i_t angle of stabilizer with respect to thrust line, positive when trailing edge is down, degrees

δ control–surface deflection, measured in a plane perpendicular to hinge axis, degrees

β propeller blade angle at 0.75 radius, degrees

n_p neutral–point location, percent wing mean aerodynamic chord of model

Λ leading–edge sweep angle, degrees

Γ wing dihedral angle, degrees

λ taper ratio (Tip chord/Root chord)

$d\epsilon/d\alpha$ rate of change of downwash with angle of attack

Subscripts:

a aileron

a_L left aileron

e elevator

r rudder

f flap (rear lift flap)

f_n nose flap

t   horizontal tail

ψ   denotes partial derivative of a coefficient with respect to

$$\text{yaw} \left(\text{example:} \quad C_{l_\psi} = \frac{\partial C_l}{\partial \psi} \right)$$

APPARATUS AND TESTS

Model

General.— The airplane which the model simulated (references 1 and 2) is a sweptback-wing version of a conventional fighter-type airplane which was adapted for tests by sweeping the wing back 35° from a point just outboard of the intake ducts in the manner shown in figures 1, 3, and 4 and by redesign of the wing tips. The modifications resulted in a wing having the following parameters: 38.7° sweep of the leading edge, 4.51 aspect ratio, and 0.54 taper ratio. The $\frac{1}{4.5}$-scale model used in the present investigation is shown in figure 3 mounted in the tunnel for testing.

Propeller.— The propeller on the model is a three-blade exact-scale model of the propeller used on the full-scale airplane. The blade angle used for all tests was 28° at the 0.75 radius.

Wing modifications.— The wing was so constructed that a slotted section could be fitted along the leading edge of the sweptback part. The percentage of swept span covered by these slots could be varied in four steps measured from the wing tip — 40, 60, 80, and 100 percent span — as shown in figure 4. Typical sections through the slot are shown in figure 5. When the slots are closed, the configuration is referred to as the plain nose or plain wing. The outer 40-percent-wing span could also be fitted with a droop-nose flap having a 30° deflection. A typical section of the nose flap is shown in figure 6. A center-section nose fairing was used in some tests to fill in the unswept part of the wing in front of the intake ducts and thereby to give the entire leading edge a sweep of 38.7°. (See fig. 7.) For part of the investigation the wing section was changed to a simulated circular-arc section by the addition of a sheet metal fairing with a circular-arc contour at the leading edge of the wing. The fairing extended from the fuselage intersection to the tip of the wing. The resultant airfoil thickness was approximately 14.8 percent of the extended chord. This modification resulted in a chord increase of 13.0 percent and an area increase of 12.69 percent over that of the original wing. (See fig. 8.) The outer 40 percent span of the circular-arc wing was equipped with replacable nose flaps of 0°, 15°, or 30° deflections. Figure 9 shows the circular-arc model equipped with the 15° nose flap. Typical sections of the circular-arc wing are shown in figure 10.

All wing configurations had plain lift flaps and ailerons of airfoil

contour with the flap and aileron chord 15.1 percent of the wing chord perpendicular to the hinge axis. The flap span was 52 percent of the wing span.

Tail configurations.— The modifications to increase the fuselage length of the model were different from those of the full—scale airplane of references 1 and 2. On the full—scale airplane a 4—foot section, which would correspond to 10.667 inches on the model, of constant cross-sectional area, was added just behind the cockpit at a point that would correspond to the 51.44—inch station on the model and provisions were made for decreasing the stabilizer incidence 4° as indicated by the dash line of figure 11. On the model the tail length was increased by adding a section of constant cross—sectional area behind the 68.88—inch station with no change in tail height as shown by the heavy line of the figure. The stabilizer of the model was adjustable.

The model was tested with various ventral—fin arrangements shown in figure 11. The model originally had a small ventral fin extending some distance along the fuselage; this model configuration is referred to herein as the model with ventral fin 1. Ventral fins 2 and 3 were large fins attached to the model with the extended fuselage, as shown in figures 7 and 12. The general arrangement of the various tail configurations is shown in figure 11.

TEST CONDITIONS AND PROCEDURE

The investigation was made in the Langley 300 MPH 7— by 10—foot tunnel at a dynamic pressure of approximately 40.85 pounds per square foot for most tests. For the few power tests that were made, the dynamic pressure was reduced to a value of 15.12 to secure the desired thrust coefficient. For some of the tests, a turbulence net was installed in the tunnel which increased the effective Reynolds number by a factor of 2.24, as determined from sphere tests at the pivot point. The effective Reynolds number of the tests varied from 2.05×10^6 with the net out to 4.59×10^6 with the net installed. The effective Reynolds number at which each test was made is noted on the figures.

The stability and control characteristics of the $\frac{1}{4.5}$-scale model were obtained by maintaining control surfaces at the desired setting and by varying the angle of attack or angle of yaw, depending on the desired characteristic. The lateral and directional—stability derivatives were obtained from pitch tests at angles of yaw of ±5° by assuming linear characteristics over the small yaw range. Aileron effectiveness was measured from data taken with only the left aileron deflected, the right aileron being maintained at zero deflection.

In order to obtain data consistent with the flight data of references 1 and 2, the tests of the model were conducted with the main wheels down, as retraction of the main wheels on the airplane was impossible. The nose–wheel door of the model was also left off for tests with the simulated circular–arc wing.

Most of the tests were made with the propeller windmilling, a few with the propeller removed, and a few with the power on. For the power–on tests a level–flight condition was approximated by varying the propeller rotational speed to obtain zero net drag with the tunnel operating. For powered yaw tests the propeller rotational speed was held constant at approximately 3000 rpm for the condition corresponding to zero net drag at 0° yaw. For these tests the model propeller torque coefficient was slightly less than that for a corresponding power condition on the full–scale airplane.

For the purpose of obtaining some information on effective dihedral, the wing was tested without the fuselage. In this case, the main landing gear remained on the wing.

All tail–off tests were made with the ventral fin removed.

Some tests were made with wool tufts attached to the wing to observe the air flow along the surface of the wing. The results of some of these visual observations are reported in the paper.

Corrections

Approximate jet–boundary corrections based on methods used for unswept wings have been applied to the angles of attack, the longitudinal–force coefficients, and the tail–on pitching–moment coefficients. The corrections were computed as follows by the use of reference 3:

$$\Delta\alpha = 1.42C_L \text{ (deg)}$$

$$\Delta C_X = -0.0198C_L^2$$

$$\Delta C_m = 0.0132C_L$$

All jet–boundary corrections were added to the test data.

All data were corrected for blocking by the method given in reference 4. (The correction factor was 1.0204.) An increment in longitudinal–force coefficient of 0.0006 has been added to take into account the horizontal buoyancy effected by the longitudinal static–pressure gradient in the tunnel for all tests.

· Tare tests were not made; hence the data are uncorrected for the
effect of the model support struts.

<p align="center">RESULTS AND DISCUSSION</p>

<p align="center">Presentation of Data</p>

The aerodynamic characteristics in pitch for the various model
configurations are presented in figures 13 to 34. The effect of leading-
edge slots on the lift characteristics are compared in figures 13 to 16.
The results of stabilizer tests to determine the longitudinal stability
are presented in figures 17 to 25 whereas the neutral points, which
summarize the results on longitudinal stability, are presented in
figures 26 to 29. The corresponding dynamic pressure ratios and downwash
angles are given in figures 30 to 32. The longitudinal control charac-
teristics of the various models are summarized in figures 33 and 34.

The lateral and directional stability derivatives, which were obtained
at $\pm 5^\circ$ yaw, are presented in figures 35 to 48. Figures 49 to 59 contain
the aerodynamic characteristics between $\pm 30^\circ$ yaw from which the lateral
and directional stability at large angles of yaw may be determined. The
effect of aileron deflection on the aerodynamic characteristics in pitch,
are given in figure 60. The lateral control characteristics of the model
which include an estimation of the rate-of-roll of the airplane, are
presented in figures 61 to 65. Directional control characteristics are
given in figures 66 to 68.

<p align="center">Lift Characteristics</p>

Plain sweptback wing.— Because of the sweep designed into the air-
plane wing, the lift characteristics would probably be materially changed
from those of the unswept wing. Characteristics usually affected are the
slope of the lift curve and the angle of attack at which stall occurs.
The slope of the tail-off lift curve C_{L_α} for the swept-wing model
is 0.059 (fig. 21) as compared with 0.077 for the unswept wing model
(from unpublished data). The swept-wing value of C_{L_α} obtained from
tests is only slightly smaller than the calculated value of 0.060 obtained
by using the value for the unswept wing and multiplying by the cosine of
the angle of sweep of the leading edge. Reference 5 states that for
moderate angles of sweep the maximum lift coefficient is independent of
the angle of sweep but the angle of attack for the maximum lift varies
inversely as the cosine of the angle of sweepback. In the present
investigation, the maximum lift coefficient obtained for the tail-off
configuration was 1.04, which is in good agreement with that obtained

for the unswept wing. The angle of attack at which $C_{L_{max}}$ occurred on the unswept wing was 16.4° (unpublished data) and for the swept wing 21.3° as shown in figures 14 and 15. These values indicate agreement with the inverse cosine relationship previously stated.

Leading-edge slots.— As high-lift devices the leading-edge slots designed for the airplane were effective in producing additional lift for each incremental increase in slot span. Figure 15(a) shows that, with the propeller removed and flaps up, $C_{L_{max}}$ varied from 1.03 with no slots to 1.27 for the 100-percent-span slots. Similar results were obtained with flaps down (fig. 15(b)). The effectiveness of the flaps appeared to be a function of the slot span. For 40-percent-span slots, $C_{L_{max}}$ increased from 1.09 to 1.14 when the flaps were deflected; whereas for 100-percent-span slots $C_{L_{max}}$ increased from 1.27 to 1.43.

Nose flap.— The outboard 40-percent-span slots were replaced in some of the tests by a leading-edge droop-nose flap deflected 30°. This arrangement was responsible for an increase in $C_{L_{max}}$ of 0.07 (fig. 22), a small increase in the lift-curve slope, and, like the slot, gave greater drag in the low angle-of-attack range.

Wing-center-section fairing.— The faired center section, which increased the wing area, gave an increase in $C_{L_{max}}$ of about 0.07 (see fig. 23) and also a small increase in the slope of the lift curve. These increases were not entirely accounted for by the wing-area increase.

Circular-arc wing.— The circular-arc-wing data presented in figures 24 and 25 are based on the area of the plain wing. The coefficients may be reduced to the basis of the circular-arc wing by multiplying the lift- and longitudinal-force coefficients by 0.888 and the pitching-moment coefficients by 0.772. The slopes of the tail-off lift curve based on the respective wing areas, was 0.051 for the circular-arc wing as compared with 0.059 for the plain wing. The maximum lift coefficient, also based on the respective areas, was 0.88 for the circular-arc wing as compared with 1.04 for the plain wing. The angle of attack for $C_{L_{max}}$ was reached for the tail-off configuration at $\alpha = 20^\circ$, but with the other configurations it was not apparent whether the point at which testing ceased ($\alpha = 24^\circ$) was the angle of attack for $C_{L_{max}}$. The nose flaps were effective in increasing the maximum lift coefficient by an increment $\Delta C_{L_{max}} \approx 0.07$; however, the 30° deflection appeared to be no more effective than the 15° deflection.

Figures 24 and 25 show a rapid rise in the longitudinal-force coef-
ficient with lift coefficient for values of $C_L > 0.5$ which will result
in the circular-arc wing having large sinking speeds at landing velocities
with power off. For a wing loading of 32 pounds per square foot and
a $C_L \approx 1.0$ (115 mph) the sinking speed of the circular-arc wing will
be about 75 feet per second as compared with 25 feet per second with the
plain sweptback wing. The sinking speed for the circular-arc wing is a
minimum of about 35 feet per second at a $C_L \approx 0.65$. A large amount of
power will no doubt be needed to make a satisfactory landing with the
circular-arc wing.

Longitudinal Stability

The stick-fixed neutral points n_p of figures 26 to 28 were computed
from the data of figures 17 to 23 by the graphical method described in
reference 6. A large margin of stability is indicated through most of the
lift range with the center of gravity at 18-percent mean aerodynamic chord.
The neutral points are believed to represent fairly closely the stability
of the model until the region of maximum lift is attained. In a small
range of lift coefficient near maximum lift the pitching-moment coefficient
changes rapidly with lift coefficient, first becoming less stabilizing,
then becoming extremely stabilizing. The neutral points through this
small range of lift coefficient are indicative of the trend in stability
rather than the absolute value of the margin of stability. The difficulty
in determining neutral points for the plain wing was also encountered for
the circular-arc wing over a larger range of lift coefficient than for the
plain wing.

Presence of the propeller.— Because of its sweptback wing the test
airplane might be considered a high-speed airplane in which the low-speed
characteristics were to be determined. In such a case the propeller would
be replaced by a jet and the longitudinal stability would be different
because of the absence of forces on the propeller, which are known to be
destabilizing. The neutral points of figure 26 show the destabilizing
effect of the windmilling propeller; the neutral points are farther for-
ward on the mean aerodynamic chord than with the propeller off. The
static margin varies from 0— to 4—percent mean aerodynamic chord through
the lift range.

Tail length.— The directional stability of the original configuration
was inadequate, and the fuselage was therefore lengthened. The result of
this modification on the stick-fixed neutral points of the model is shown
in figure 27. As would be expected, the neutral-point position was
farther rearward. This rearward movement of the neutral point represents
an increase in longitudinal stability, which is partly a result of the
increase in the tail moment arm. Also with the extended fuselage the tail
is situated in a region of more favorable downwash as figure 30 shows
$d\epsilon/d\alpha$ is smaller through the angle-of-attack range. The stability of
the extended-fuselage model (fig. 27) approaches that of the original model
with the smaller tail length at high angles of attack. This result may be

accounted for by the rapid decrease in dynamic pressure at the tail for the large angles of attack for the extended fuselage.

Leading-edge slots.- The pitching-moment characteristics of the original model have been replotted to a staggered scale in figure 15 to show the effect of varying the slot span on the pitching-moment coefficients near maximum lift. The coefficients for the 60-percent- and 80-percent-span slots tend to increase in a positive direction just before maximum lift is reached, indicating a decrease of stability. With 100-percent-span slots the model does not exhibit a decrease of stability with zero flap deflection.

The neutral points for the 0-, 40-, and 80-percent-span slot configuration are shown in figure 28 for the flaps-up condition. Also shown is the aerodynamic-center variation of the wing-fuselage combination for each slot configuration. The variation of aerodynamic-center location with lift coefficient closely resembles the neutral-point variation with lift coefficient for a given configuration. This variation indicates the relative influence of the wing itself on the stability of the complete model at any lift coefficient.

The 80-percent-span slots gave the greatest margin of stability for a range of lift coefficients from 0.3 to 0.9 (fig. 28). The rate of change of downwash with angle of attack (fig. 31) is smaller for the 80-percent-span slots than for the 0-percent-span slots (0.28 as against 0.41). This result would be a factor tending to increase the stability with the 80-percent-span slotted wing; however, a factor tending to make the 80-percent-span slotted wing less stable would be the lower dynamic pressure that exists at the tail for this configuration.

The tendency of the pitching-moment-coefficient curve to increase in a positive direction near maximum lift, mentioned in connection with the 60- and 80-percent-span slots configuration with flaps up, is magnified when the flaps are deflected by a sharp break near the stall, both with the tail off and with the tail on. (See figs. 19 and 20.) The cases of instability near $C_{L_{max}}$, therefore, seem to be mainly a function of the stall pattern.

Nose flap.- The pitching-moment-coefficient data for the wing with the 30° deflected nose flap (40-percent span) are compared with data for the plain nose in figure 22. The stability characteristics appear to be quite similar.

Wing-center-section fairing.- Addition of a faired center section to the wing tended to increase the pitching moment in a positive direction and thus to make the model less stable as shown by figure 23. This addition probably increased the relative loading of the wing at the root with a forward shift of the aerodynamic center. Some additional downwash at the tail might have also resulted. Visual observations of a model with

wool tufts attached to the surface indicated that the faired center sec-
tion delayed separation at the root near the trailing edge until a very
high angle of attack was obtained.

   Circular-arc wing.— The addition of the circular-arc leading edge
to the model caused a marked change in the longitudinal stability charac-
teristics with lift coefficient as figures 24 and 25 indicate. The
static margin of stability is large at low lift coefficients, is negative
at lift coefficients between 0.4 and 0.9 depending on the flap config-
uration, and the stability rapidly increases at higher lift coefficients.
As an example of the change in stability the case where $\delta_f = 0^{\circ}$
and $\delta_{f_n} = 15^{\circ}$ (fig. 29) may be considered; as the lift coefficient
increases, the neutral point moves rapidly forward from the 37-percent
mean-aerodynamic-chord point at $C_L = 0$ to the leading edge or farther
at a $C_L = 0.66$, from which it moves rapidly to an extreme rearward
position at $C_{L_{max}}$.

   This variation in stability may be explained in part by the similar
manner in which the aerodynamic center of the wing-fuselage combination
varies with lift coefficient (fig. 29). At $C_L = 0$ the tail-off aero-
dynamic center is at 13 percent mean aerodynamic chord; whereas at $C_L = 0.60$
the position is at -9-percent mean aerodynamic chord; then at $C_{L_{max}}$ the
position is extremely rearward. The large rate of change of downwash with
angle of attack (fig. 32) is also responsible in part for the large degree
of instability exhibited in this model. Brief tuft studies show that, for
values of α between 3° and 4° and $\delta_f = 0^{\circ}$, the flow changes direction
just back of the leading edge, at about half the semispan, from a normal
direction to a spanwise outboard flow parallel to the leading edge. At
this angle of attack $\left(dC_m/dC_L\right)_{tail\ on}$ changes from a negative value to
a positive value (fig. 25). At a slightly higher angle of attack $(\alpha = 6^{\circ})$,
additional spanwise area is affected and $d\epsilon/d\alpha$ changes from a value
of 0.3 at $\alpha = 3^{\circ}$ to 1.06 at $\alpha = 6^{\circ}$. Separation in the normal sense does
not take place at the tip until $\alpha \approx 9^{\circ}$ is reached. The increase in the
relative loading of the inboard section probably accounts for the large
positive variation in dC_m/dC_L and $d\epsilon/d\alpha$ and consequently the decrease
of stability.

Longitudinal Control

   An estimate was made from the data of figure 33 of the elevator
deflection required for trim in steady flight for the test airplane and
is presented in figure 34. These data show the individual effect of
moving the center of gravity and extending the fuselage. The data of
figure 33 were used as a basis to estimate the elevator deflection required
for trim for the extended fuselage model and also for the original model.

wool tufts attached to the surface indicated that the faired center sec-
tion delayed separation at the root near the trailing edge until a very
high angle of attack was obtained.

Circular-arc wing.— The addition of the circular-arc leading edge
to the model caused a marked change in the longitudinal stability charac-
teristics with lift coefficient as figures 24 and 25 indicate. The
static margin of stability is large at low lift coefficients, is negative
at lift coefficients between 0.4 and 0.9 depending on the flap config-
uration, and the stability rapidly increases at higher lift coefficients.
As an example of the change in stability the case where $\delta_f = 0^\circ$
and $\delta_{f_n} = 15^\circ$ (fig. 29) may be considered; as the lift coefficient
increases, the neutral point moves rapidly forward from the 37-percent
mean—aerodynamic—chord point at $C_L = 0$ to the leading edge or farther
at a $C_L = 0.66$, from which it moves rapidly to an extreme rearward
position at $C_{L_{max}}$.

This variation in stability may be explained in part by the similar
manner in which the aerodynamic center of the wing—fuselage combination
varies with lift coefficient (fig. 29). At $C_L = 0$ the tail—off aero—
dynamic center is at 13 percent mean aerodynamic chord; whereas at $C_L = 0.60$
the position is at —9—percent mean aerodynamic chord; then at $C_{L_{max}}$ the
position is extremely rearward. The large rate of change of downwash with
angle of attack (fig. 32) is also responsible in part for the large degree
of instability exhibited in this model. Brief tuft studies show that, for
values of α between 3° and 4° and $\delta_f = 0^\circ$, the flow changes direction
just back of the leading edge, at about half the semispan, from a normal
direction to a spanwise outboard flow parallel to the leading edge. At
this angle of attack $\left(dC_m/dC_L\right)_{tail\ on}$ changes from a negative value to
a positive value (fig. 25). At a slightly higher angle of attack ($\alpha = 6^\circ$),
additional spanwise area is affected and $d\epsilon/d\alpha$ changes from a value
of 0.3 at $\alpha = 3^\circ$ to 1.06 at $\alpha = 6^\circ$. Separation in the normal sense does
not take place at the tip until $\alpha \approx 9^\circ$ is reached. The increase in the
relative loading of the inboard section probably accounts for the large
positive variation in dC_m/dC_L and $d\epsilon/d\alpha$ and consequently the decrease
of stability.

Longitudinal Control

An estimate was made from the data of figure 33 of the elevator
deflection required for trim in steady flight for the test airplane and
is presented in figure 34. These data show the individual effect of
moving the center of gravity and extending the fuselage. The data of
figure 33 were used as a basis to estimate the elevator deflection required
for trim for the extended fuselage model and also for the original model.

change of C_{l_ψ} with C_L has been calculated as 0.0036 for the wing alone
by an empirical method based on data obtained in the Langley 300 MPH
7- by 10-foot tunnel which compares favorably with the measured slope
of 0.0032 for the unslotted wing (fig. 35). This method considers only
a fully swept wing; whereas, the airplane has an unswept center section
which would tend to reduce the variation of C_{l_ψ} with C_L.

Effect of slots.— The slots show their greatest effect on lateral
stability by delaying tip stall and thereby maintaining effective dihedral
at the low Reynolds number as was discussed under "Scale effect". There
are some other effects. The breaks in the curve of C_{l_ψ} plotted
against C_L at a $C_L \approx 0.2$ (figs. 35 to 40) are probably due to an
interference between the slot and the leading edge of the airfoil. The
unslotted wing of figure 41 does not show the break in the curve. Nearly
all arrangements of slots for the complete model give a value
of C_{l_ψ} = 0.0020 at C_L = 1.0. Because the slots are effective in
increasing $C_{L_{max}}$ the effective dihedral is maintained to a larger lift
coefficient, especially with 80-percent-span slots.

Tail modifications.— The lateral stability derivatives of the original
model (ventral fin 1) and the model with the extended fuselage are compared
in figure 39. The effects of ventral fin 2 are also shown. The extended-
fuselage model shows slightly less dihedral effect than the original model,
probably because the center of pressure of the vertical tail is relatively
lower. For the same reason, the addition of a large ventral fin to the
model reduced the effective dihedral from that of the model without the
ventral fin. The use of a still larger ventral fin (fin 3) on the model
gave similar results (fig. 40 (b)). The same effects are also shown in
the characteristics at large angles of yaw (figs. 51 and 52).

Power effect.— The effect of power on the effective dihedral is shown
in figure 42. Through most of the lift range the effective dihedral is
approximately 2° more with power on than with propeller windmilling.

Nose flap.— A nose flap deflected 30° and covering 40 percent of the
sweptback-wing span decreased the rate of change of C_{l_ψ} with C_L
from 0.0021 to 0.0018 as shown in figure 43. The maximum values of C_{l_ψ}
were not changed appreciably from the values obtained with the plain wing.

Wing-center-section fairing.— The addition of a faired center section
to the wing (fig. 44) gave about 1° less dihedral effect than the plain
wing for a given lift coefficient, that is C_{l_ψ} is approximately 0.0002
less than that for the unfaired wing.

change of C_{l_ψ} with C_L has been calculated as 0.0036 for the wing alone
by an empirical method based on data obtained in the Langley 300 MPH
7- by 10-foot tunnel which compares favorably with the measured slope
of 0.0032 for the unslotted wing (fig. 35). This method considers only
a fully swept wing; whereas, the airplane has an unswept center section
which would tend to reduce the variation of C_{l_ψ} with C_L.

Effect of slots.— The slots show their greatest effect on lateral
stability by delaying tip stall and thereby maintaining effective dihedral
at the low Reynolds number as was discussed under "Scale effect". There
are some other effects. The breaks in the curve of C_{l_ψ} plotted
against C_L at a $C_L \approx 0.2$ (figs. 35 to 40) are probably due to an
interference between the slot and the leading edge of the airfoil. The
unslotted wing of figure 41 does not show the break in the curve. Nearly
all arrangements of slots for the complete model give a value
of $C_{l_\psi} = 0.0020$ at $C_L = 1.0$. Because the slots are effective in
increasing $C_{L_{max}}$ the effective dihedral is maintained to a larger lift
coefficient, especially with 80-percent-span slots.

Tail modifications.— The lateral stability derivatives of the original
model (ventral fin 1) and the model with the extended fuselage are compared
in figure 39. The effects of ventral fin 2 are also shown. The extended-
fuselage model shows slightly less dihedral effect than the original model,
probably because the center of pressure of the vertical tail is relatively
lower. For the same reason, the addition of a large ventral fin to the
model reduced the effective dihedral from that of the model without the
ventral fin. The use of a still larger ventral fin (fin 3) on the model
gave similar results (fig. 40 (b)). The same effects are also shown in
the characteristics at large angles of yaw (figs. 51 and 52).

Power effect.— The effect of power on the effective dihedral is shown
in figure 42. Through most of the lift range the effective dihedral is
approximately 2° more with power on than with propeller windmilling.

Nose flap.— A nose flap deflected 30° and covering 40 percent of the
sweptback-wing span decreased the rate of change of C_{l_ψ} with C_L
from 0.0021 to 0.0018 as shown in figure 43. The maximum values of C_{l_ψ}
were not changed appreciably from the values obtained with the plain wing.

Wing-center-section fairing.— The addition of a faired center section
to the wing (fig. 44) gave about 1° less dihedral effect than the plain
wing for a given lift coefficient, that is C_{l_ψ} is approximately 0.0002
less than that for the unfaired wing.

Circular-arc wing.— The lateral stability characteristics of the
model with circular-arc wing with several nose flap deflections are
compared in figures 45 and 58. For the wing with $\delta_{f_n} = 0^\circ$ the effective
dihedral reaches a maximum value of 7° $\left(C_{l_\psi} = 0.0015\right)$ at a $C_L \approx 0.5$
after which the dihedral effect decreases. This decrease is probably
the result of tip stall of the leading wing. Nose flaps which tended to
delay tip stall also reduced the variation of effective dihedral with
lift coefficient. Deflection of the trailing-edge flaps produced no
significant changes in C_{l_ψ} (fig. 46).

Directional Stability

Original model.— The directional-stability parameter C_{n_ψ} (figs. 35
and 38) indicates that the wing alone possesses a large amount of direc-
tional stability which increases with lift coefficient to the point where
the wing stalls. The increased stability is probably the result of the
increased drag differences between the two wing panels at high values
of lift coefficient. In the process of stalling the effect is reversed,
and increasing lift coefficient decreases the directional stability. The
fuselage and propeller contribute their normal destabilizing action which
affects C_{n_ψ} by approximately 0.0014 at $C_L = 0.6$. The contribution of
the vertical tail to the directional stability of the model, ΔC_{n_ψ} varies
from −0.0021 at low lift coefficient to −0.0013 near stall for the flaps—
up configuration. The contribution of the vertical tail to the directional
stability is slightly greater for the flaps—down configuration. With
leading-edge slots C_{n_ψ} of the complete model is small (about −0.001)
through most of the lift range except at $C_{L_{max}}$ where $C_{n_\psi} \approx 0$.

The model showed a net gain in directional stability as a result of
sweeping the wings back even though the tail length was effectively
shortened in the process. At a $C_L = 0.4$ (fig. 38) the plain wing model
gave a value of −0.00105 for the slope of the yawing-moment-coefficient
curve, which included the destabilizing effect of the windmilling propeller.
Figure 54, which is for a different model configuration, shows that the
destabilizing effect of the windmilling propeller was an increment
of C_{n_ψ} of 0.00063 $\left(C_{n_{\psi_{propeller\ off}}} - C_{n_{\psi_{propeller\ on}}}\right)$. Therefore the
plain swept wing model minus propeller would give a value of −0.00168
for C_{n_ψ} as compared with a value −0.00135 for the unswept wing model.

The net gain in the directional-stability parameter as a result of
sweeping the wings back was an increment in C_{n_ψ} of −0.00033.

Effect of slots.— The effect of slots on the directional stability
is negligible except near stall where the directional stability is
maintained to higher lift coefficients (figs. 35 to 41).

Tail modifications.— One of the reasons for extending the tail
length on the airplane was to increase the directional stability at high
lift coefficients. The effect on C_{n_ψ} of increasing the model tail length
by 10.9 inches is shown in figure 39 for both flap configurations. This
modification, denoted as the extended fuselage, increased the directional
stability at low lift coefficients but gave stability at high lift coef-
ficients which was about equal to or less than that provided by the original
configuration. The loss in stability of the extended—fuselage model might
be the result of the lower values of dynamic pressure at the tail. (See
fig. 30.) The addition of a large ventral fin (fin 2) to the model with
the extended tail provided an appreciable increase in stability for both
flap configurations.

A slightly larger ventral fin (fin 3) with the 40—percent—span slot
configuration gave a slight increase in directional stability. (Compare
figs. 39(b) with 40(b).)

For all tail configurations mentioned the yawing—moment—coefficient
curves of figures 50 to 52 have a stable slope throughout the yaw range
tested, $\psi = \pm 30^\circ$. There is no evidence of tail stall with the undeflected
rudder.

Level flight power.— Because the flight tests were conducted with a
windmilling propeller to simulate more closely the conditions of a jet-
propelled high—speed aircraft, the effect of power—on directional
stability is of small importance. However, for the level—flight power
conditions represented in figure 42, C_{n_ψ} is approximately —0.002 from

$C_L = 0$ to $C_{L_{max}}$. Other data showing the effects of power—on directional
stability appear in figures 55 and 56.

Nose flap.— The data for the nose flap, which was deflected 30°, are
given in figures 43 and 57 and indicate a slight increase in directional
stability over that of the plain airfoil or of the airfoil with undeflected
nose flap.

Wing—center—section fairing.— The effect of the faired center section
on the directional stability of the model was negligible. (See fig. 44.)

Circular—arc wing.— The circular—arc wing model (extended fuselage,
ventral fin 3) shows a large decrease in directional stability with
increased lift coefficient throughout the lift range for any of the three
leading—edge flap configurations. (See fig. 45.) For example, with the

leading-edge flap deflected 15°, the value of C_{n_ψ} is -0.002 at

$C_L = 0.5$ and C_{n_ψ} is zero at $C_{L_{max}}$. The large loss in stability

appears to be the result of a blanketing effect of the wing on the tail,
as would seem to be indicated by the absence of a similar loss of stability
with the tail off (fig. 46). Additional directional stability data at
a $C_L \approx 0.7$ and large angles of yaw are given in figures 58 and 59.

Lateral Control

The aileron characteristics for several leading-edge configurations
on the airplane model are given in figures 60 to 64. The aileron
effectiveness $C_{l_{\delta_a}}$ for the various configurations are presented in the

following table:

δ_f (deg)	$C_{l_{\delta_a}}$		
	80-percent-span slotted wing	Plain wing	Circular-arc wing
0	0.00090	0.00086	0.00088
45	.00083	.00090	.00078

The values presented in the table represent the average slope of the
rolling-moment-coefficient curve between -10° and 10° aileron deflection
and 0° and 18° angle of attack. The variation in that range was small.
The ailerons of the plain sweptback wing appear to be more effective with
the flaps down than with the flaps up, whereas in the other two cases the
reverse is true.

The ailerons of both the 80-percent-span slotted wing and the
circular-arc wing appear to be effective throughout the angle-of-attack
range for each deflection tested (figs. 60 and 64). However, at about
19° angle of attack the rolling moment provided by the ailerons of the
plain wing decreased to zero and had a reverse effect (fig. 63). Such an
effect, however, might be the result of the low Reynolds number of the
test. Apparently the slots aid in controlling the flow over the aileron.
The ailerons of the circular-arc wing show no tendency to decrease in
effectiveness even near maximum lift coefficient.

The effectiveness of the left aileron in yaw with the 80-percent-
span slotted wing is shown in figure 61 for a $C_L \approx 0.6$. The data have

been replotted in figure 62 and applied to both ailerons deflected
simultaneously as would result with the airplane in a sideslip. The up
aileron which is on the leading wing panel becomes more effective as the
yaw angle is increased. The down aileron of the trailing wing panel
becomes, of course, less effective as is indicated in figure 62. It is
estimated from the data of figure 52, which is for a high angle of attack,
that the aileron will trim the model in yaw, flaps up, at approximately 13.5°
with the aileron deflected ±15° (airplane limits).

The aileron characteristics for the 80-percent-span slotted wing are
summarized in figure 65 where the wing-tip helix angle $pb/2V$ is given
as a function of aileron deflection for several velocities. The value
of the damping coefficient in roll C_{l_p} used to evaluate $pb/2V$ was 0.333 and
was determined from data of full-scale tests on sweptback wings, corrected
for taper, aspect ratio, and sweep angle. The values of $pb/2V$ presented
were reduced by 25 percent as an arbitrary correction for rolling due to
sideslip and the lack of wing torsional rigidity, both of which were
known to be of appreciable magnitude for the test airplane.

The maximum calculated value of $pb/2V$ obtainable on the test air-
plane would be about 0.063 with flaps up and 0.056 with flaps down, based
on a maximum value of airplane aileron deflection of ±15°.

In the following table are given values of $pb/2V$ obtained for
various model configurations based on 20° total aileron deflection:

Velocity (mph)	δ_f (deg)	$pb/2V$		
		80-percent-span slotted wing	Plain wing	Circular-arc wing
200	0	0.039	0.037	0.036
150	0	.045	.040	.038
150	45	.040	.038	.036
110	45	.040	-----	.036

The 80-percent-span slotted wing generally shows the largest values
of $pb/2V$ and the circular-arc wing generally shows the smallest values
of $pb/2V$ for the three leading-edge configurations. The missing value
for the plain wing is not given because of pronounced irregularity in the
rolling-moment data at a lift coefficient corresponding to $V = 110$ miles
per hour.

Directional Control

Rudder effectiveness appears to be high for the airplane in the original configuration as is indicated by the rudder characteristics of the original model presented in figure 66. The rudder gives about 1.13° of sideslip for 1° of rudder deflection $\frac{\partial \psi}{\partial \delta_r} = -1.13$ for $\delta_r = \pm 10^\circ$.

A rudder deflection of 20° trims the model at $\psi = 19^\circ$ with flaps up and at $\psi = 23^\circ$ with flaps down. Note that large rudder deflections cause an appreciable change in dihedral effect. For example, C_{l_ψ} changed from 0.0014 at $\delta_r = 0^\circ$ to 0.0019 at $\delta_r = 30^\circ$ with the flaps up and a like amount with flaps down (fig. 66).

Because of the increased stability resulting from adding a large ventral fin to the extended fuselage, the rudder effectiveness $\partial \psi/\partial \delta_r$ was reduced, and the model trimmed at approximately 17.5° for $\pm 20^\circ$ rudder deflection with flaps up (fig. 68). The yaw angle is limited, however, to about 12.5° because of the low aileron effectiveness and the high dihedral effect.

CONCLUSIONS

The results of a low-speed wind-tunnel investigation of a $\frac{1}{4.5}$-scale model of a sweptback-wing airplane with several wing leading-edge and tail configurations indicated the following conclusions:

1. The lift-curve slope of the swept-wing model compared favorably with the calculated value obtained by multiplying lift-curve slope for the unswept wing by the cosine of the angle of sweep. The maximum lift coefficient for the swept-wing model with no auxiliary lifting devices compared favorably with that of the unswept-wing model, and the angle of attack for which the maximum lift coefficient occurred was in good agreement with a theoretical value obtained from an empirical cosine relationship.

2. The use of slots as antistall devices resulted in an increase in the maximum lift coefficient which was roughly proportional to the slot span. The 40-percent-span 30° nose flap had about the same effect on the maximum lift coefficient as the 40-percent-span slot.

3. The circular-arc wing gave a value of 0.051 for the tail-off lift-curve slope and a maximum value of the lift coefficient of 0.88. The nose flaps which were the same span as the 40-percent slots on the plain wing gave an increment in maximum lift coefficient of about 0.07. The 30° nose

flap appeared no more effective in this respect than the 15° nose flap.

4. In general, the model showed a large margin of static longitudinal stability about a center of gravity at 18 percent of the mean aerodynamic chord. At lift coefficients near stall there was a lessening of stability and sometimes instability existed with the flaps deflected through a small range of lift coefficients but, as the lift coefficient increased further, the stability again increased.

5. The simulated circular–arc wing in either flap configuration gave a large variation of longitudinal stability with lift coefficient. The static margin of stability was large at low lift coefficients, was negative at lift coefficients between 0.4 and 0.9 depending on the flap configuration, and the stability rapidly increased at higher lift coefficients.

6. The elevator is capable of trimming the airplane at maximum lift coefficient at any probable center–of–gravity location, but at maximum lift there may be a large upward movement of the elevator with no change in speed because of the very large increase in stability at stall and loss in elevator effectiveness.

7. The effective dihedral of the model increased with lift coefficient in a manner similar to that obtained with other swept wings and the variation of effective dihedral with lift coefficient for the wing alone was in good agreement with the calculated value. At a lift coefficient of 1.0 the effective dihedral of the plain–wing model was about 10°. A good correlation of wing–fuselage interference effect on effective dihedral was obtained between the test model and other American and German data.

8. At a low Reynolds number of about 2.05×10^6 and at high lift coefficients the slots delayed tip stall and thereby maintained the dihedral effect; however, with the plain wing the dihedral effect decreased sharply under the same conditions.

9. The maximum value of effective dihedral for the circular–arc wing was about 7° at a lift coefficient of 0.5. Above this lift coefficient the effective dihedral decreased rapidly. Nose flaps which tended to delay tip stall also reduced the variation of effective dihedral with lift coefficient.

10. The directional stability of the original model was small. It was increased at low lift coefficients by lengthening the tail moment arm and improved appreciably throughout the lift range by the addition of a large ventral fin.

11. The aileron effectiveness was found to be small with the 80–percent slotted wing and even smaller for the plain and circular–arc wings. The aileron effectiveness remained fairly constant up to and beyond maximum lift for both the slotted and the circular–arc wings.

12. The rudder was capable of trimming both models at a large angle of yaw; but the yaw angle was limited because of the low aileron effectiveness and the high dihedral effect.

Langley Aeronautical Laboratory
    National Advisory Committee for Aeronautics
        Langley Field, Va., August 16, 1948

REFERENCES

1. Sjoberg, S. A., and Reeder, J. P.: Flight Measurements of the Lateral and Directional Stability and Control Characteristics of an Airplane Having a 35° Sweptback Wing with 40-Percent-Span Slots and a Comparison with Wind-Tunnel Data. NACA TN No. 1511, 1948.

2. Sjoberg, S. A., and Reeder, J. P.: Flight Measurements of the Longitudinal Stability, Stalling, and Lift Characteristics of an Airplane Having a 35° Sweptback Wing without Slots and with 40-Percent-Span Slots and a Comparison with Wind-Tunnel Data. NACA TN No. 1743, 1948.

3. Gillis, Clarence L., Polhamus, Edward C., and Gray, Joseph L., Jr.: Charts for Determining Jet-Boundary Corrections for Complete Models in 7- by 10-Foot Closed Rectangular Wind Tunnels. NACA ARR No. L5G31, 1945.

4. Thom, A.: Blockage Corrections in a Closed High-Speed Tunnel. R.& M. No. 2033, British A.R.C., 1943.

5. Letko, William, and Goodman, Alex: Preliminary Wind-Tunnel Investigation at Low Speed of Stability and Control Characteristics of Swept-Back Wings. NACA TN No. 1046, 1946.

6. Schuldenfrei, Marvin: Some Notes on the Determination of the Stick-Fixed Neutral Point from Wind-Tunnel Data. NACA RB No. 3I20, 1943.

7. House, Rufus O., and Wallace, Arthur R.: Wind-Tunnel Investigation of Effect of Interference on Lateral-Stability Characteristics of Four NACA 23012 Wings, an Elliptical and a Circular Fuselage, and Vertical Fins. NACA Rep. No. 705, 1941.

8. Möller, E: Systematische Sechskomoponentensmessungen an Flügel/Rumpfanordnungen mit Pfeilflügeln konstanter Tiefe. Forschunsbericht Nr. 1318/4, Deutsche Luftfarhtforshung (Braunsweig), 1943.

Areas

Wing, sq ft 12.36
Vertical tail, sq ft 1.17
Horizontal tail, sq ft 2.29

C.G. at 0.18 M.A.C.

Model pivot point

87.57

82.78

45.03

38.71

1.12'

.280

6.90

38.85

4.44

8.74

12.11

6.22

1.78 15.37

10.11

0.25 chord

17.51

8.73

8.73

8.73

77.86

23.58

3.51

5.01

1.78

26.23

82.64

30.88

35.36

Wing basic dimensions
Taper ratio 0.544
Mean aerodynamic chord 20.8
Aspect ratio 4.51
Geometric twist, deg 1.70
Aerodynamic twist, deg 1.01
Dihedral, deg 0
Root section 66,2X-116, a = 0.6
Tip section 66,2X-216, a = 0.6

NACA

Figure 1.- Three-view drawing of $\frac{1}{4.5}$-scale model of the test airplane. (All linear dimensions are in inches.)
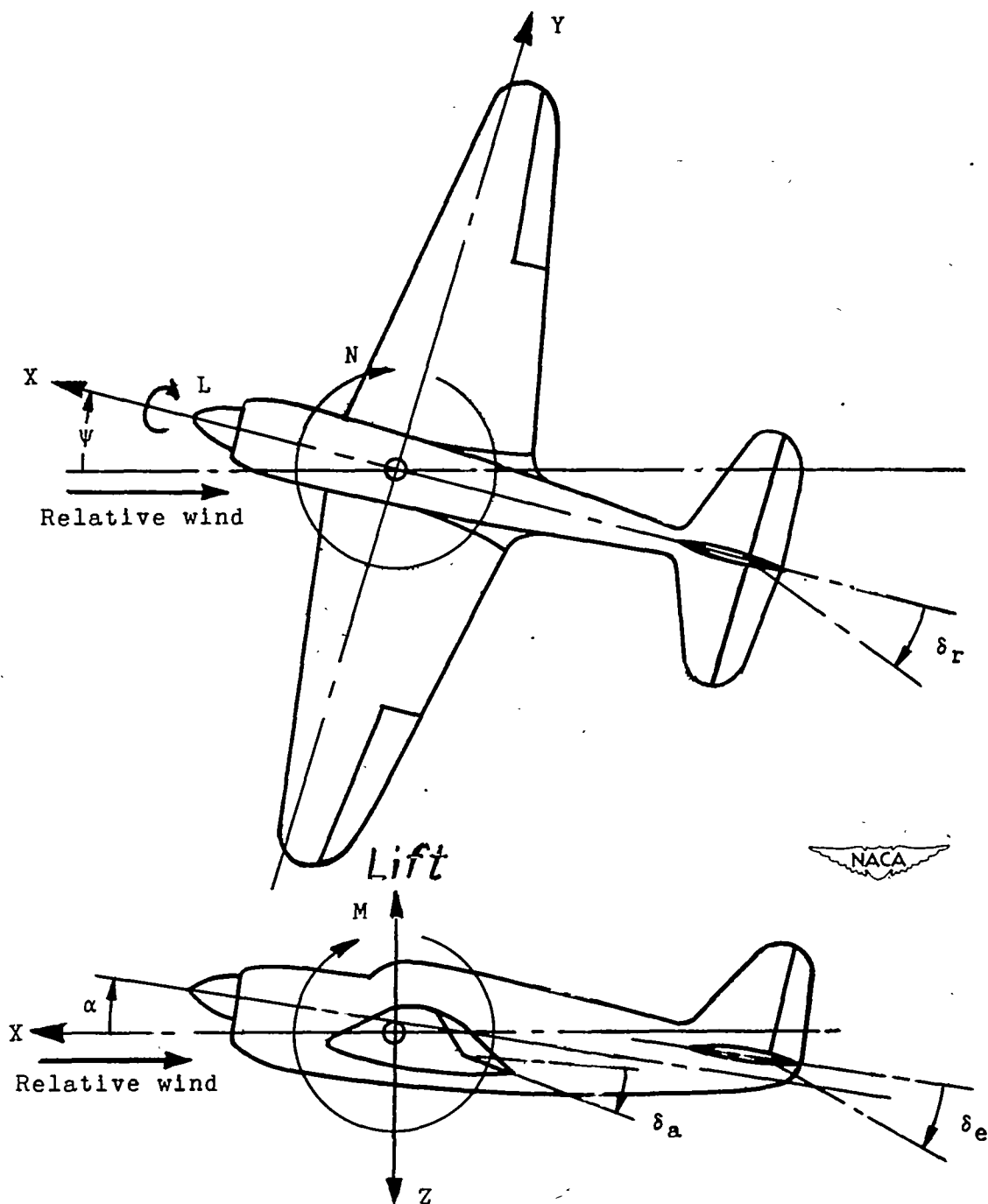
Figure 2.- System of axes and control-surface hinge moments and deflections. Positive values of forces, moments, and angles are indicated by arrows.
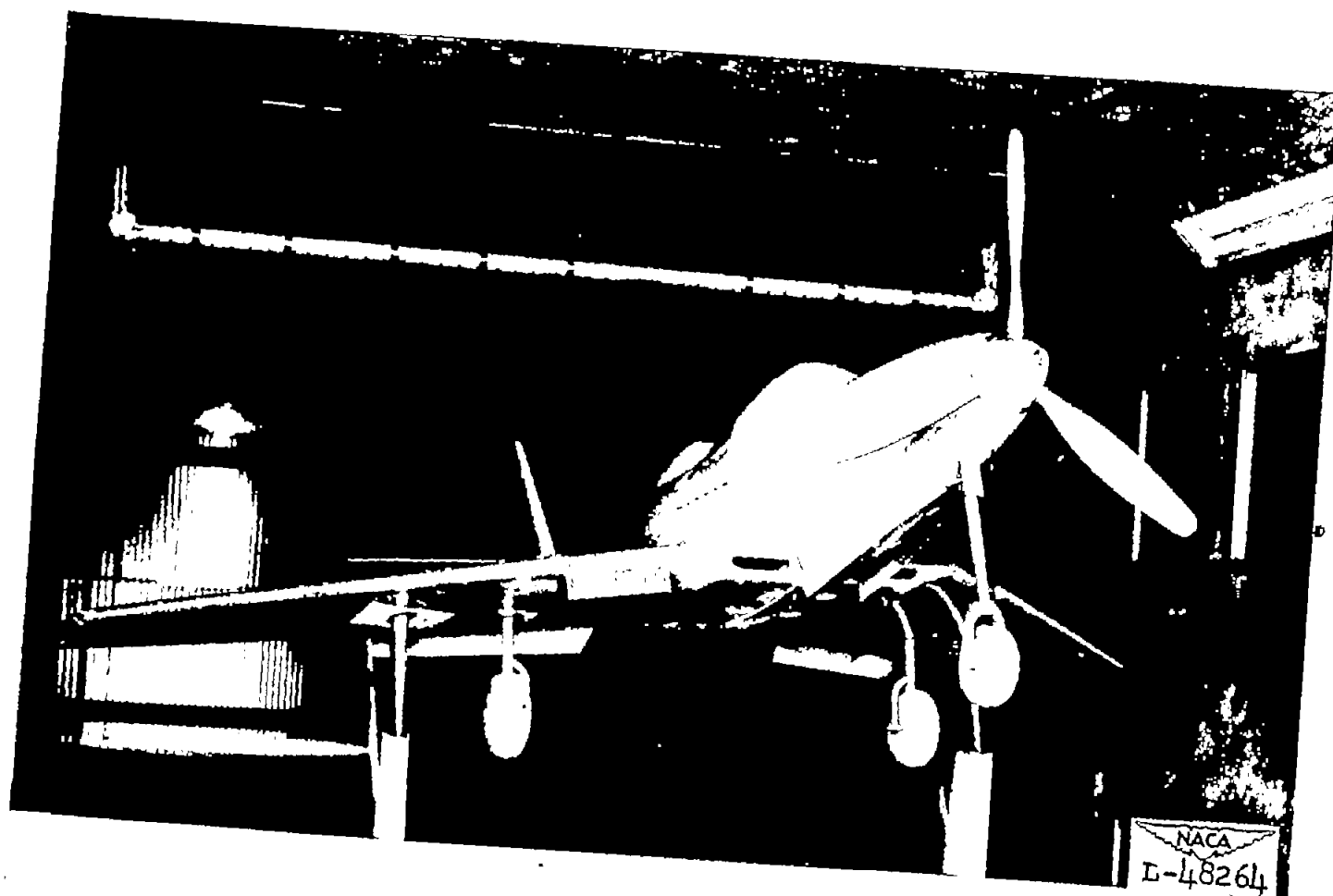
(a) Three-quarter front view.

Figure 3.-   Views of $\frac{1}{4.5}$-scale model of the test airplane in tunnel.
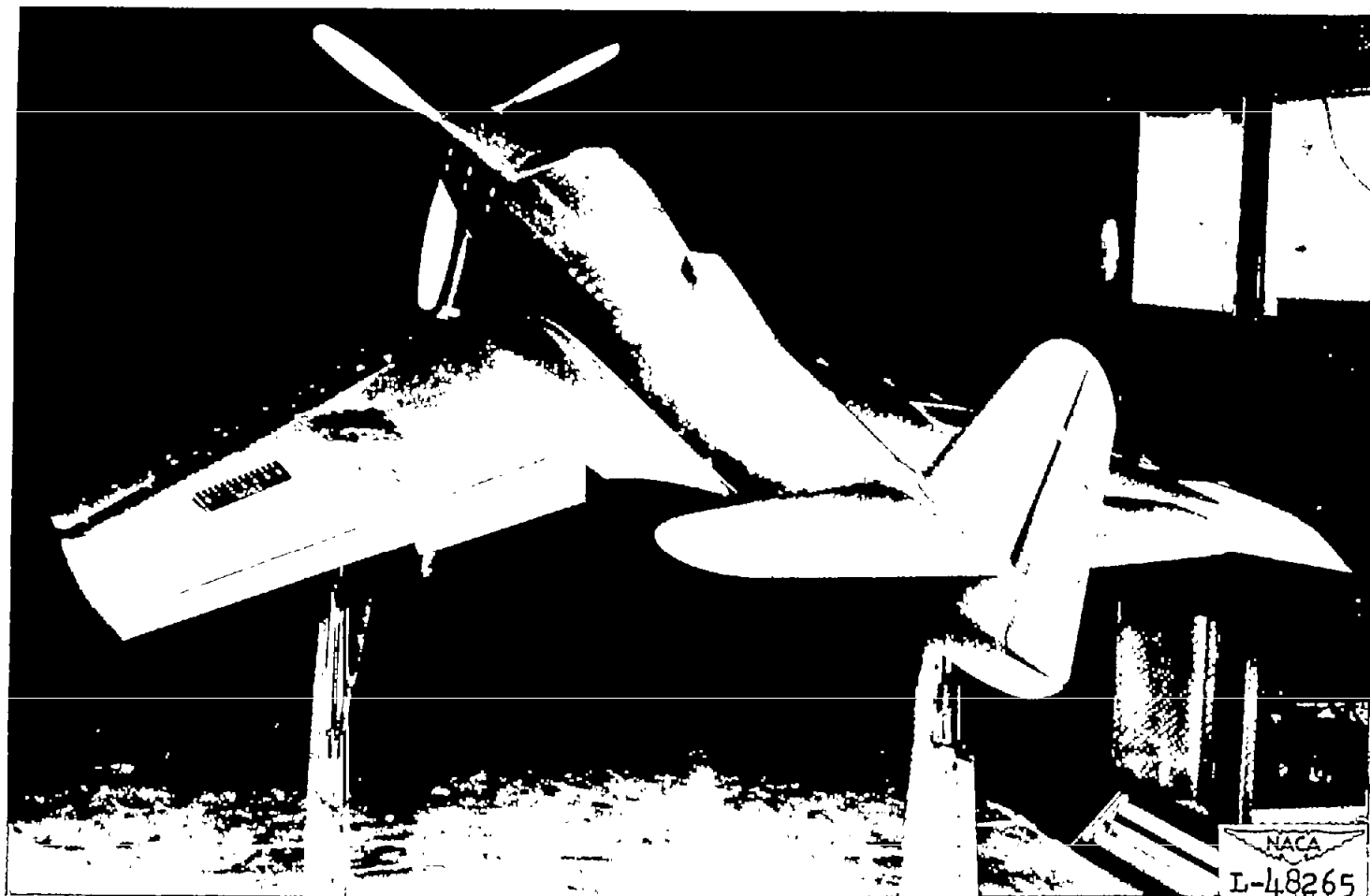
(b) Three-quarter rear view.

Figure 3.- Concluded.
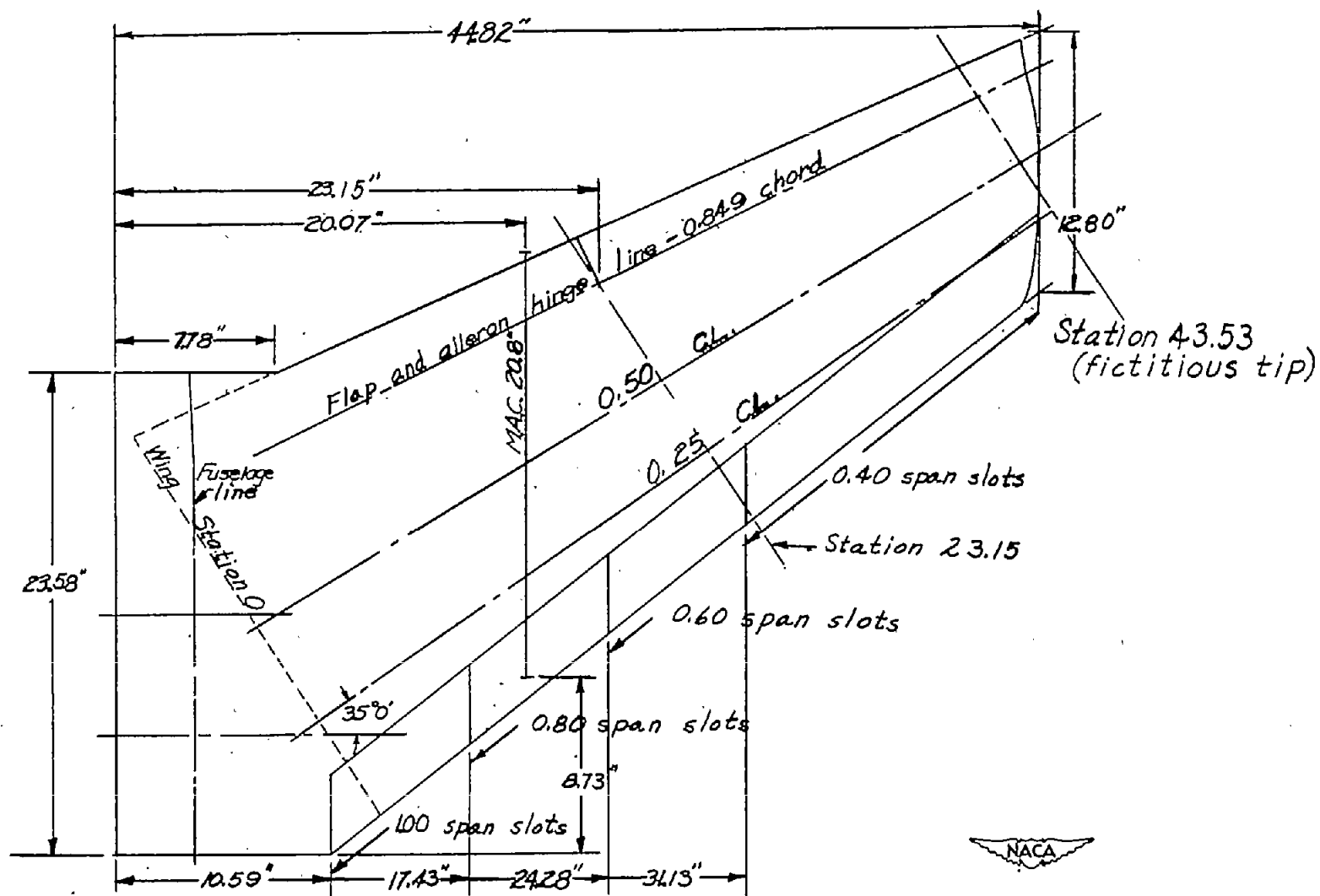
Figure 4.- Wing geometry of $\frac{1}{4.5}$-scale model of test airplane.

Slot
———— Open
— — — Closed

.411"

.311"

Wing chord line

1.11"
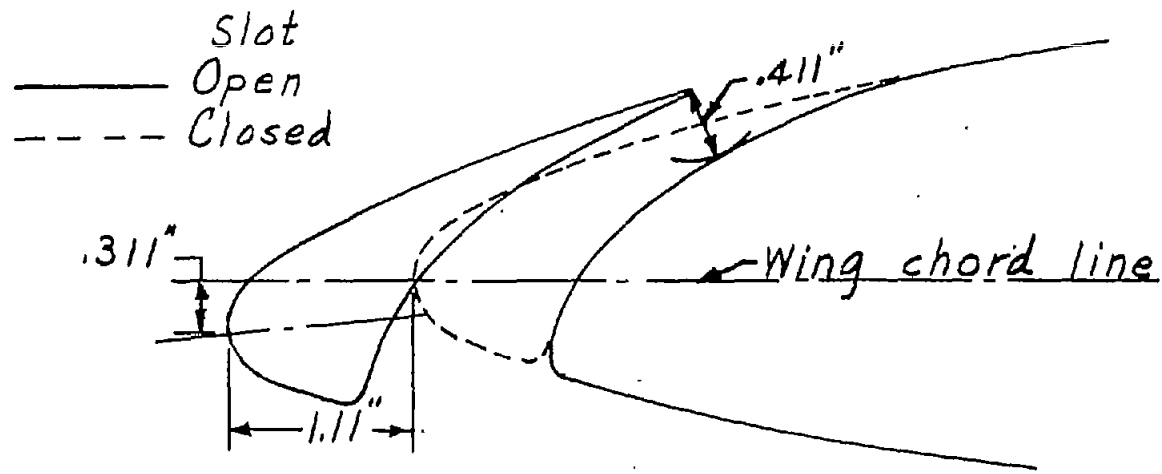
(a) Section at 43.53-inch station (fictitious tip).

.344"

.311"

Wing chord line

1.11"
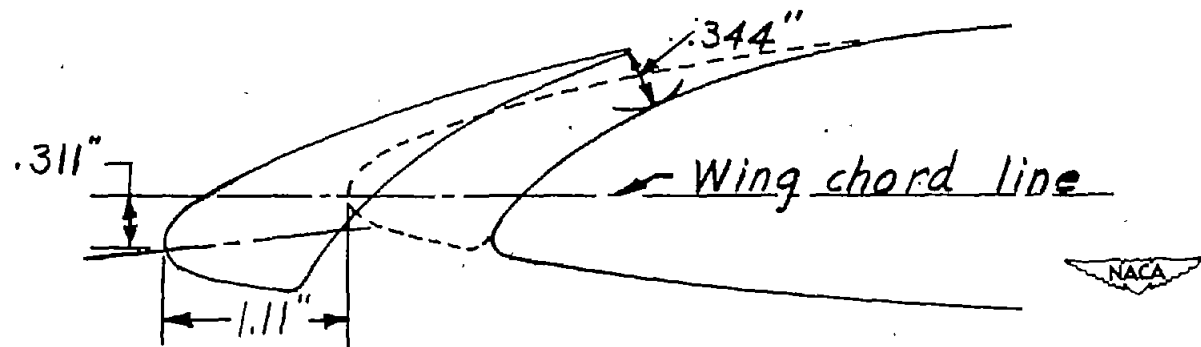
(b) Section at zero station.

Figure 5.- Sections at wing leading edge showing gap and position of slots.
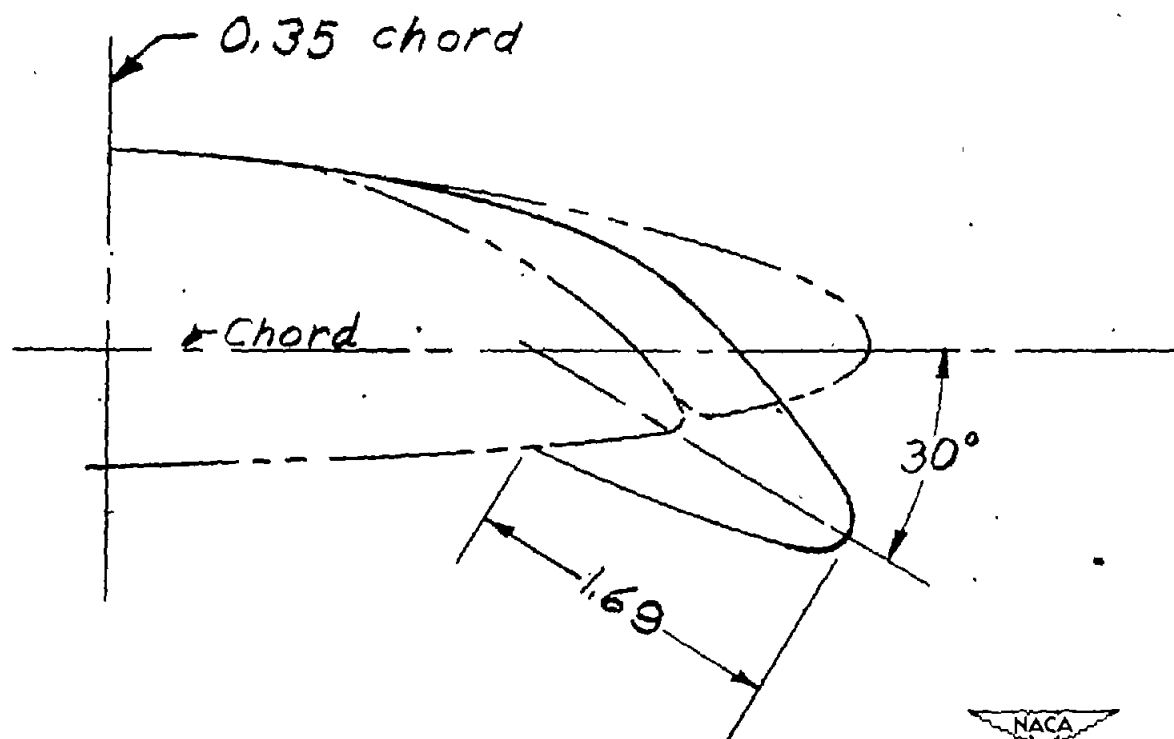
Figure 6.- Typical section of 30° droop-nose flap on $\frac{1}{4.5}$-scale model of test airplane.

(a) Three-quarter rear view.

Figure 7.- The $\frac{1}{4.5}$-scale model of test airplane. Extended fuselage; ventral fin 3; faired center section; turbulence net in tunnel.
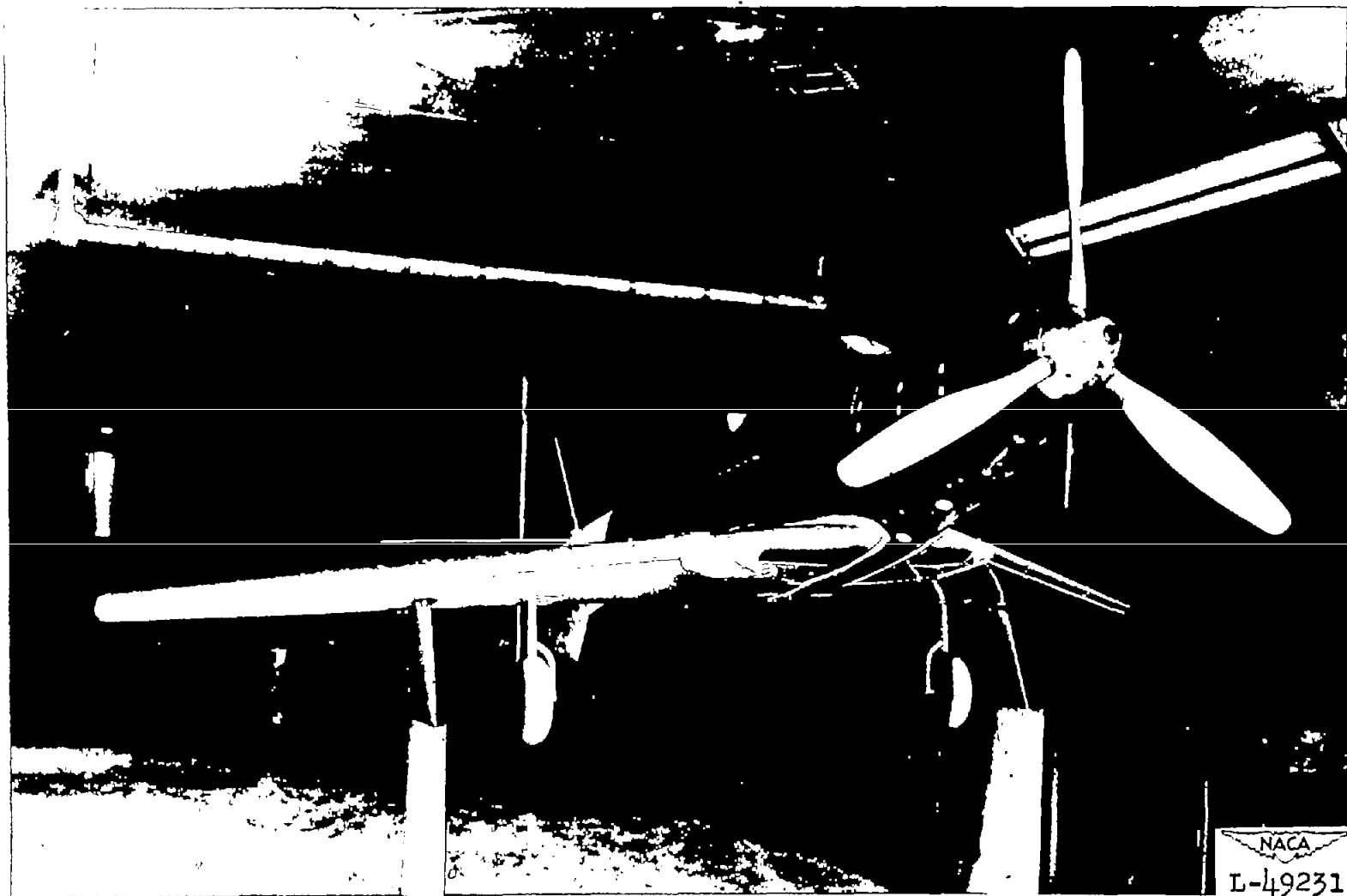
(b) Three-quarter front view.

Figure 7.- Concluded.
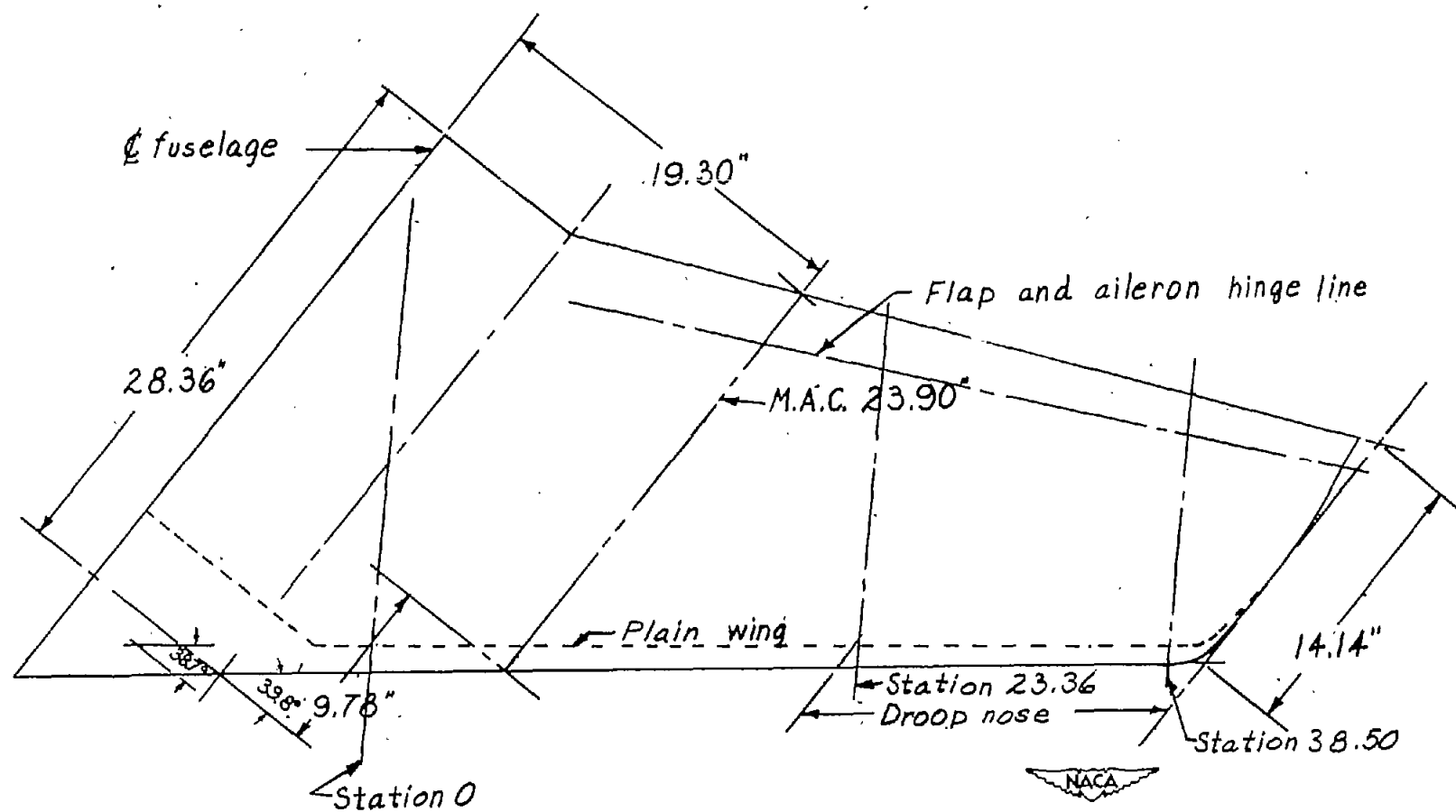
Figure 8.- Wing geometry of simulated circular-arc wing.
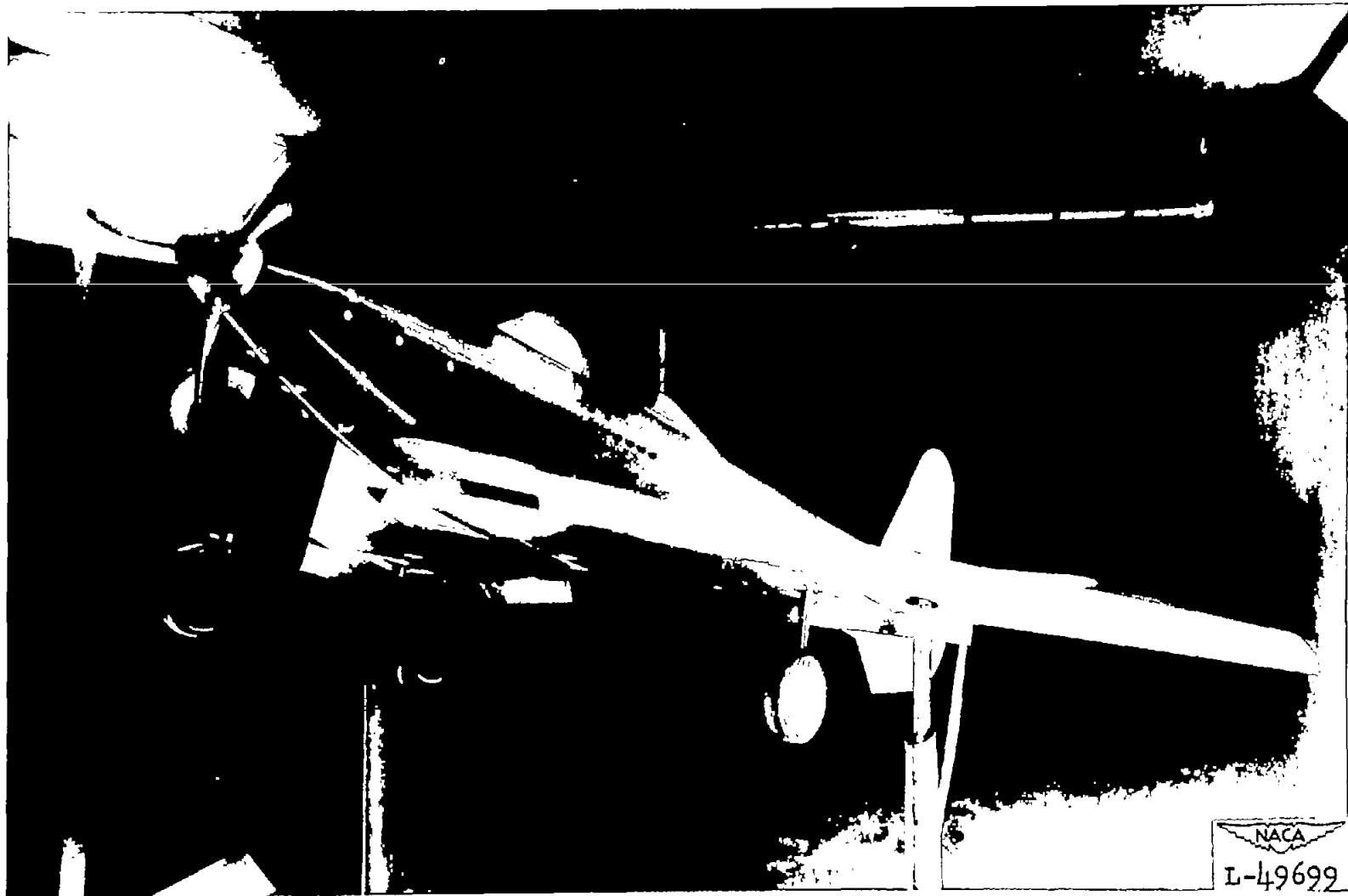
Figure 9.- The $\frac{1}{4.5}$-scale model of test airplane equipped with circular-arc leading edges. $\delta_{f_n} = 15°$.
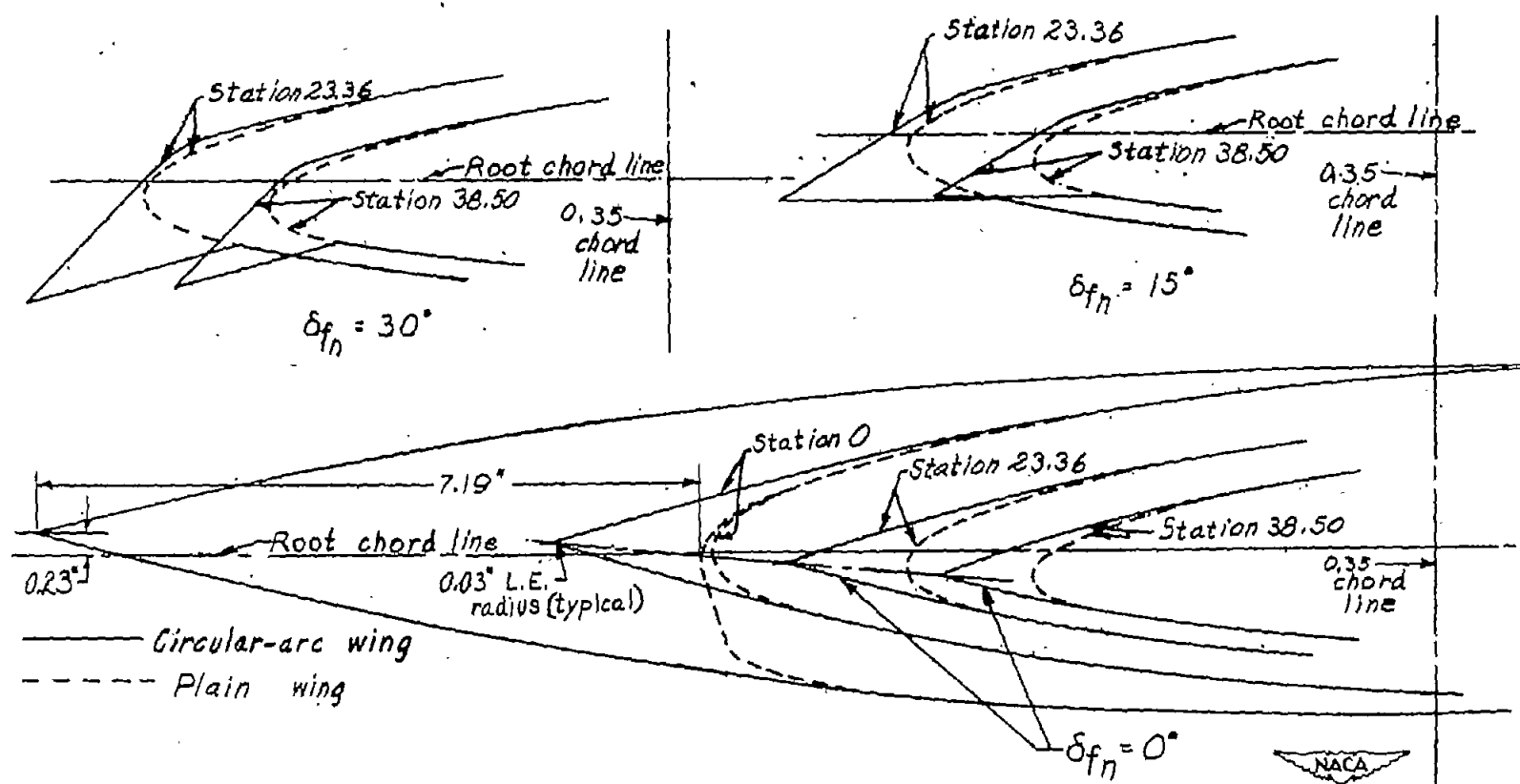
Figure 10.- Sections of circular-arc wing of $\frac{1}{4.5}$ -scale model of test airplane.

Ventral fin 2

Ventral fin I

Ventral fin 3

Model dimensions

Station 51.44

Station 68.88

2.19

10.667

$i_t = -3°$

$i_t = 1°$

4°

10.667

NACA

Tail configuration
Original
Airplane modification (scaled down)
Model modification
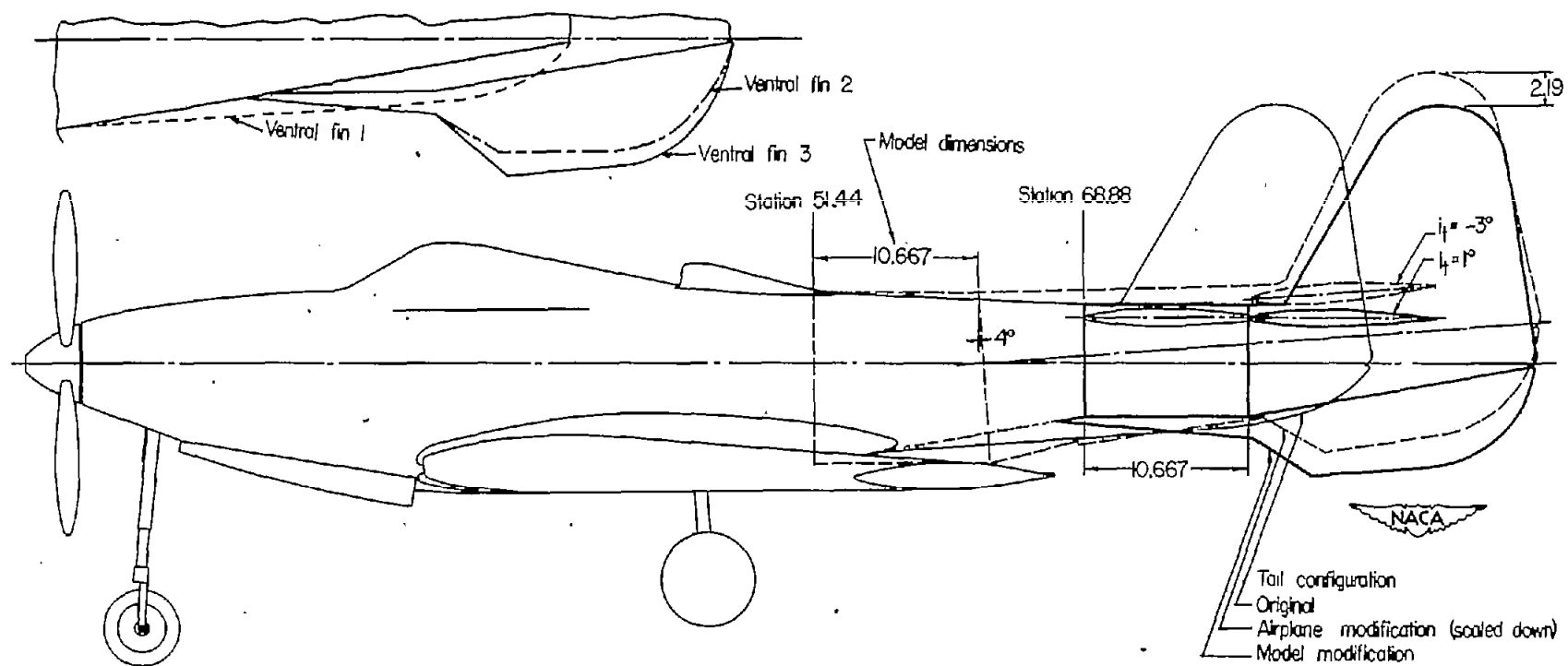
Figure 11.- Tail modifications of test airplane and model. (All linear dimensions are in inches.)
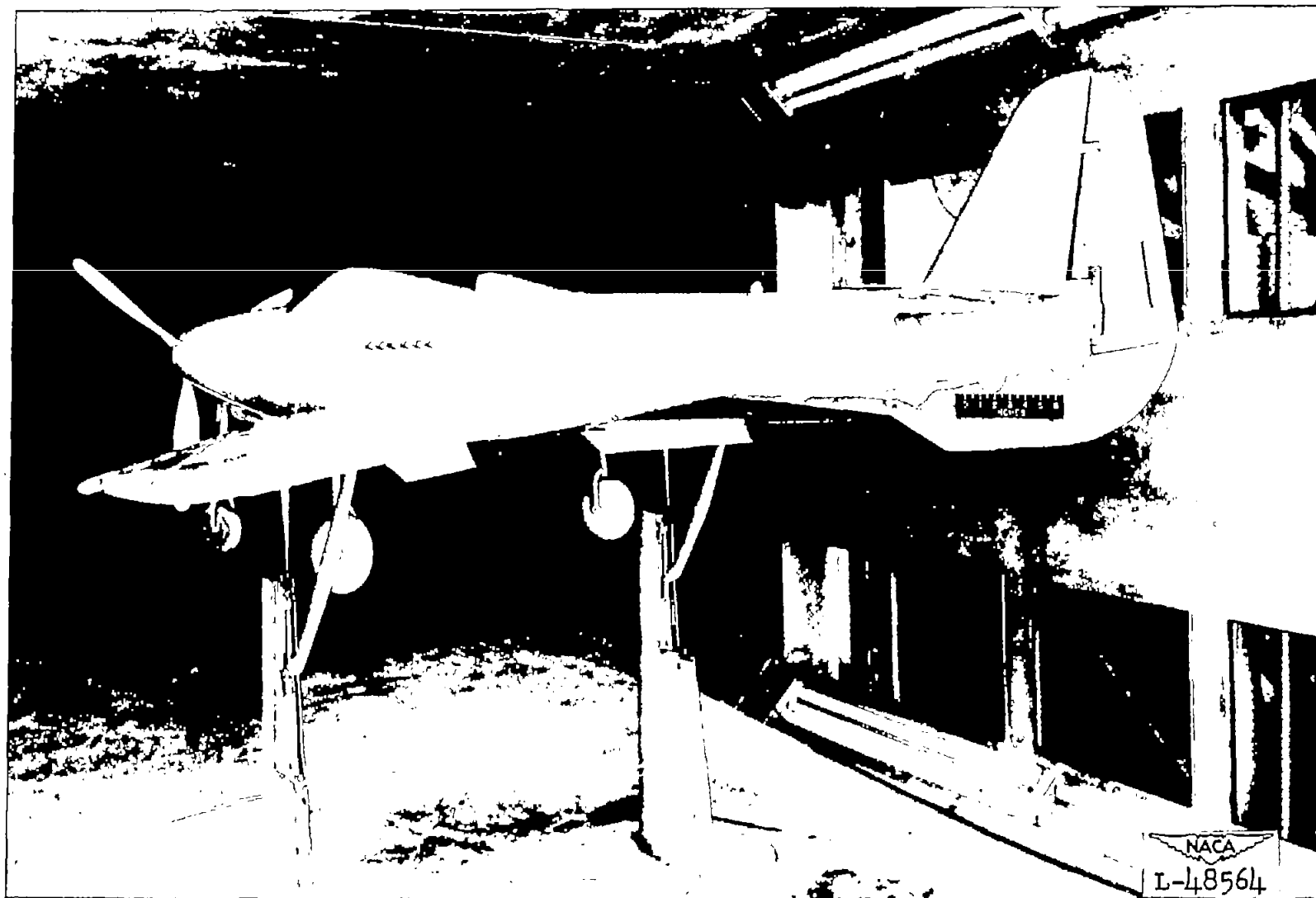
Figure 12.- The $\frac{1}{4.5}$-scale model of the test airplane. Extended fuselage; ventral fin 2; slots extended.
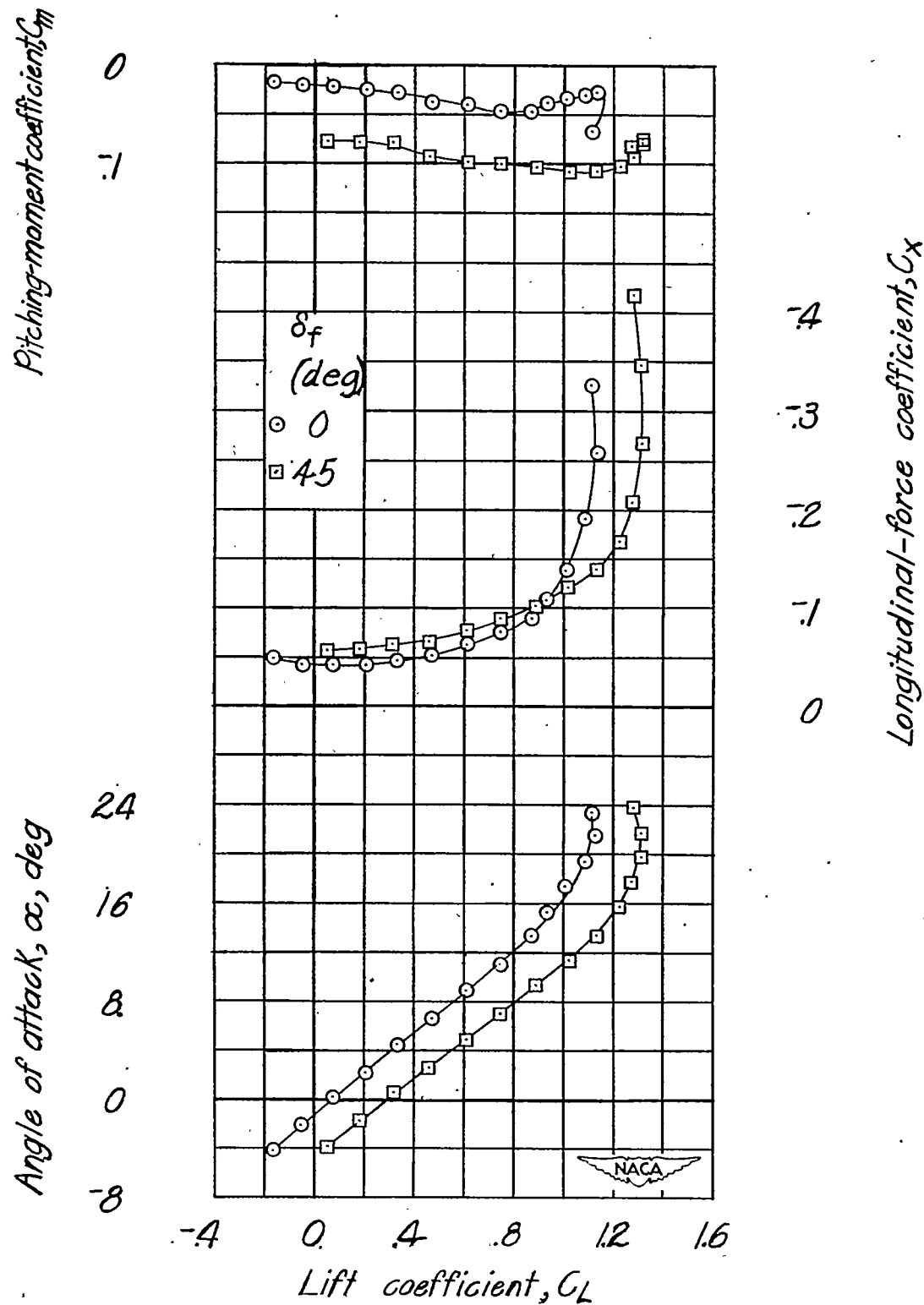
Figure 13.- Effect of flap deflection on aerodynamic characteristics in pitch. Wing alone; 80-percent-span slots; R = 2.05 × 10^6.
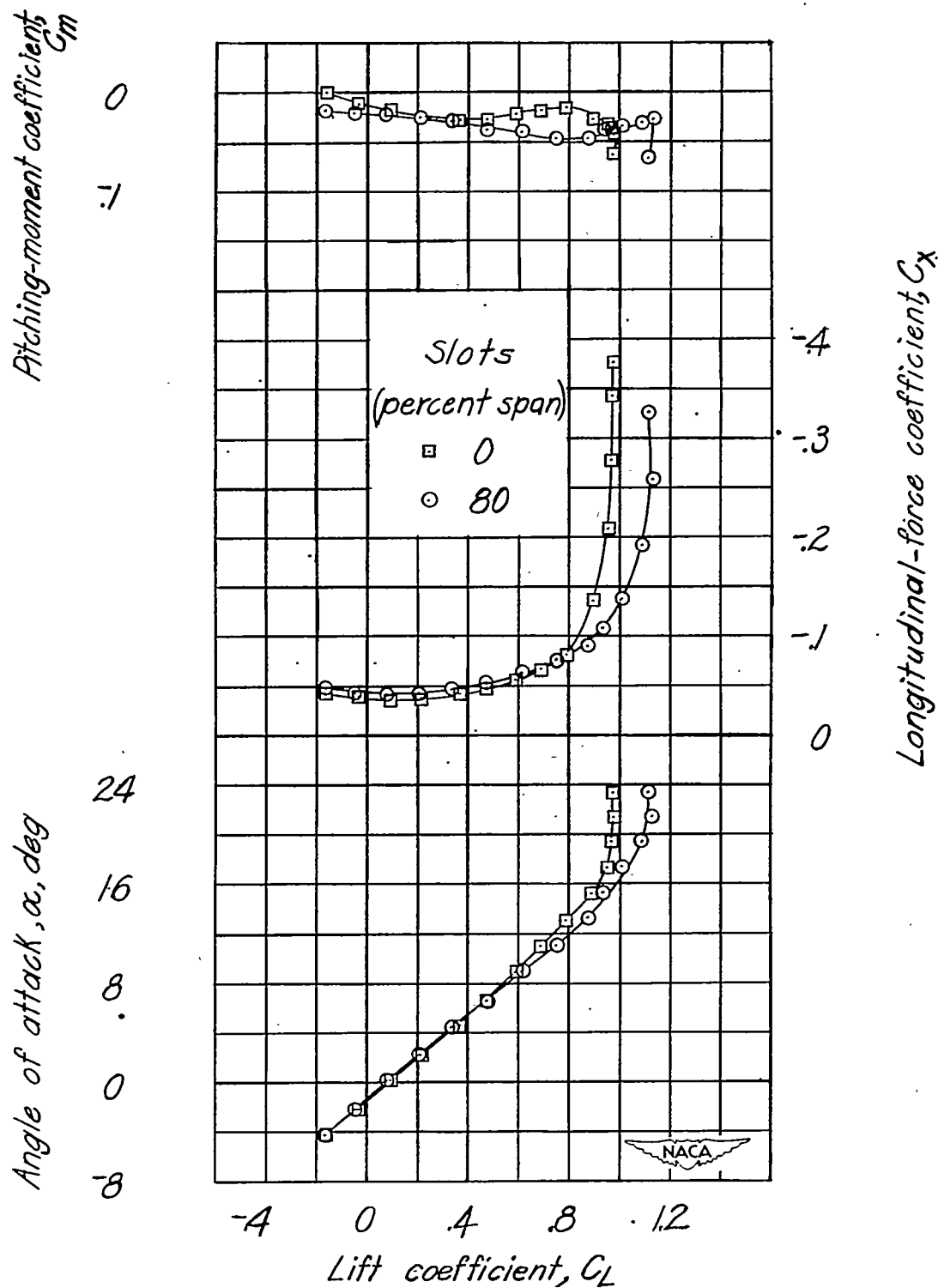
Figure 14.- Effect of slot extension on aerodynamic characteristics in pitch. Wing alone; $\delta_f = 0°$; landing gear on; $R = 2.05 \times 10^6$.
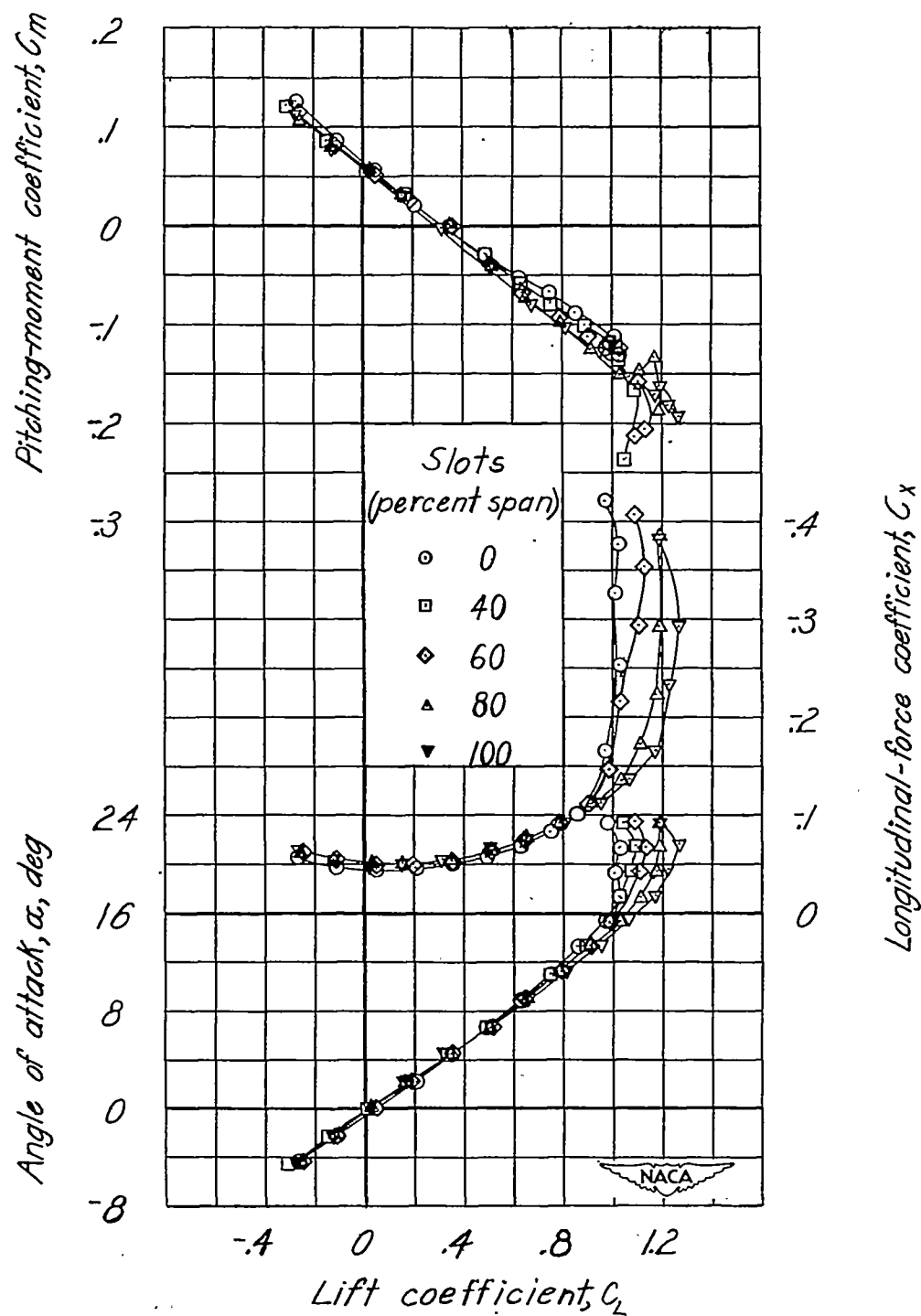
(a) $\delta_f = 0°$.

Figure 15.- Effect of slot extension on aerodynamic characteristics in pitch.
Propeller off; $i_t = -0.9°$; R = 2.05 × 10⁶.

Pitching-moment coefficient, C_m

Slots
(percent span)

o   0
□   40
◇   60
△   80
▽   100

$C_L = 0$

0

0

0

0

.2   .1   0   -.1   -.2   -.3

-.8   -.4   0   .4   .8   1.2

Lift coefficient, C_L

NACA
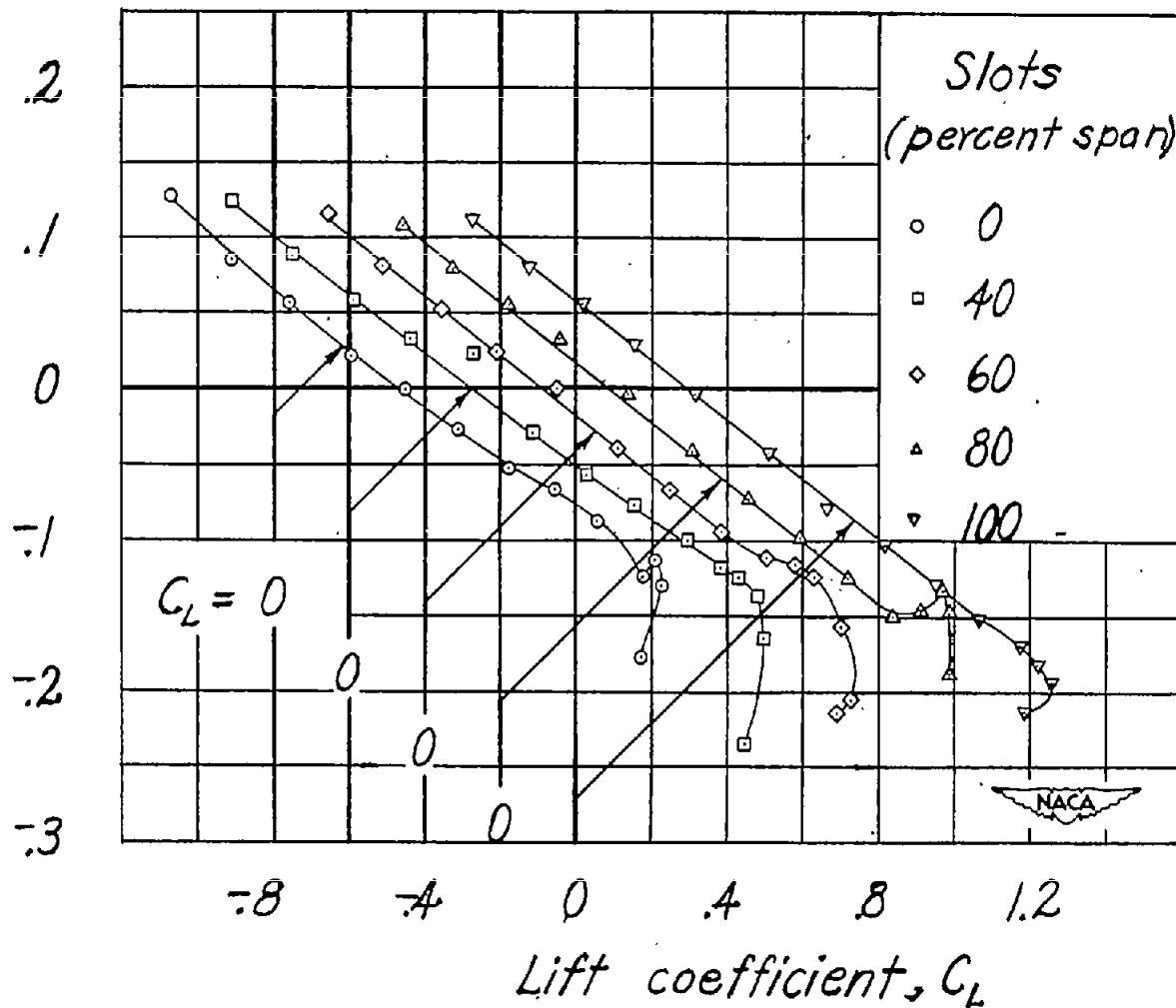
(a) Concluded.

Figure 15.- Continued.

(b) $\delta_f = 45^o$.
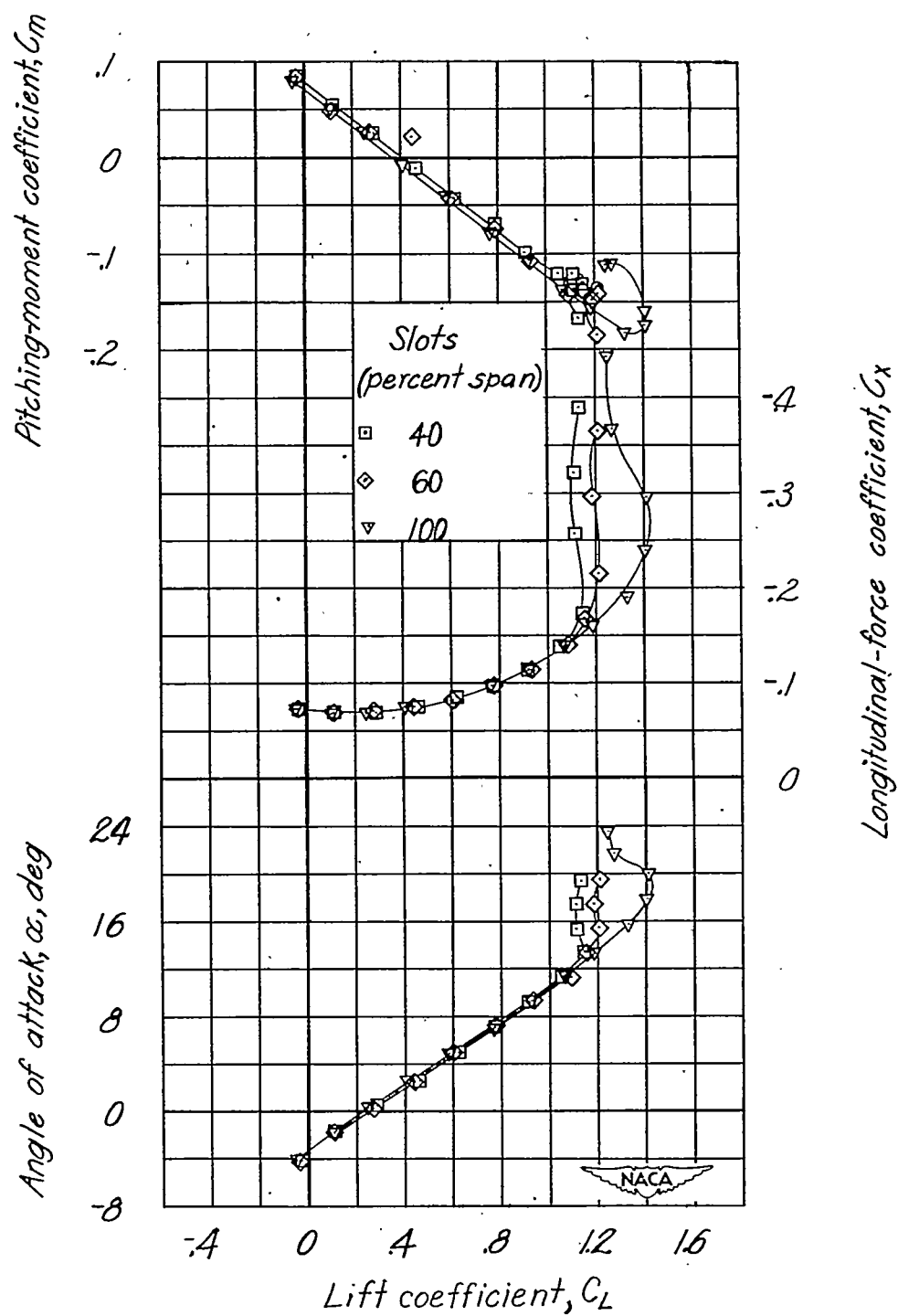
Figure 15.- Continued.
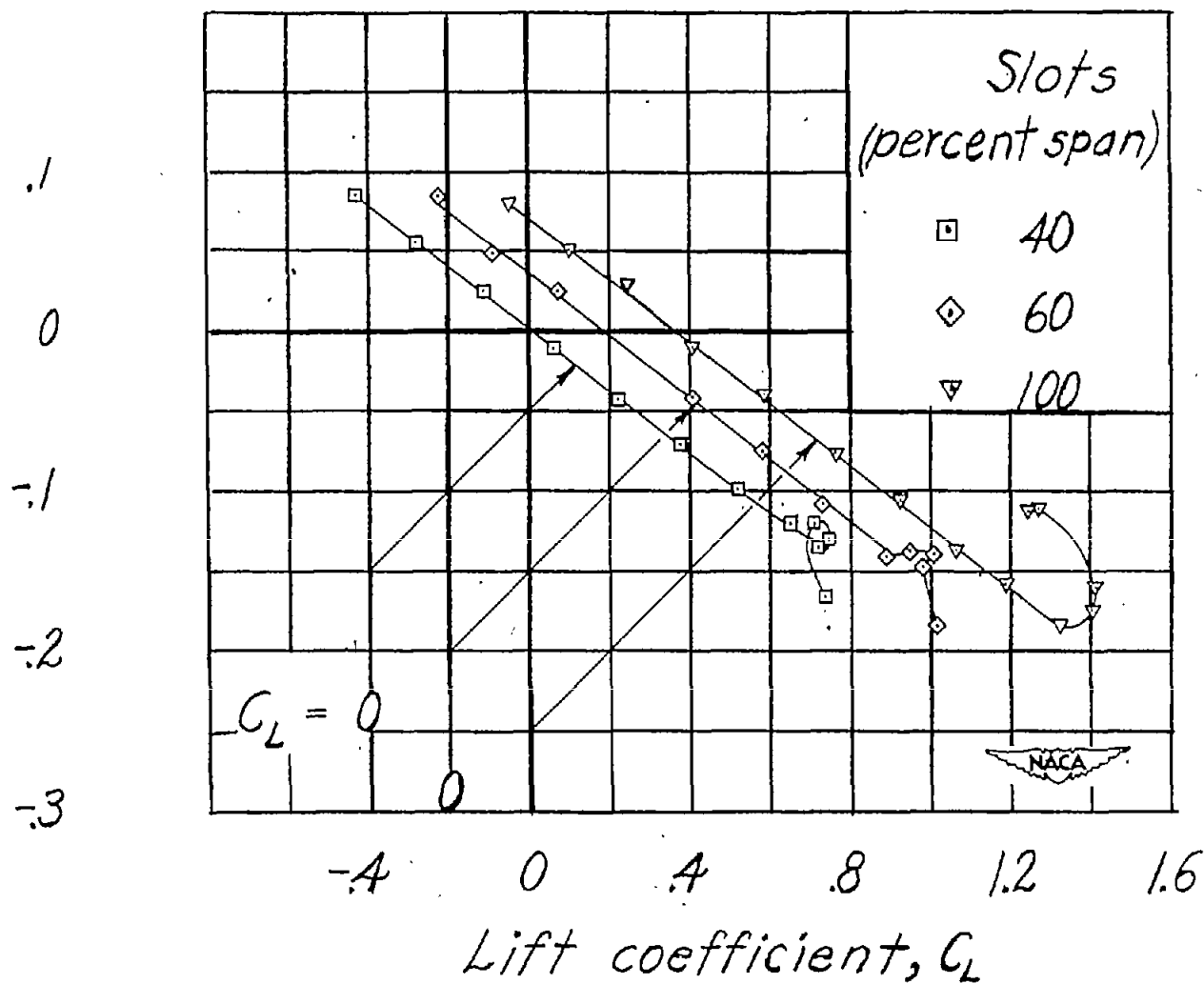
(b) Concluded.

Figure 15.- Concluded.
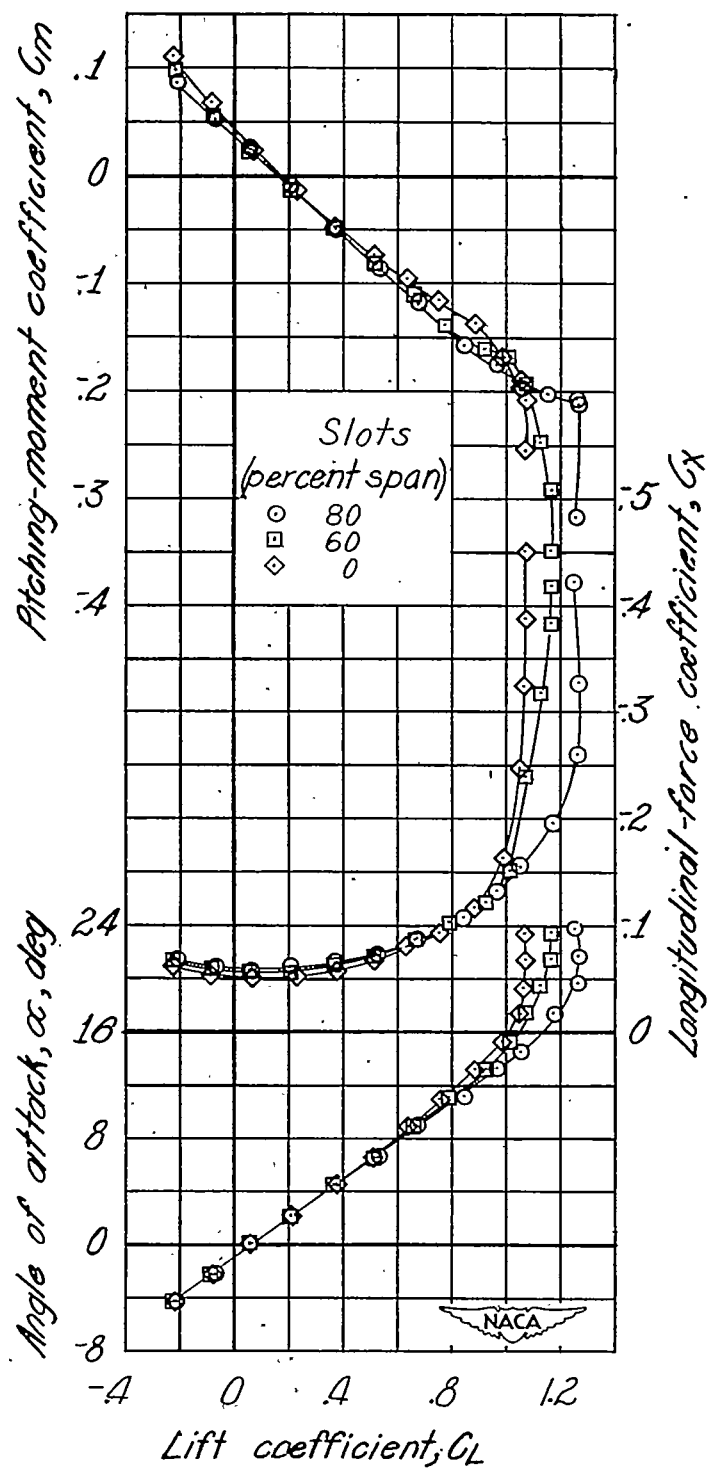
Figure 16.- Effect of slot extension on aerodynamic characteristics in pitch. Windmilling propeller; extended fuselage; i_t = 1.0°; δ_f = 0°; R = 2.05 × 10⁶.
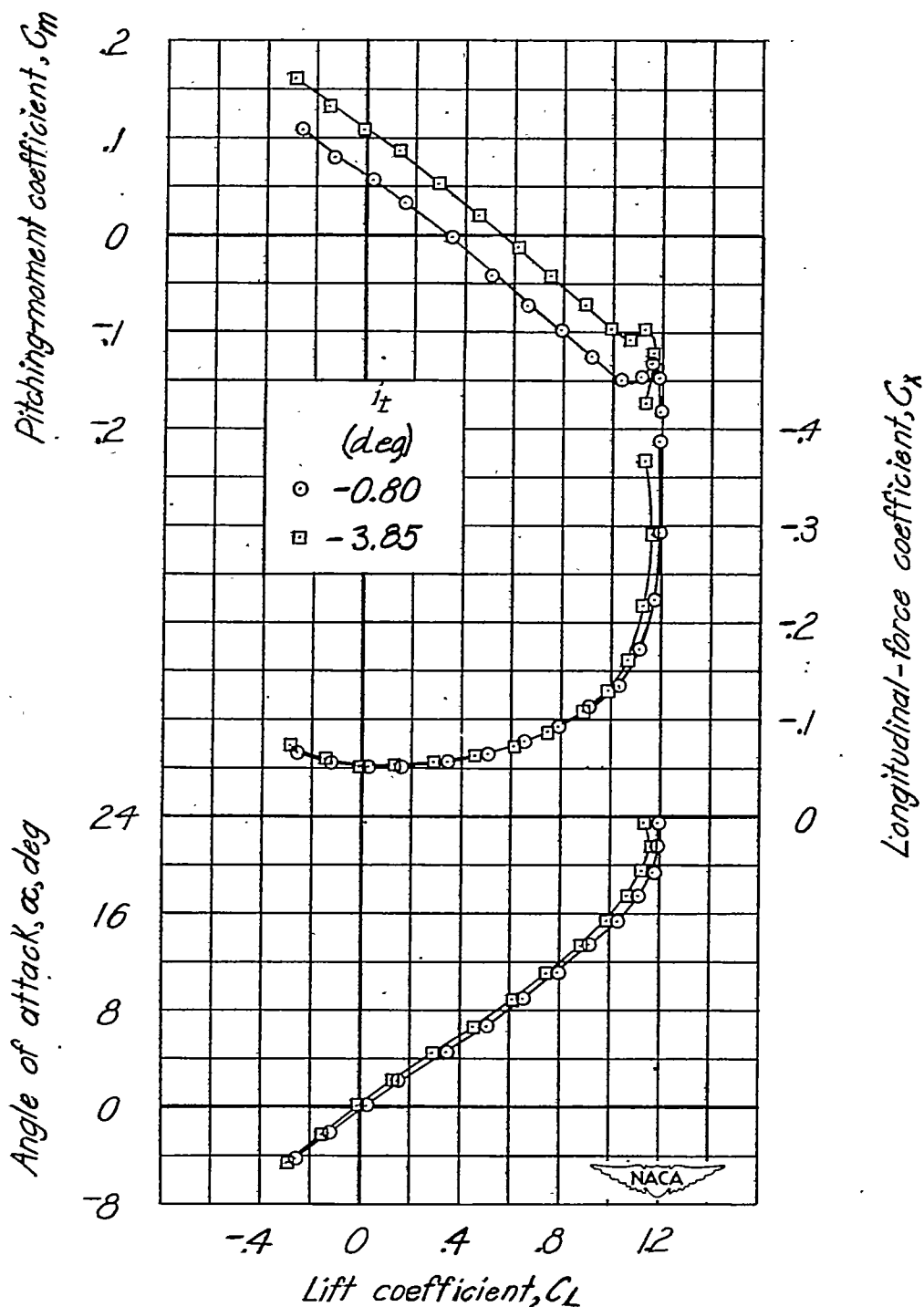
Figure 17.-   Effect of stabilizer on aerodynamic characteristics in pitch.
Propeller removed: δ_r = 0°: 80-percent-span slots;   R = 2.05 × 10⁶.
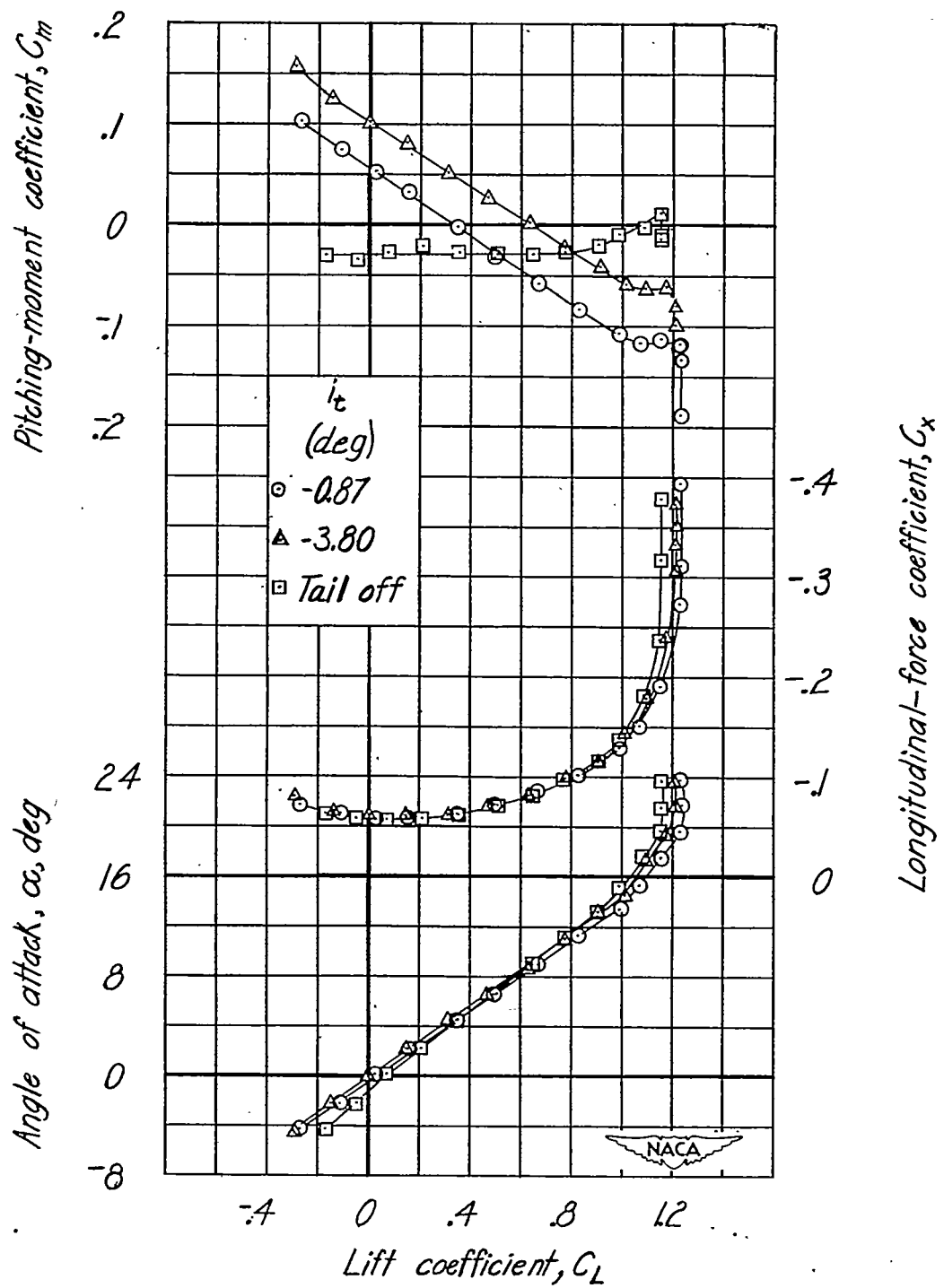
(a) $\delta_f = 0°$.

Figure 18.-   Effect of stabilizer on aerodynamic characteristics in pitch.
Windmilling propeller;   80-percent-span slots;   R = 2.05 x 10^6.
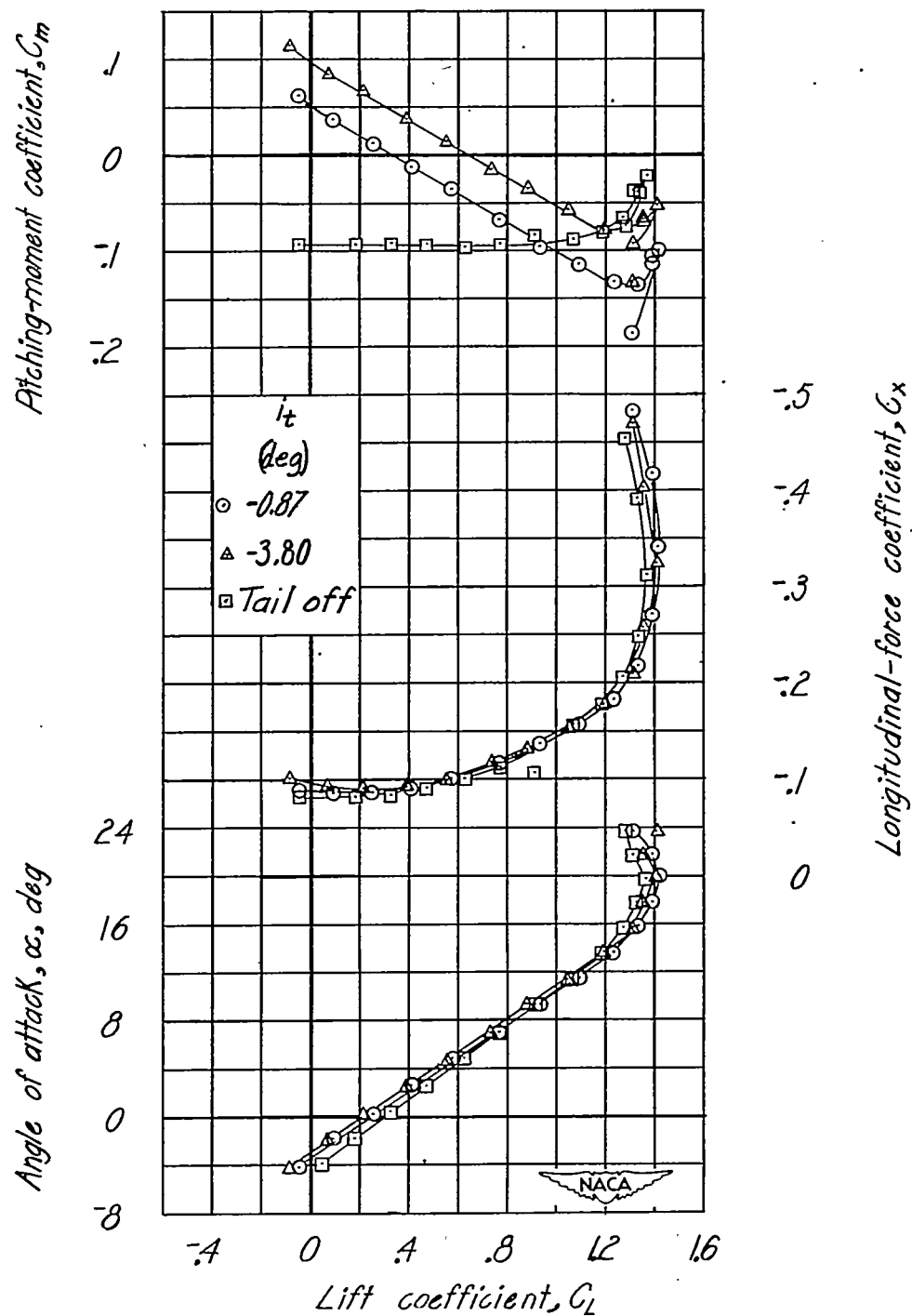
(b) $\delta_f = 45^\circ$.

Figure 18.- Concluded.
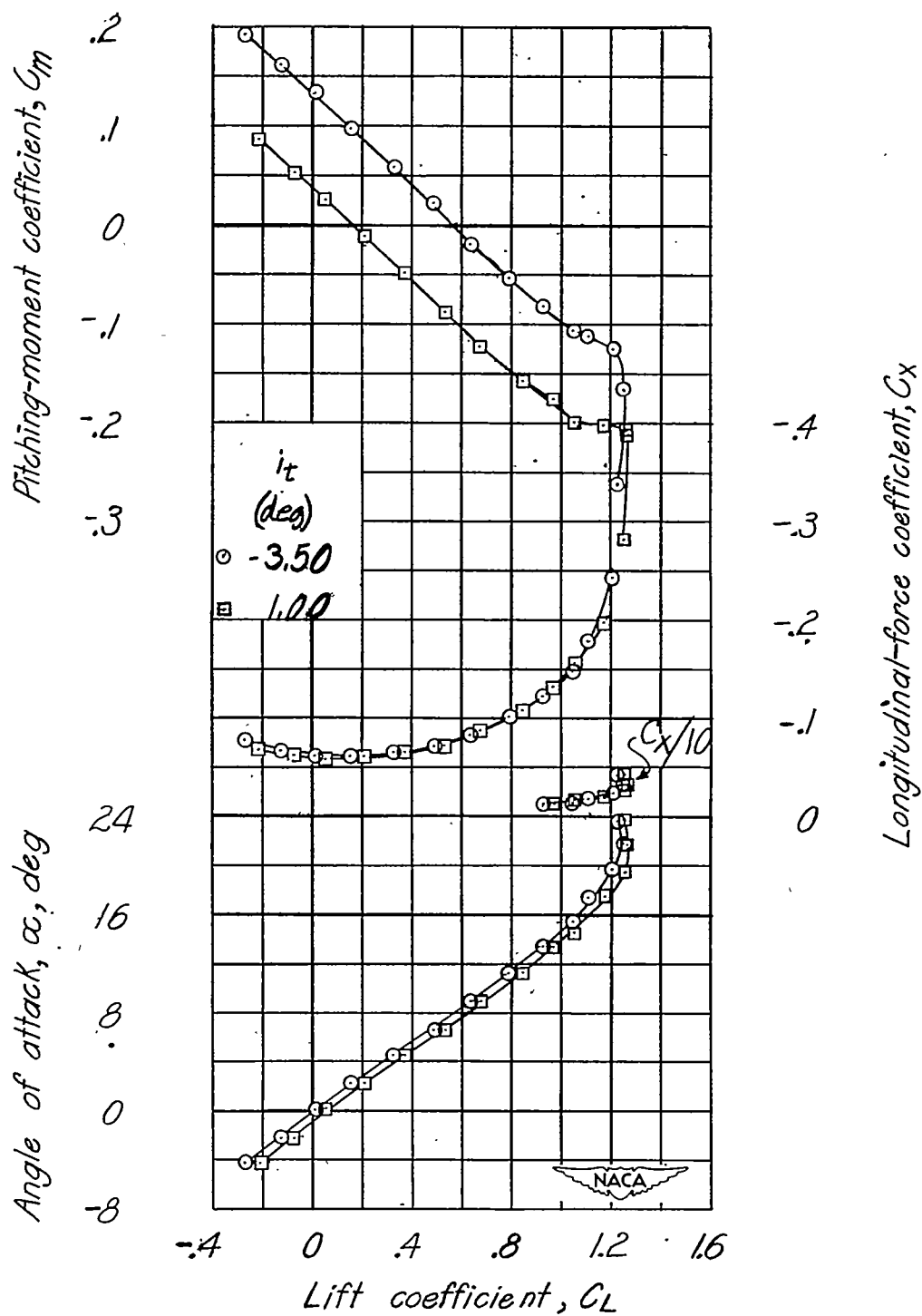
(a) $\delta_f = 0°$.

Figure 19.- Effect of stabilizer on aerodynamic characteristics in pitch. Windmilling propeller; extended fuselage; 80-percent-span slots; $R = 2.05 \times 10^6$.
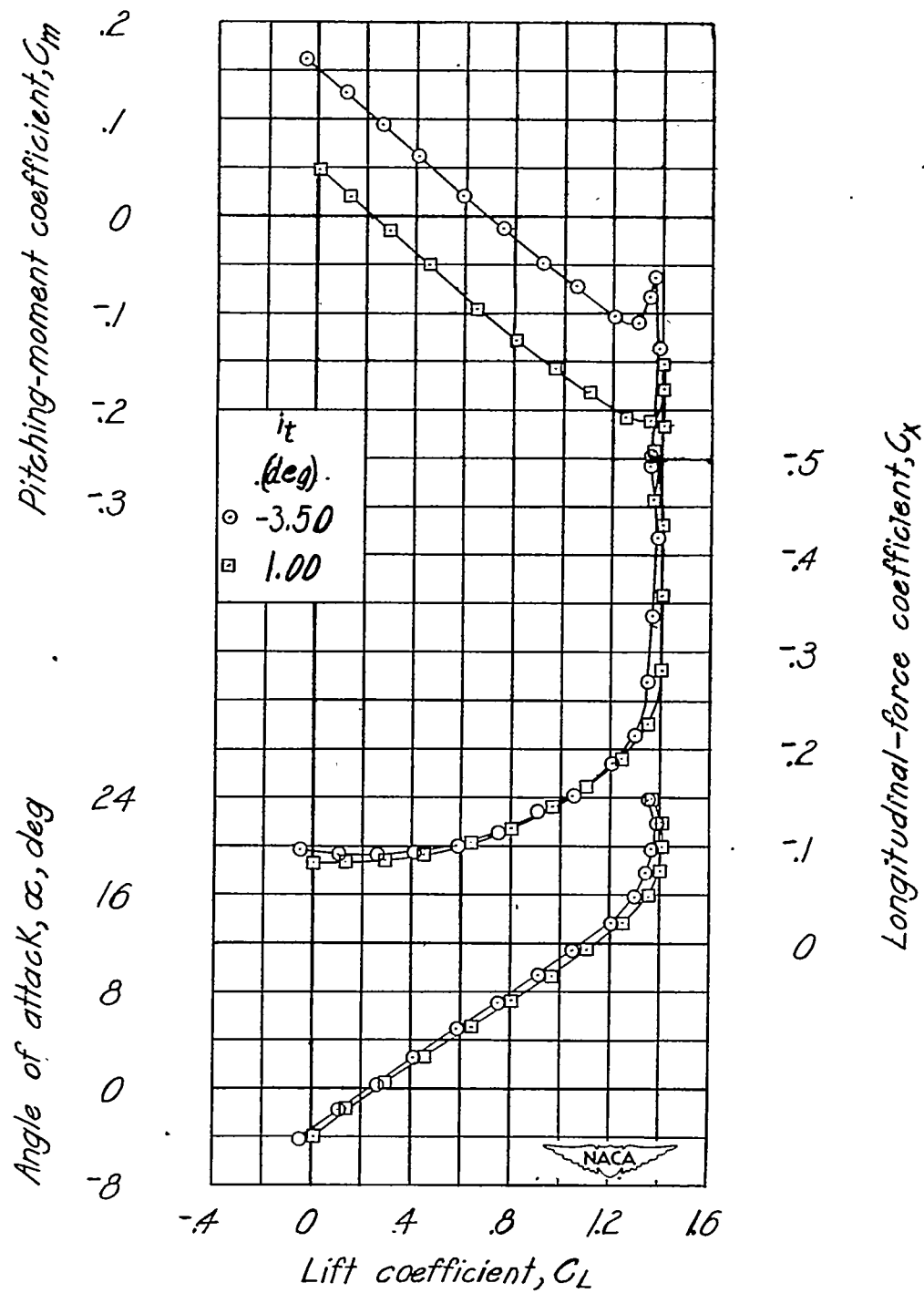
(b) $\delta_f = 45°$.

Figure 19.- Concluded.
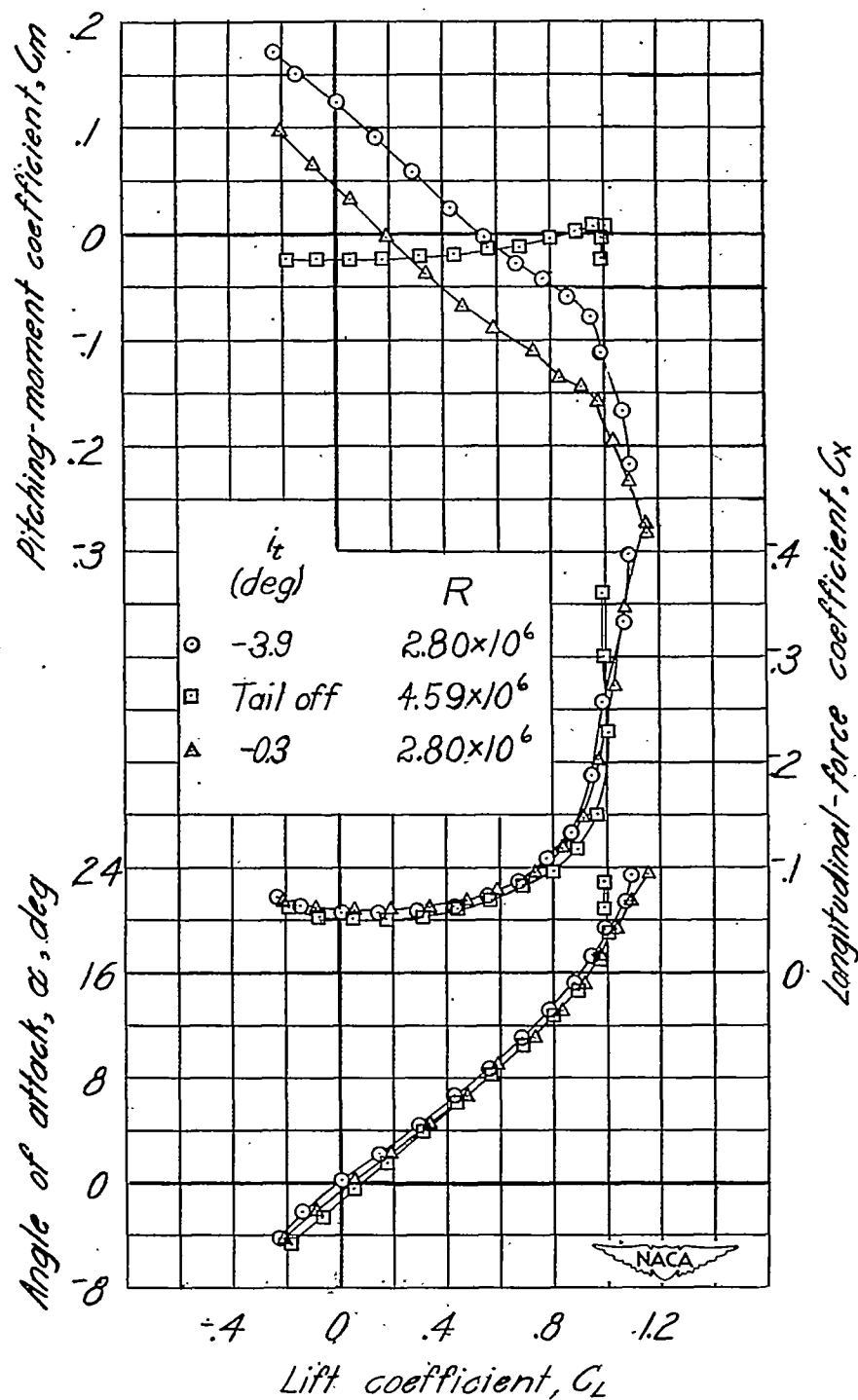
(a) $\delta_f = 0°$.

Figure 20.- Effect of stabilizer on aerodynamic characteristics in pitch.
Windmilling propeller; extended fuselage; 40-percent-span slots.
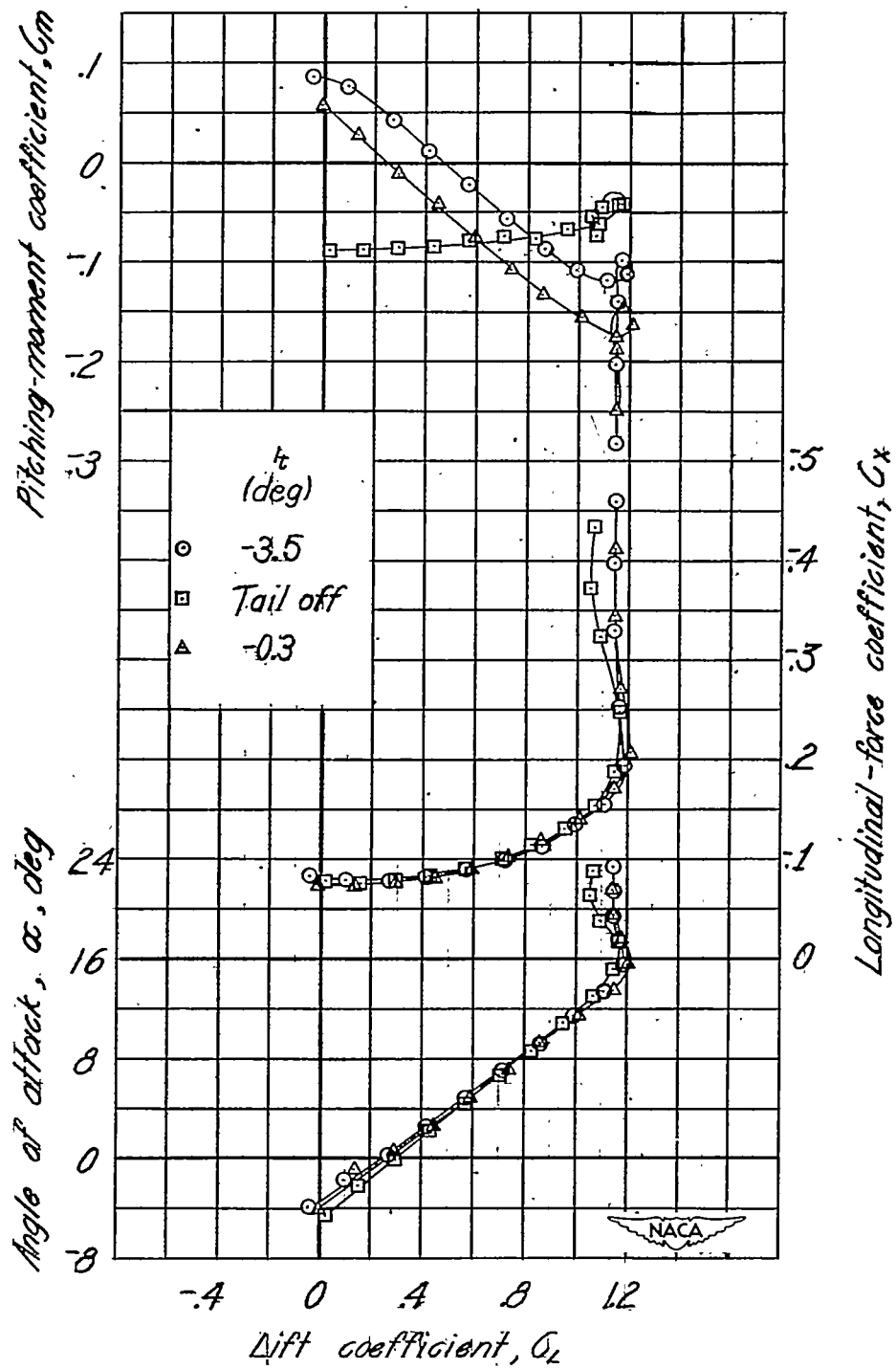
(b) $\delta_f = 45^o$; R = 4.59 × 10^6.

Figure 20.- Concluded.
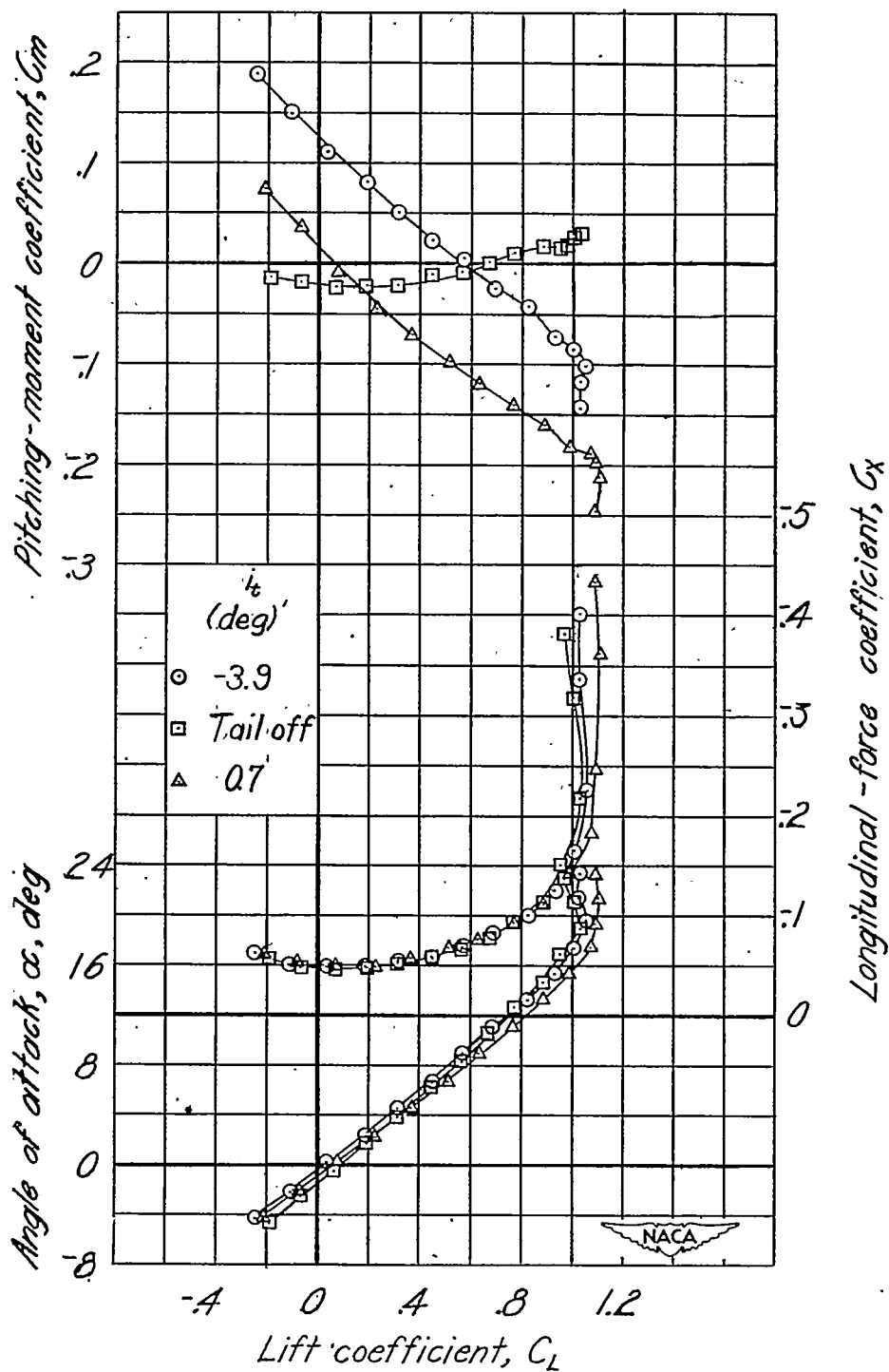
Figure 21.- Effect of stabilizer on aerodynamic characteristics in pitch. Windmilling propeller; extended fuselage; 0-percent-span slots; $\delta_f = 0^\circ$; $R = 4.59 \times 10^6$.
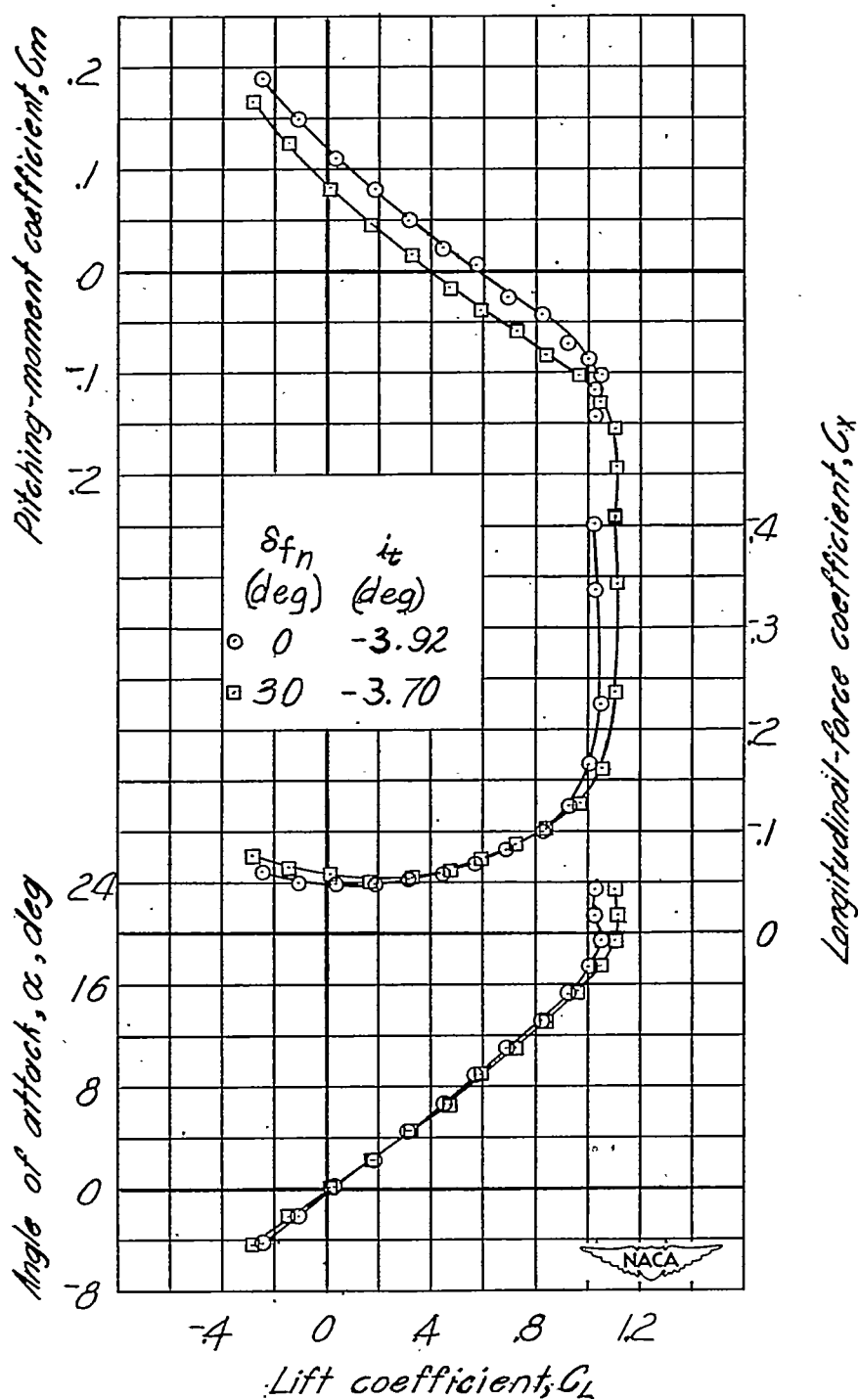
Figure 22.- Effect of nose-flap deflection on aerodynamic characteristics in pitch. Windmilling propeller; extended fuselage; $\delta_f = 0^\circ$; $R = 4.59 \times 10^6$.

Figure 23.- Effect of faired center section on aerodynamic characteristics
in pitch. Windmilling propeller; extended fuselage; i_t = -3.9°; δ_f = 0°;
0-percent-span slots; R = 4.59 x 10⁶.
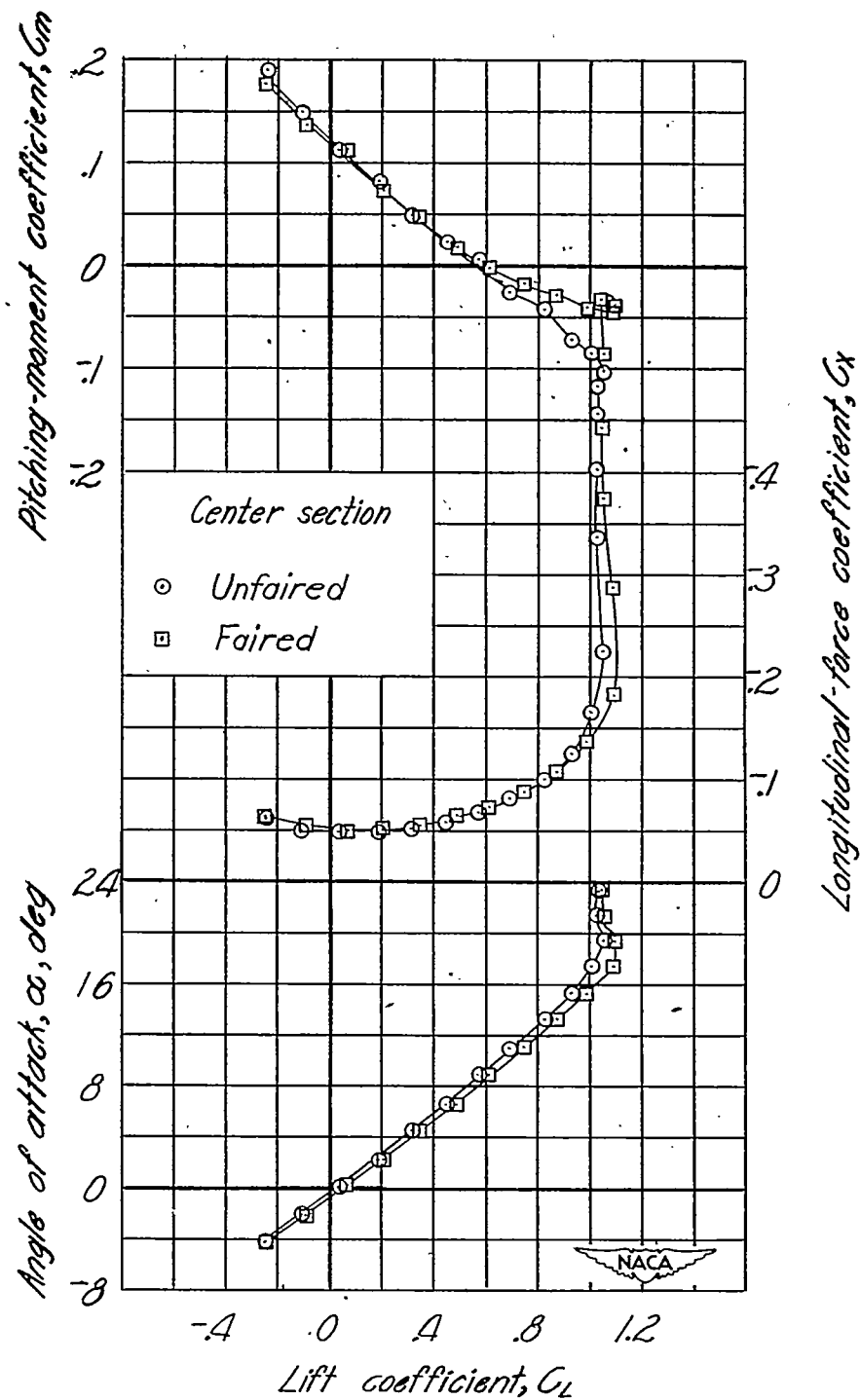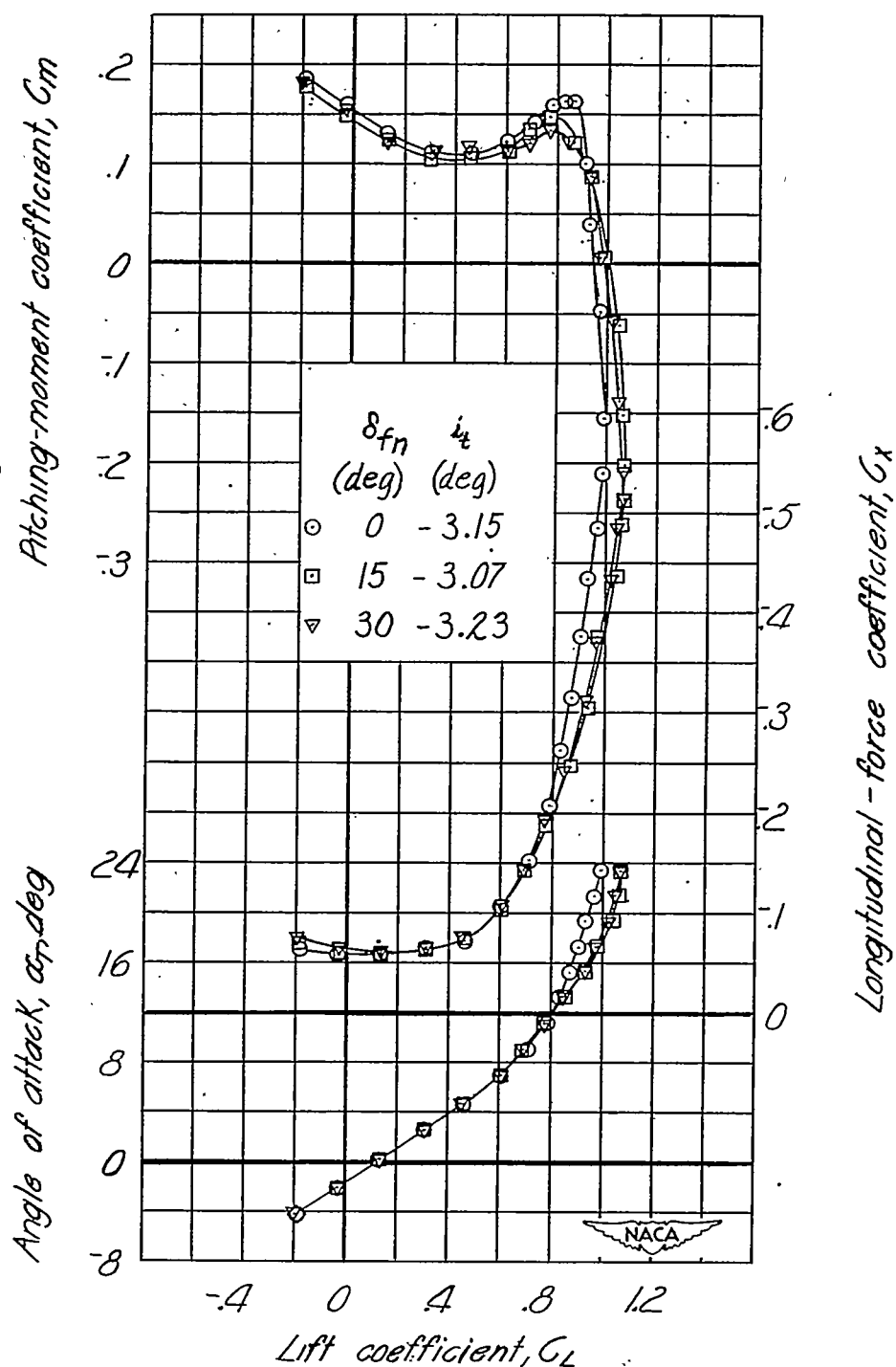
Figure 24.- Effect of nose-flap deflection on aerodynamic characteristics
in pitch of model with circular-arc wing. Windmilling propeller;
extended fuselage; $\delta_f = 0^o$; $R = 2.35 \times 10^6$.
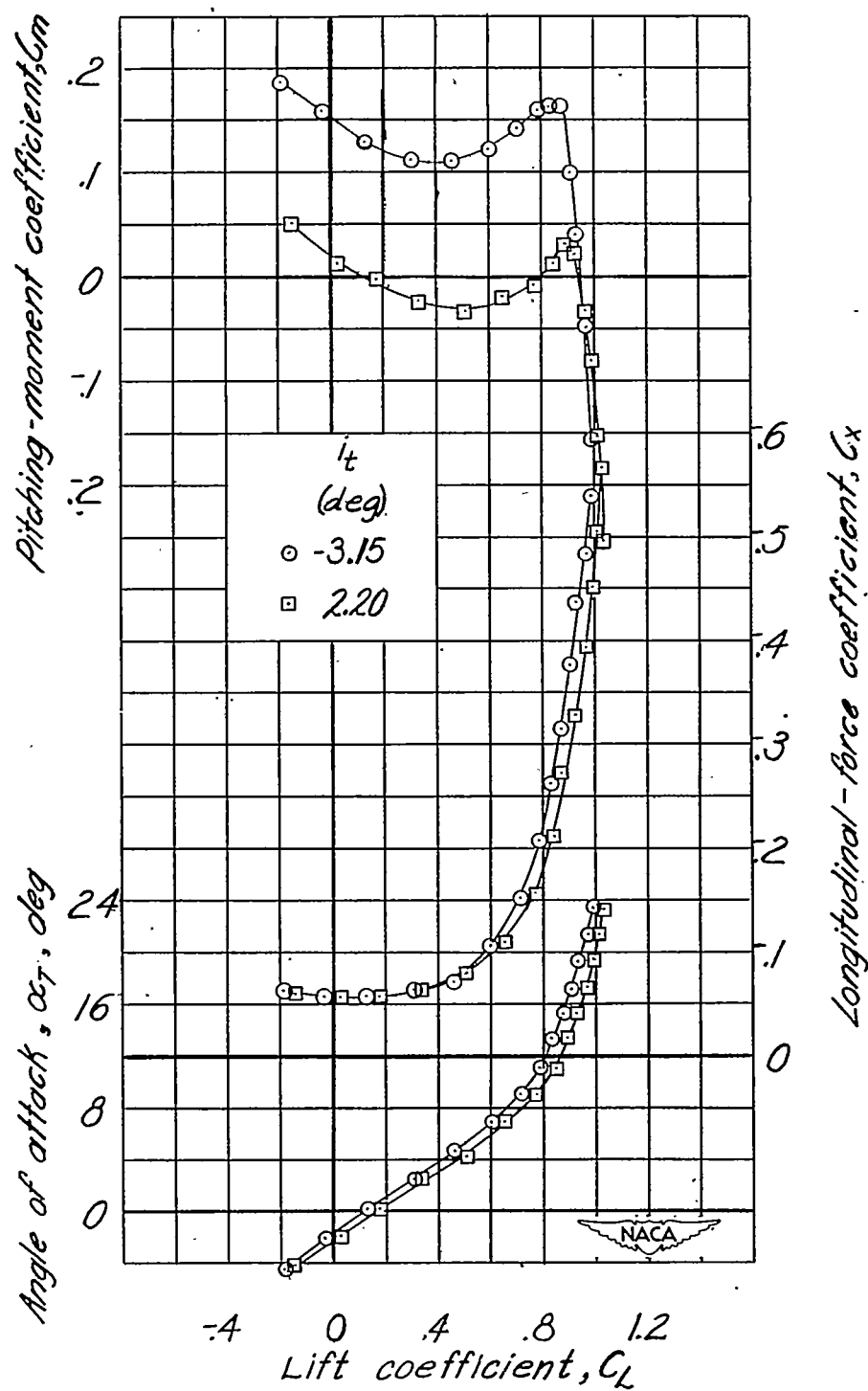
(a) $\delta_f = 0°$; $\delta_{f_n} = 0°$.

Figure 25.- Effect of stabilizer on aerodynamic characteristics in pitch of
model with circular-arc wing. Windmilling propeller; extended fuselage;
R = 2.35 × 10^{6}.

(b) $\delta_f = 0^o$; $\delta_{f_n} = 15^o$.
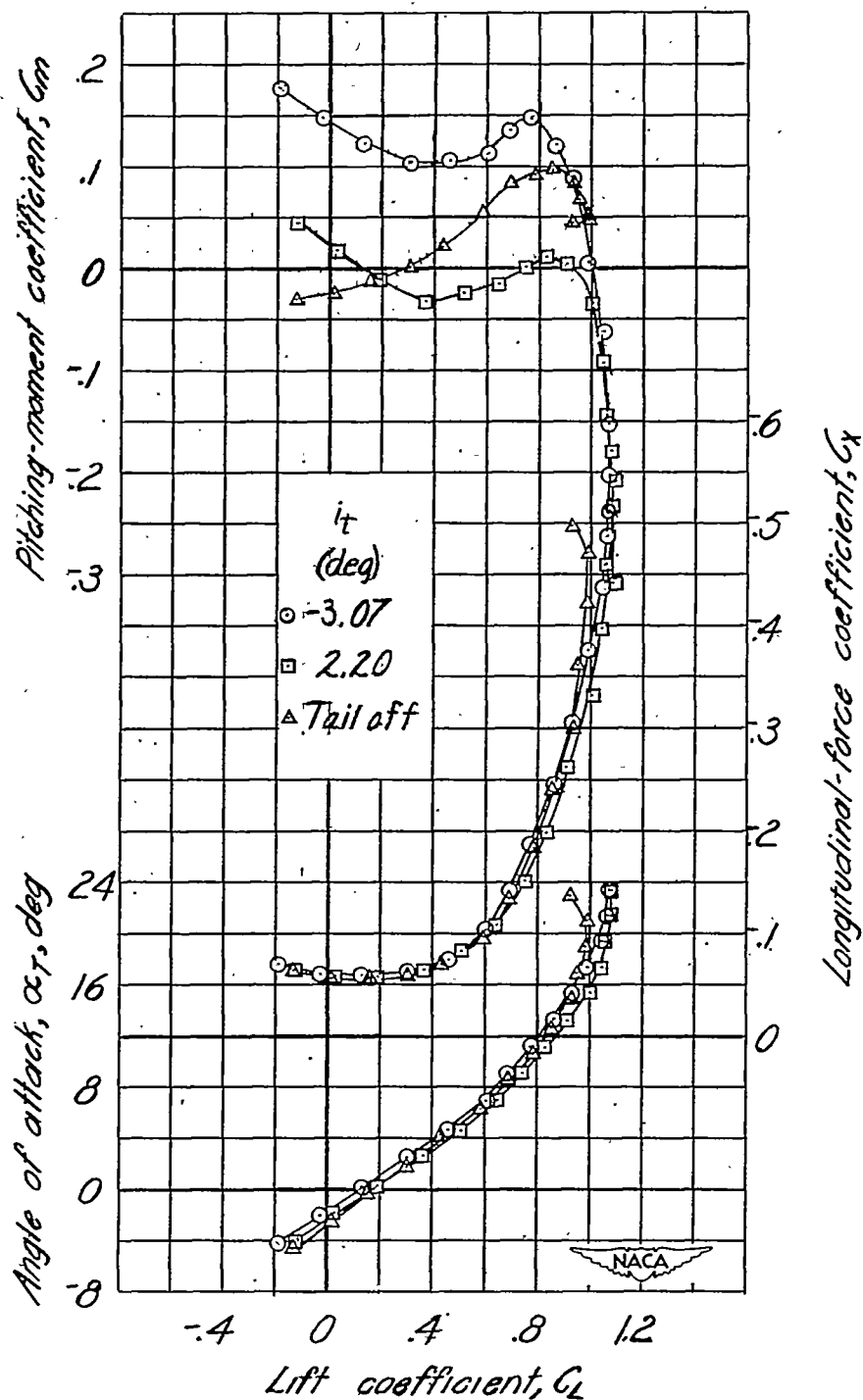
Figure 25.- Continued.
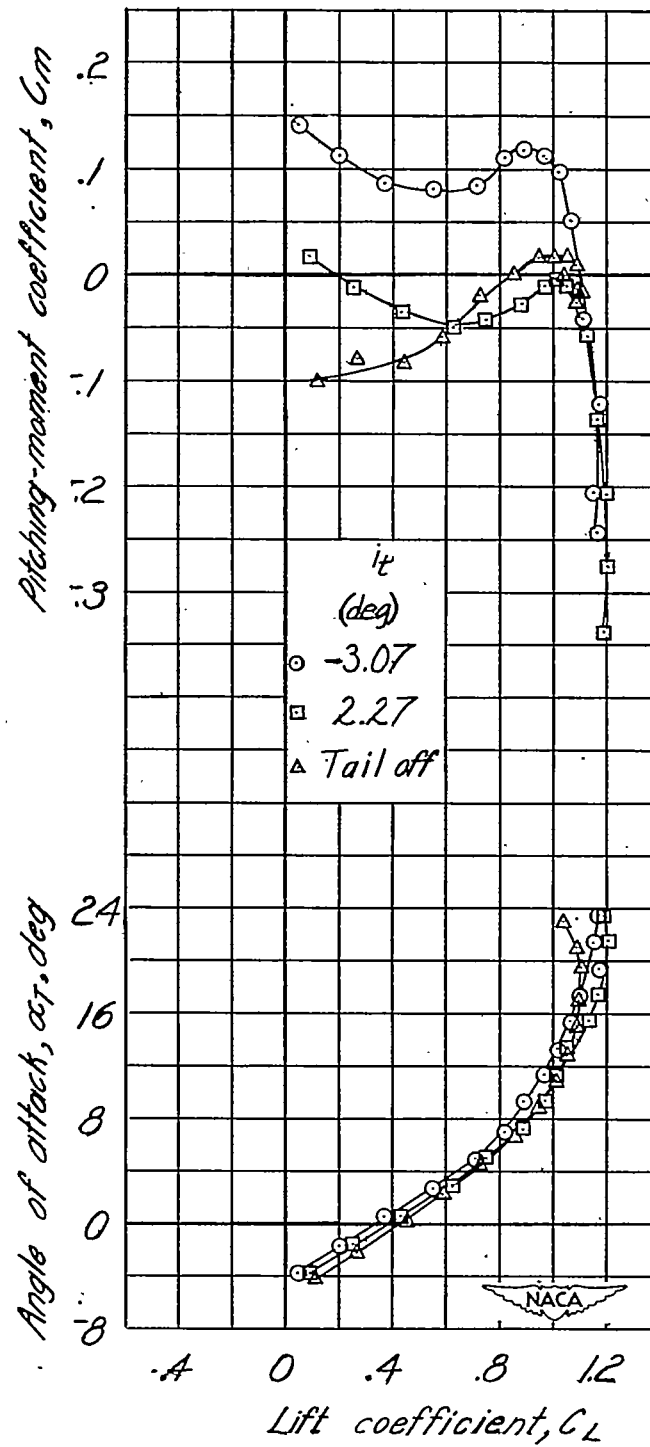
(c) $\delta_f = 45^\circ$; $\delta_{f_n} = 15^\circ$.

Figure 25.- Continued.
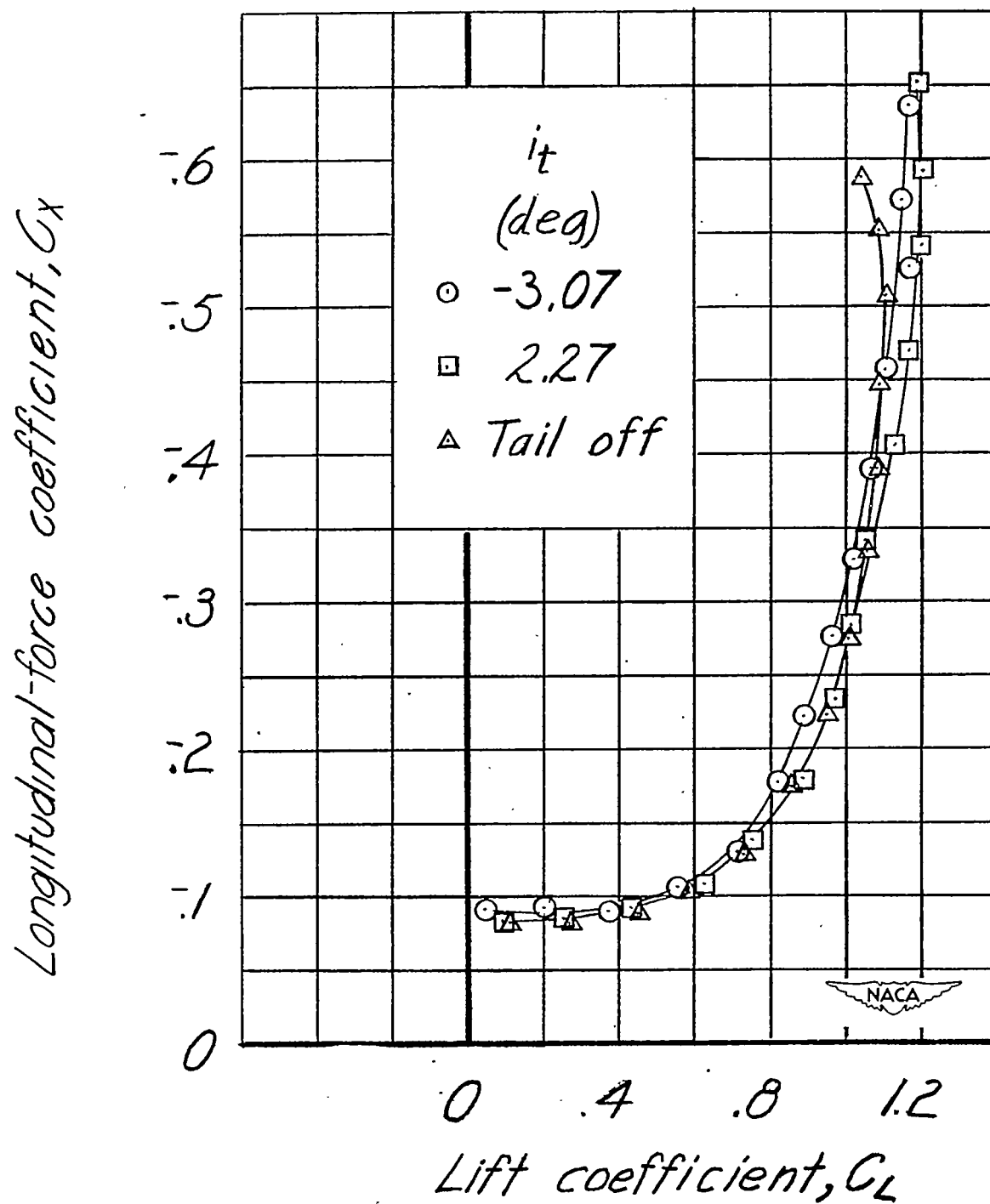
(c) Concluded.

Figure 25.- Concluded.
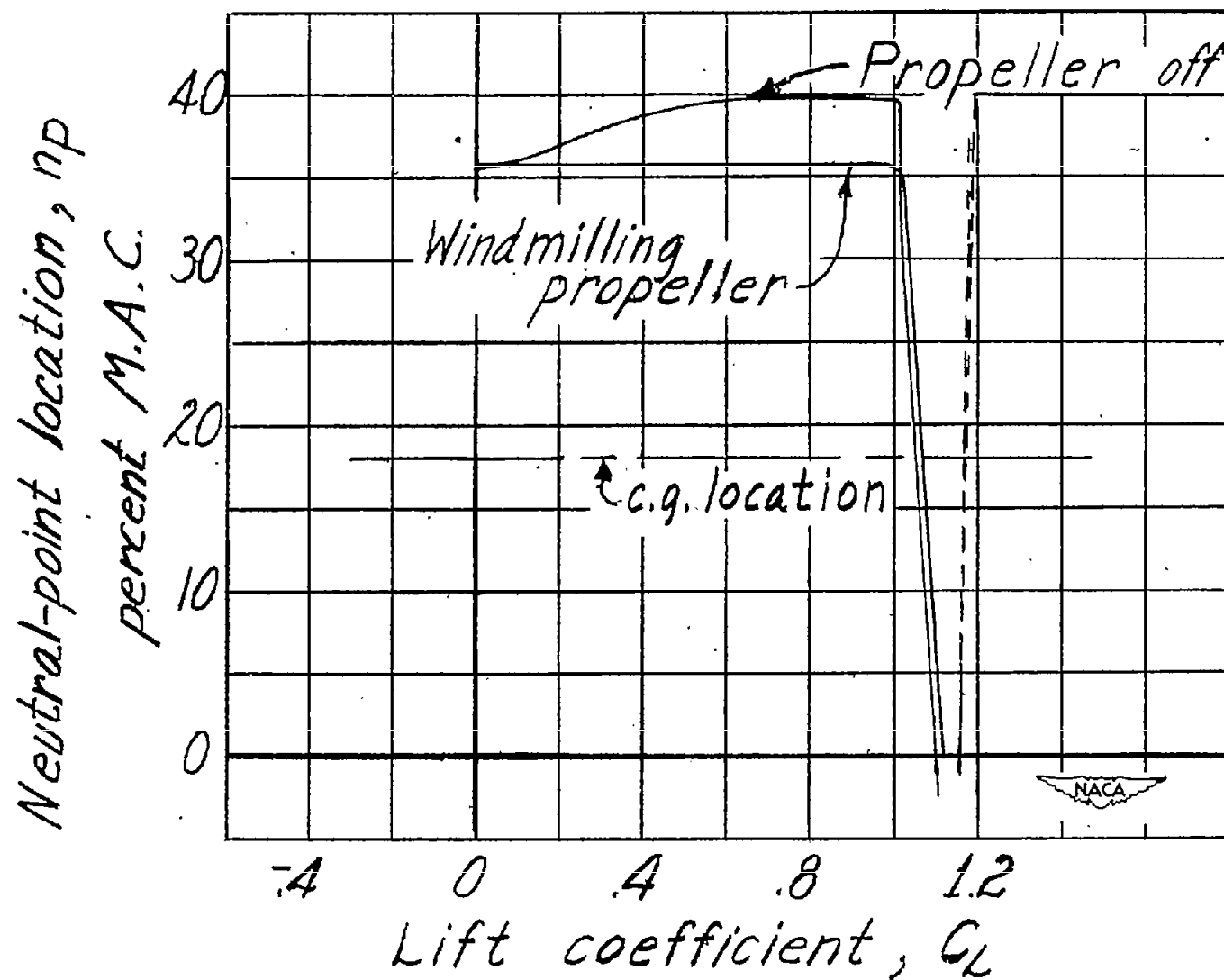
Figure 26.-   Effect of propeller on stick-fixed neutral points. $\delta_f = 0^\circ$; original model.
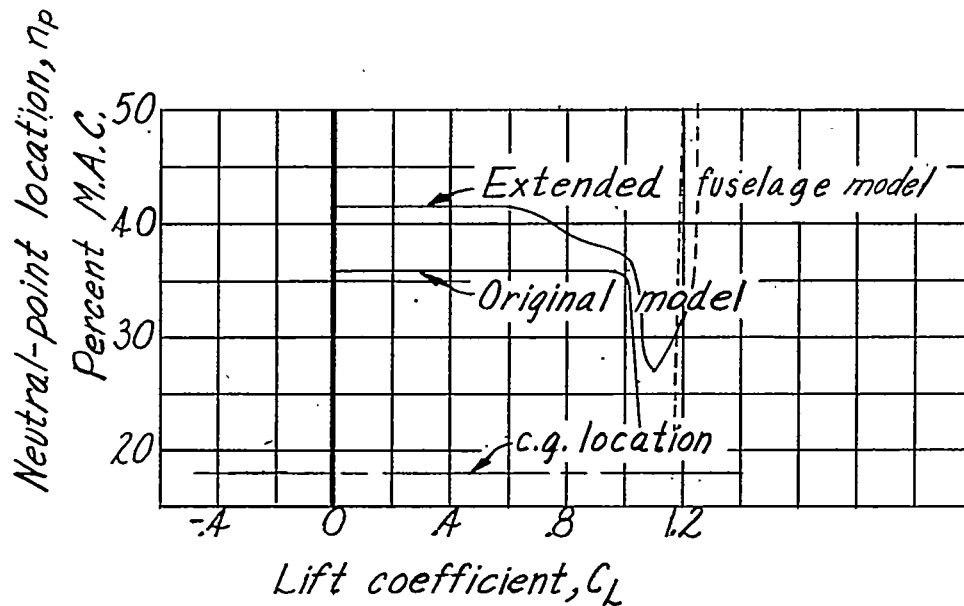
(a) $\delta_f = 0^\circ$.
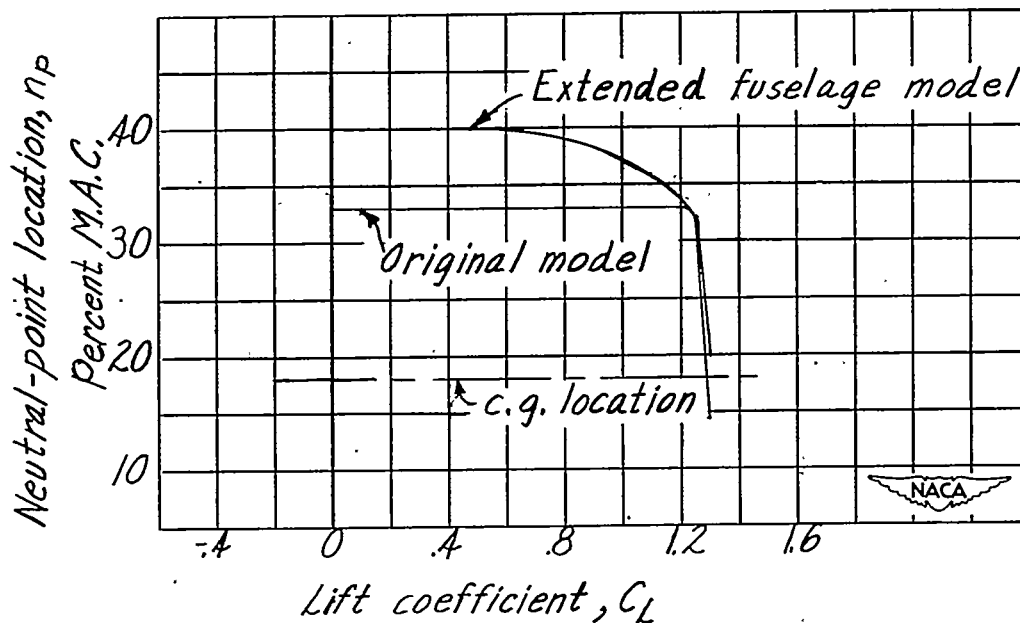
(b) $\delta_f = 45^\circ$.

Figure 27.- Effect of extended fuselage on stick-fixed neutral points. Windmilling
propeller; 80-percent-span slots; original wing.
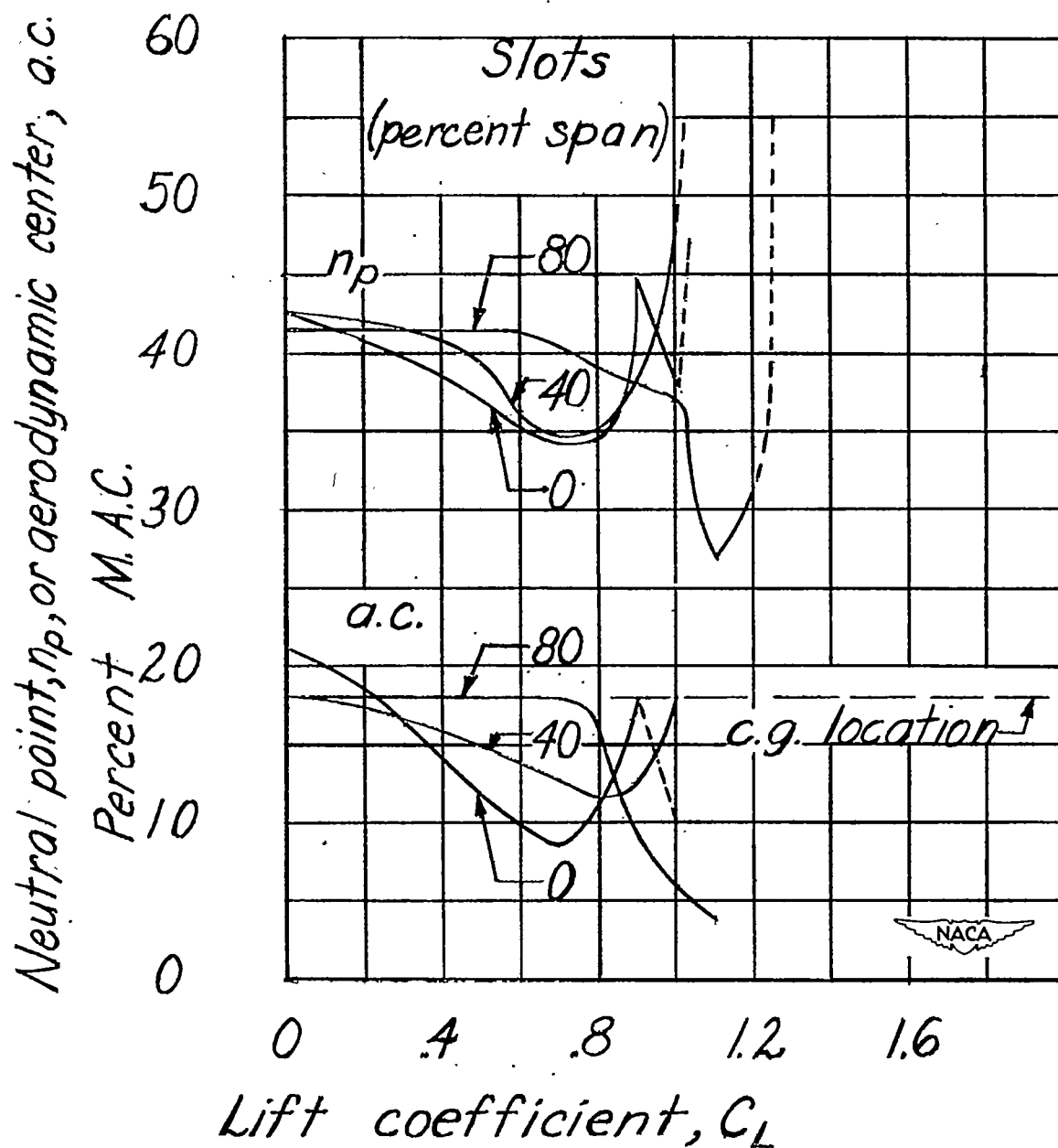
Figure 28.- Effect of slot extension on stick-fixed neutral points and aerodynamic-center locations. Windmilling propeller; extended fuselage; $\delta_f = 0°$.
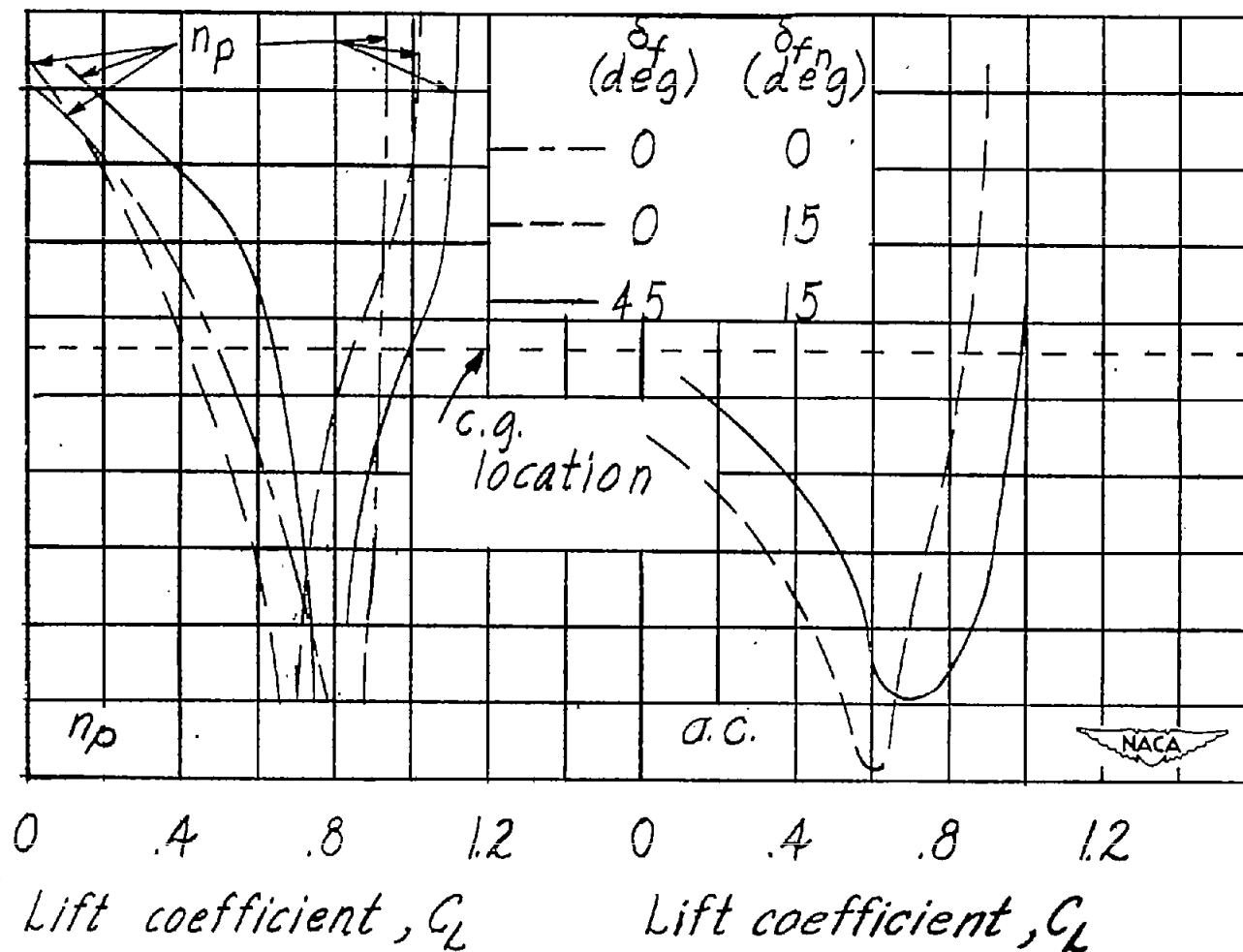
Figure 29.- Effect of flaps on stick-fixed neutral points and aerodynamic-center locations of model with circular-arc wing. Extended fuselage; windmilling propeller.
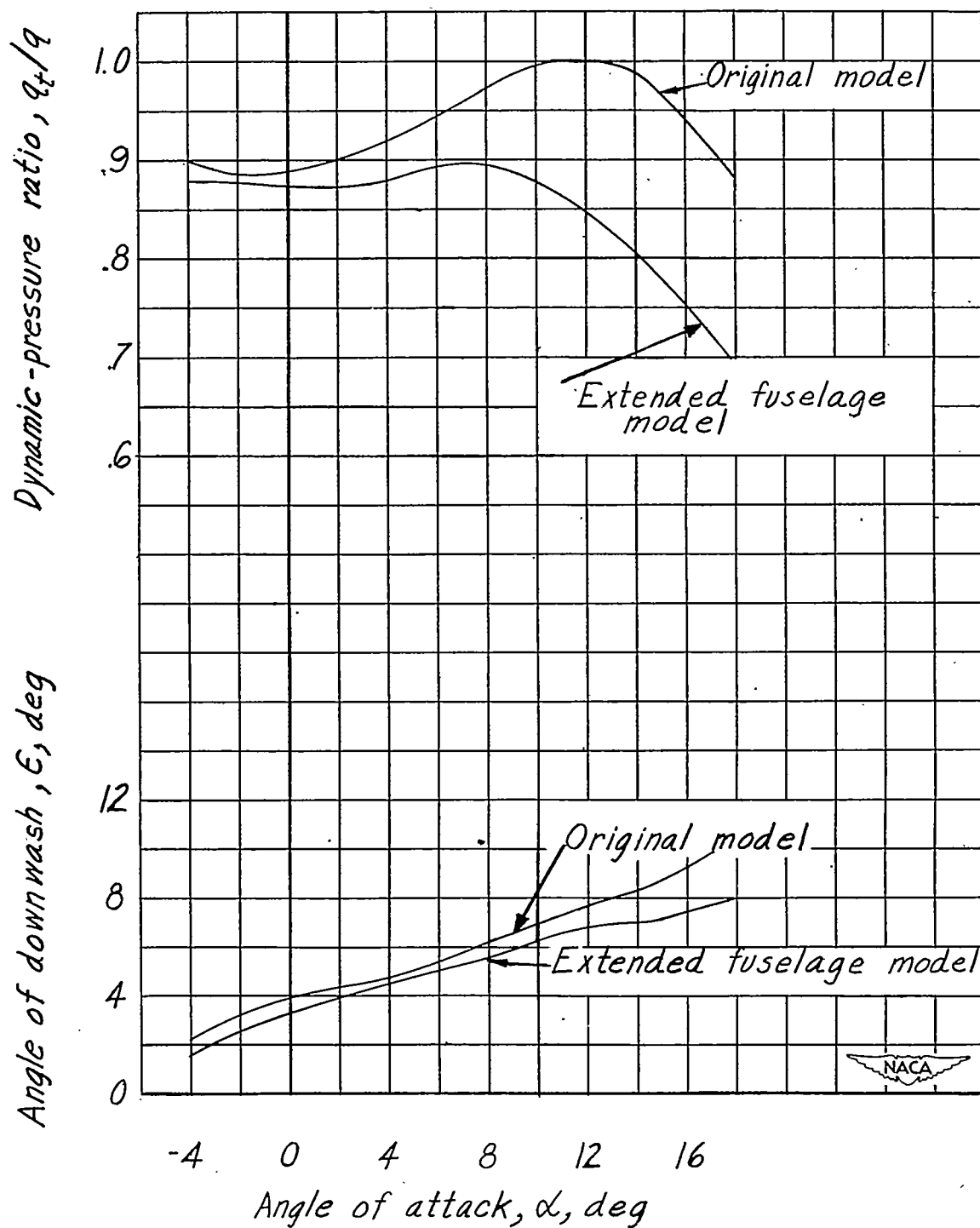
(a) $\delta_f = 0^\circ$.

Figure 30.- Effect of extended fuselage on downwash and dynamic pressure at tail. Windmilling propeller; 80-percent-span slots.
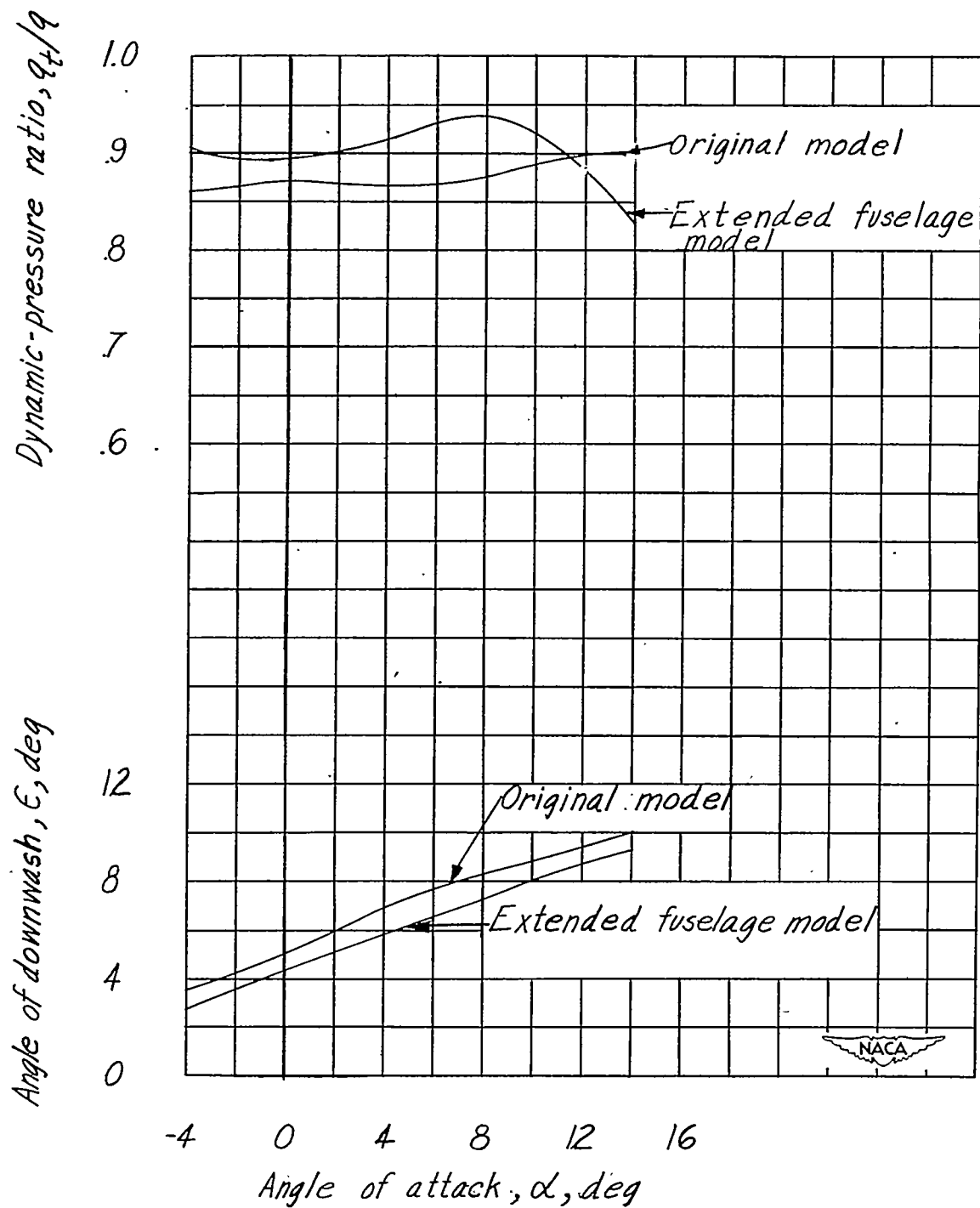
(b) $\delta_f = 45°$.

Figure 30.- Concluded.
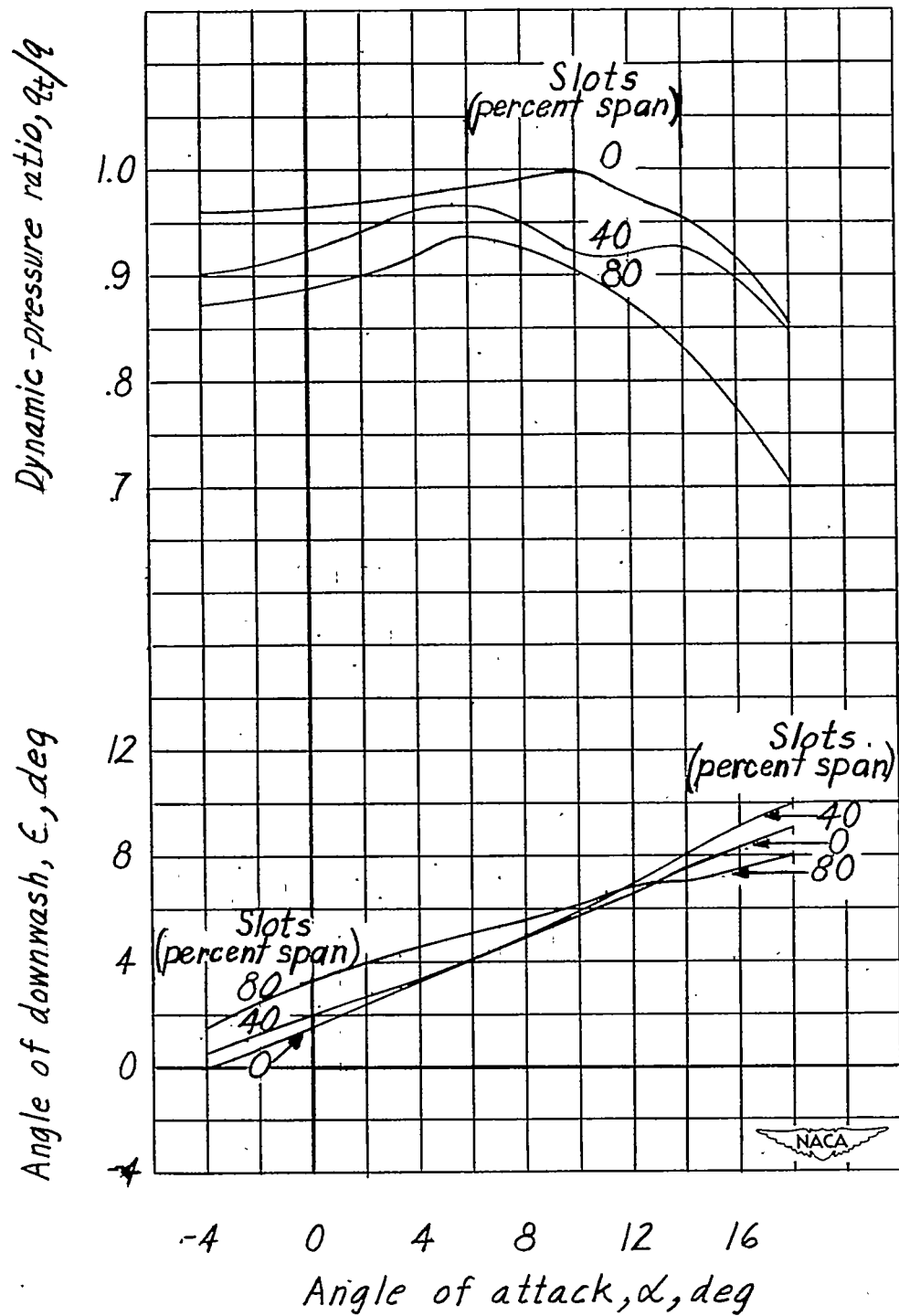
Figure 31.- Effect of slot extension on downwash and dynamic pressure at tail. Windmilling propeller; extended fuselage; $\delta_f = 0°$.
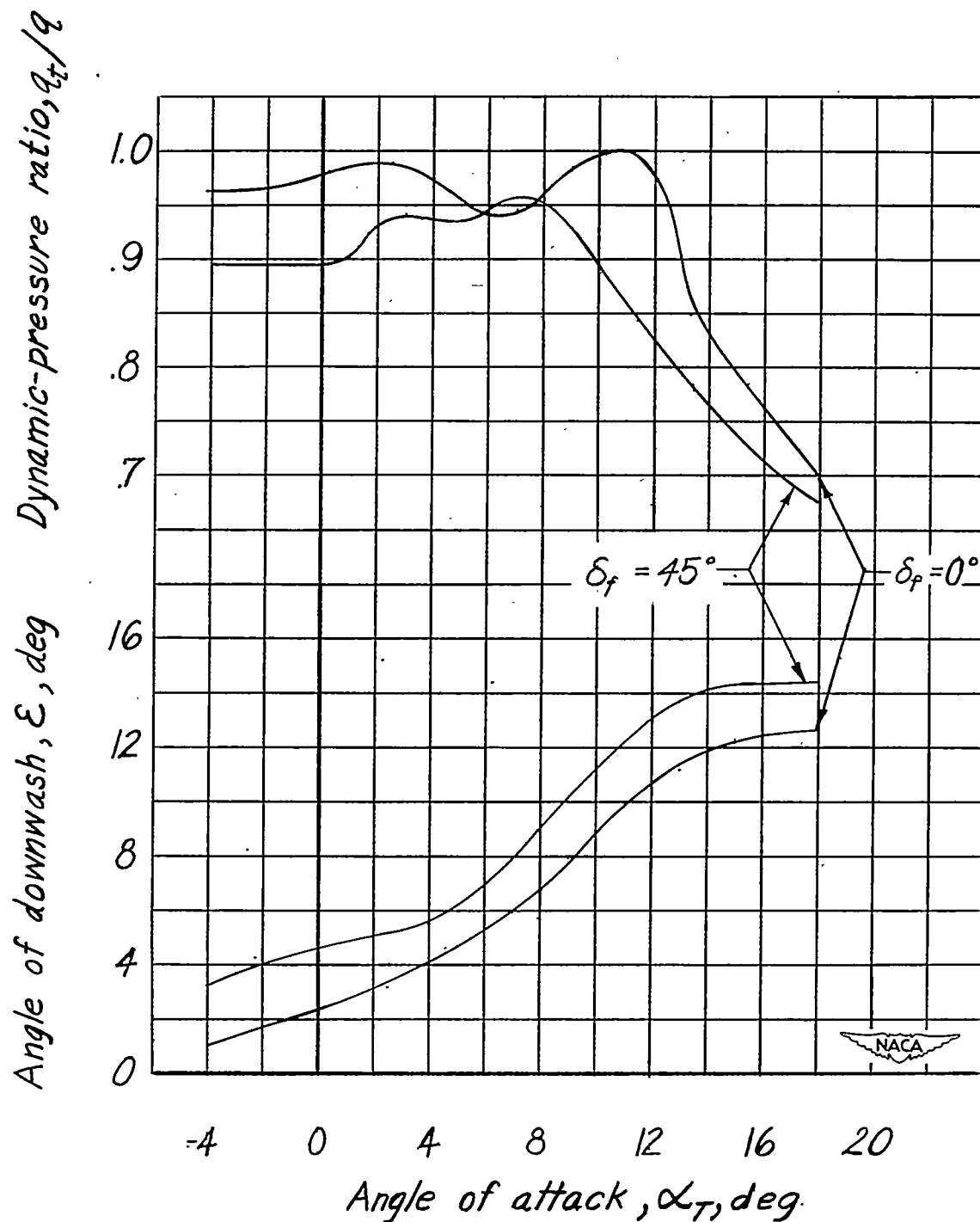
Figure 32.- Effect of flap deflection on downwash and dynamic pressure at tail of model with circular-arc wing. Windmilling propeller; extended fuselage; $\delta_{f_n} = 15°$.
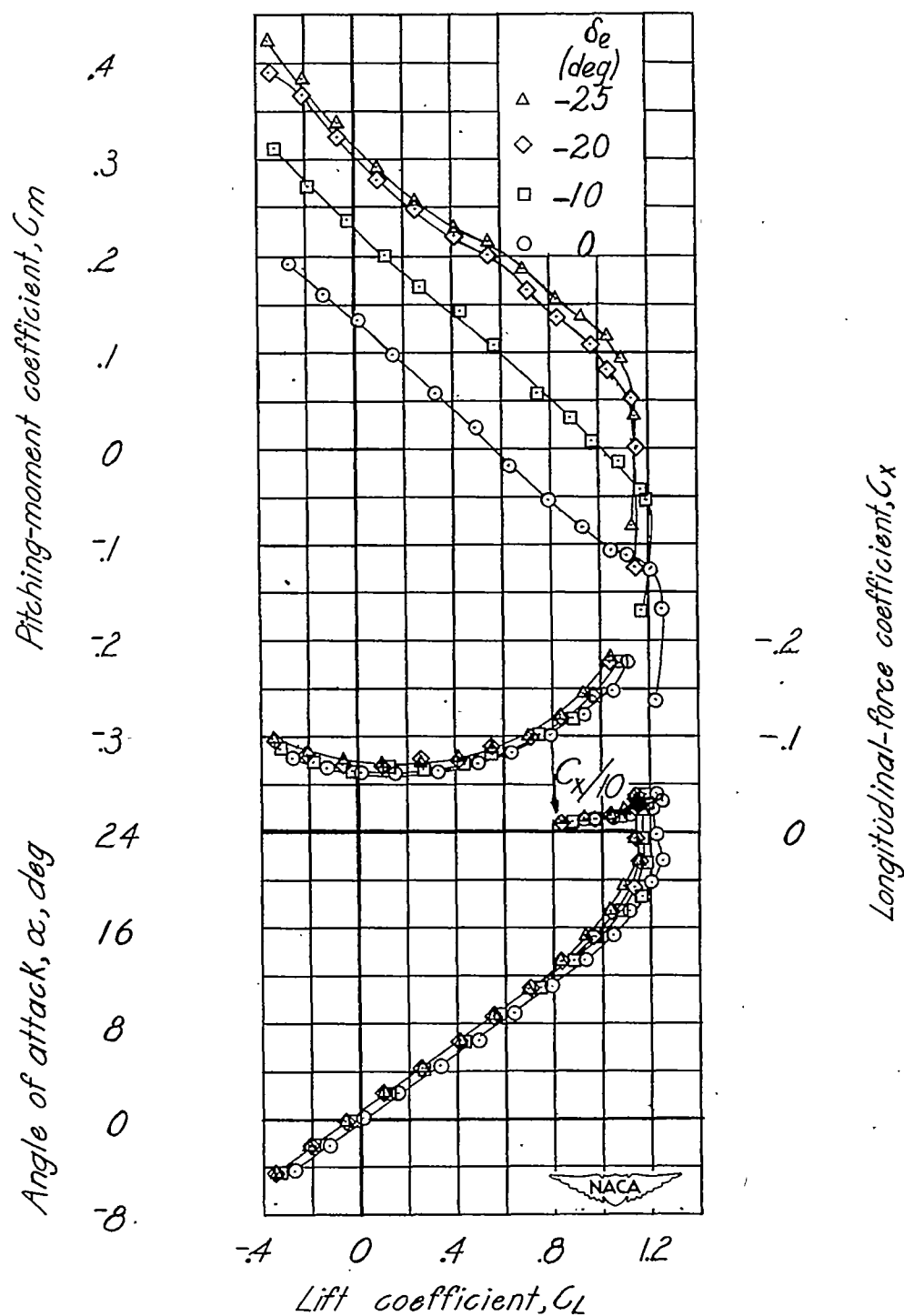
Figure 33.- Effect of elevator deflection on aerodynamic characteristics in
pitch. Windmilling propeller; extended fuselage; i_t = -3.5°; δ_f = 0°;
80-percent-span slots; R = 2.05 x 10^6.
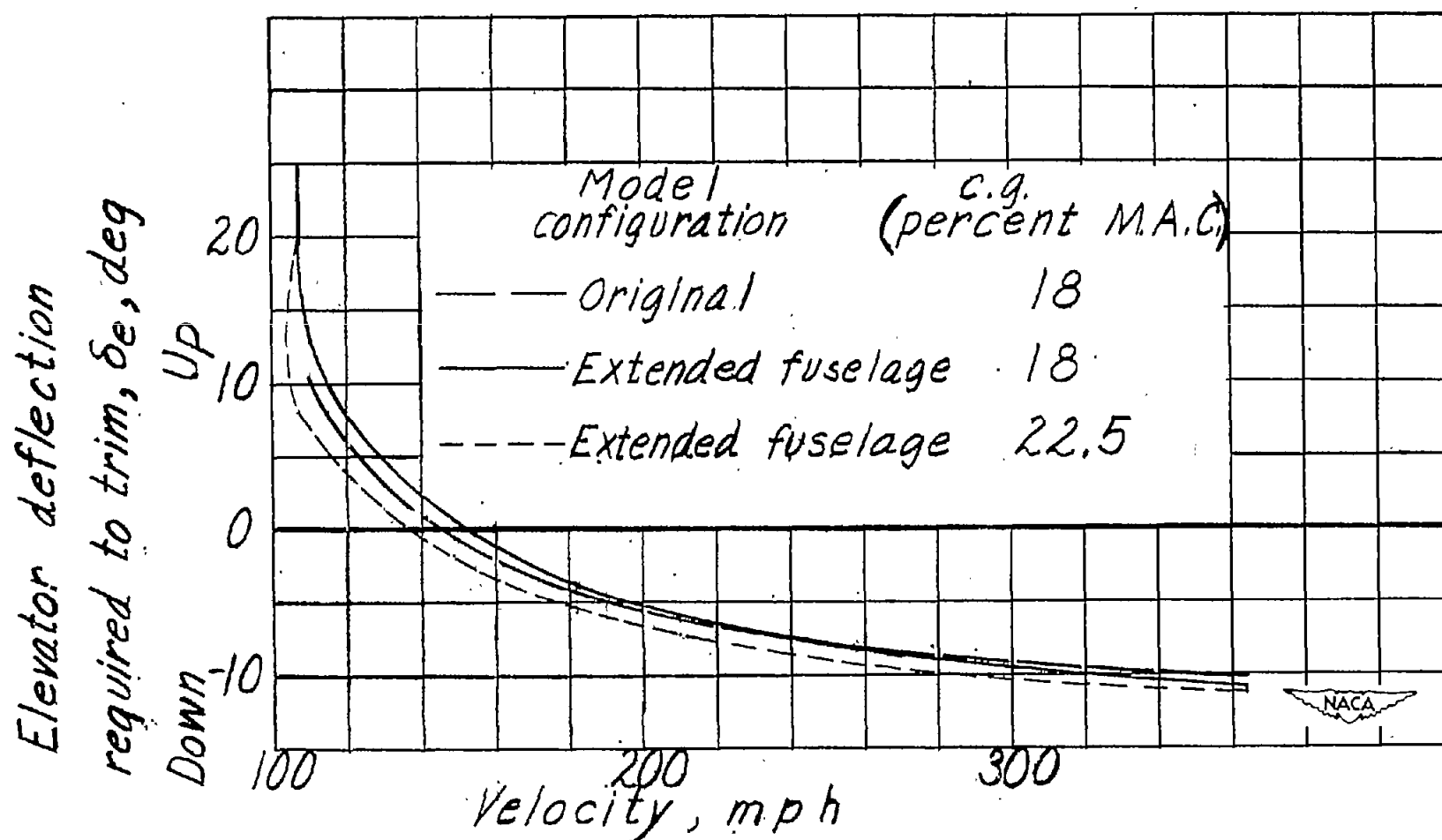
Figure 34.- Estimated elevator deflection required for trim in steady flight for test airplane. Wind-milling propeller; 80-percent-span slots; i_t = -3.5°; δ_f = 0°; gross weight = 8450 pounds.
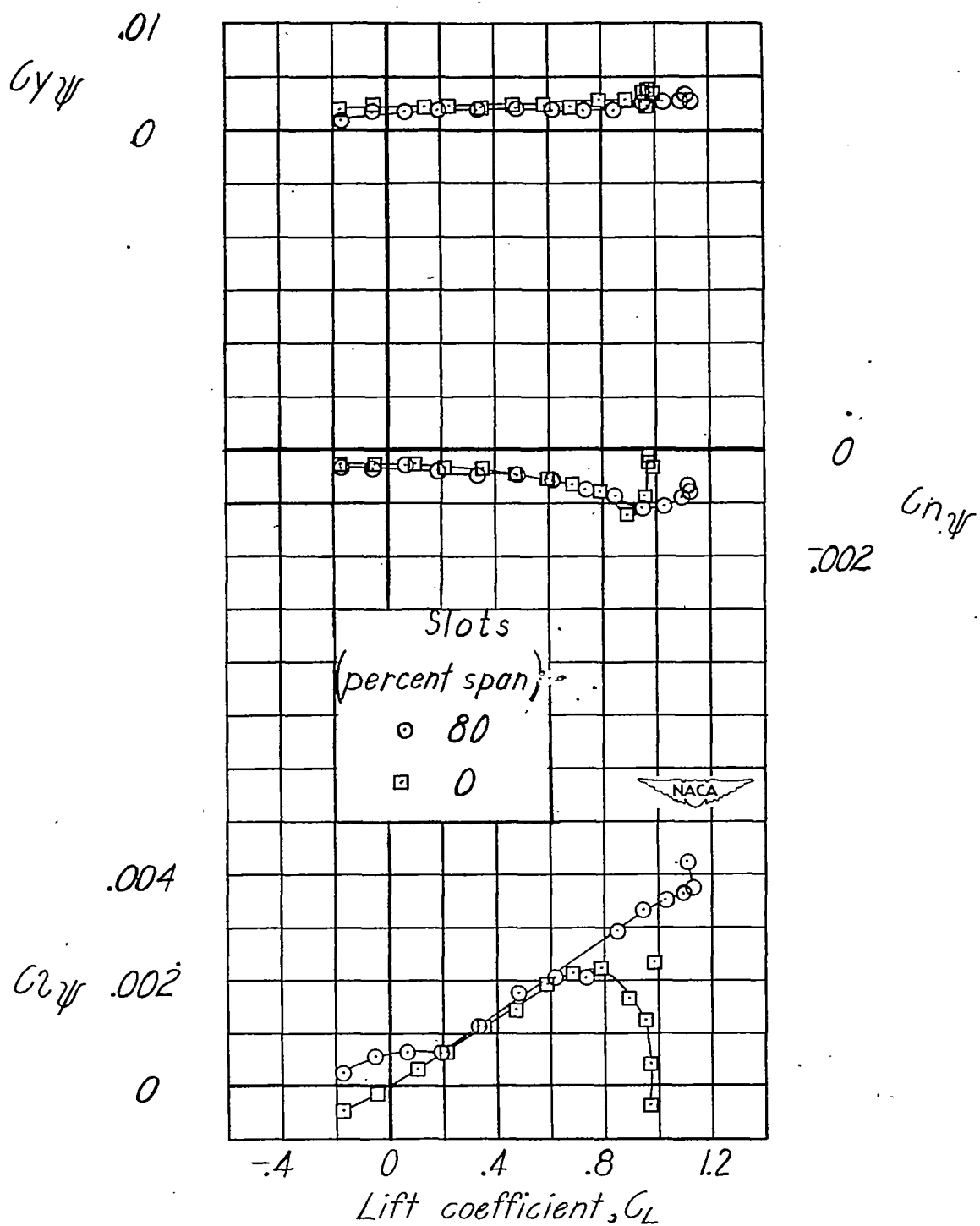
Figure 35.- Effect of slot extension on lateral-stability derivatives. Wing alone; $\delta_f = 0^\circ$; R = 2.05 × 10^6.
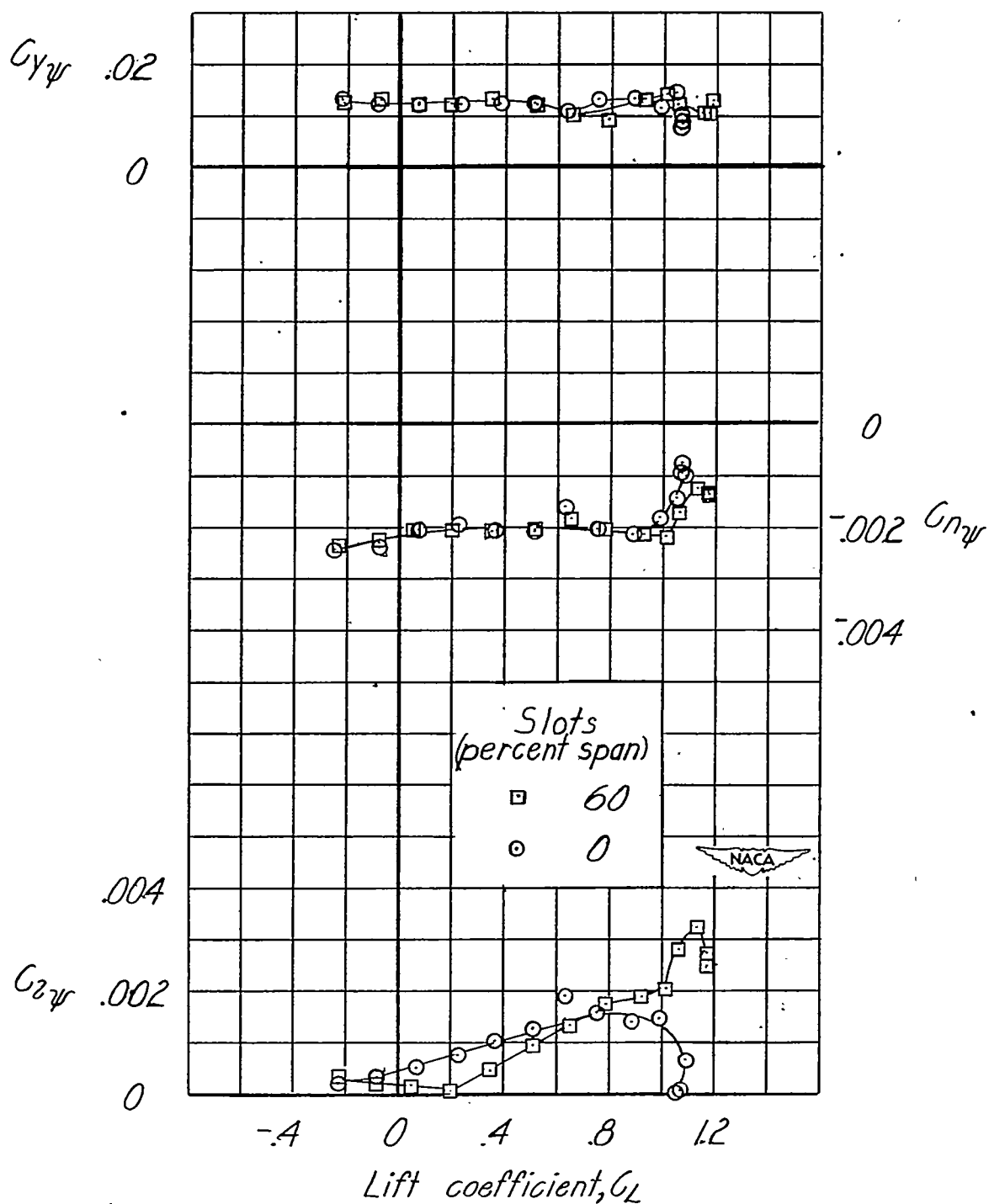
Figure 36.- Effect of slot extension on lateral-stability derivatives. Wind-milling propeller; extended fuselage; $\delta_f = 0°$; $i_t = 1.0°$; ventral fin 2; R = 2.05 × 10⁶.
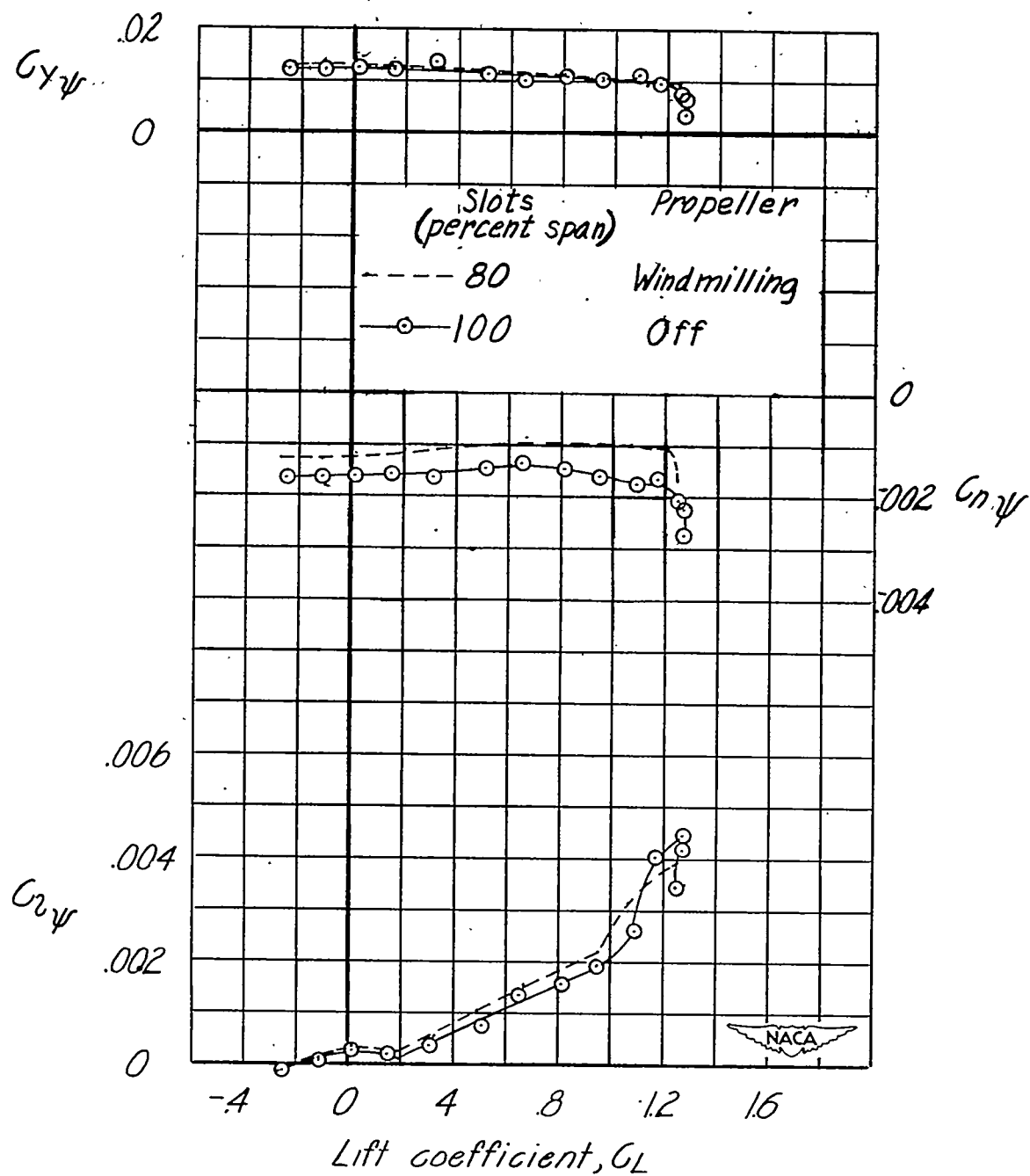
Figure 37.- Effect of propeller and slots on lateral-stability derivatives.
Ventral fin 1; $\delta_f = 0°$; R = 2.05 × 10^6.

(a) $\delta_f = 0^o$.
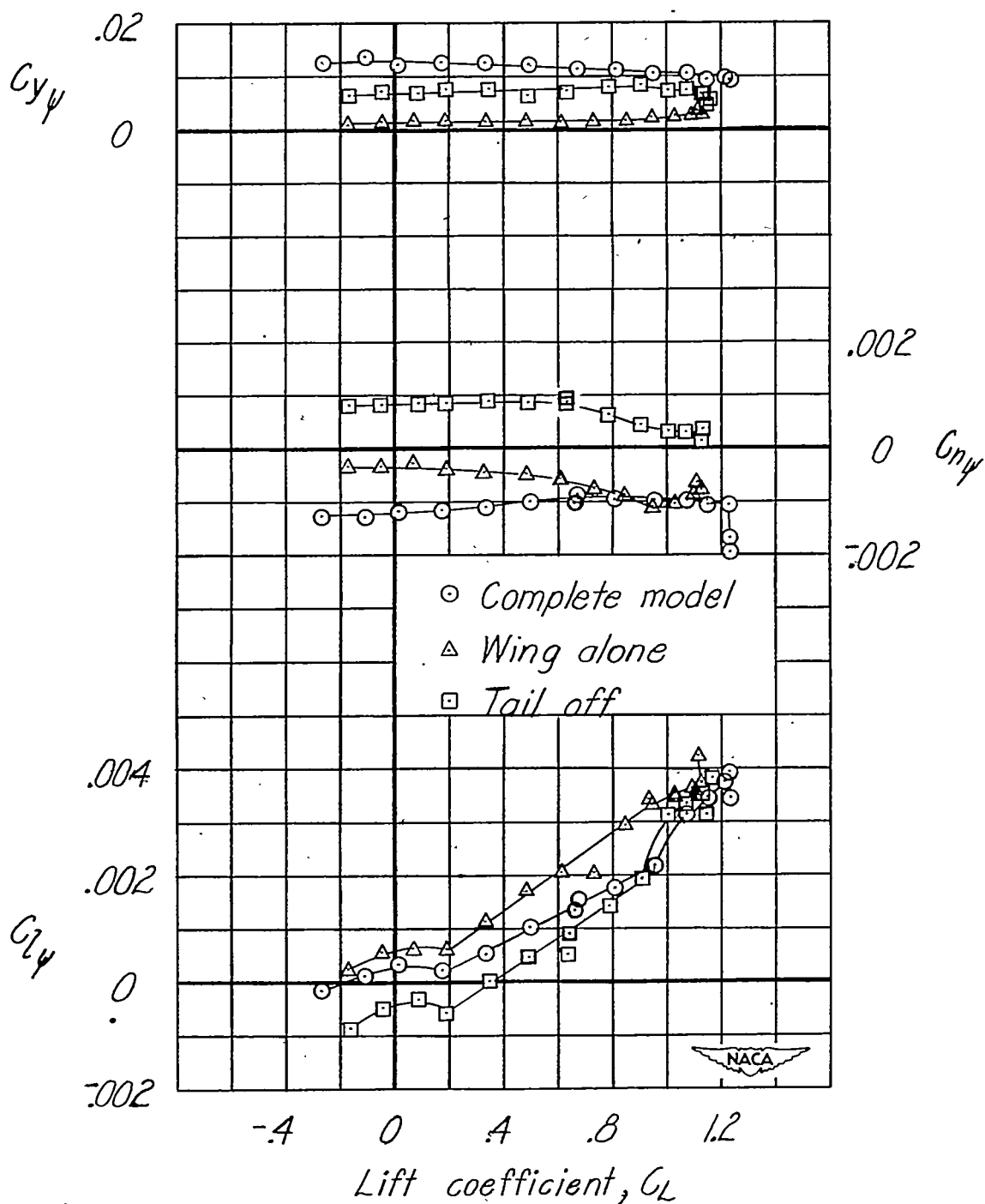
Figure 38.- Effect of wing and tail on lateral-stability derivatives. Wind-milling propeller: ventral fin 1; 80-percent-span slots; R = 2.05 × 10⁶.

(b) $\delta_f = 45^o$.
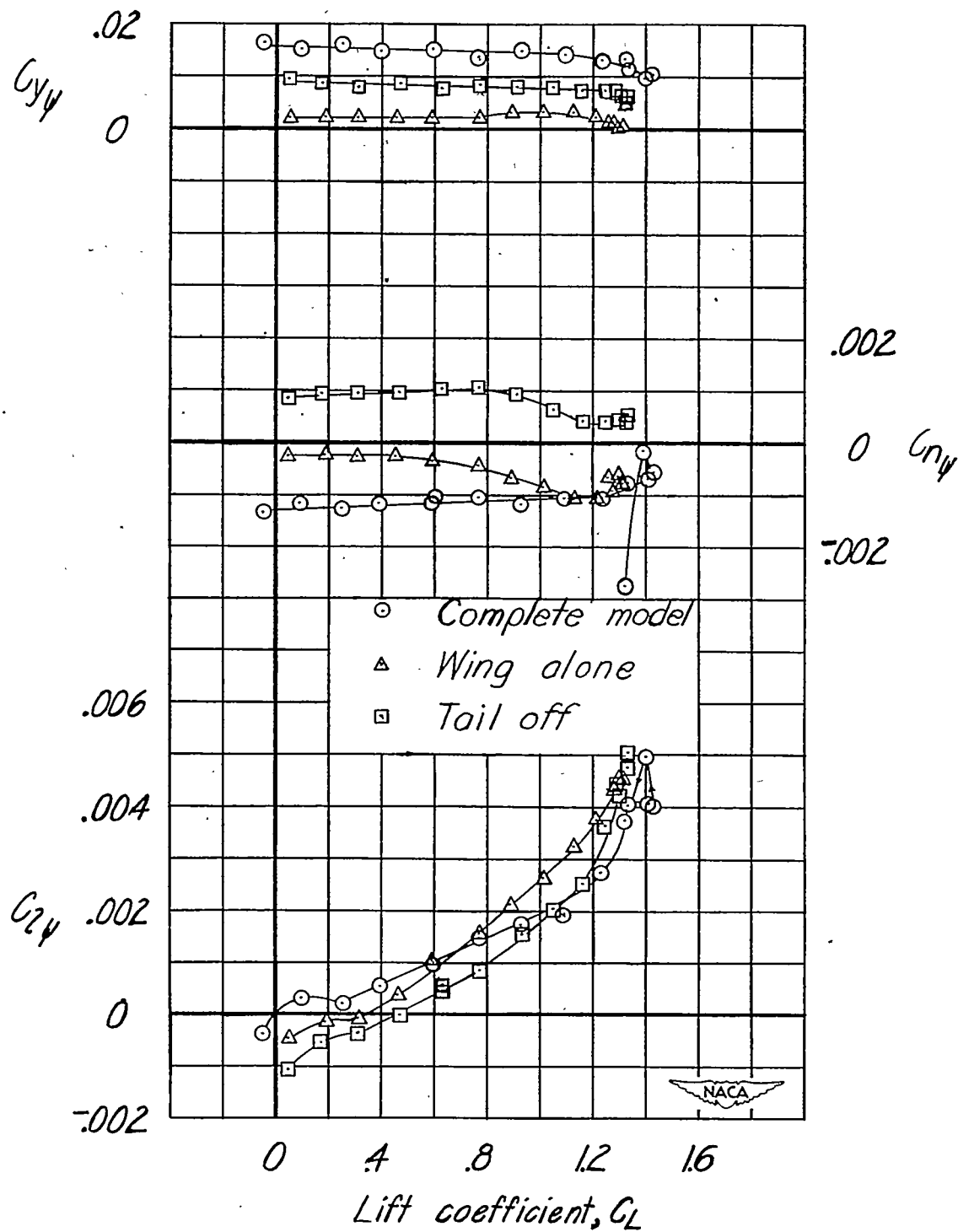
Figure 38.- Concluded.
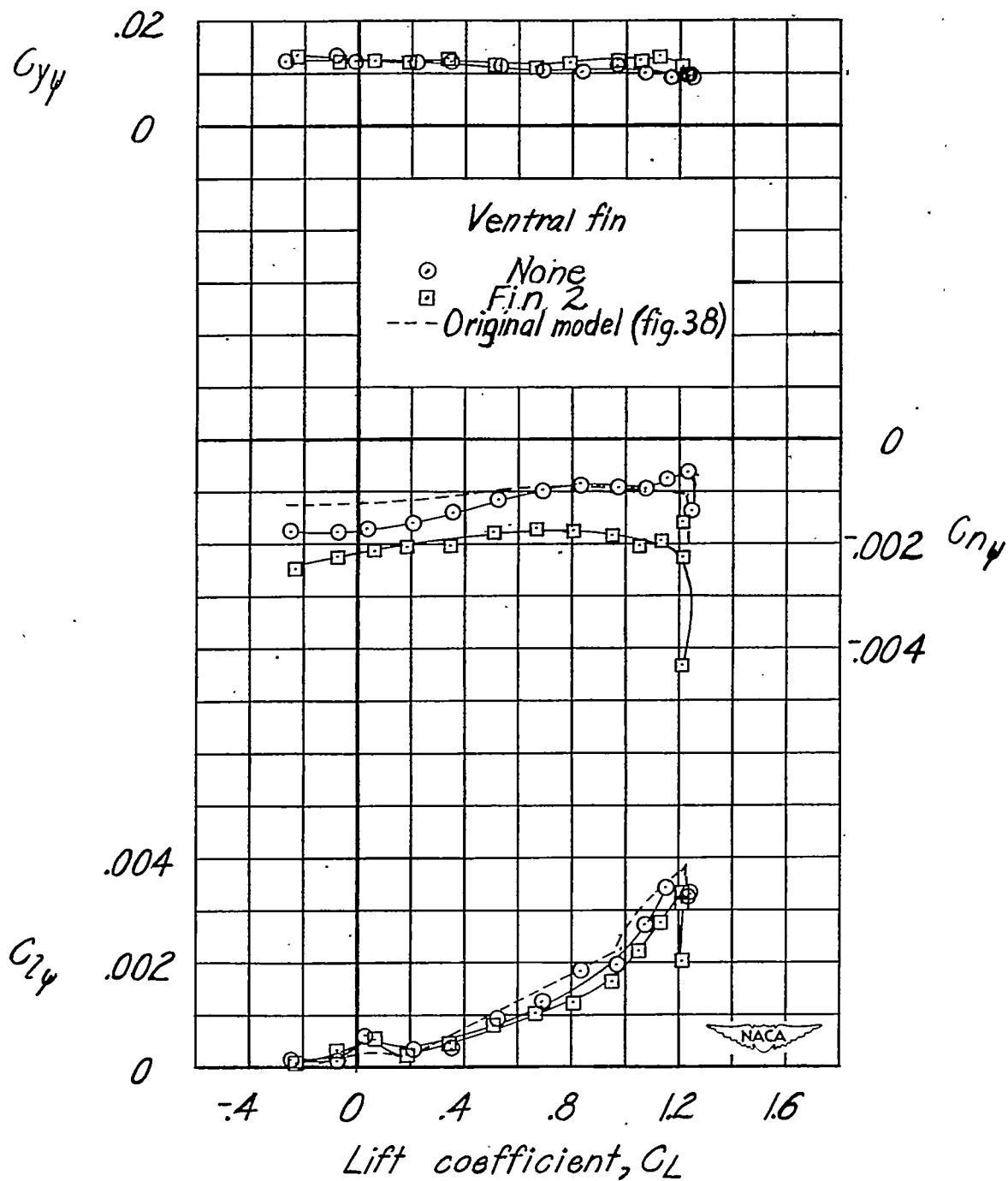
(a) $\delta_f = 0°$.

Figure 39.- Effect of ventral fin 2 on lateral-stability derivatives. Wind-
milling propeller; extended fuselage; 80-percent-span slots; R = 2.05 × 10^6.
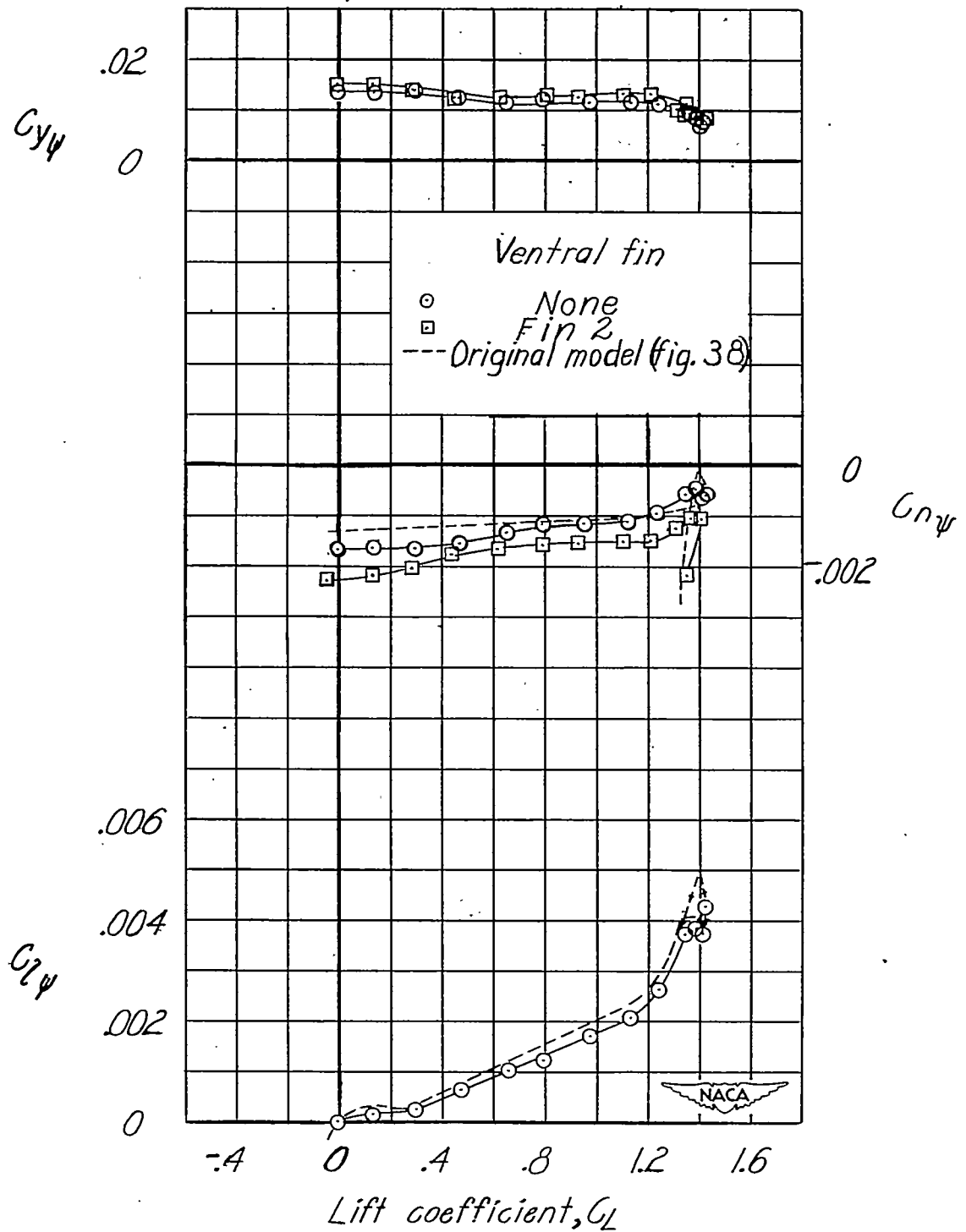
(b) $\delta_f = 45°$.

Figure 39.- Concluded.
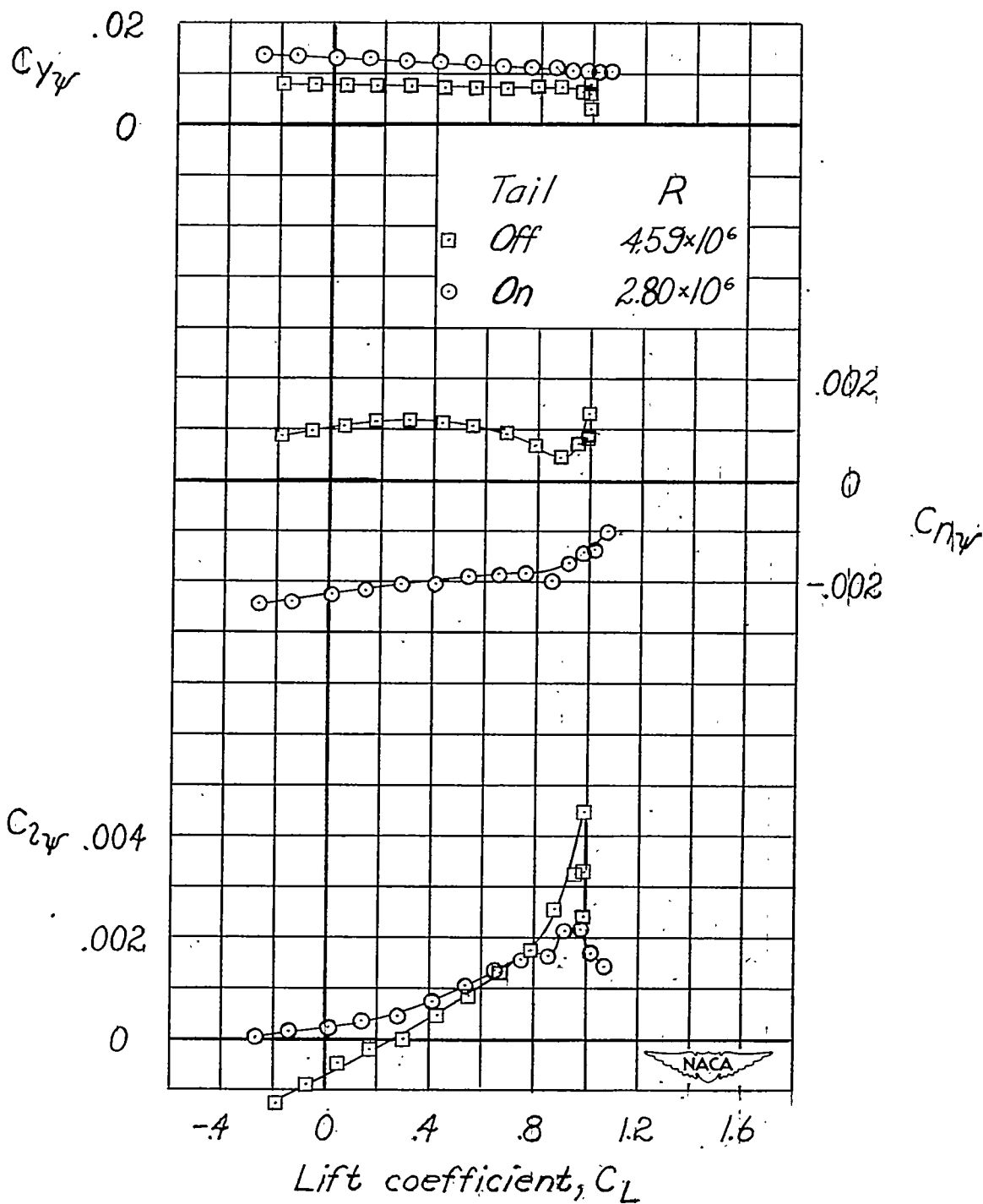
(a) $\delta_f = 0°$.

Figure 40.- Effect of tail on lateral-stability derivatives. Windmilling propeller; extended fuselage; ventral fin 3; 40-percent-span slots.
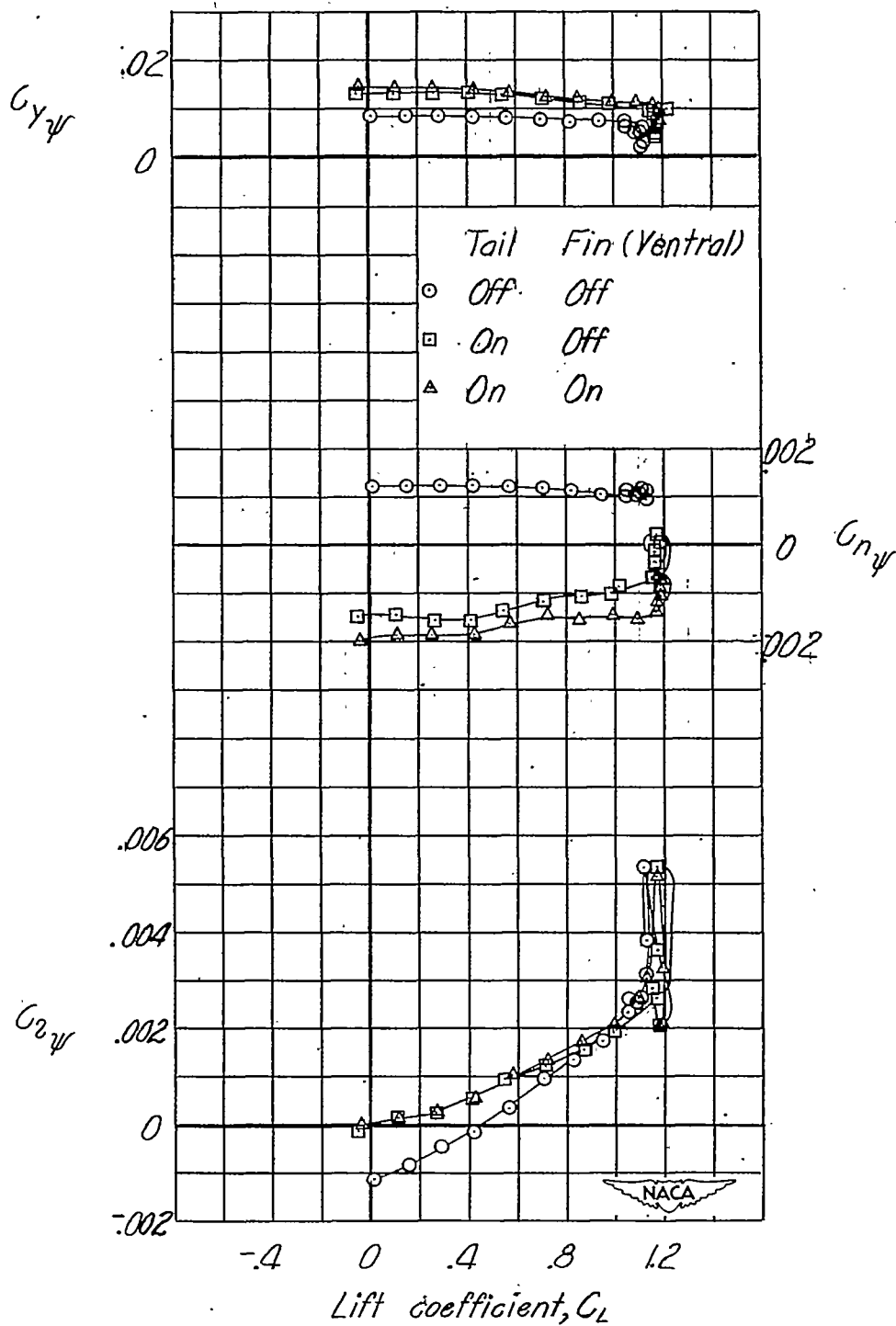
(b) $\delta_f = 45°$; $R = 4.59 \times 10^6$.

Figure 40.- Concluded.
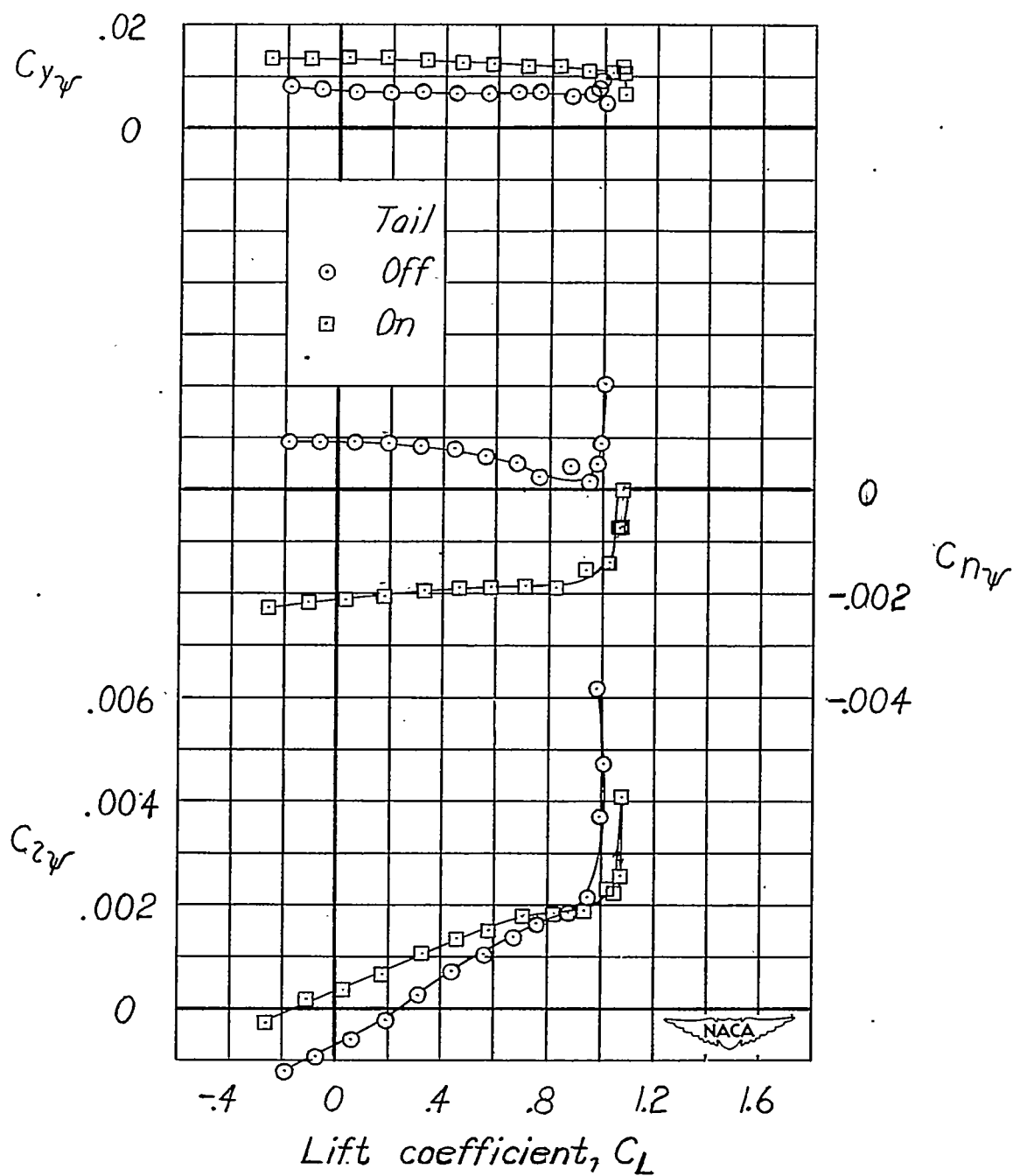
Figure 41.- Effect of tail on lateral-stability derivatives. Windmilling propeller; extended fuselage; ventral fin 3; 0-percent-span slots; $\delta_f = 0°$; R = 4.59 × 10⁶.
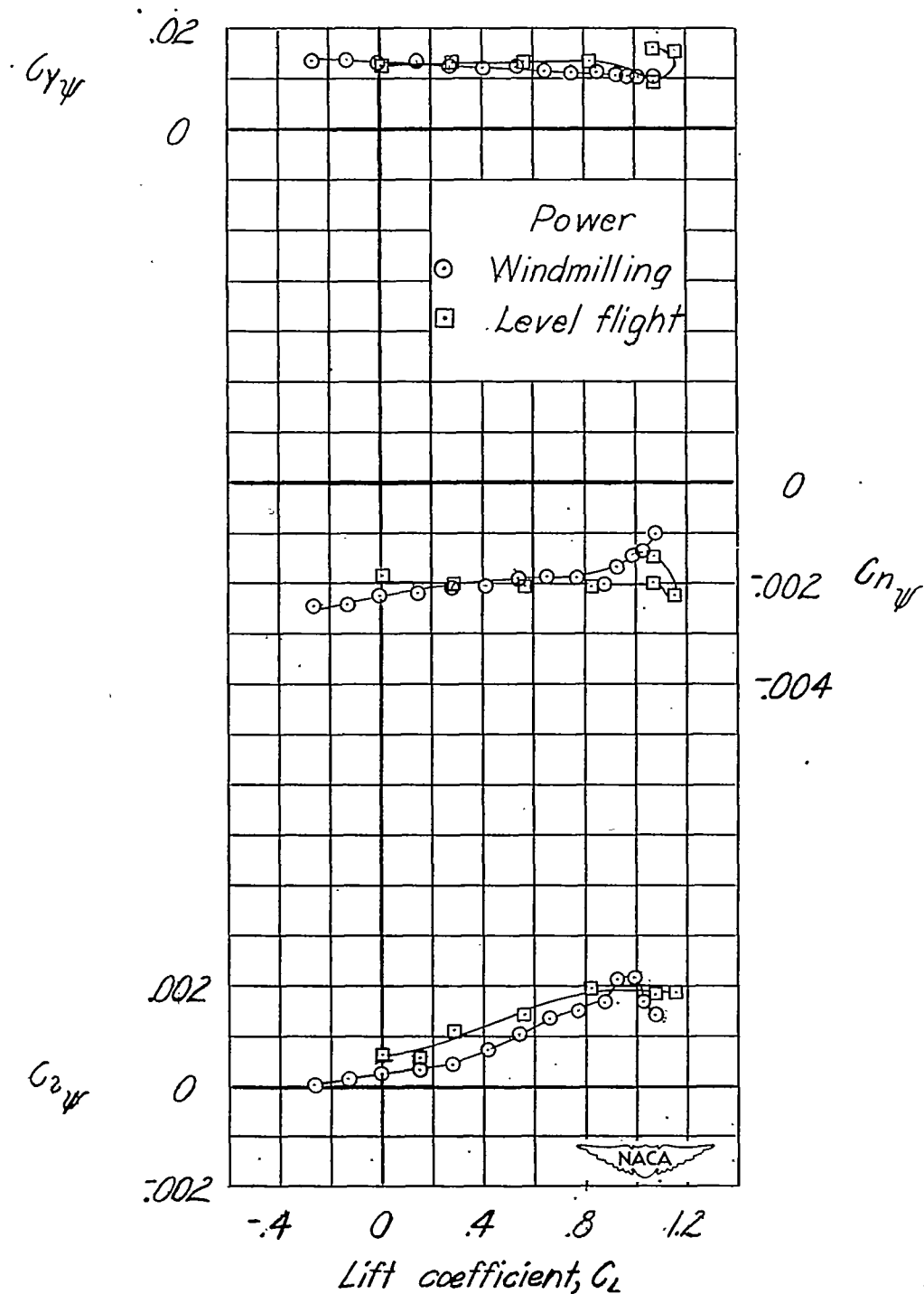
Figure 42.- Effect of power on lateral-stability derivatives. Extended fuselage; ventral fin 3; $\delta_f = 0^\circ$: 40-percent-span slots; $R = 2.80 \times 10^6$.
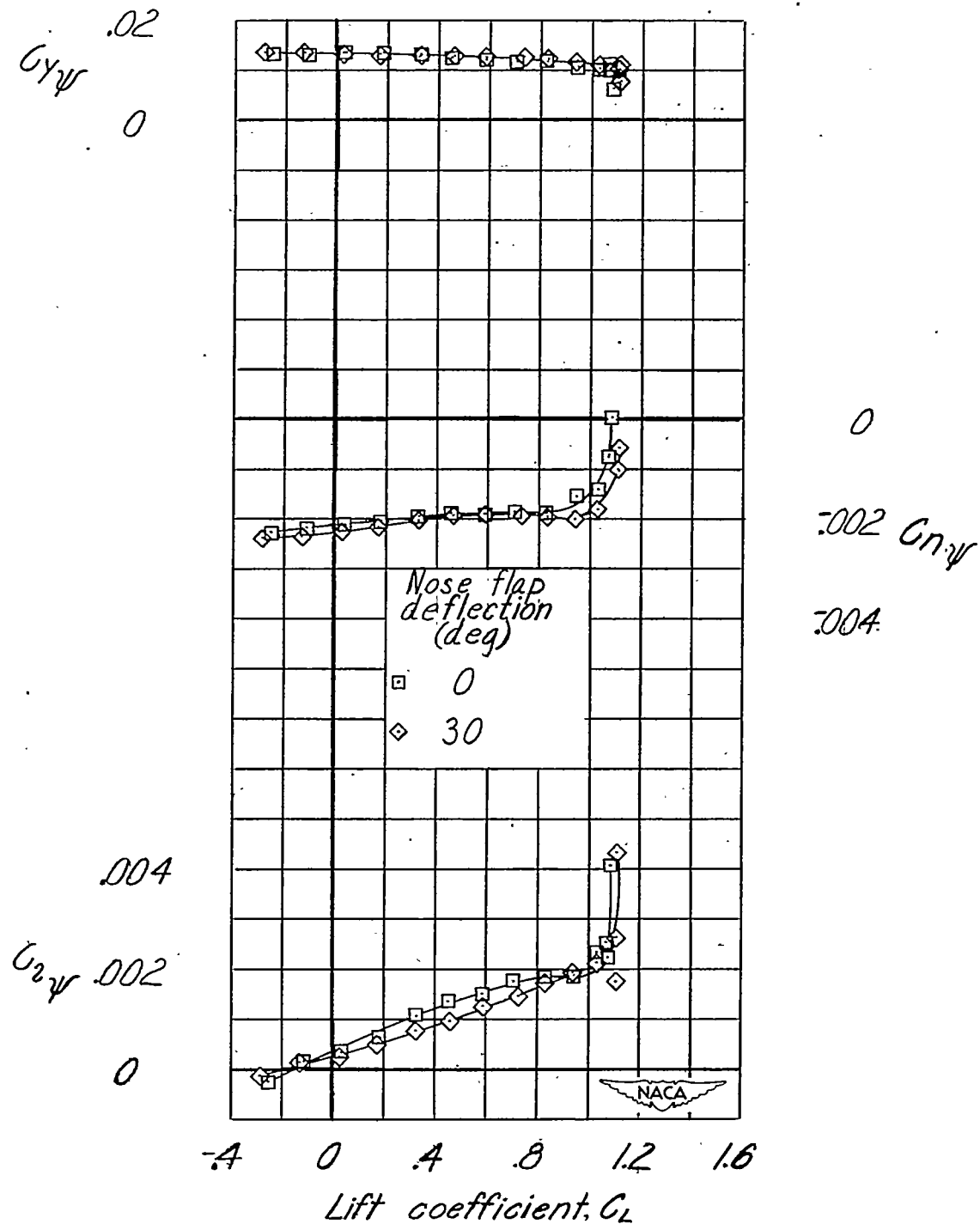
Figure 43.- Effect of nose-flap deflection on lateral-stability derivatives. Wind-milling propeller; extended fuselage; ventral fin 3; $\delta_f = 0°$; 0-percent-span slots; R = 4.59 × 10^{6}.
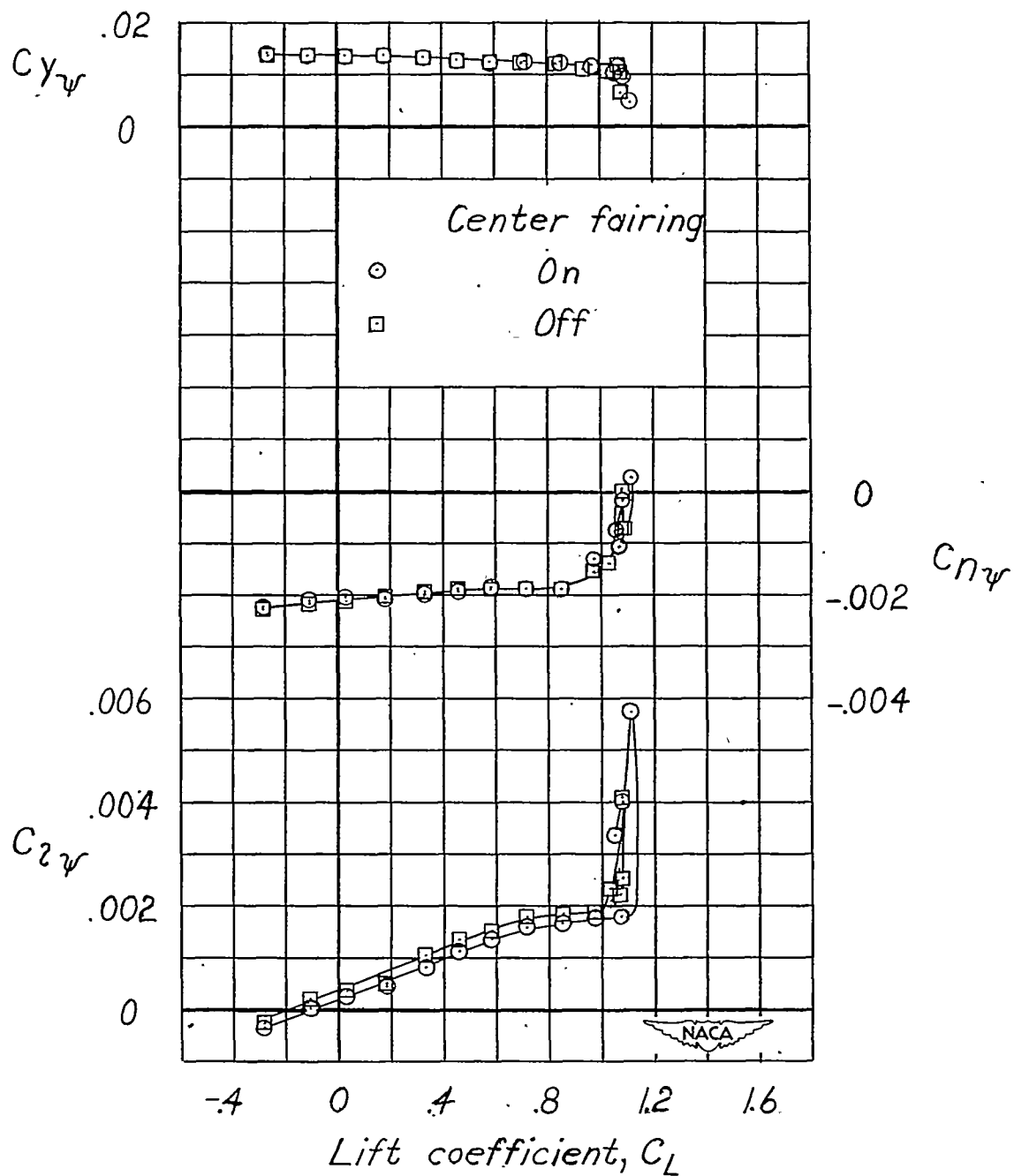
Figure 44.- Effect of faired center section on lateral-stability derivatives. Windmilling propeller; extended fuselage; ventral fin 3; $\delta_f = 0^\circ$; 0-percent-span slots; R = 4.59 × 10^6.
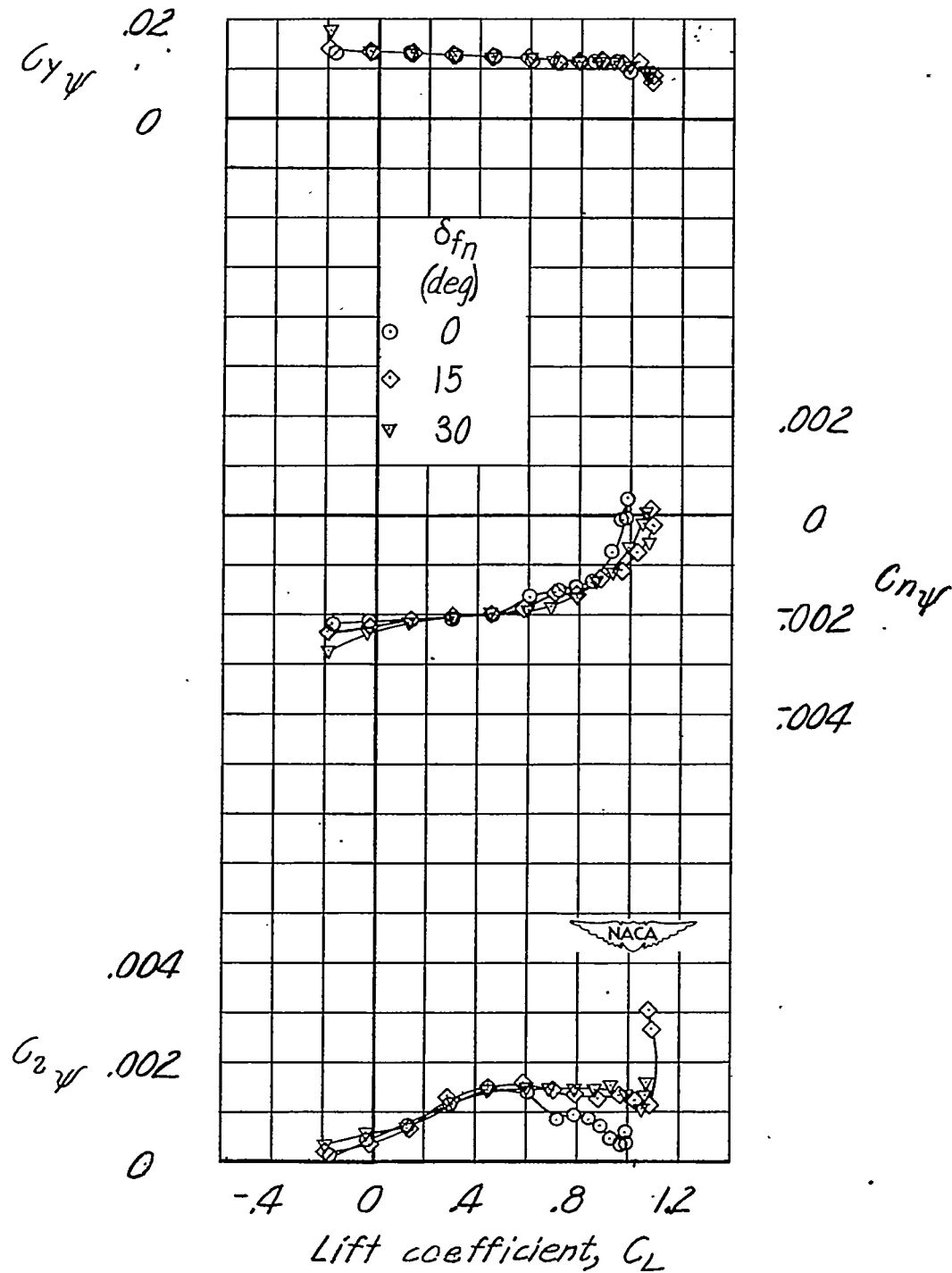
Figure 45.- Effect of nose-flap deflection on lateral-stability derivatives of
model with circular-arc wing. Windmilling propeller; extended fuselage;
ventral fin 3; $\delta_f = 0^o$; R = 2.35 × 10^6.
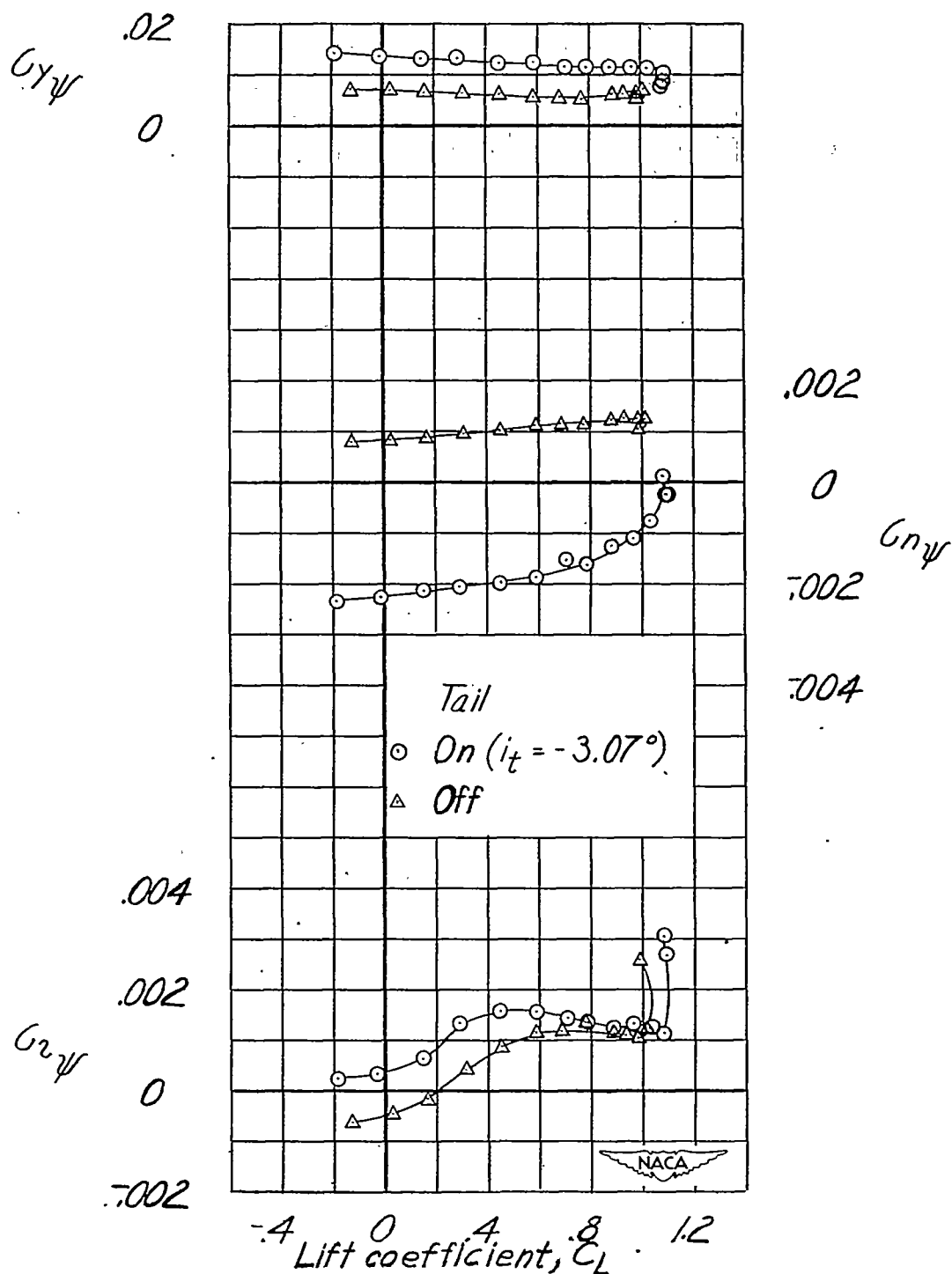
(a) $\delta_f = 0°$.

Figure 46.- Effect of tail on lateral-stability derivatives of model with circular-arc wing. Windmilling propeller; extended fuselage; ventral fin 3; $\delta_{f_n} = 15°$; R = 2.35 × 10⁶.

C_{Y_ψ}

.02

0

.002

0

C_{n_ψ}

:002

.004

Tail

⊙ On (i_t = -3.07°)

△ Off

.004

.002

C_{l_ψ} 0

:002

0   .4   .8   1.2

Lift coefficient, C_L
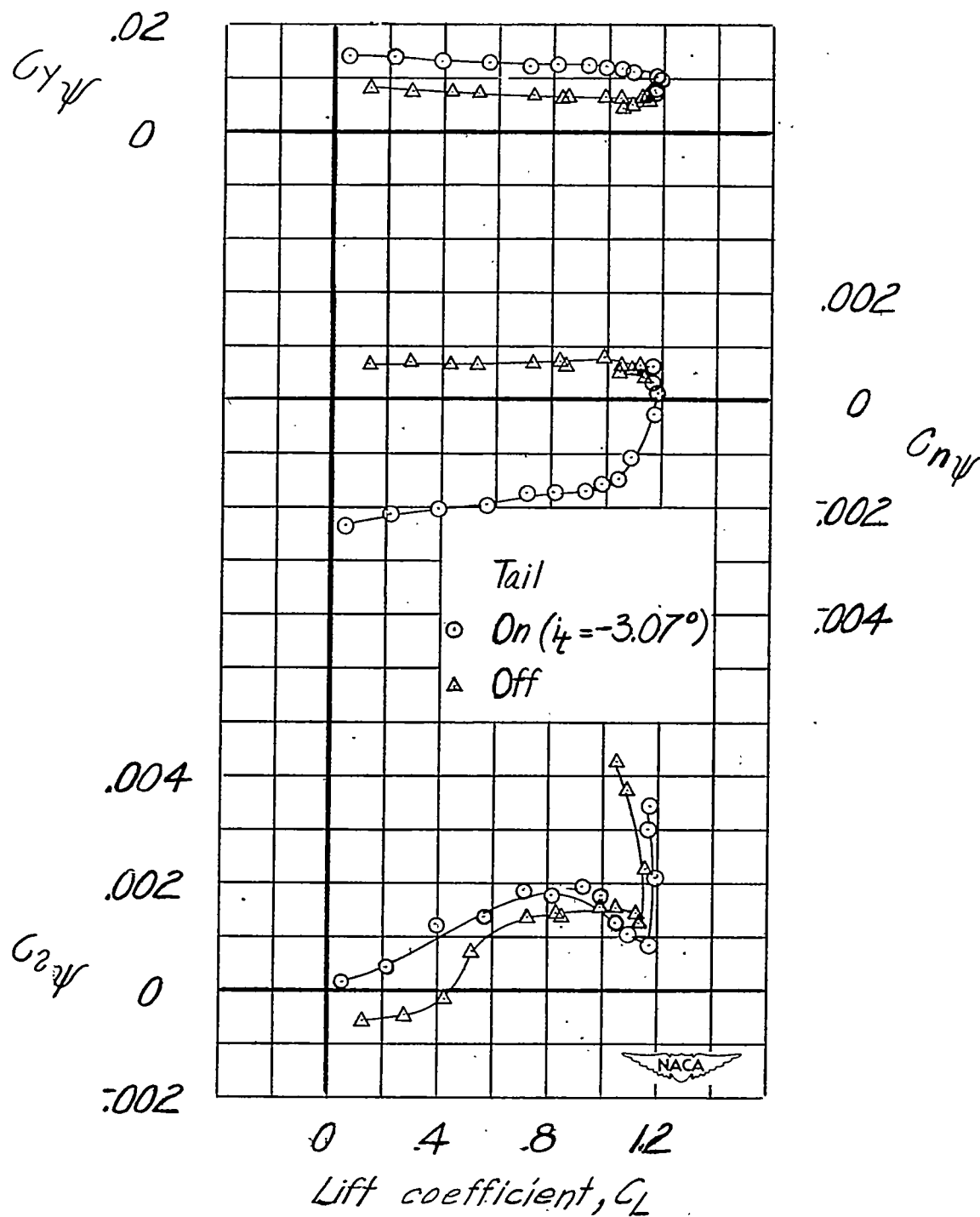
(b) δ_f = 45°.

Figure 46.- Concluded.
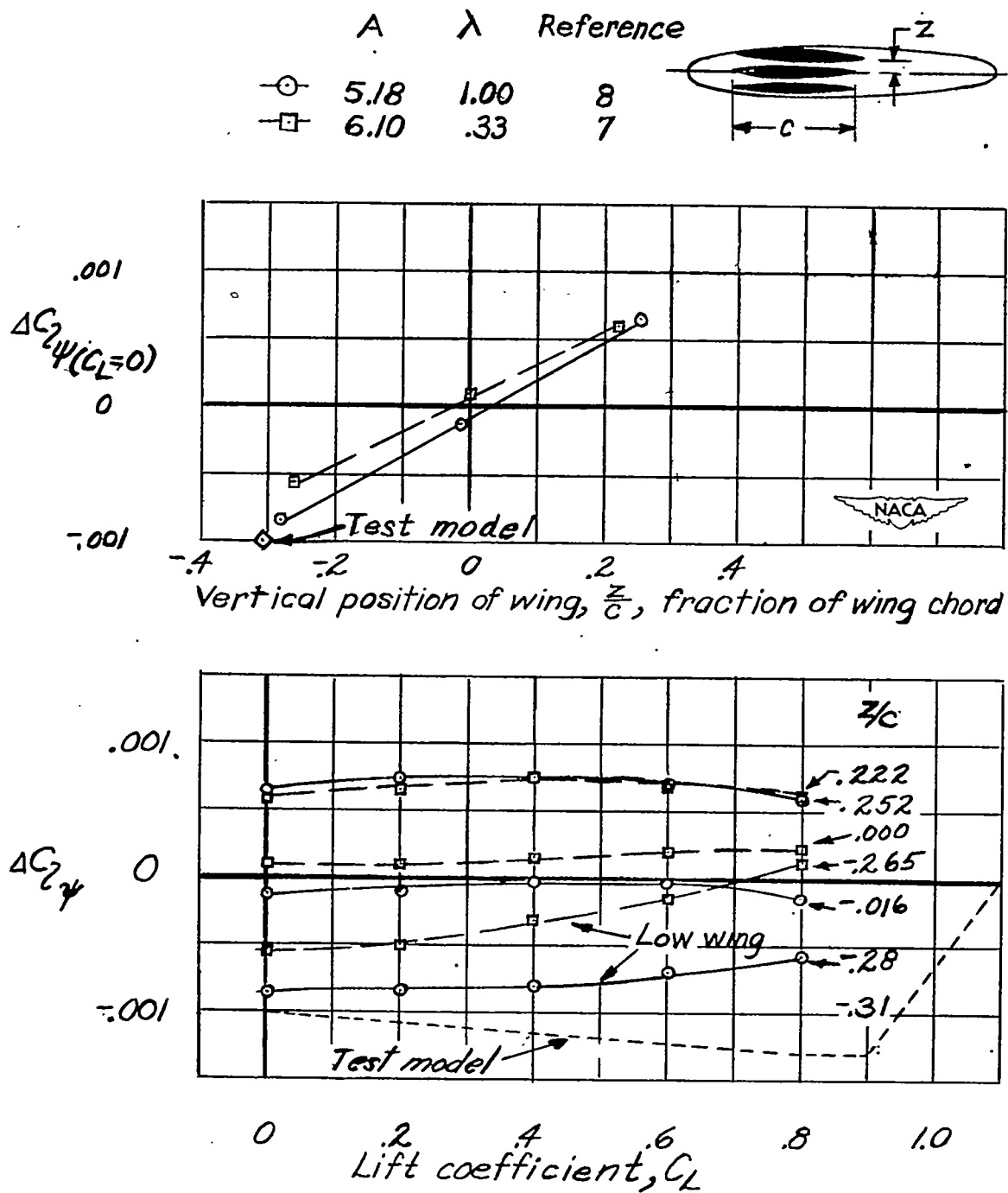
Figure 47.- Increment of C_{l_ψ} due to wing-fuselage interference. Circular fuselage; $\Lambda = 0^\circ$; $\Gamma = 0^\circ$.
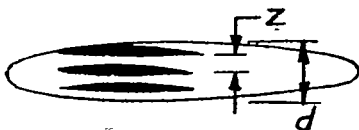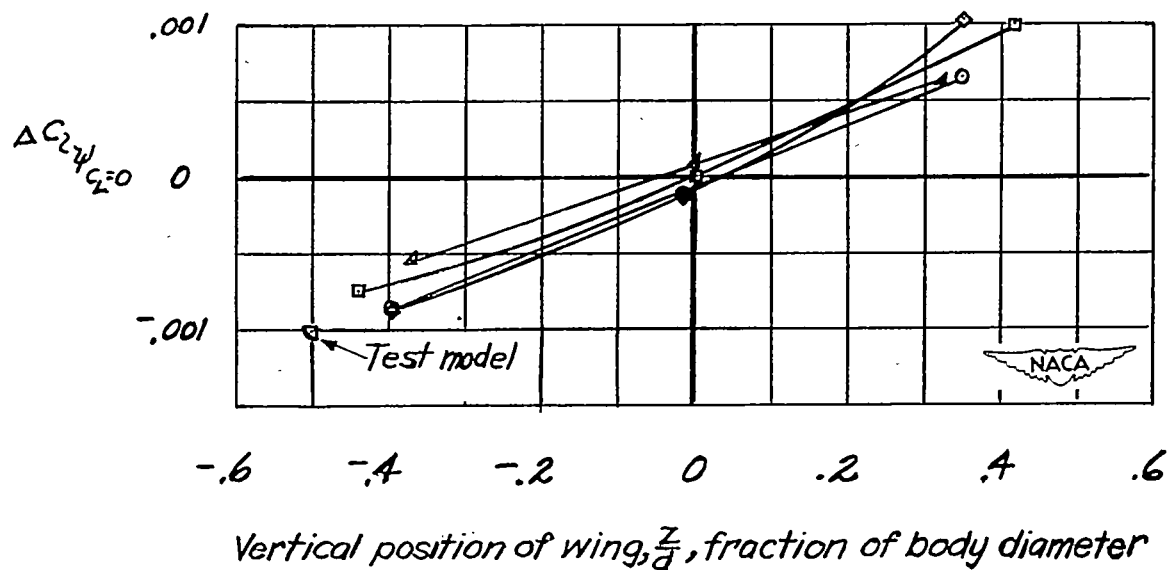
Figure 48.- Increment of C_{l_ψ} due to wing-fuselage interference. $\Gamma = 0^\circ$.
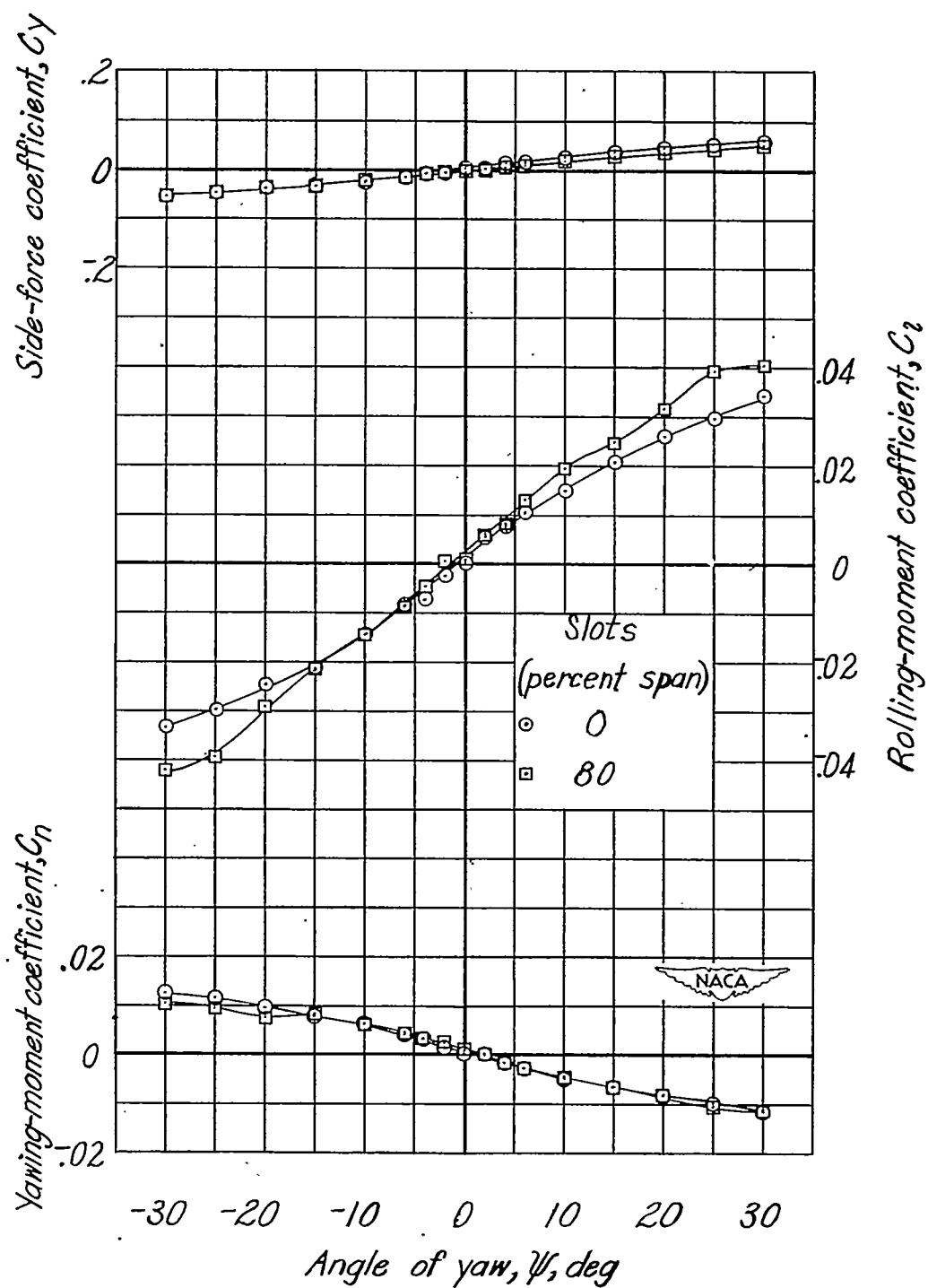
Figure 49.- Effect of slot extension on aerodynamic characteristics in yaw.
Wing alone; $\delta_f = 0^\circ$; $\alpha = 8.8^\circ$; $R = 2.05 \times 10^6$.
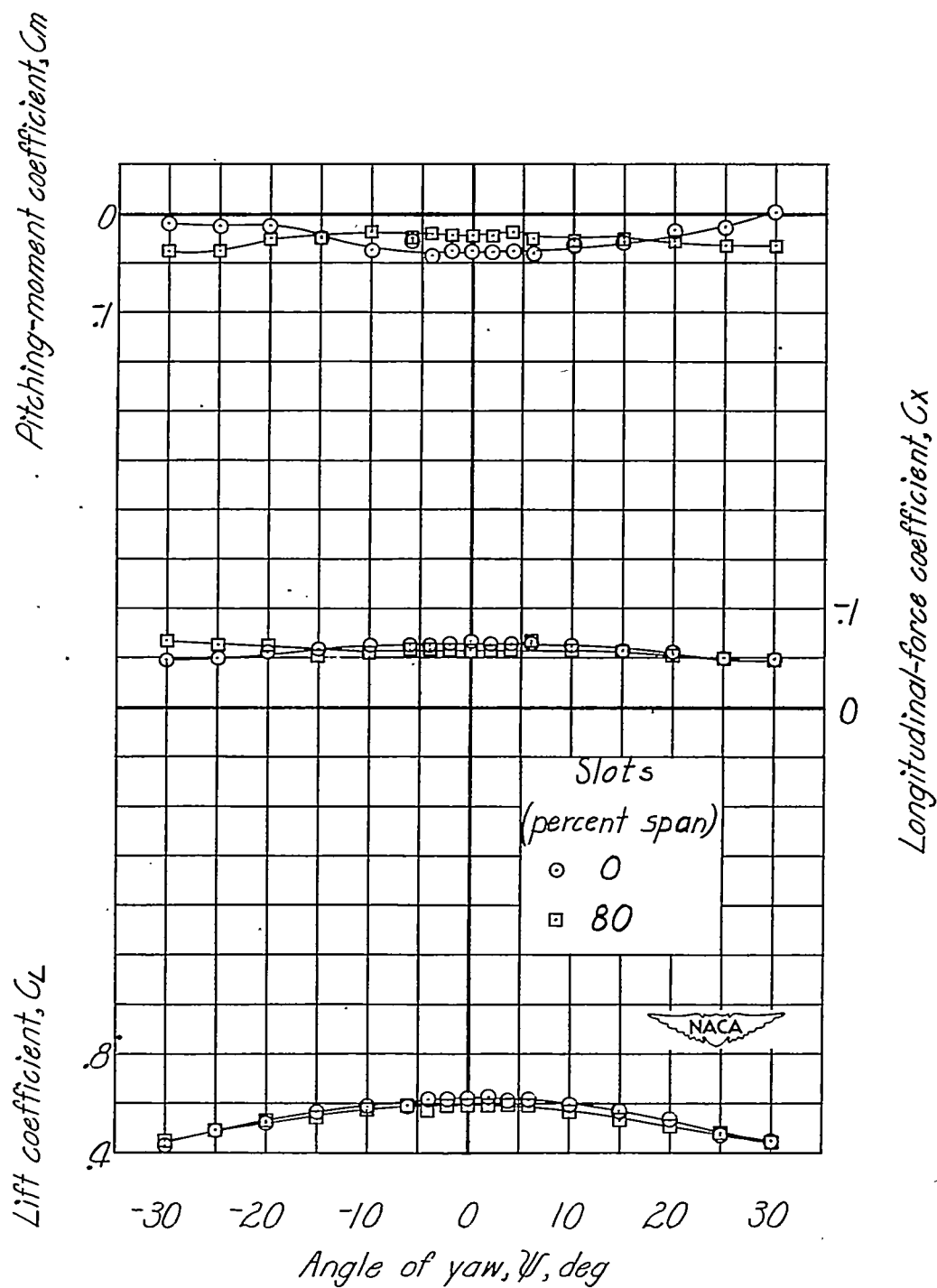
Figure 49.- Concluded.
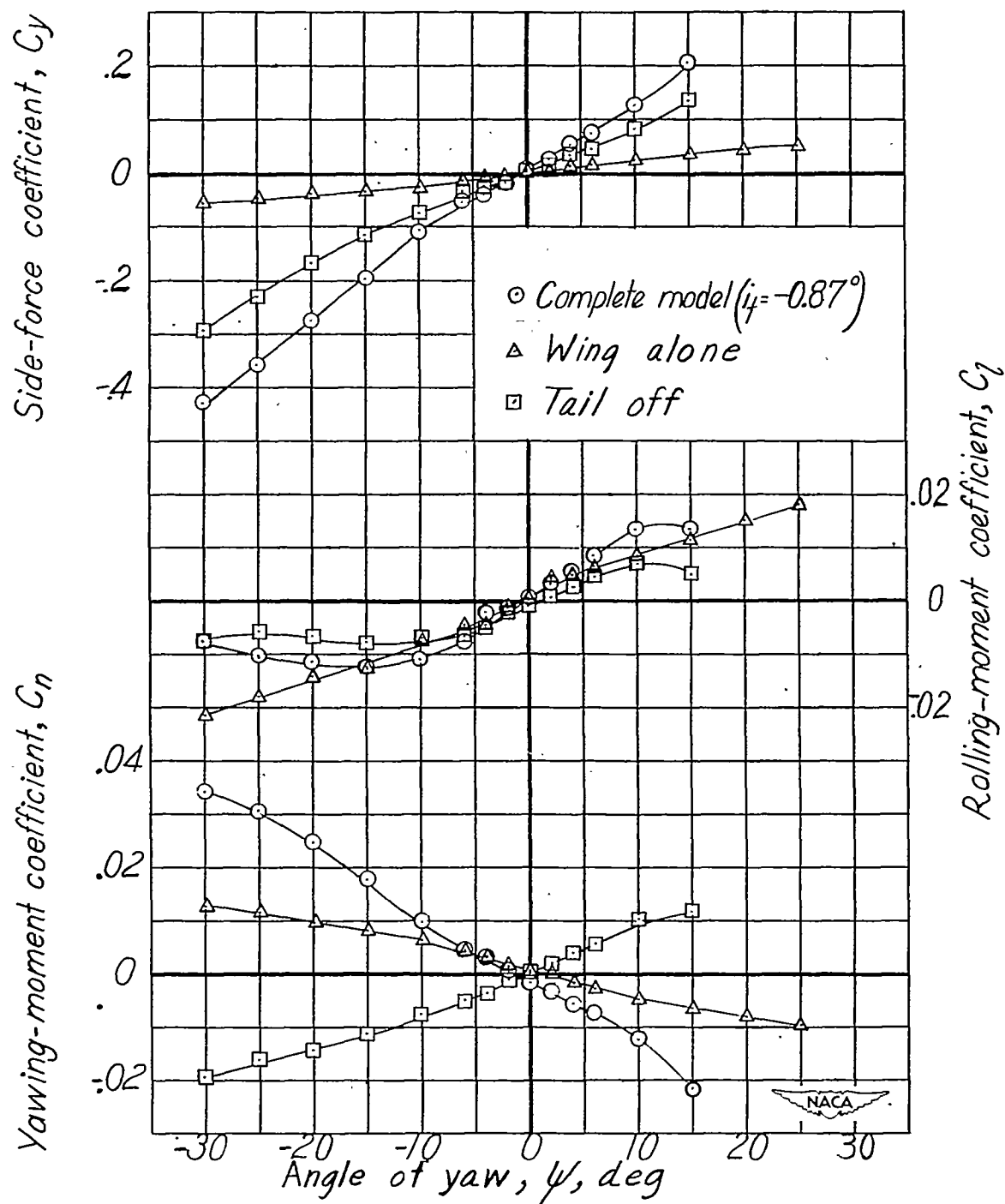
(a) $\delta_f = 0°$; $\alpha = 8.8°$.

Figure 50.- Effect of wing and tail on aerodynamic characteristics in yaw.
Windmilling propeller; ventral fin 1; 80-percent-span slots; R = 2.05 × 10^6.
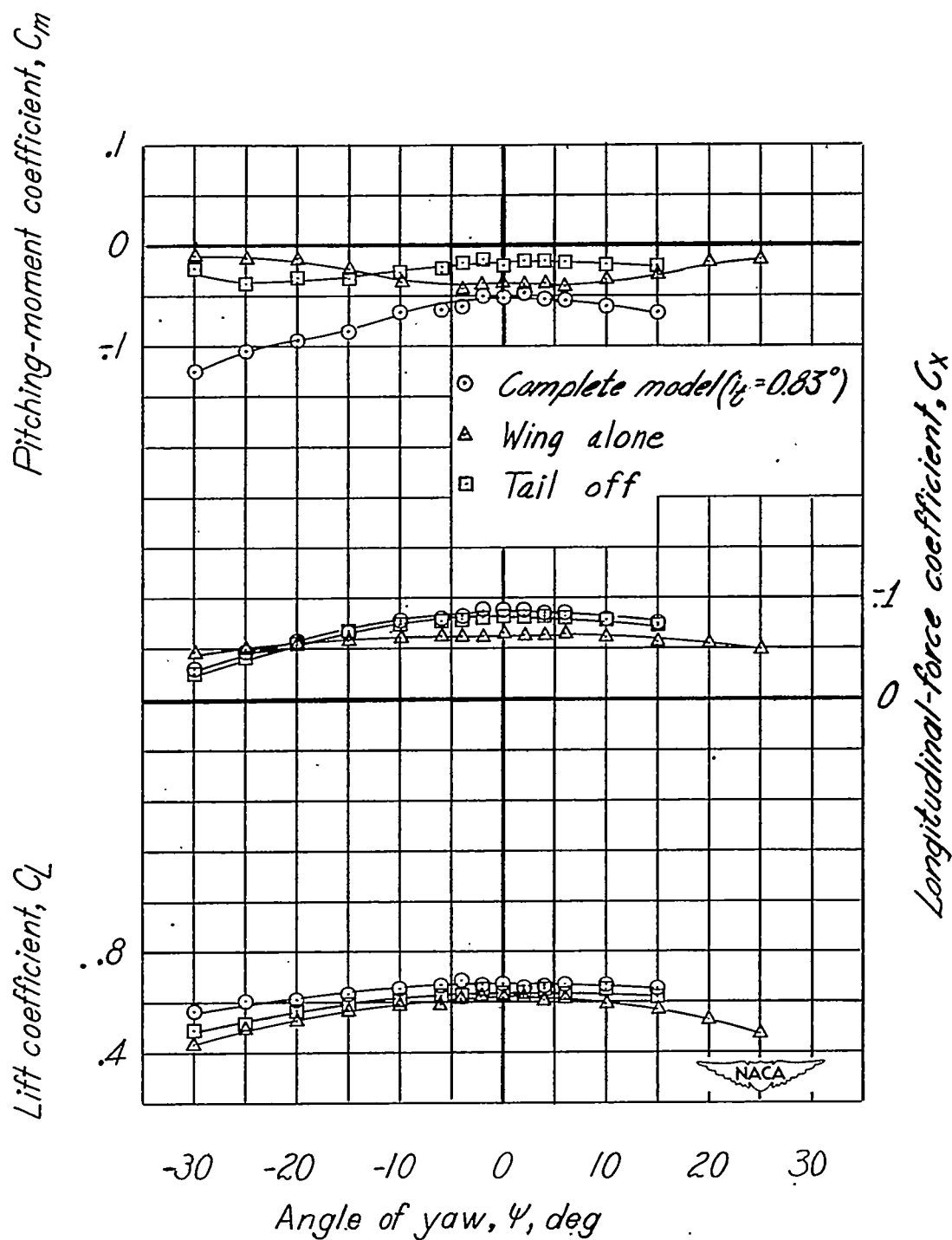
(a) Concluded.

Figure 50.- Continued.
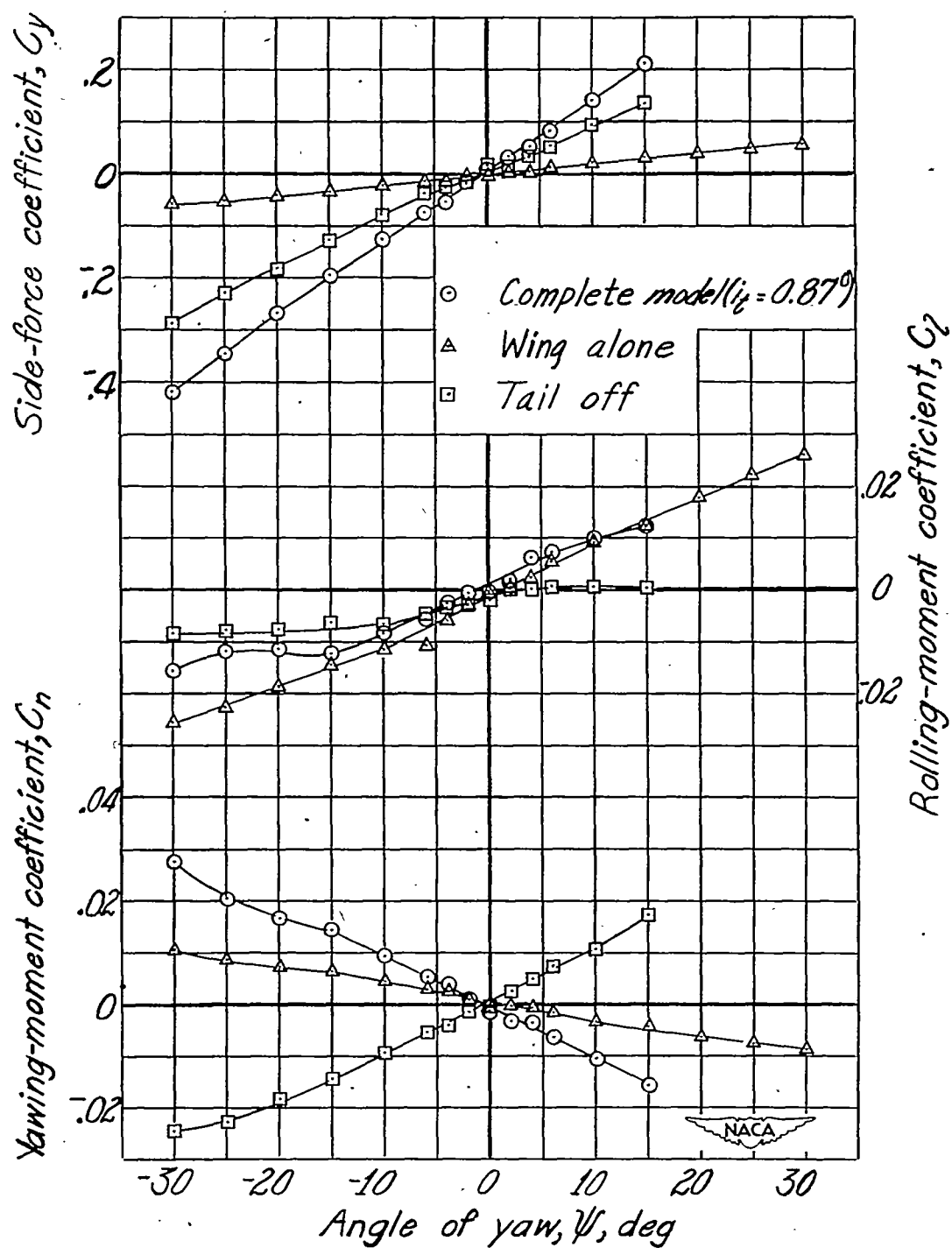
(b) $\delta_f = 45^\circ$; $\alpha = 4.8^\circ$.

Figure 50.- Continued.
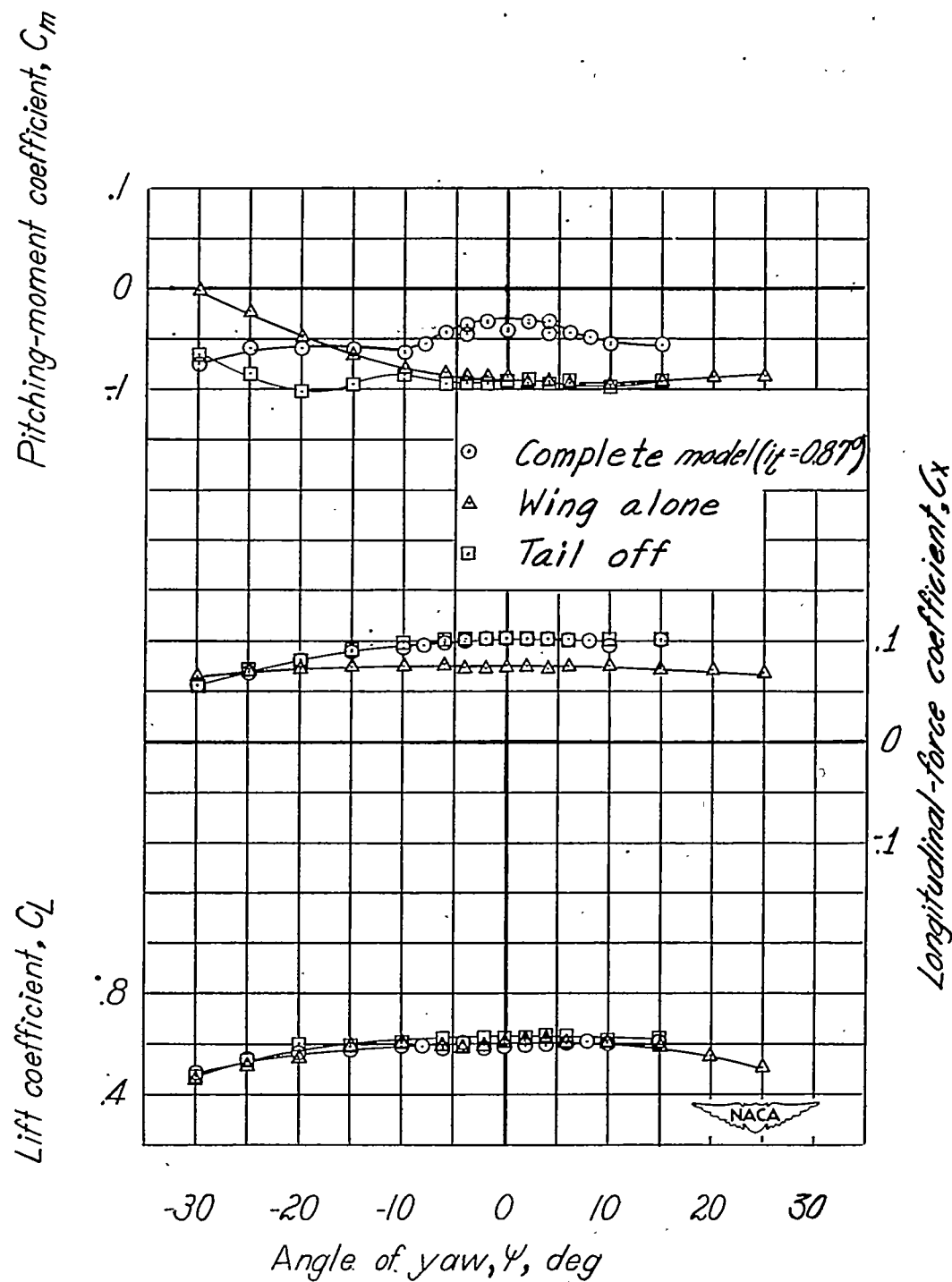
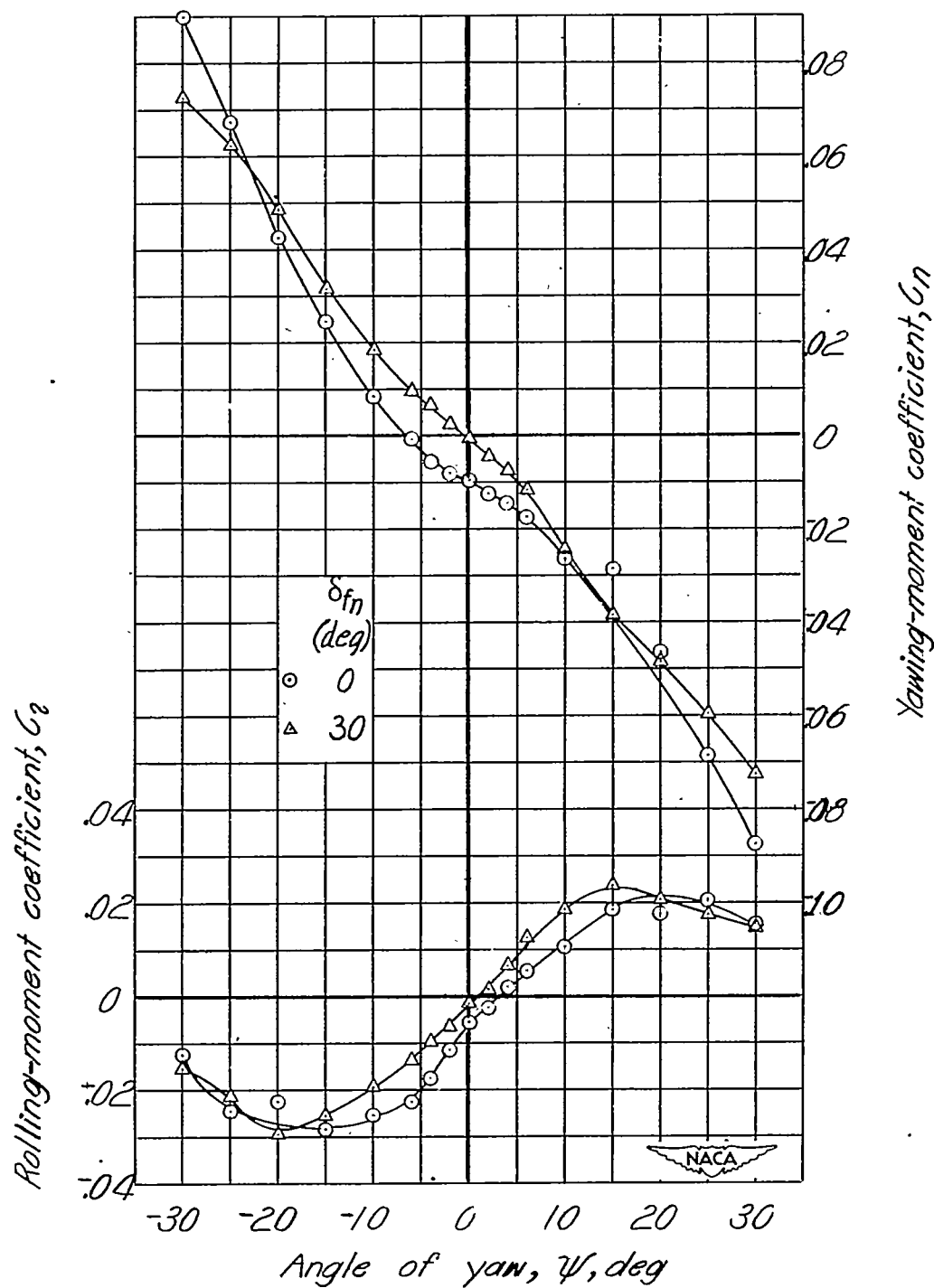(b) Concluded.

Figure 50.- Concluded.
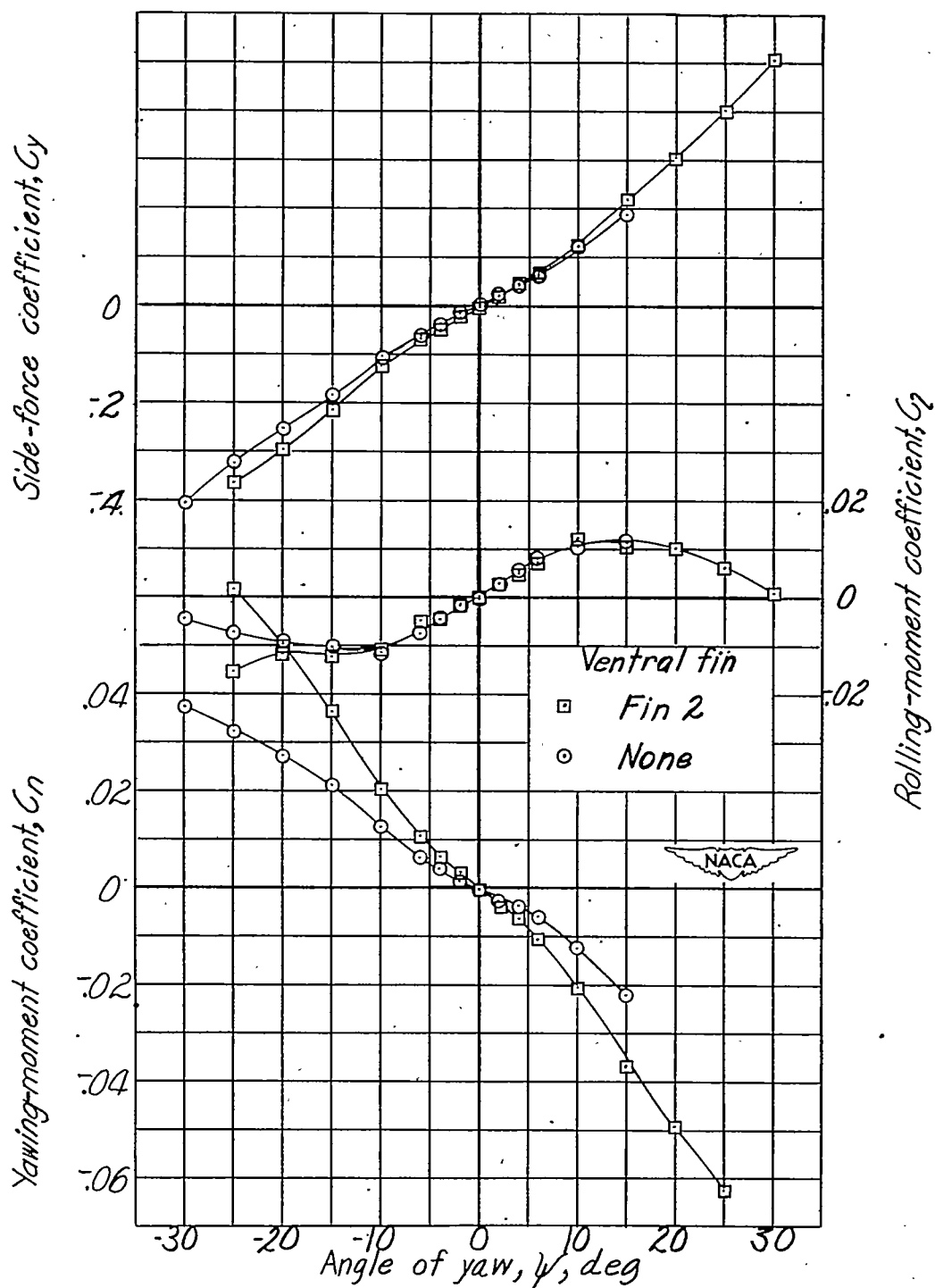
(a) $\delta_f = 0°$; $\alpha = 9.0°$.

Figure 51.- Effect of ventral fin 2 on aerodynamic characteristics in yaw.
Windmilling propeller; extended fuselage; 80-percent-span slots; $i_t = 1.02°$;
$R = 2.05 \times 10^6$.
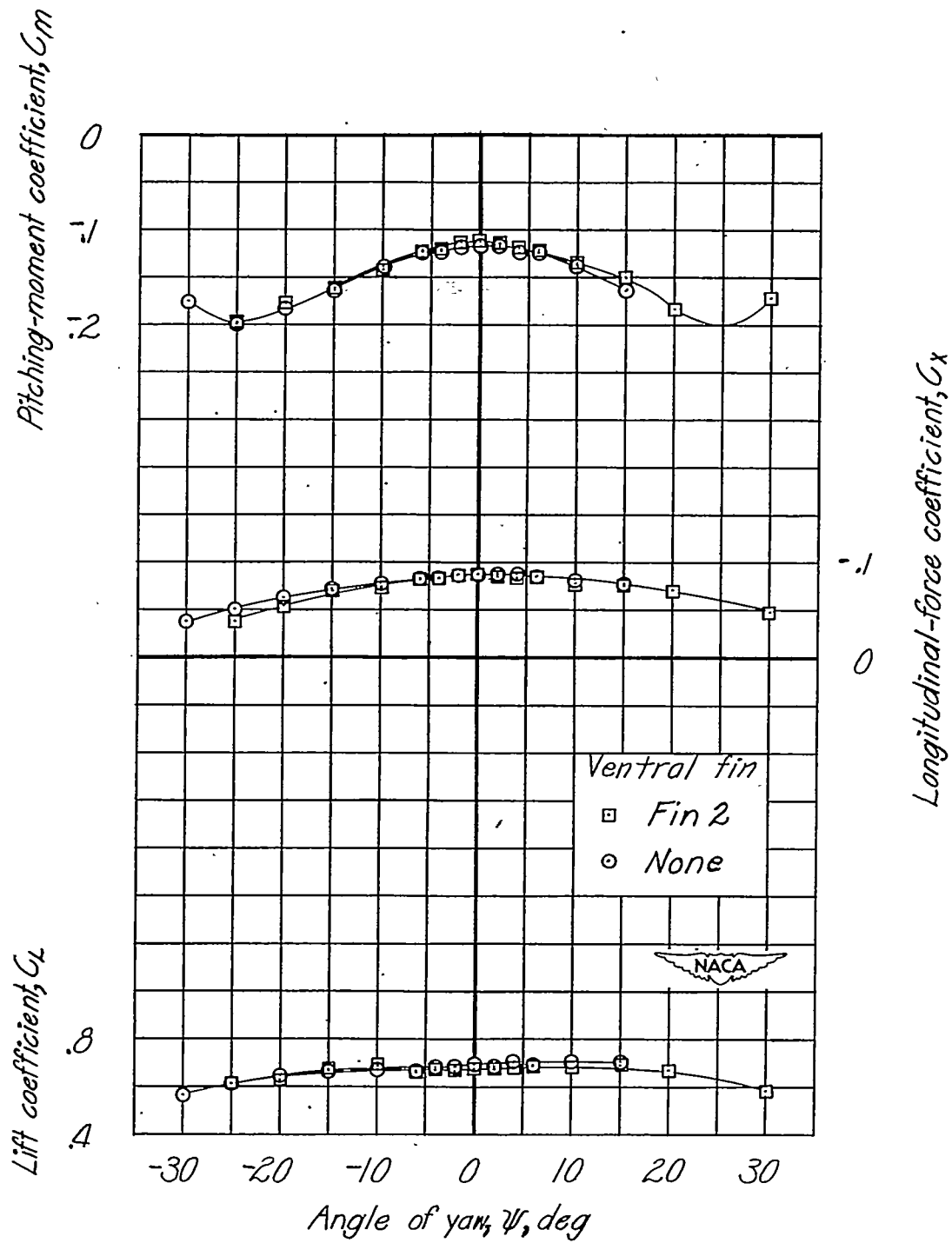
(a) Concluded.

Figure 51.- Continued.
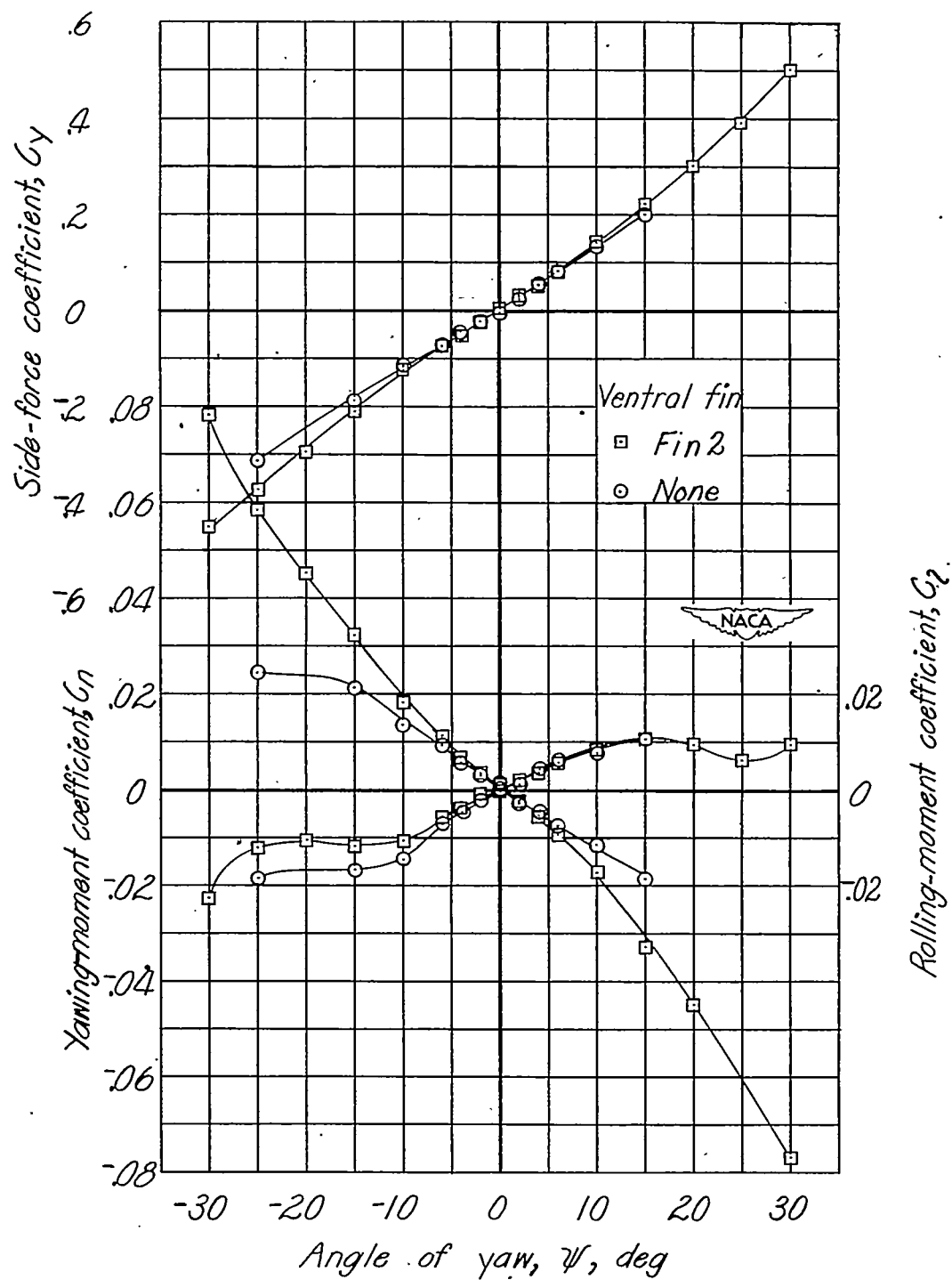
(b) $\delta_f = 45°$; $\alpha = 4.9°$.

Figure 51.- Continued.
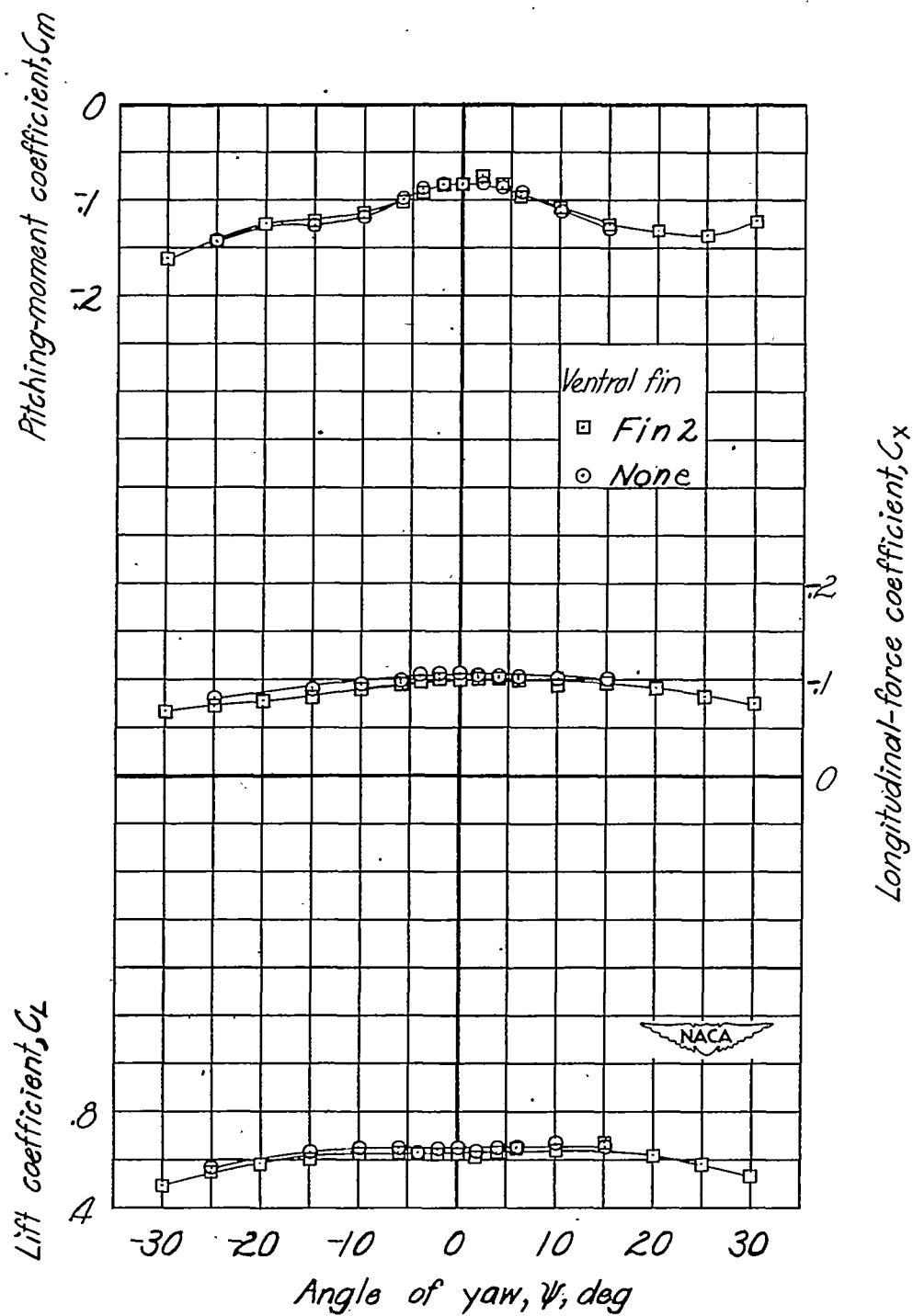
(b) Concluded.

Figure 51.- Concluded.
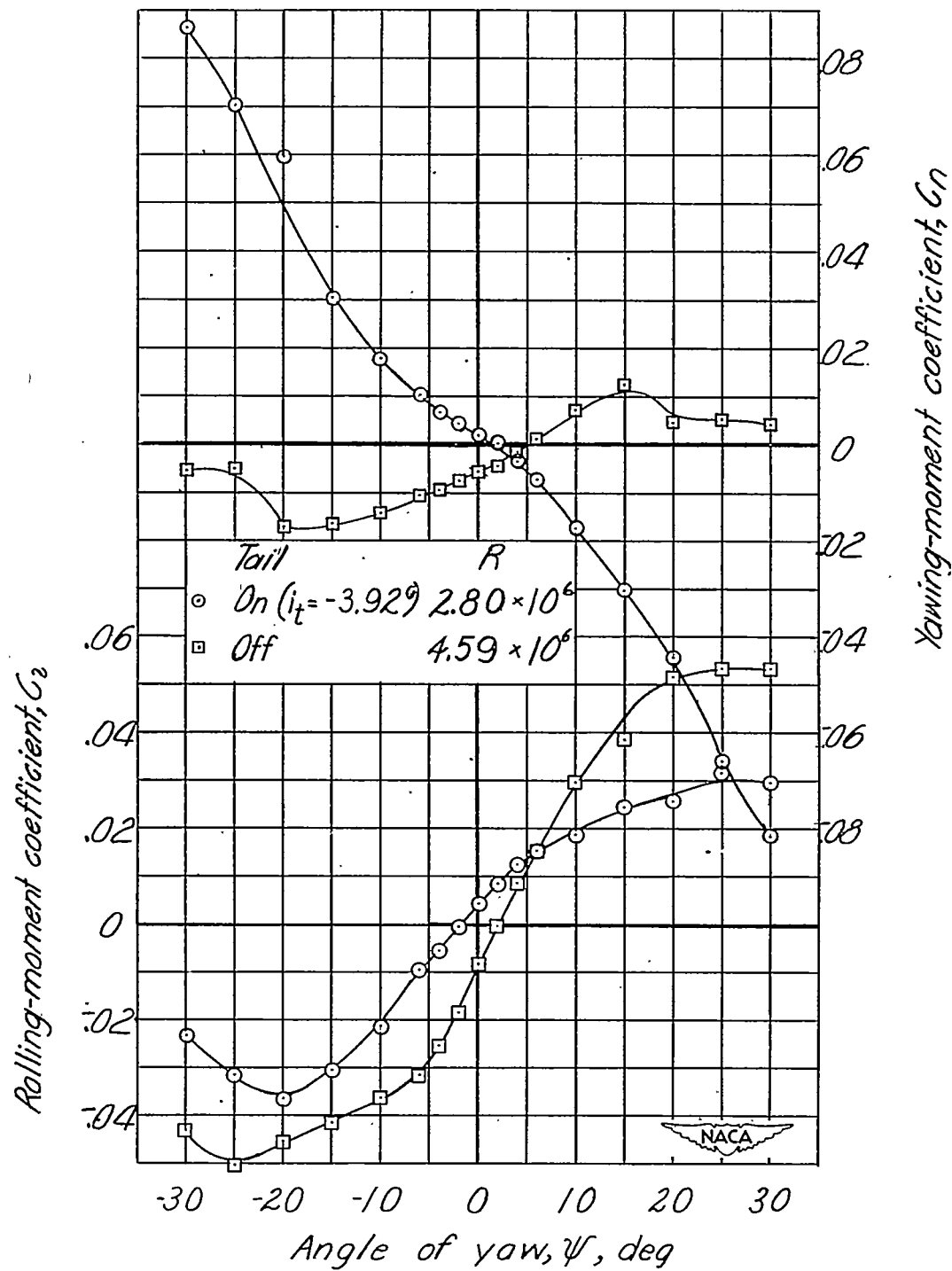
(a) $\delta_f = 0°$; $\alpha = 18.5°$.

Figure 52.- Effect of tail on aerodynamic characteristics in yaw.
Windmilling propeller; extended fuselage; ventral fin 3;
40-percent-span slots.
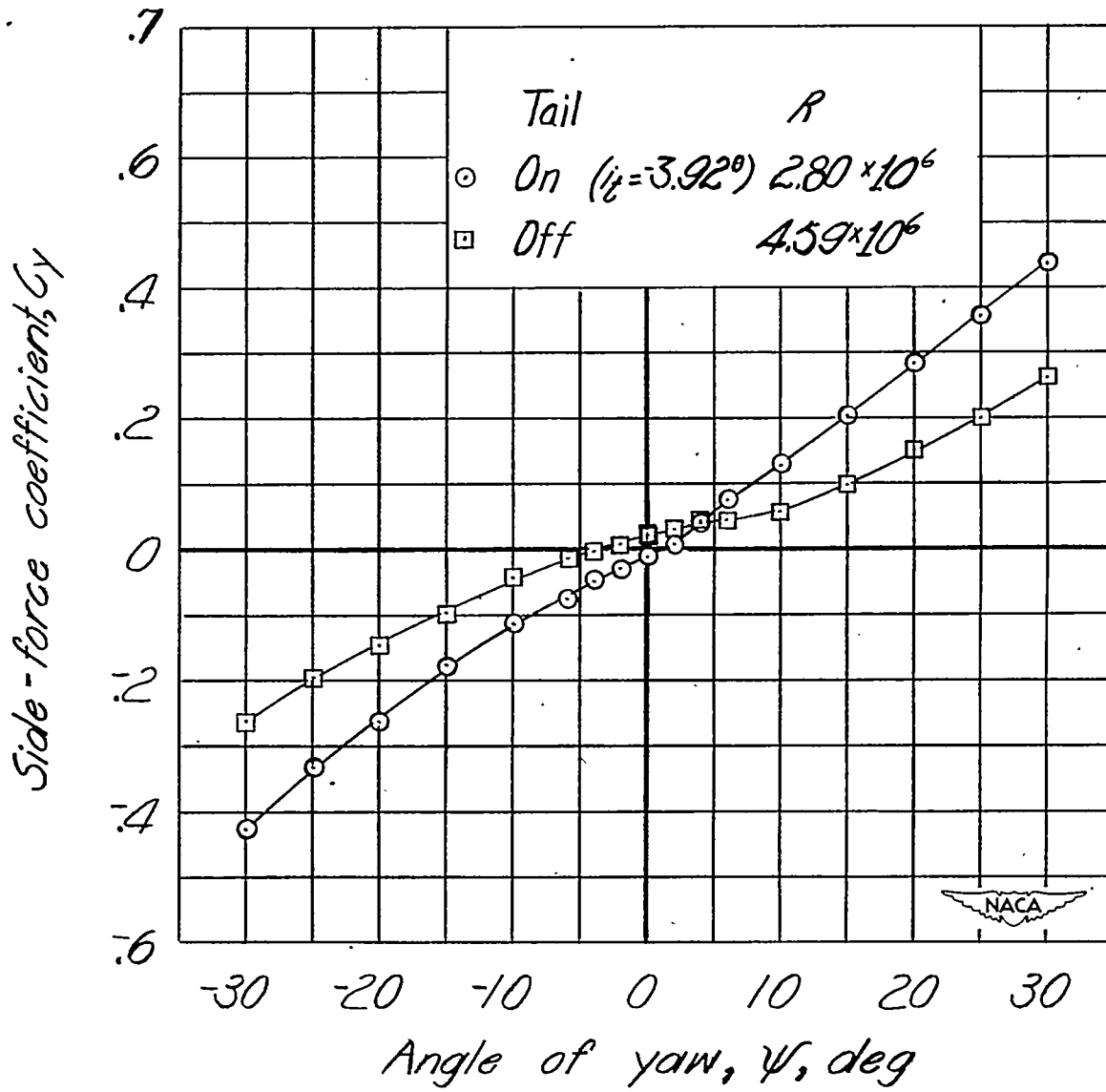
(a) Continued.

Figure 52.- Continued.
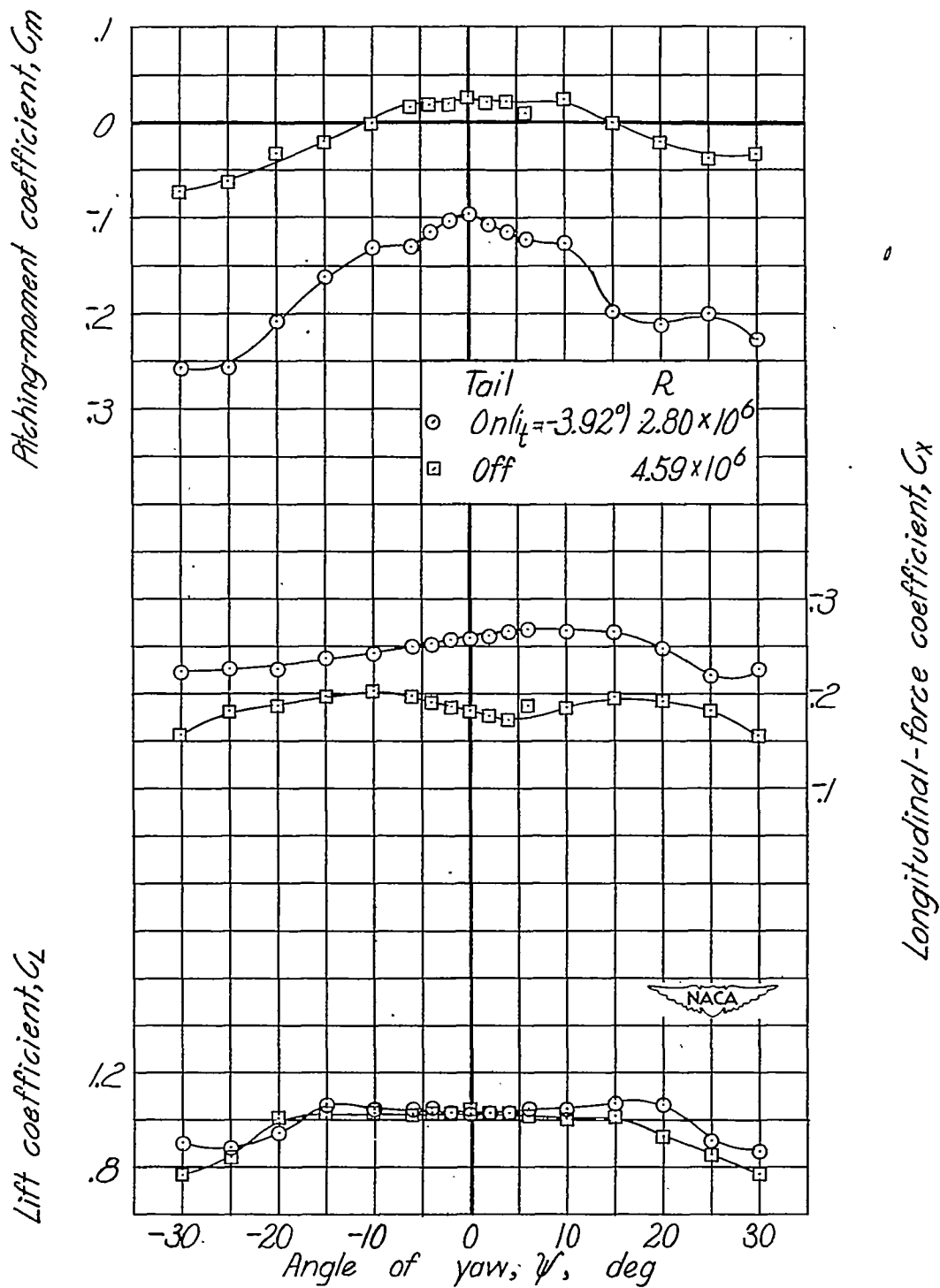
(a) Concluded.

Figure 52.- Continued.
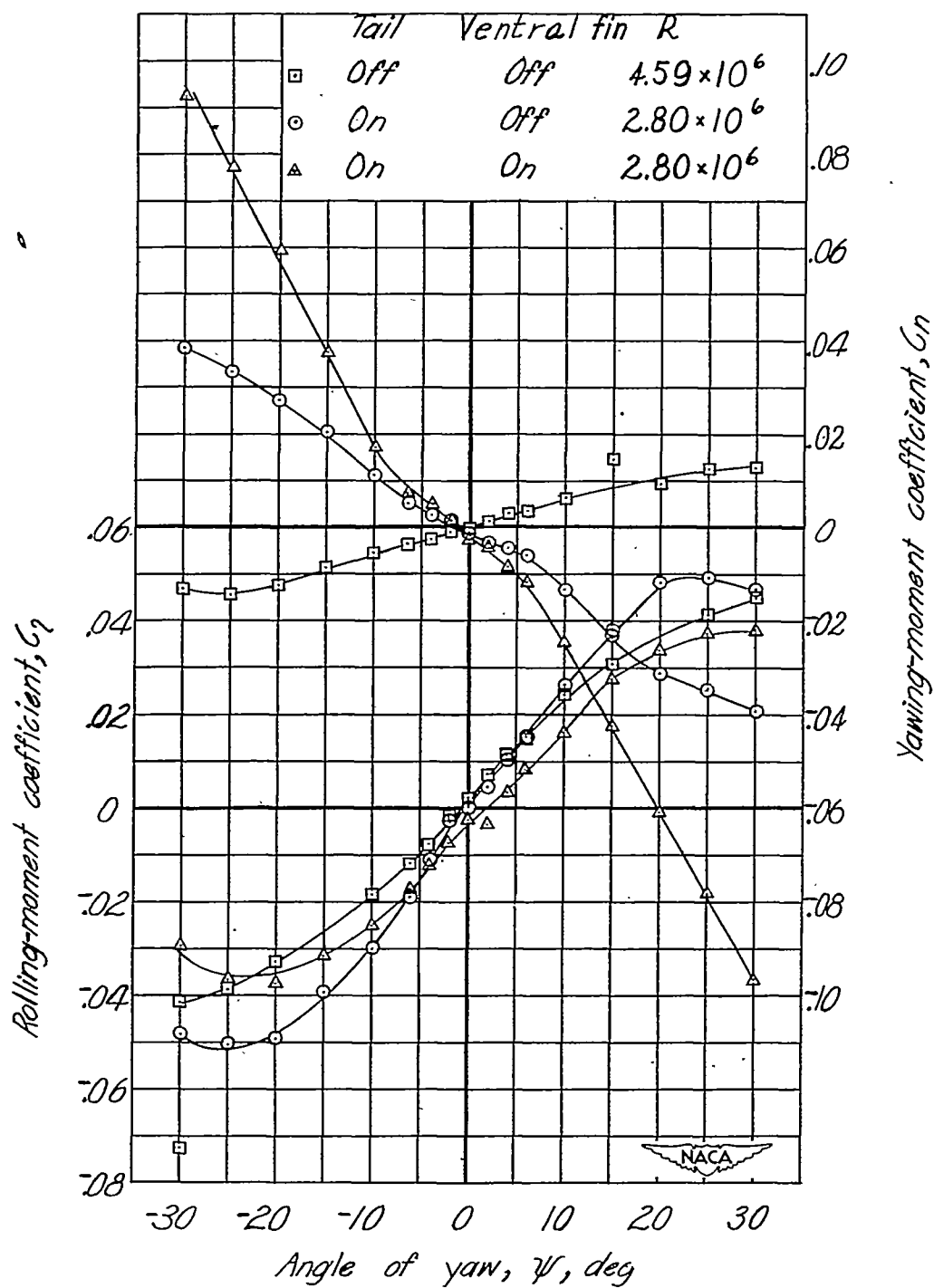
(b) $\delta_f = 45°$; $\alpha = 12.6°$.

Figure 52.- Continued.
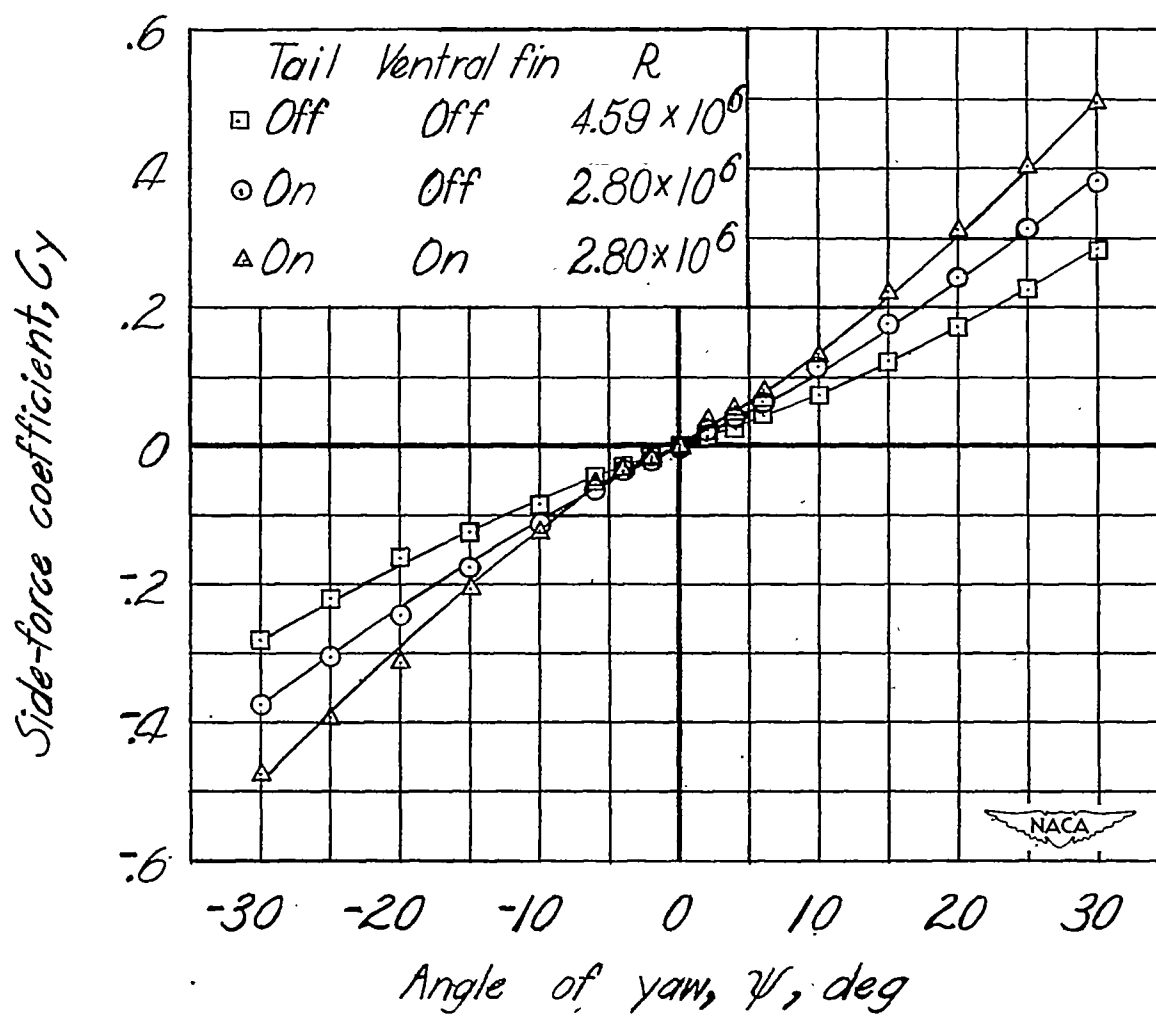
(b) Continued.

Figure 52.- Continued.
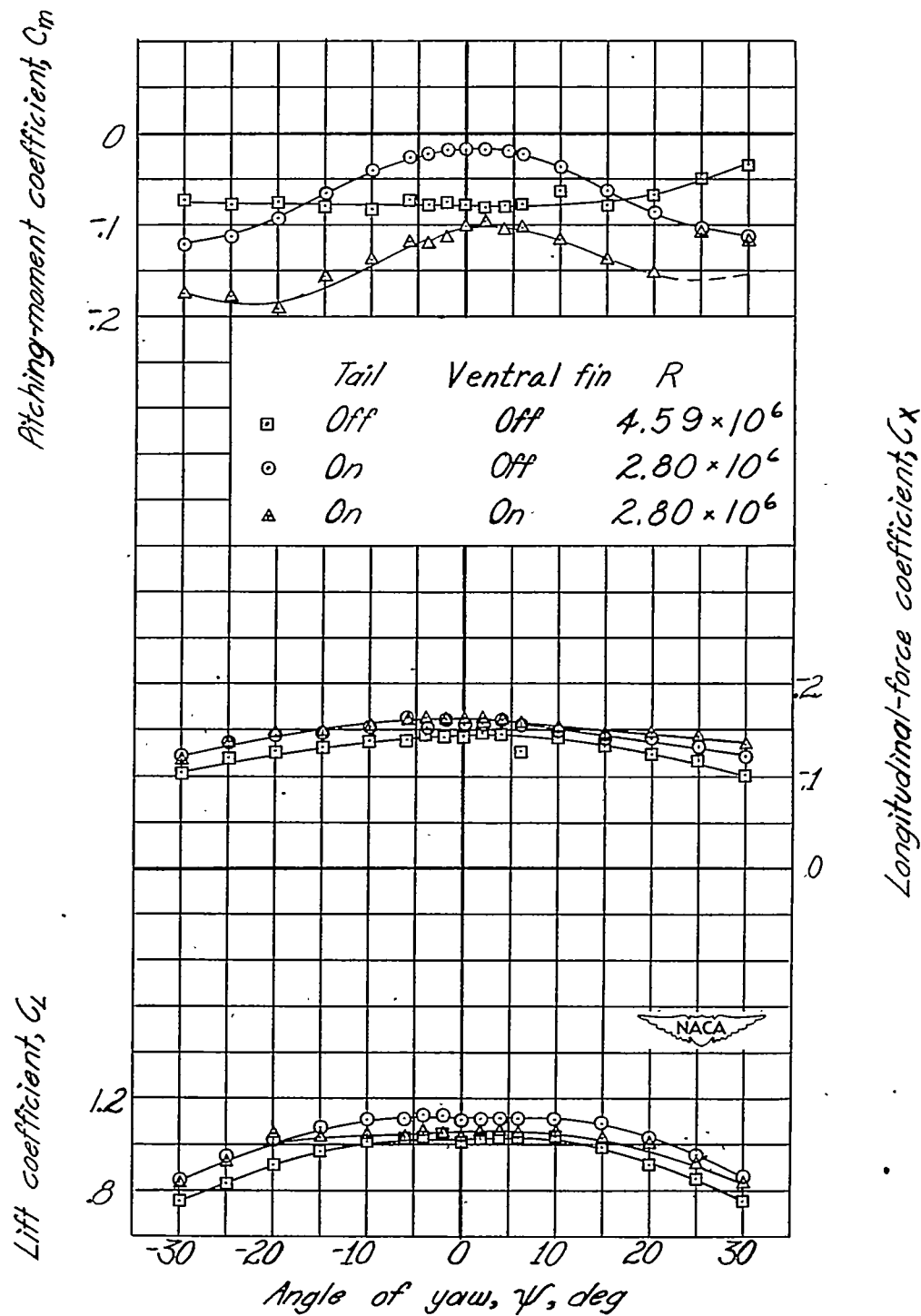
(b) Concluded.

Figure 52.- Concluded.
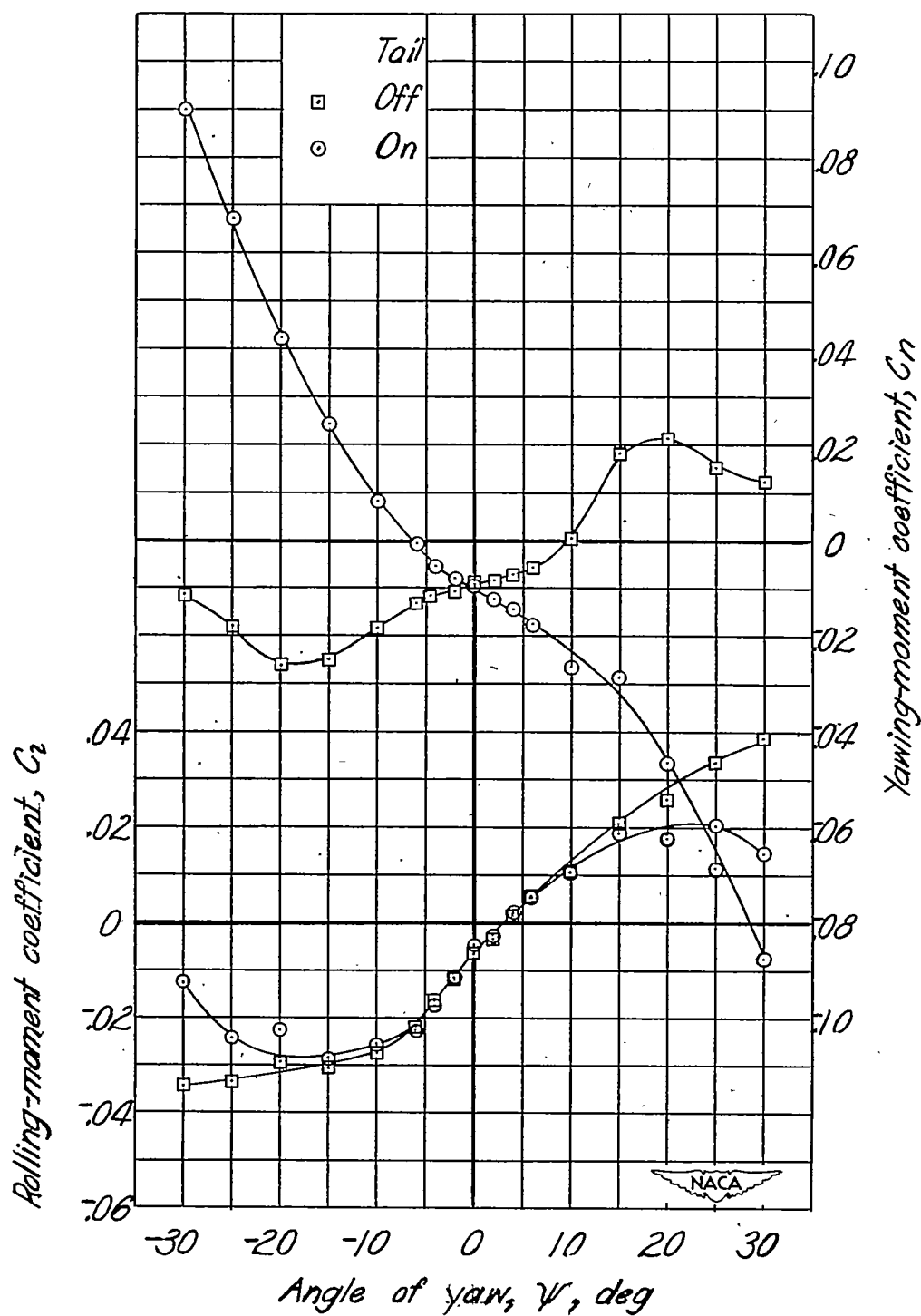
Figure 53.- Effect of tail on aerodynamic characteristics in yaw. Windmilling propeller: extended fuselage; ventral fin 3; 0-percent-span slots; $\delta_f = 0^o$; $\alpha = 16.9^o$; $R = 4.59 \times 10^6$.

Figure 53.- Continued.

Lift coefficient, C_L

Pitching-moment coefficient, C_m

Tail
□ Off
⊙ On

Angle of yaw, ψ, deg

NACA

Figure 58.- Concluded.

Longitudinal-force coefficient, C_x
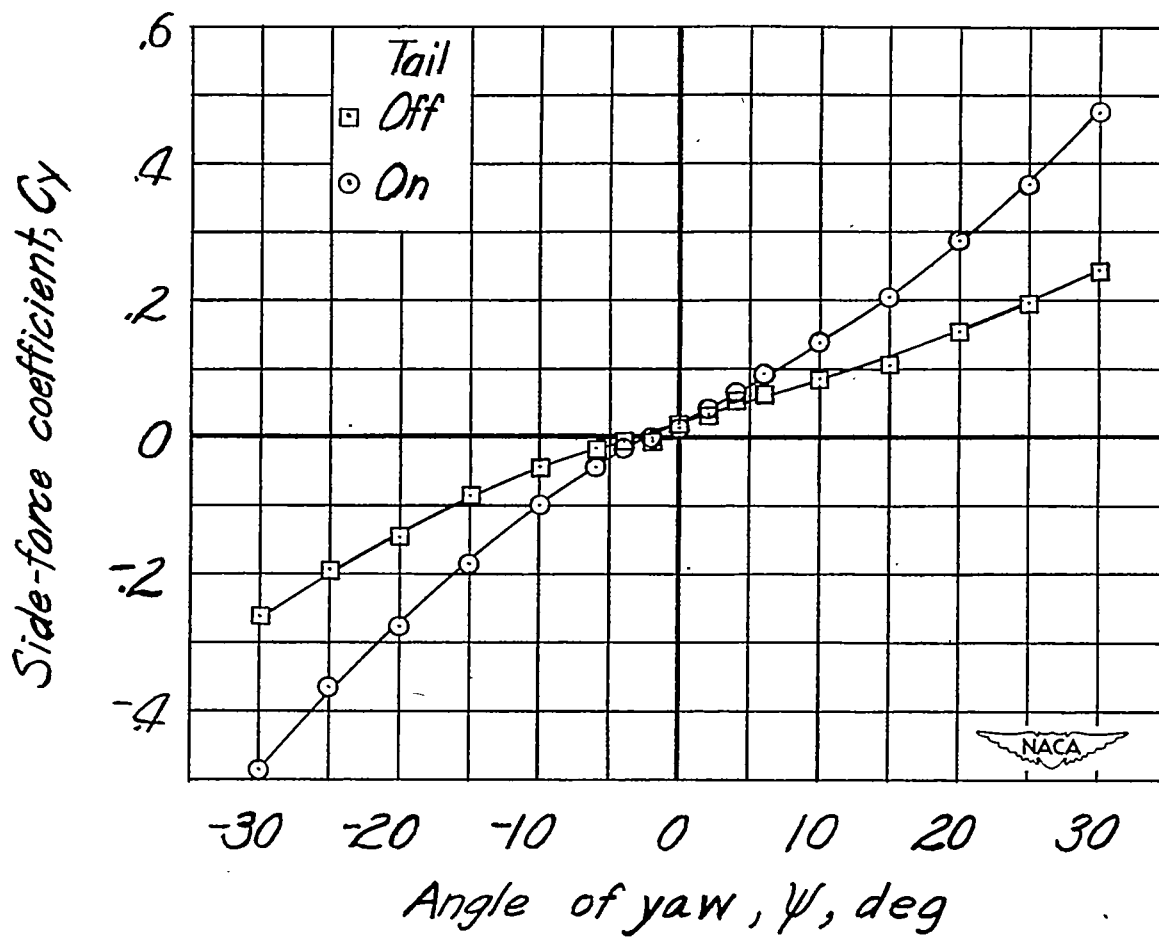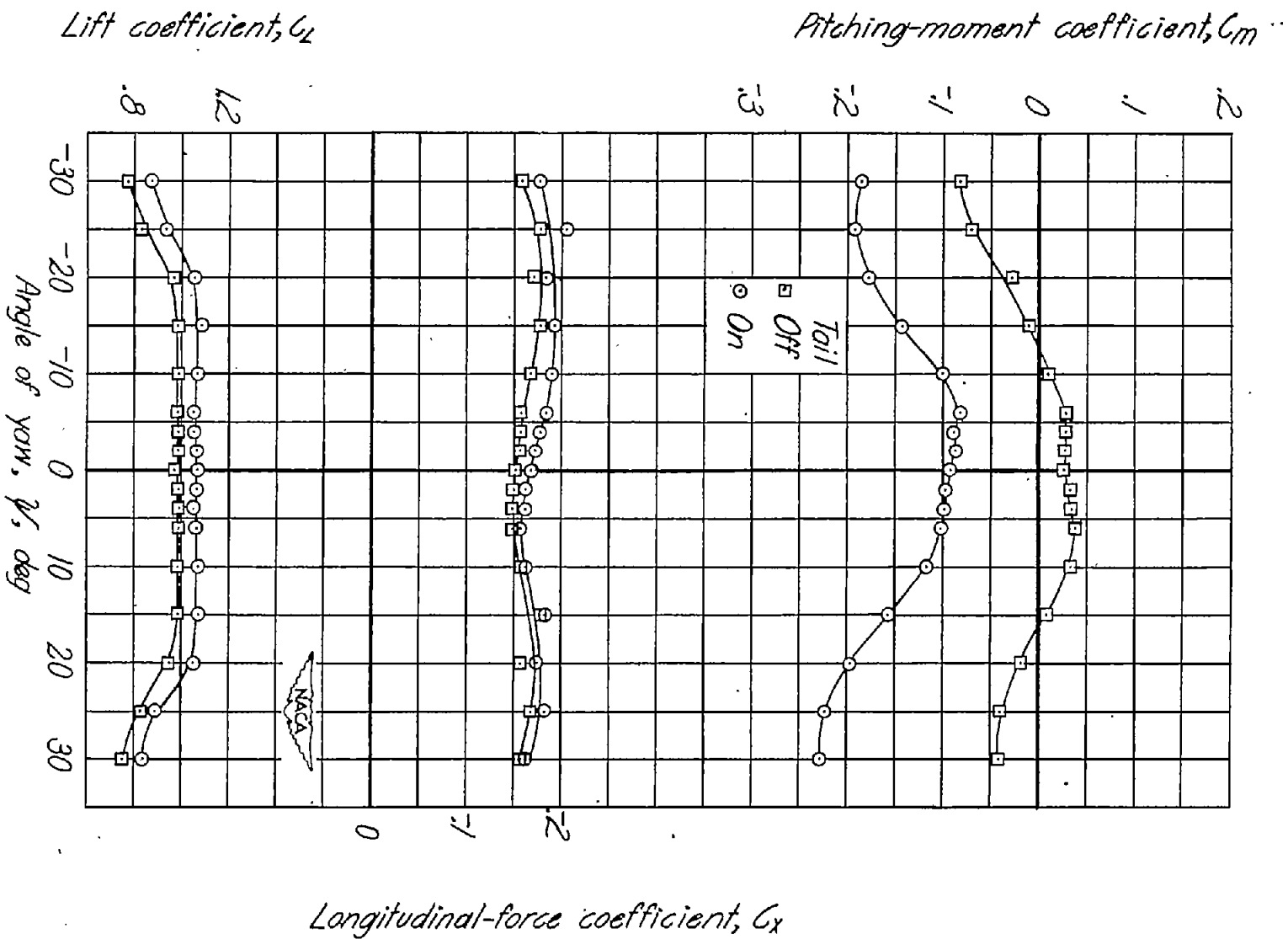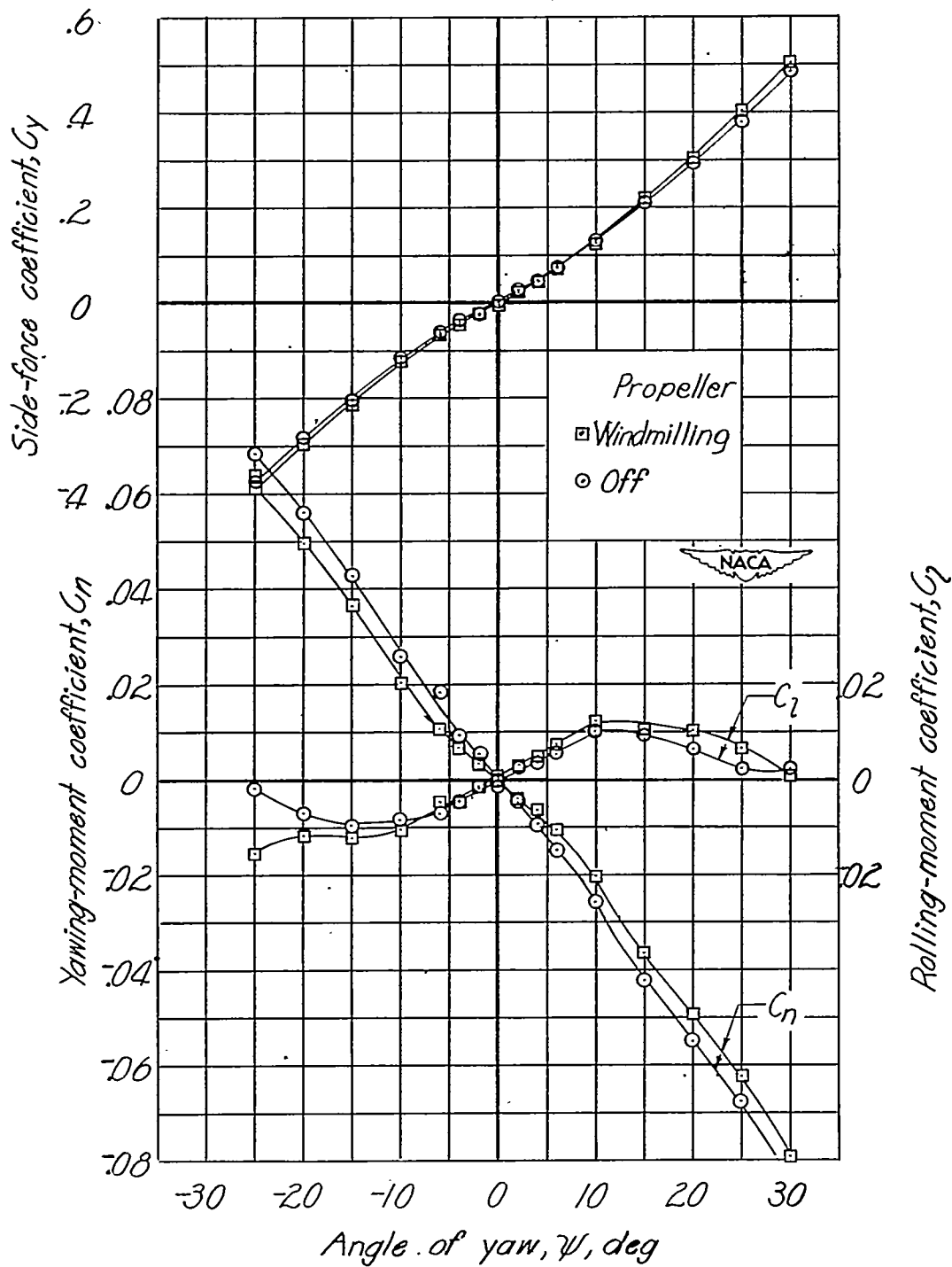
Figure 54.- Effect of propeller on aerodynamic characteristics in yaw. Extended fuselage; ventral fin 2; 80-percent-span slots; $\delta_f = 0°$; $\alpha = 9.0°$; $i_t = 1.0°$; R = 2.05 × 10^6.
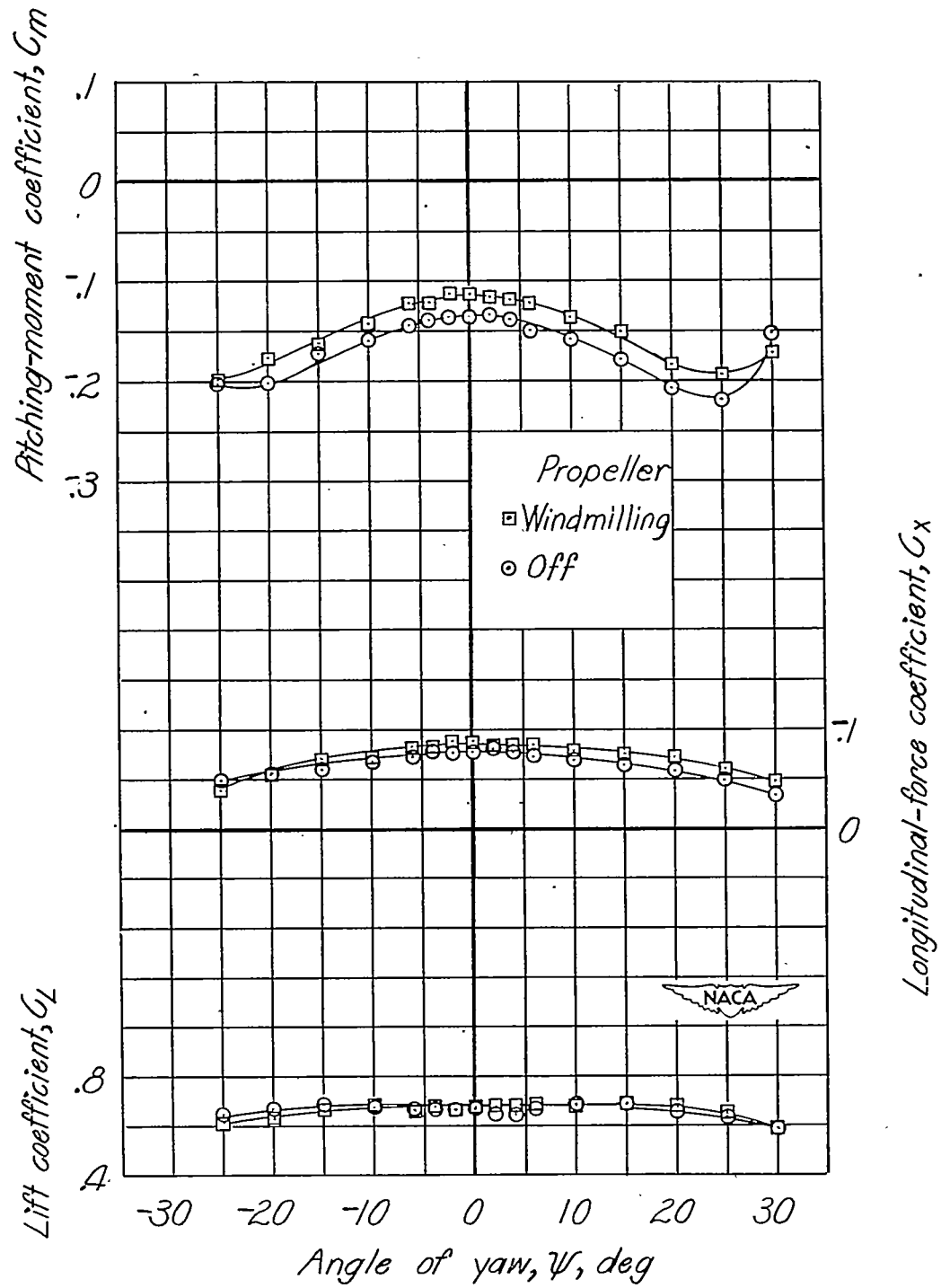
Figure 54.- Concluded.
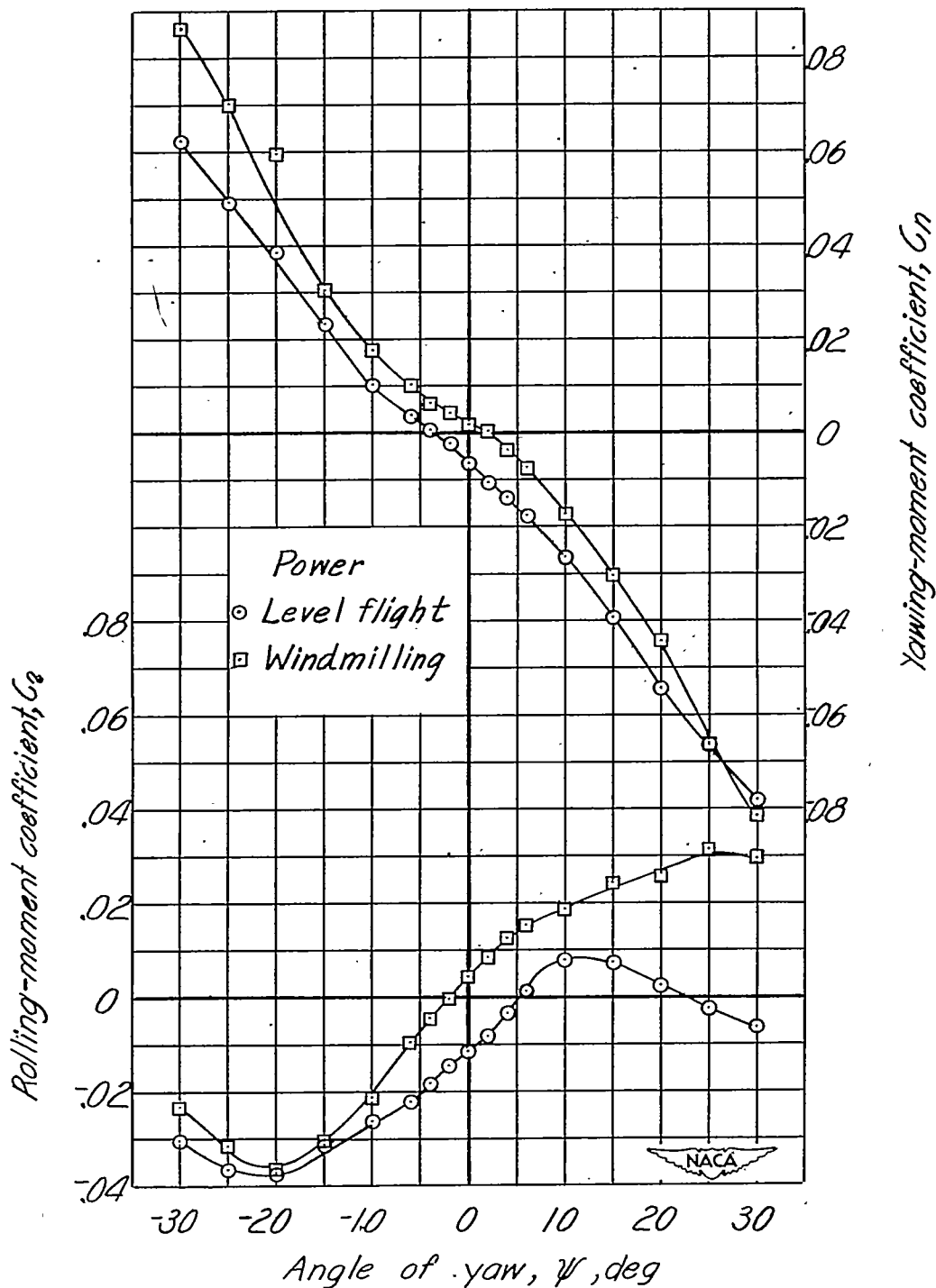
(a) $\delta_f = 0°$; $\alpha = 19.5°$.

Figure 55.- Effect of power on aerodynamic characteristics in yaw.
Extended fuselage; $i_t = -3.9°$; ventral fin 3; 40-percent-span slots;
$R = 2.80 \times 10^6$.
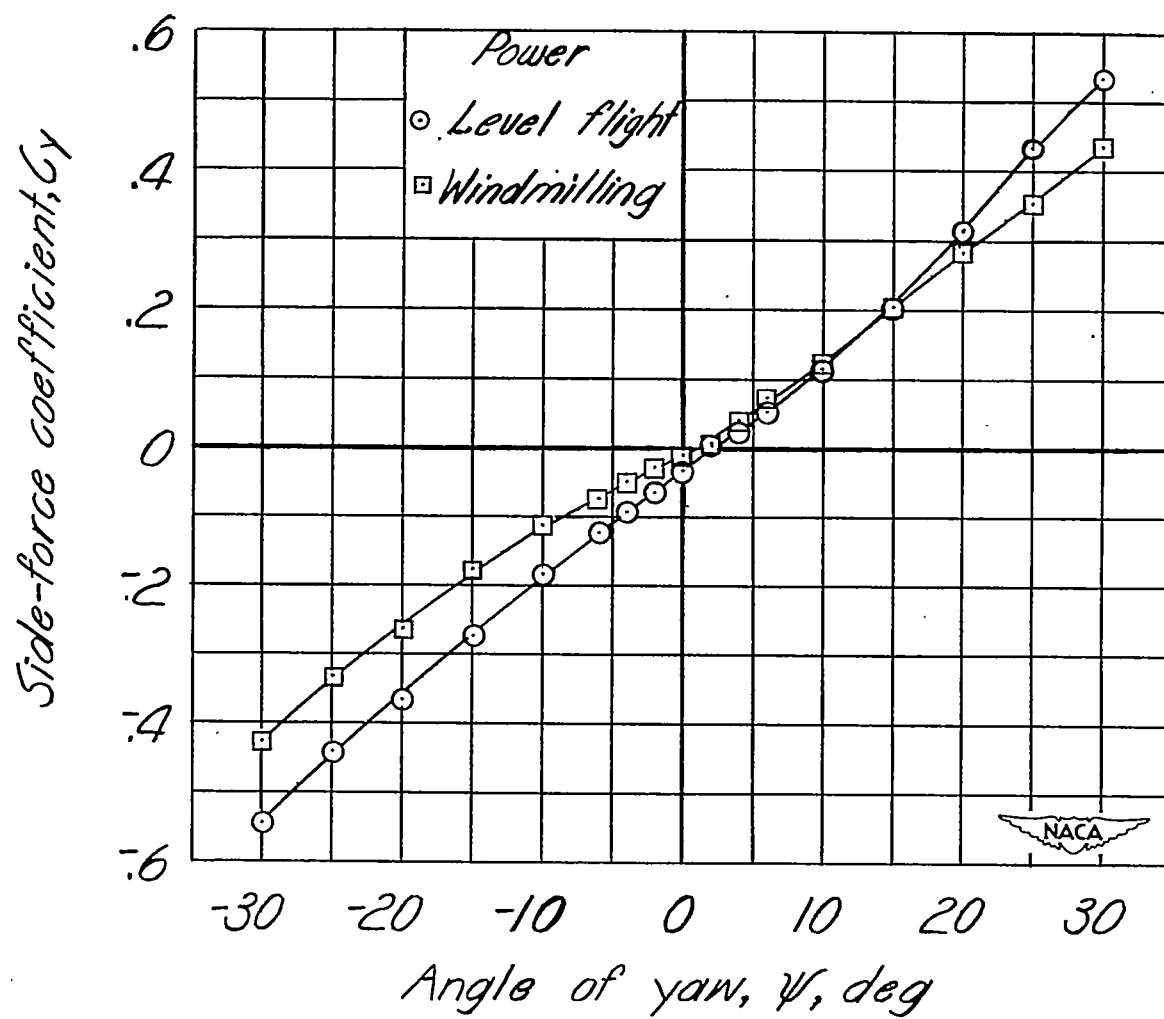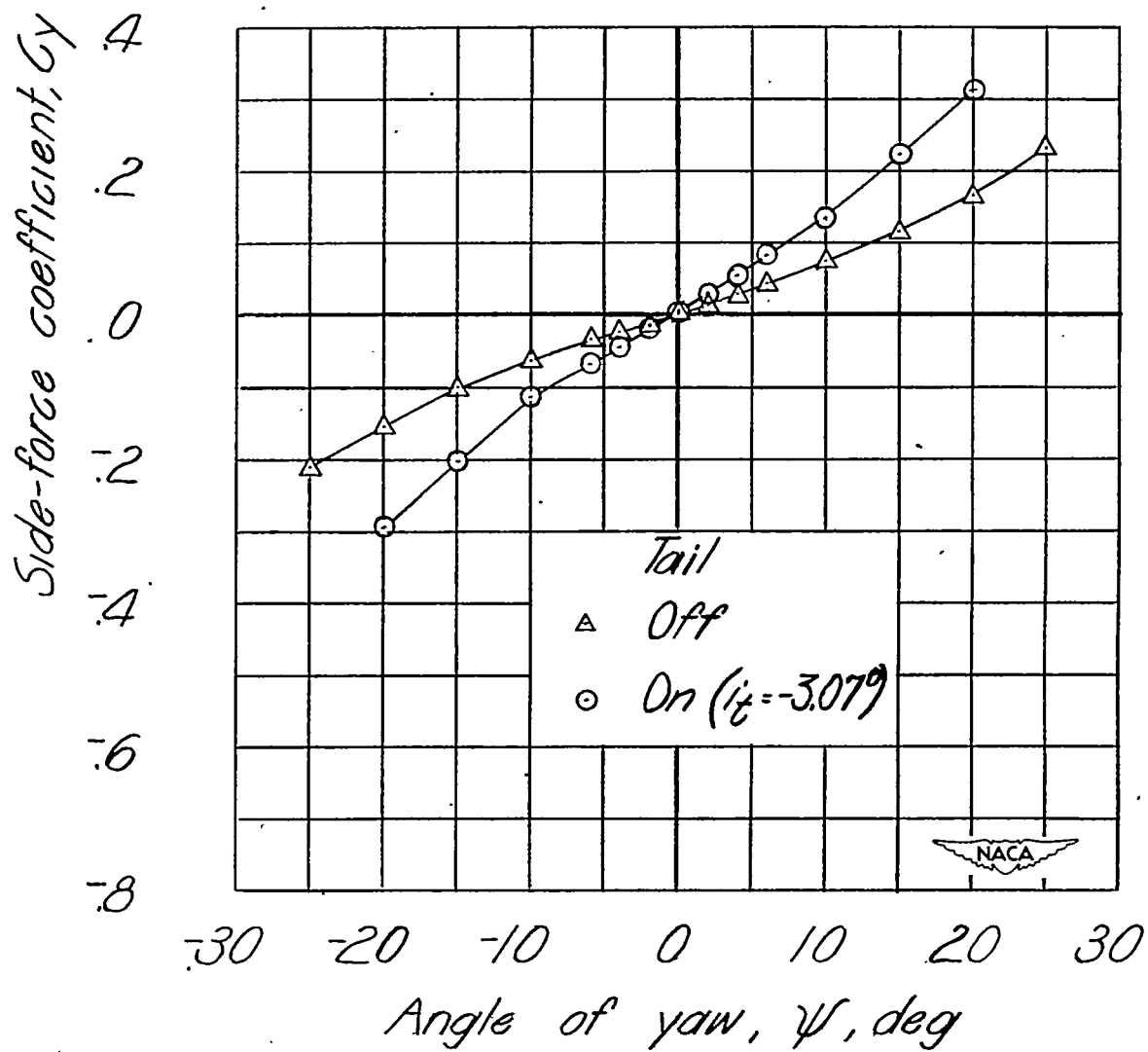
(a) Continued.

Figure 55.- Continued.
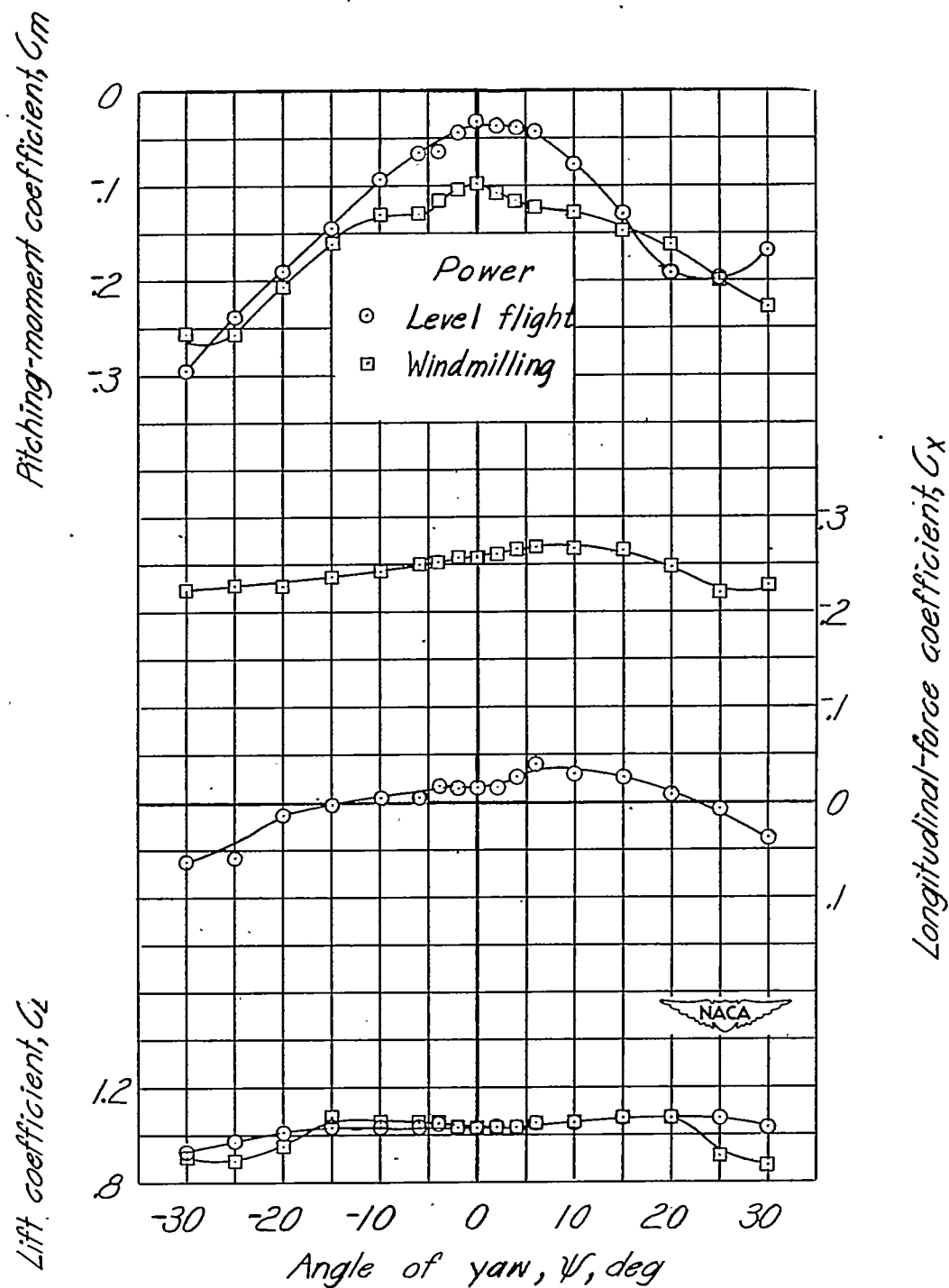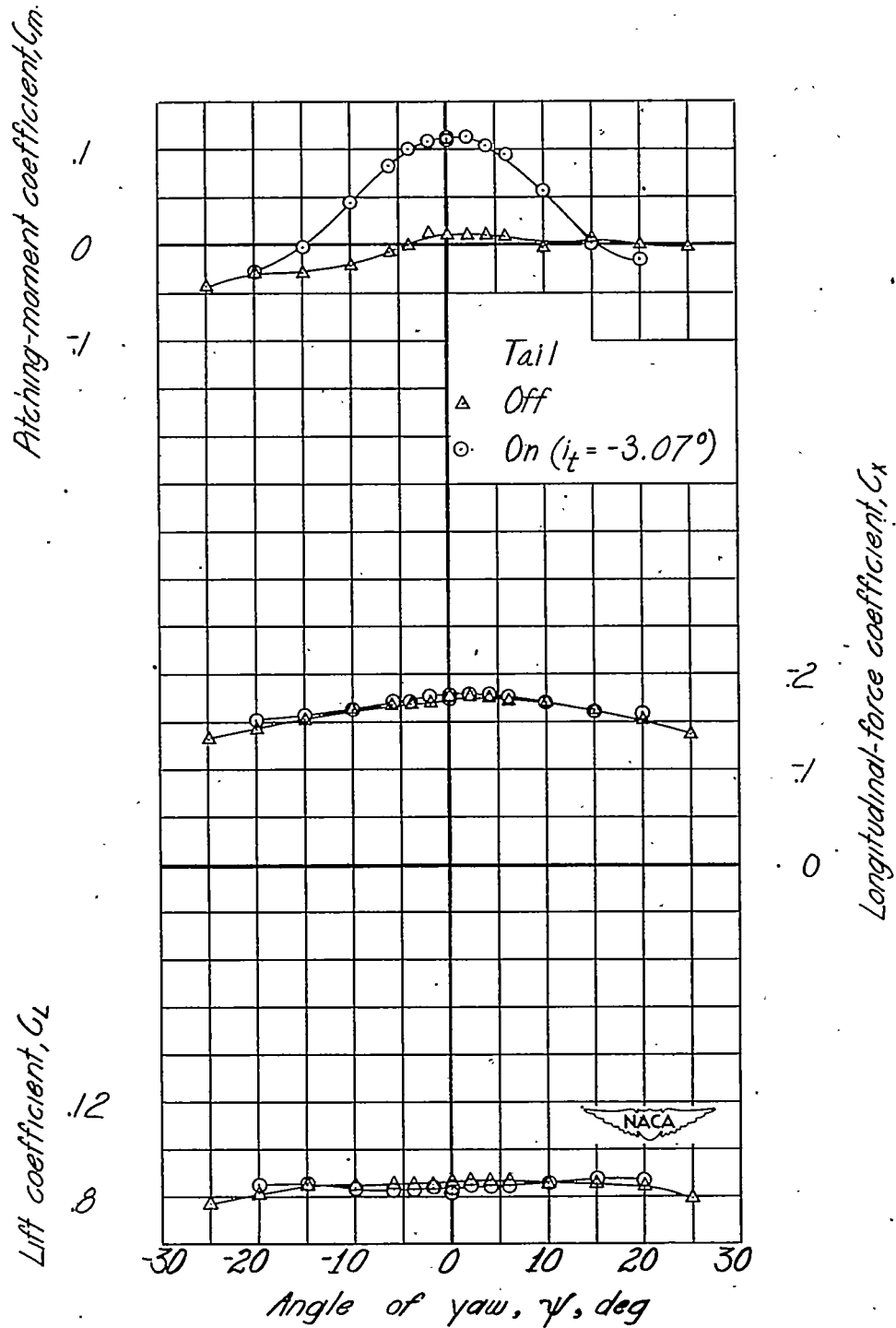
(a) Concluded.

Figure 55.- Continued.
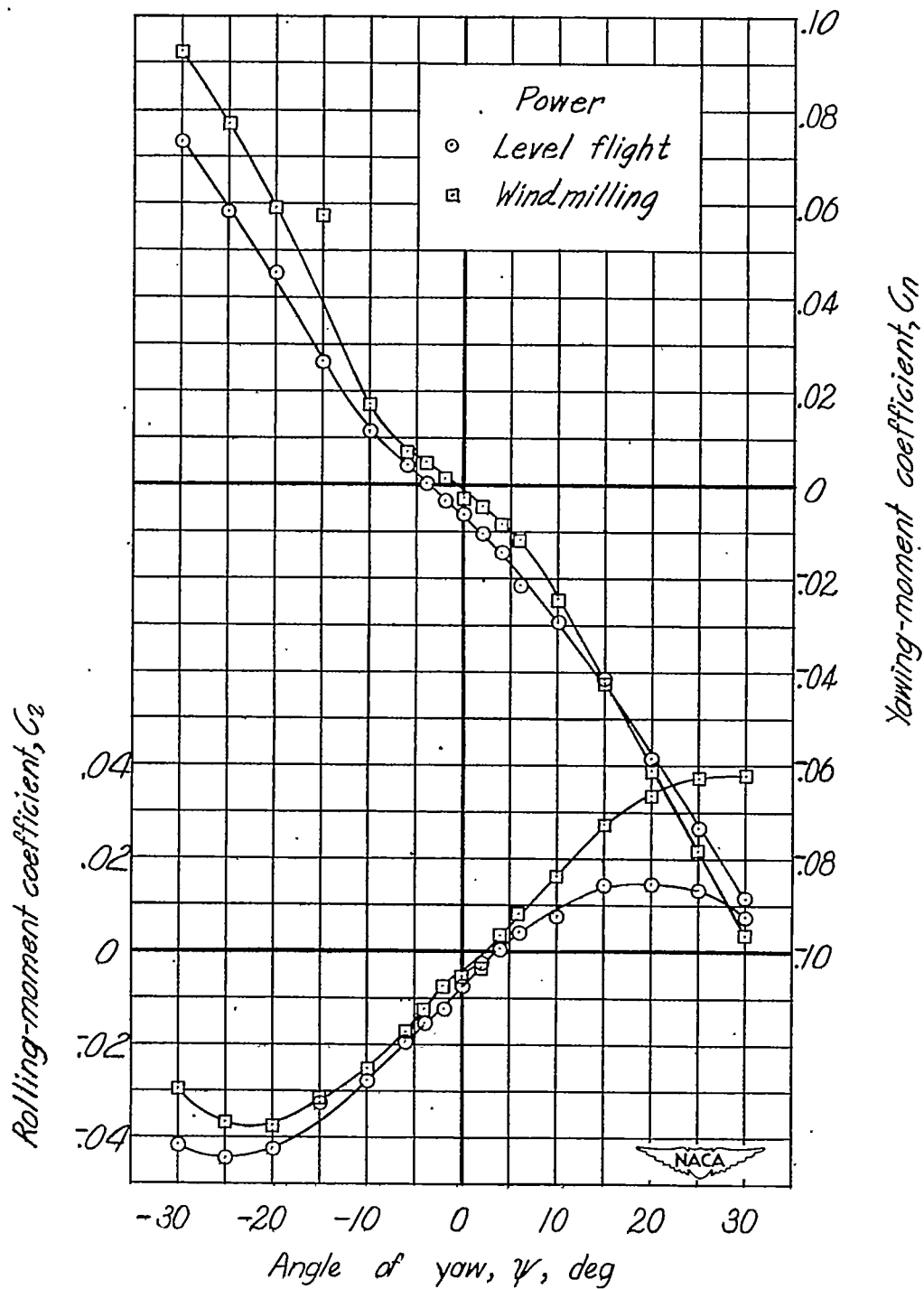
(b) $\delta_f = 45^\circ$; $\alpha = 12.5^\circ$.

Figure 55.- Continued.
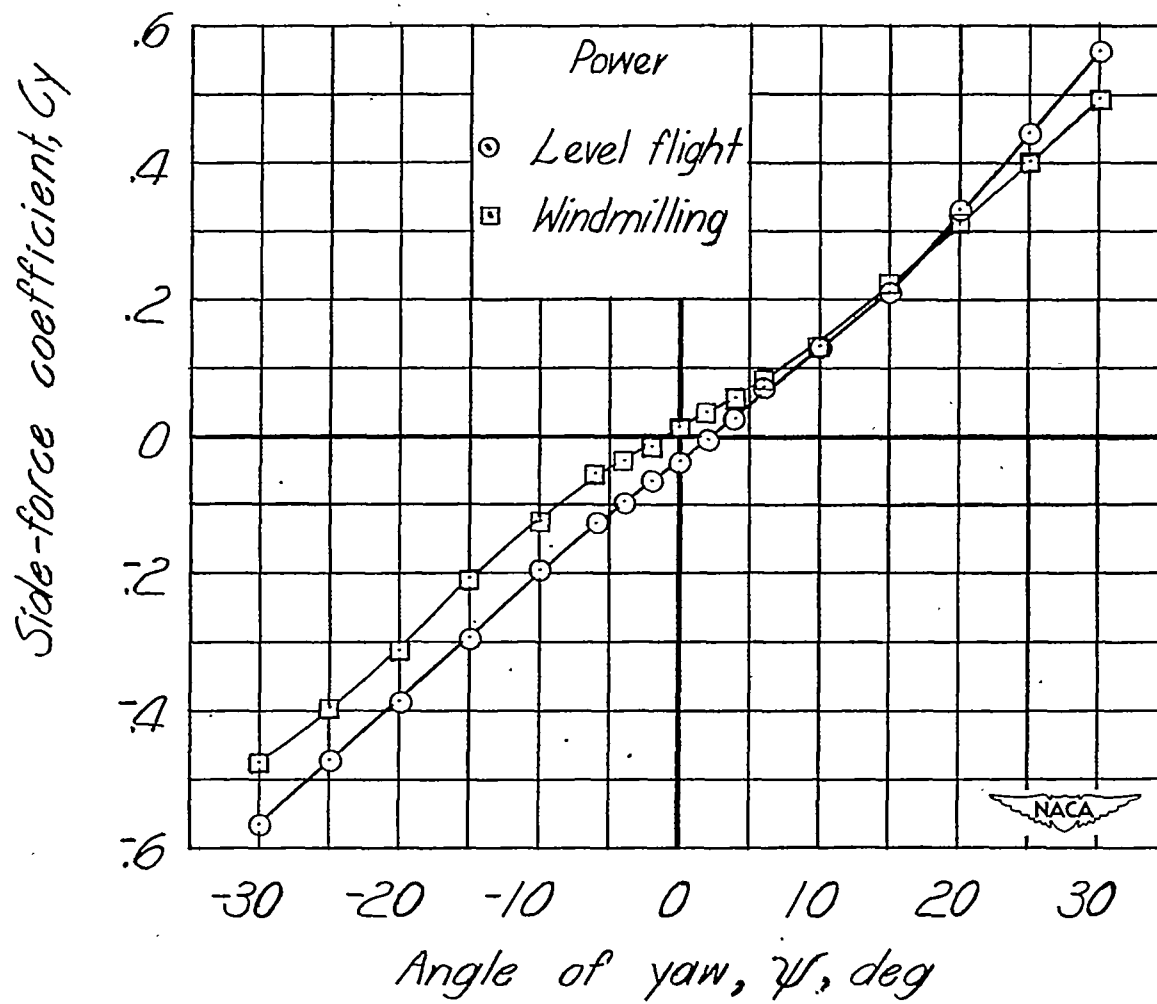
(b) Continued.

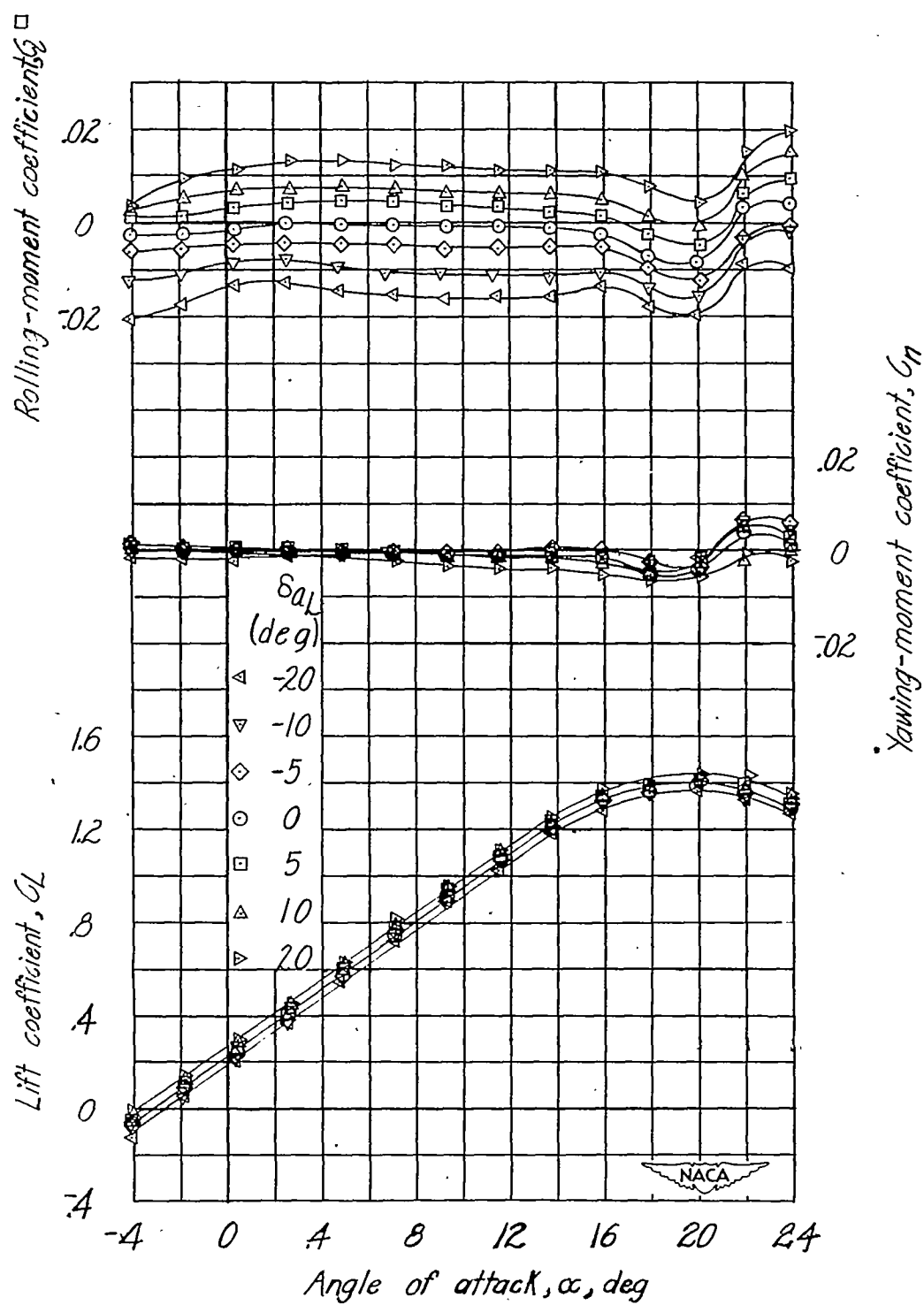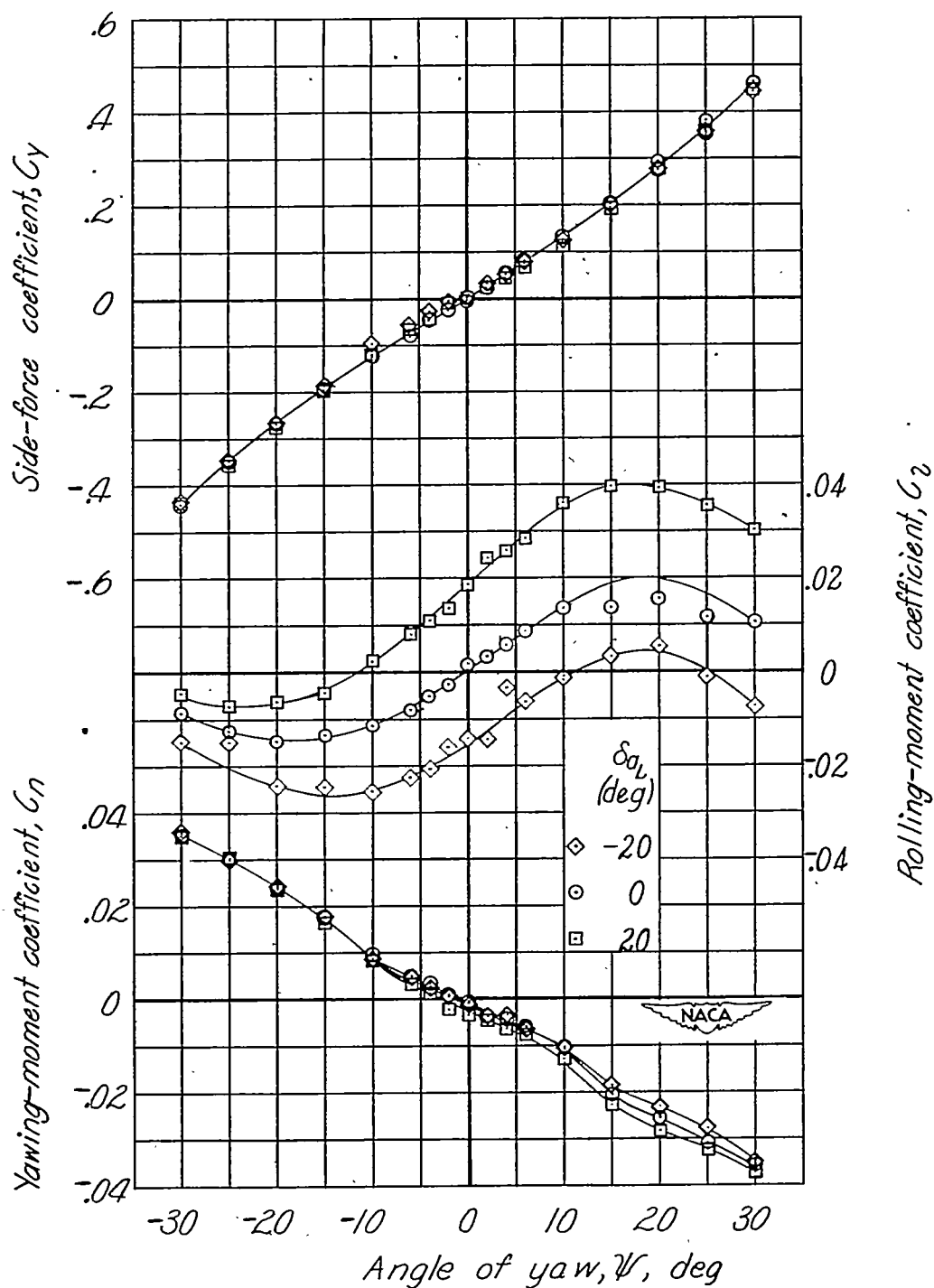Figure 55.- Continued.
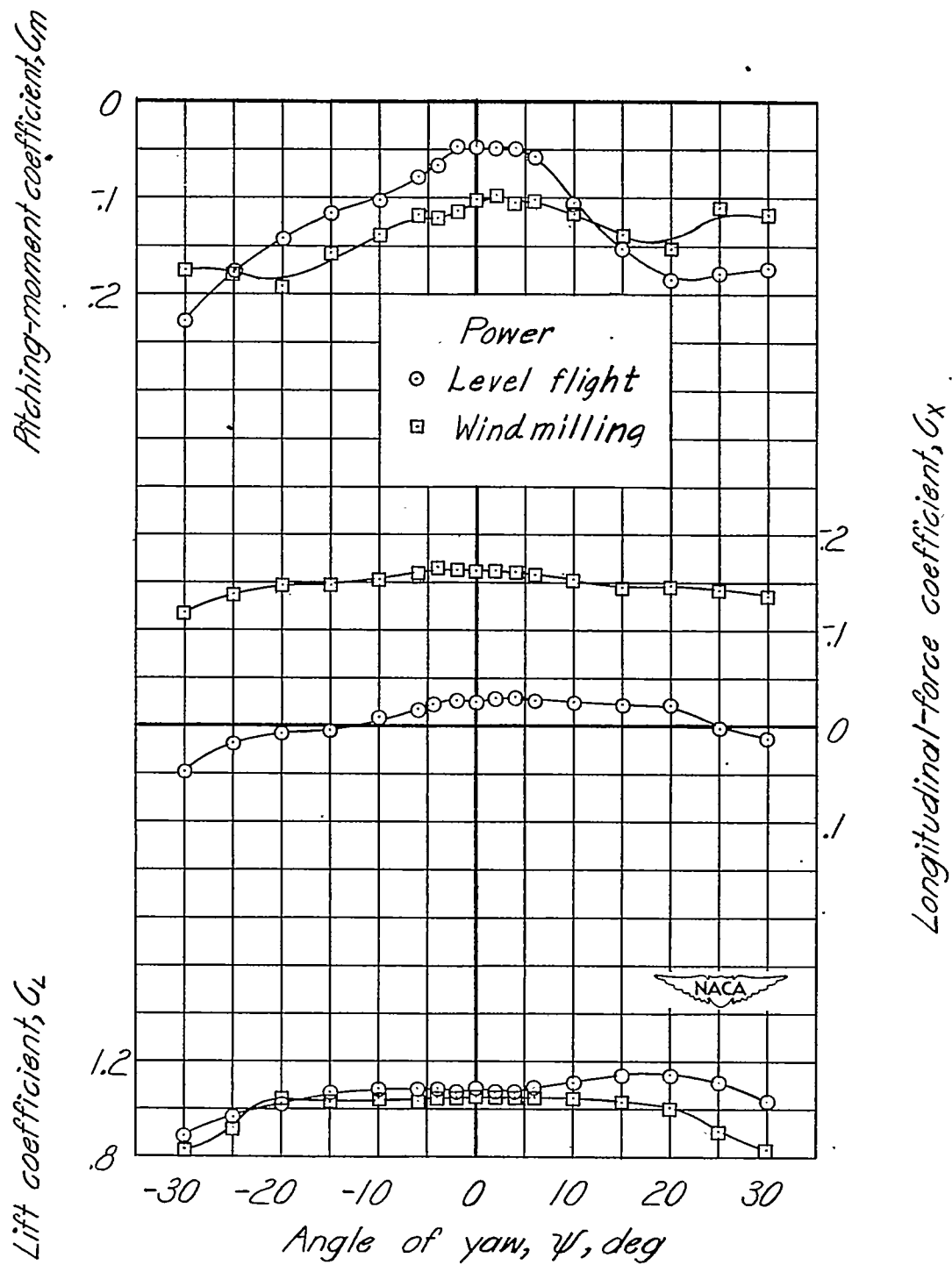
(b) Concluded.

Figure 55.- Concluded.
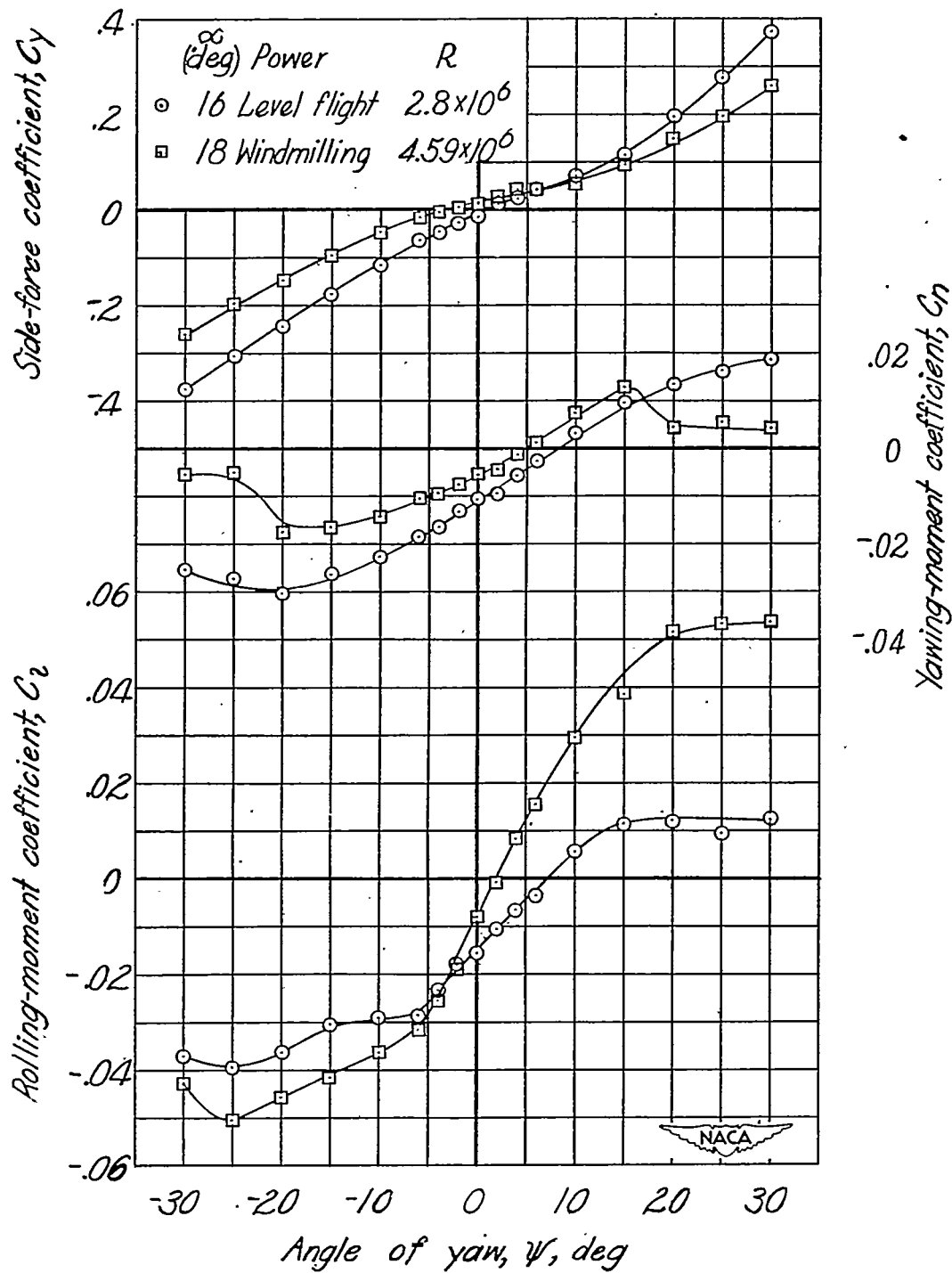
Figure 56.- Effect of power on aerodynamic characteristics in yaw. Tail off; 40-percent-span slots; $\delta_f = 0^\circ$.
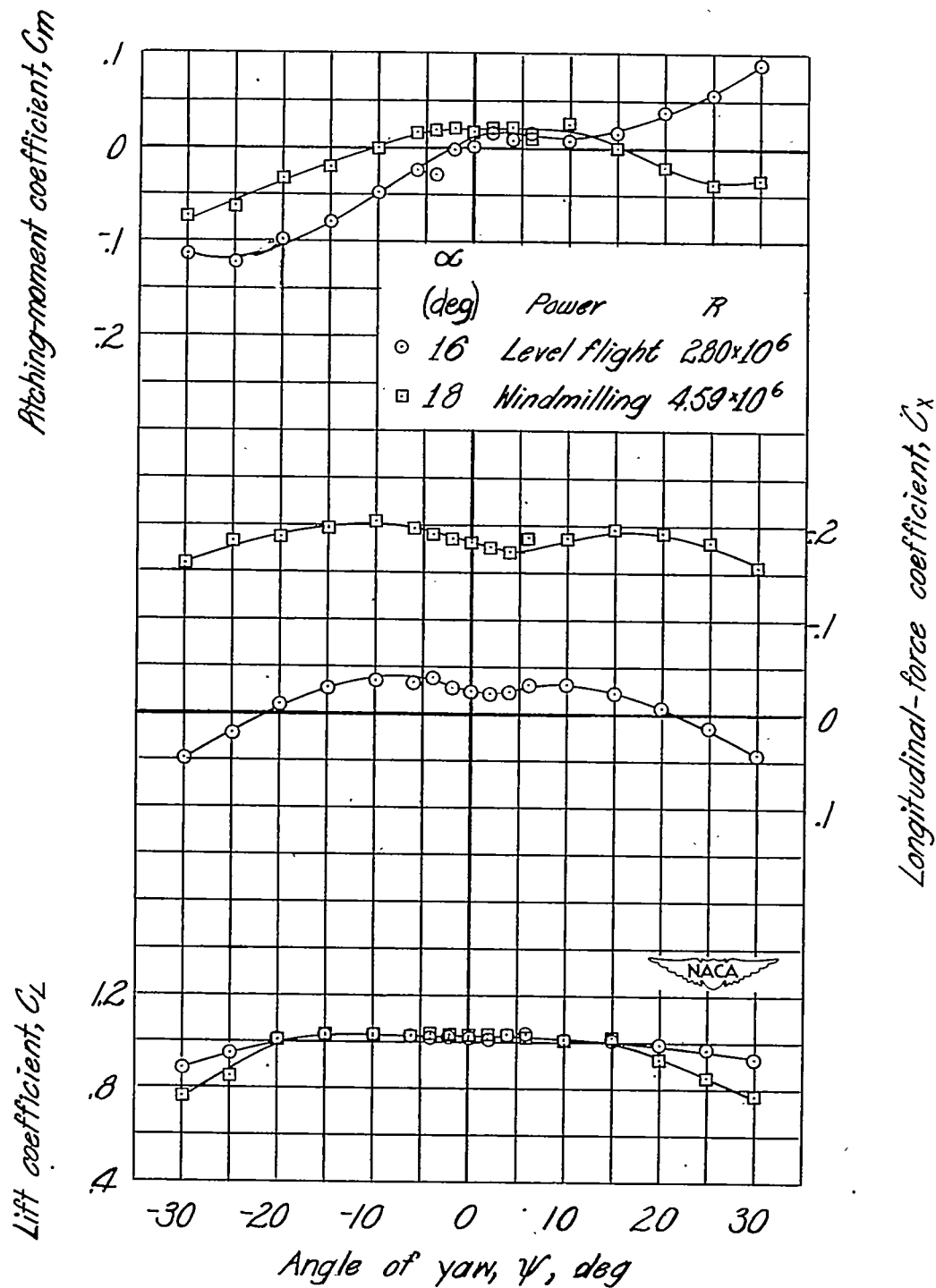
Figure 56.- Concluded.

Figure 57.- Effect of nose-flap deflection on aerodynamic characteristics in yaw.
Windmilling propeller; extended fuselage; ventral fin 3; 0-percent-span slots;
$\delta_f = 0°$; $\alpha = 15°$; $i_t = -3.7°$; $R = 4.59 \times 10^6$.
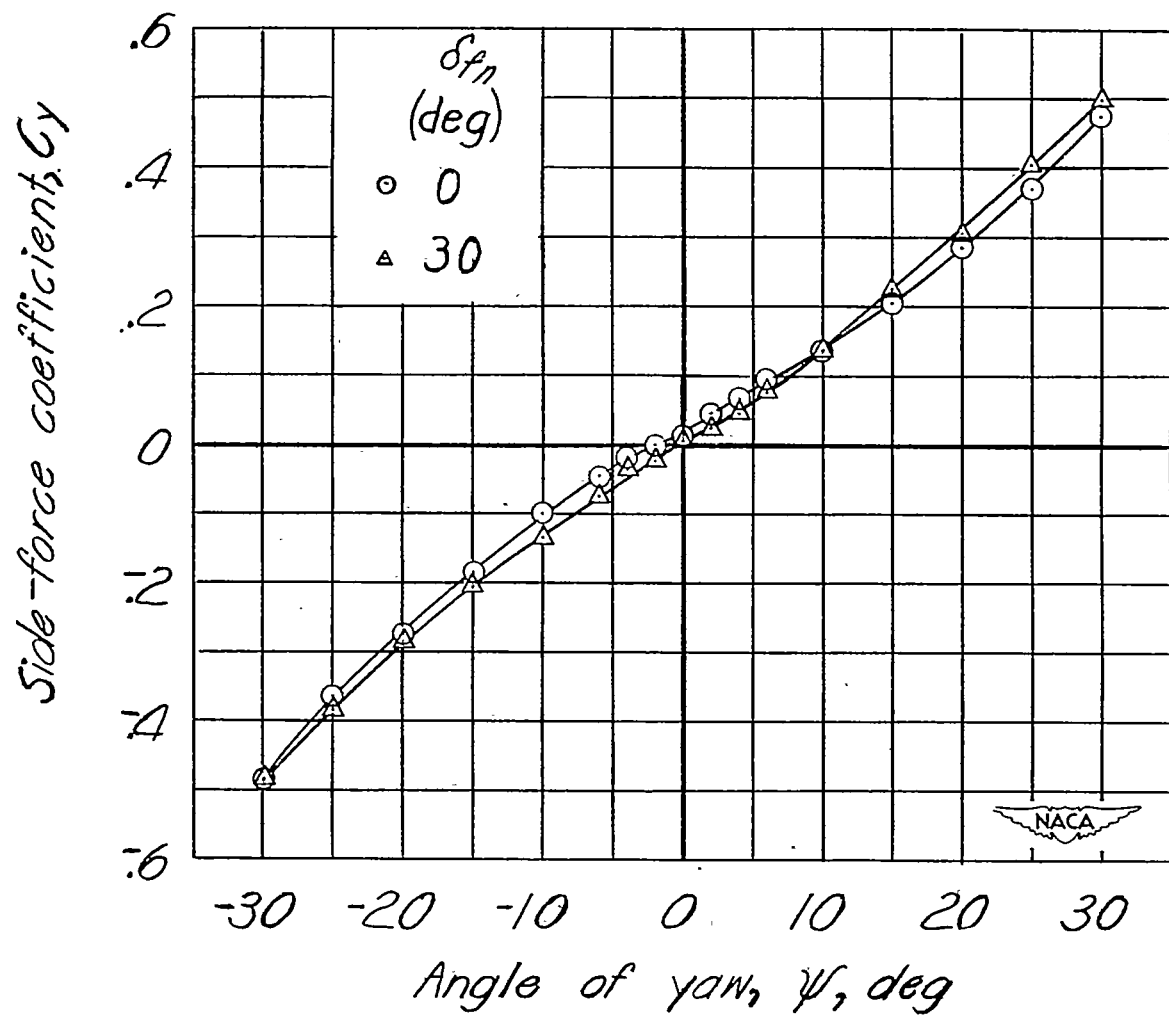
Figure 57.- Continued.
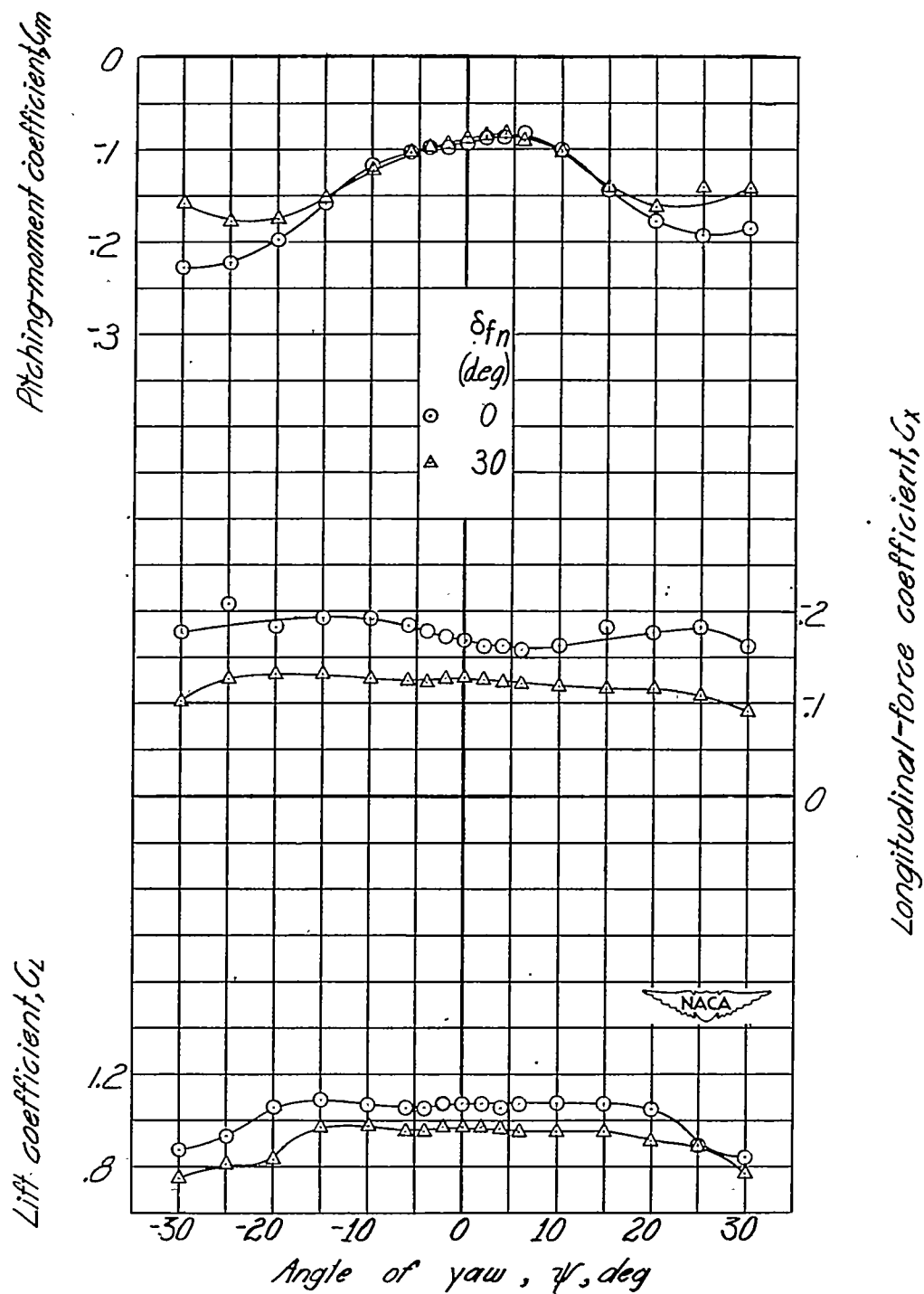
Figure 57.- Concluded.
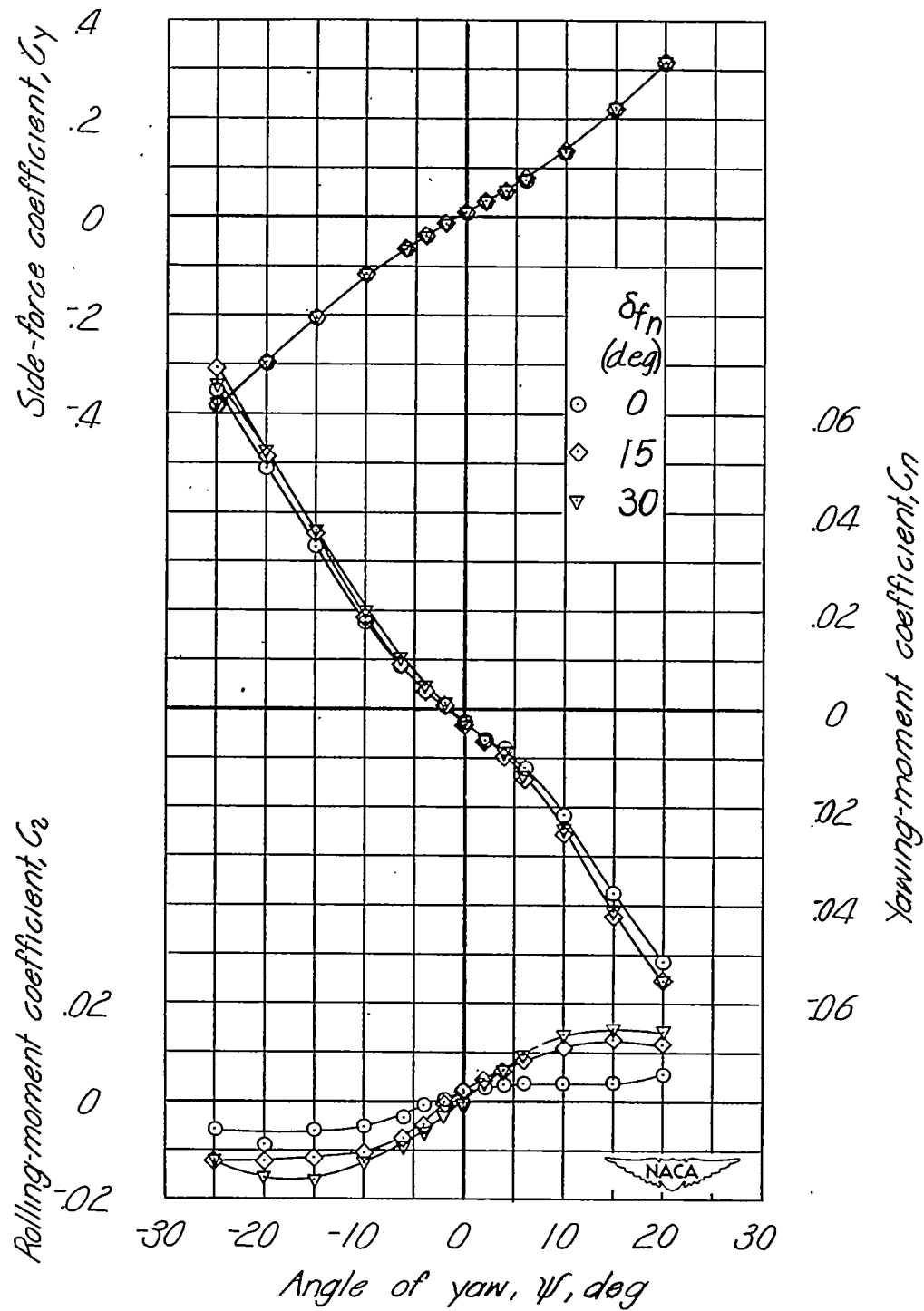
Figure 58.-   Effect of nose-flap deflection on aerodynamic characteristics in yaw of model with circular-arc wing.   Windmilling propeller; extended fuselage; ventral fin 3; δ_f = 0°; i_t = -3.07°; α_T = 9.0°;   R = 2.35 × 10^6.
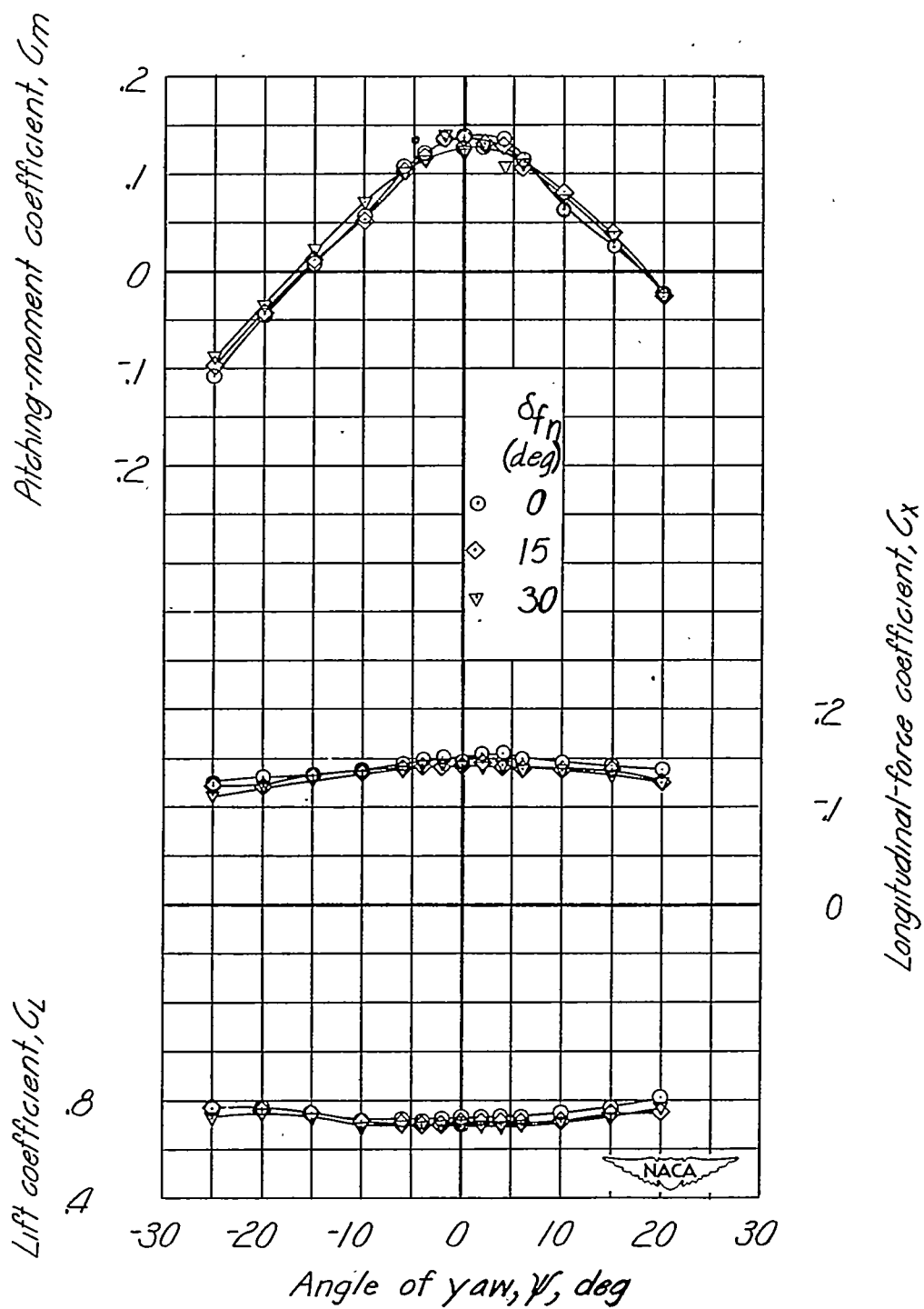
Figure 58.- Concluded.
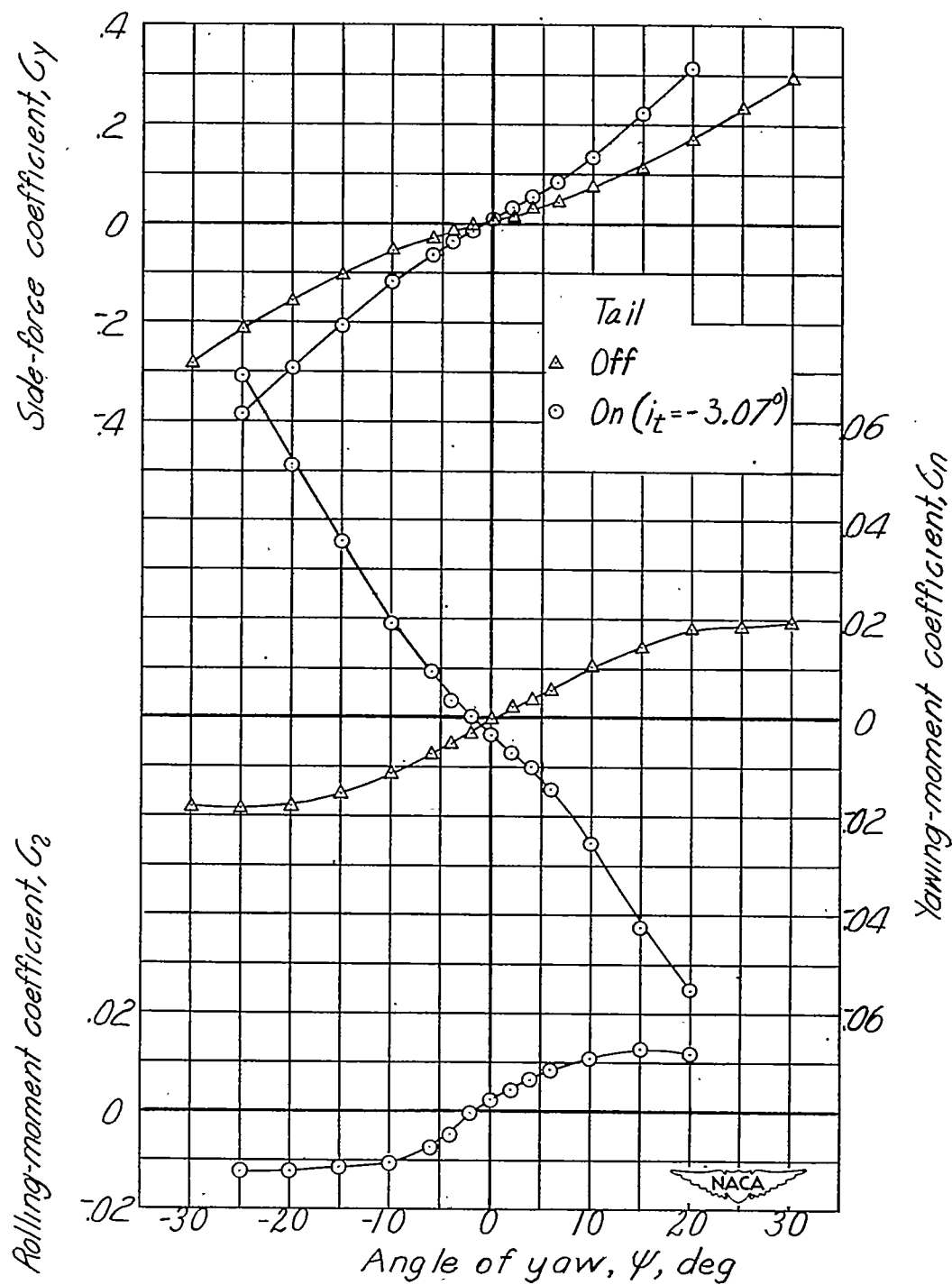
(a) $\delta_f = 0°$; $\alpha_T = 9.0°$.

Figure 59.- Effect of tail on aerodynamic characteristics in yaw of model with circular-arc wing. Windmilling propeller; extended fuselage; ventral fin 3; $\delta_{f_n} = 15°$; $R = 2.35 \times 10^6$.
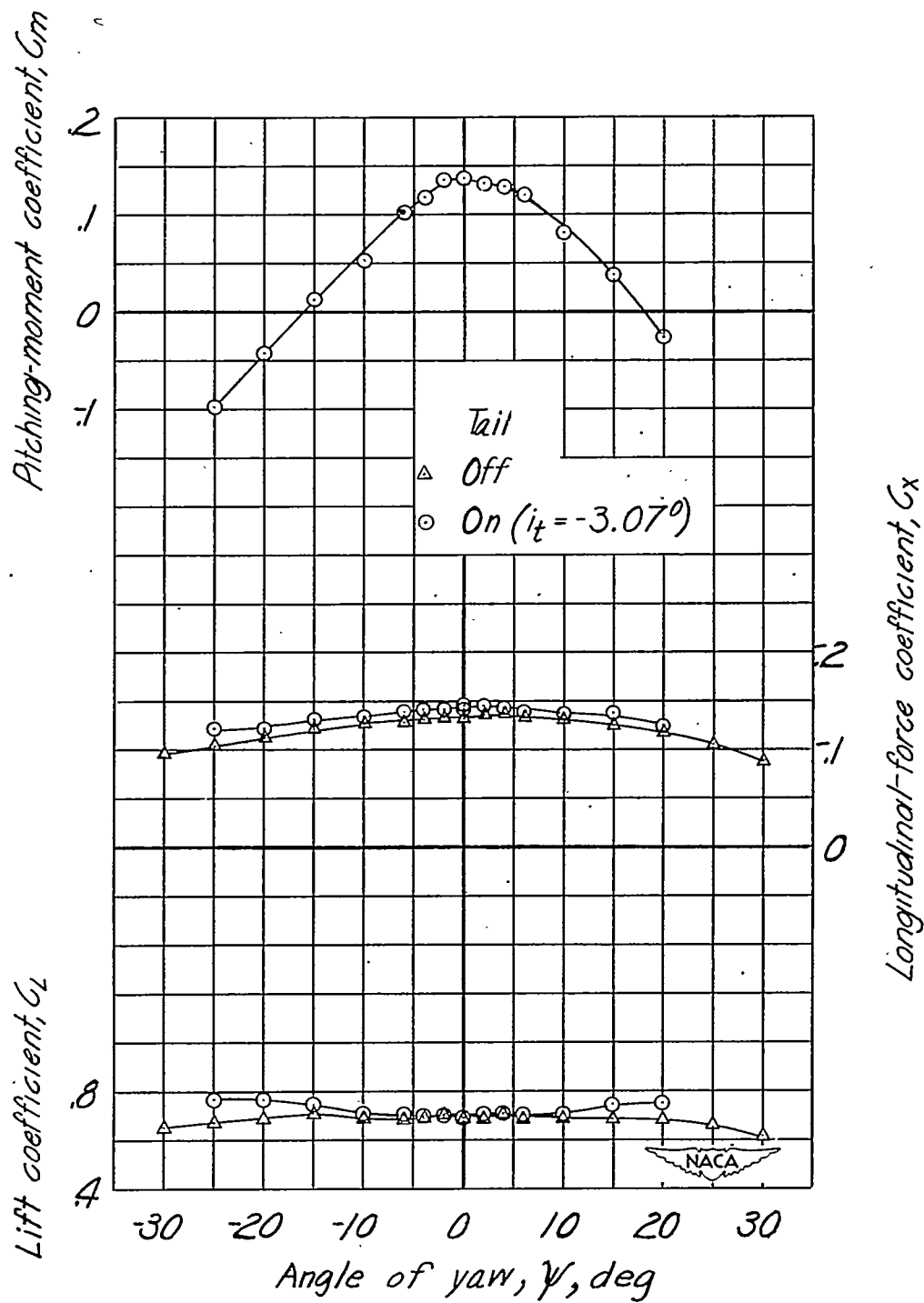
(a) Concluded.

Figure 59.- Continued.

(b) $\delta_f = 45^0$; $\alpha_T = 7.9^0$.
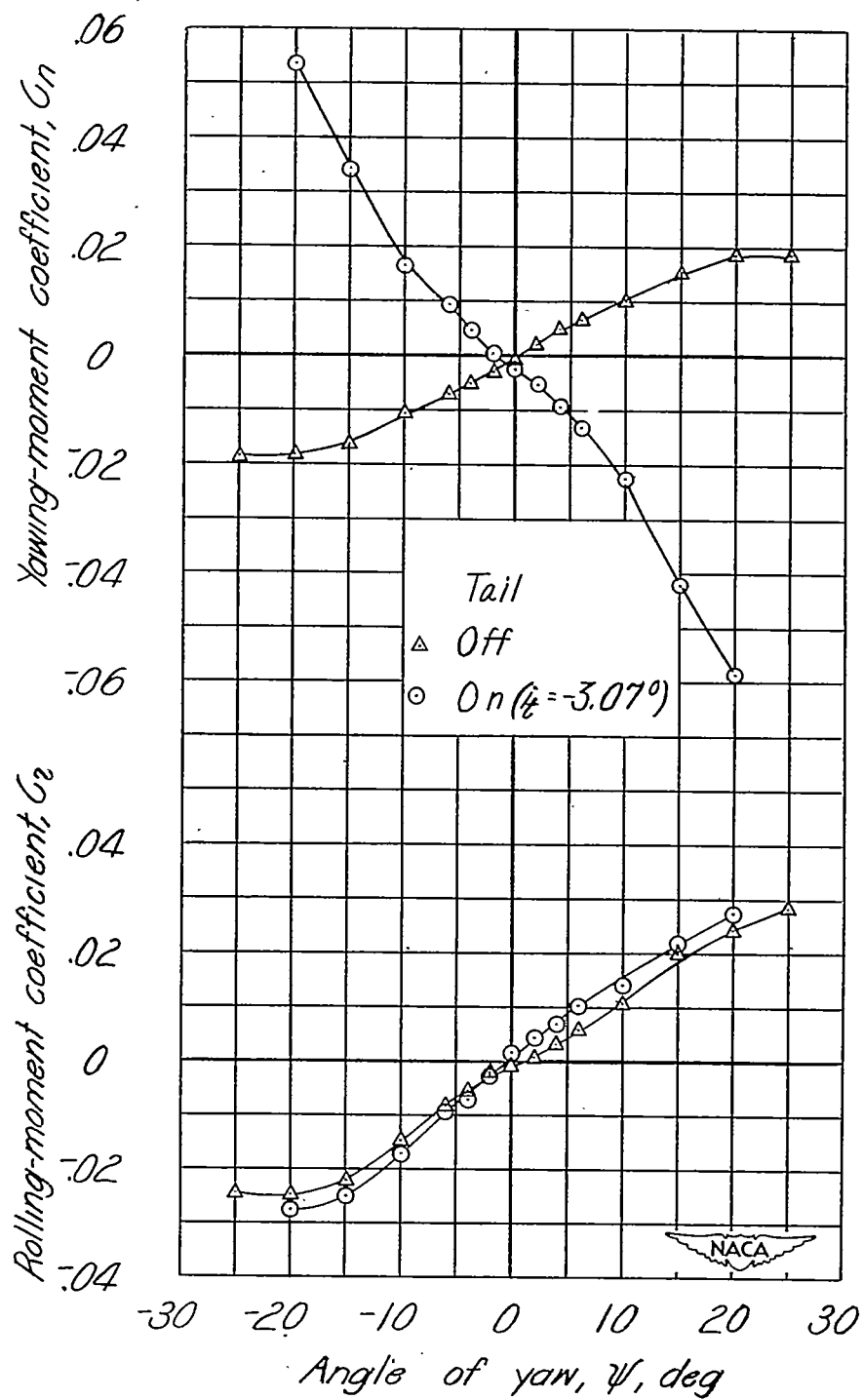
Figure 59.- Continued.

(b) Continued.

Figure 59.- Continued.

(b) Concluded.

Figure 59.- Concluded.

(a) $\delta_f = 0^o$.
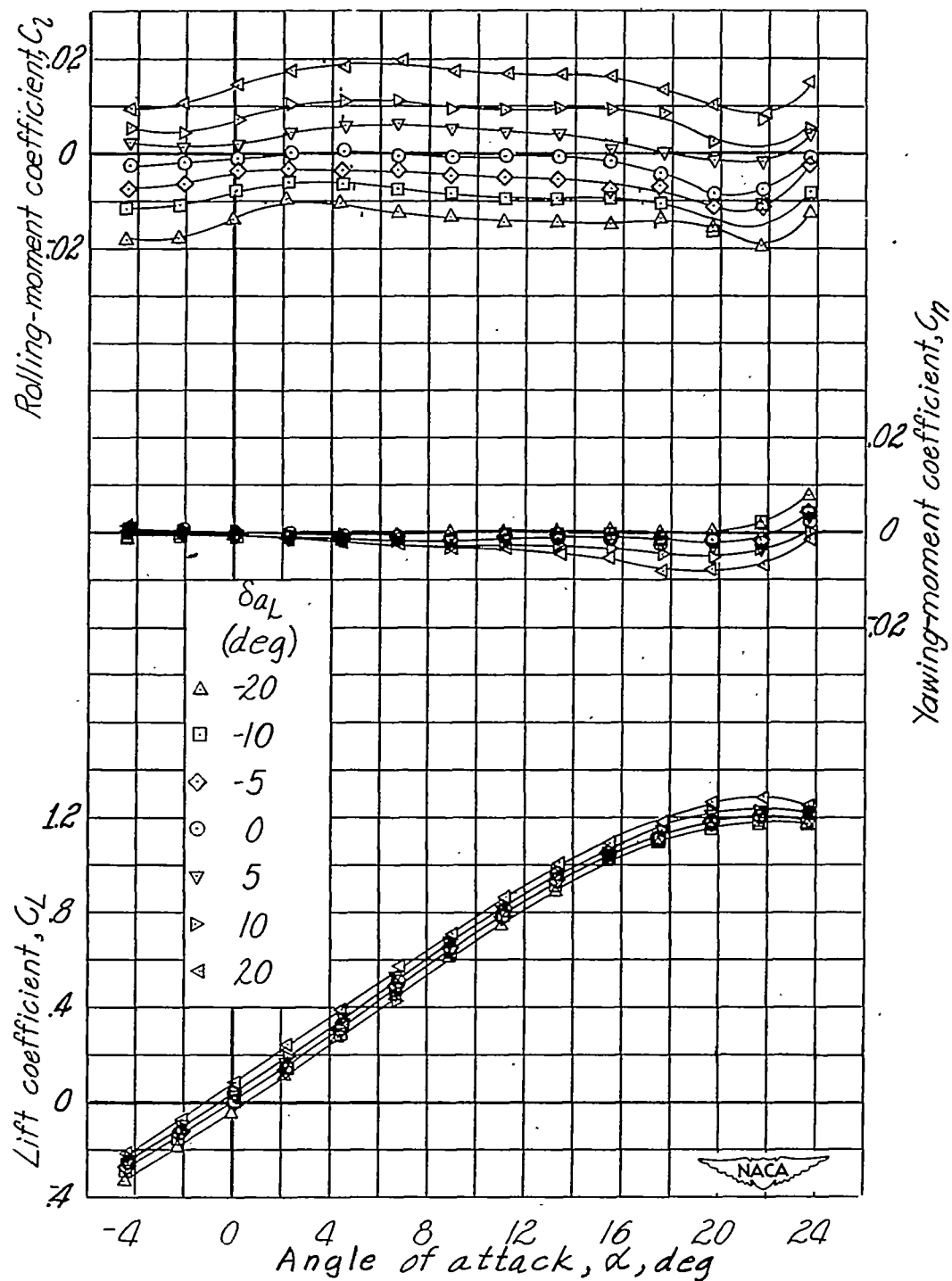
Figure 60.- Effect of aileron deflection on aerodynamic characteristics in pitch.
Windmilling propeller; ventral fin 1; 80-percent-span slots; $i_t = -0.8^o$;
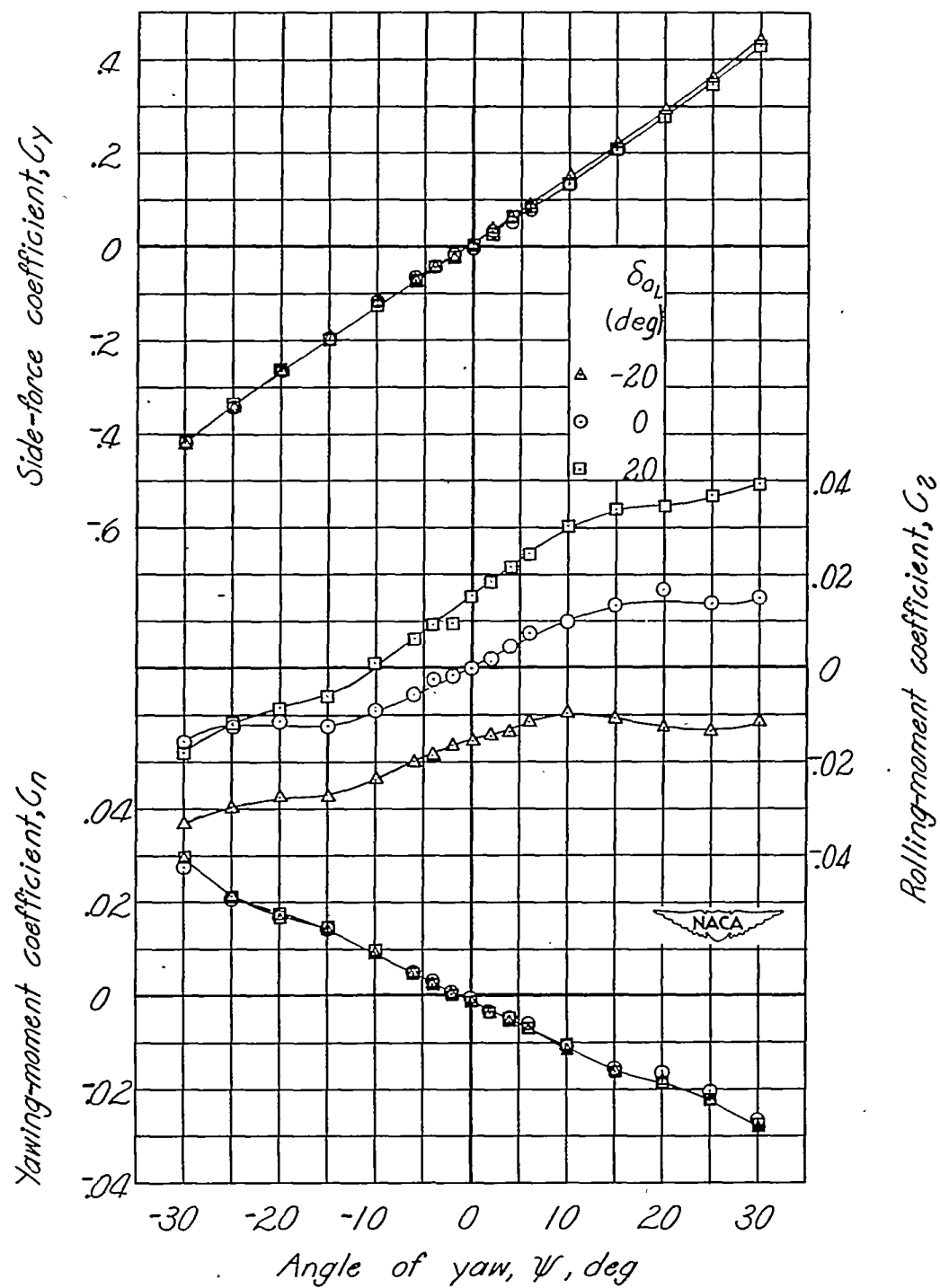R = 2.05 × 10^6.

(b) $\delta_f = 45°$.

Figure 60.- Concluded.

(a) $\delta_f = 0^o$; $\alpha = 9.0^o$.

Figure 61.- Effect of aileron deflection on aerodynamic characteristics in yaw.
Windmilling propeller; ventral fin 1; 80-percent-span slots; R = 2.05 × 10⁶.
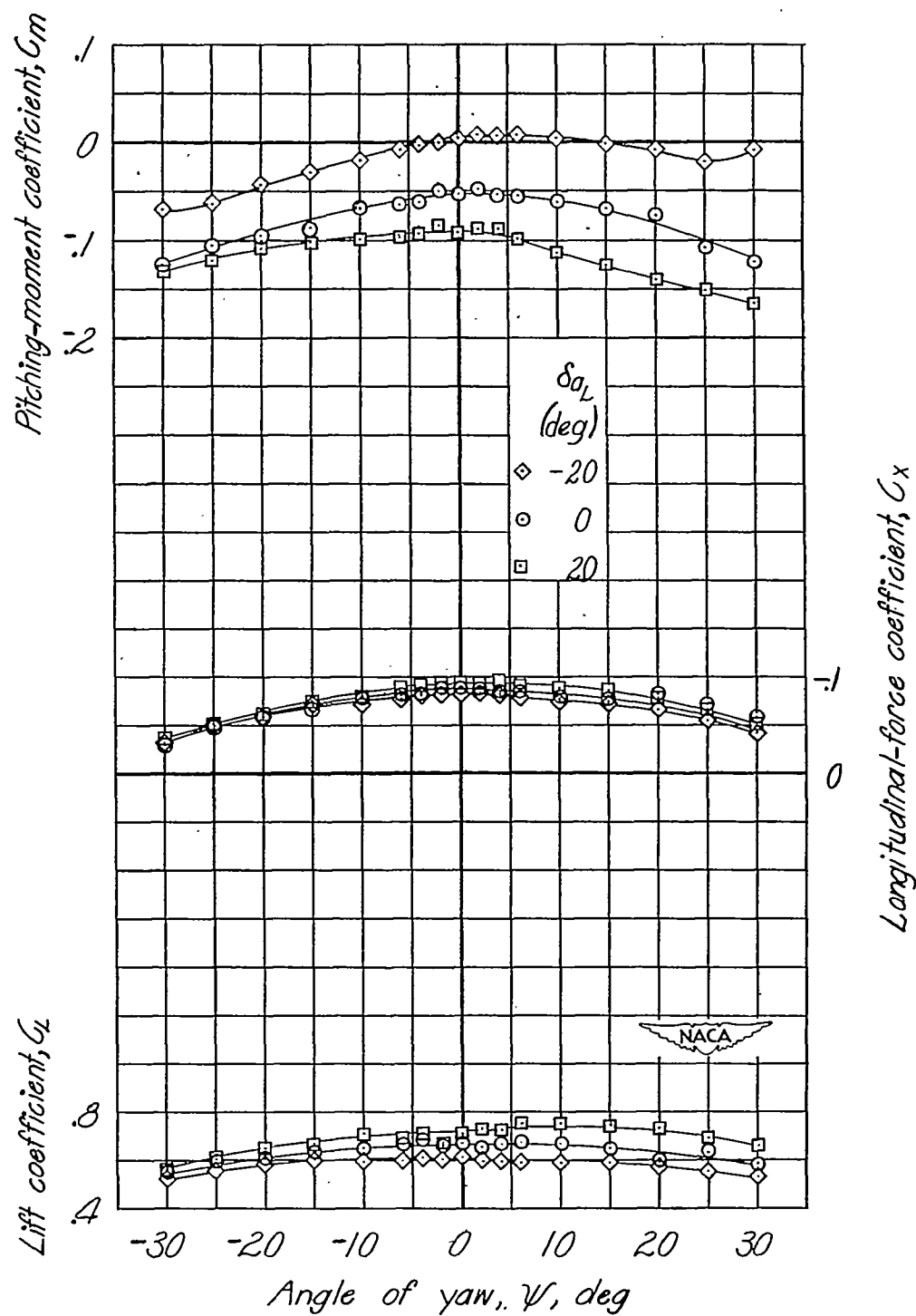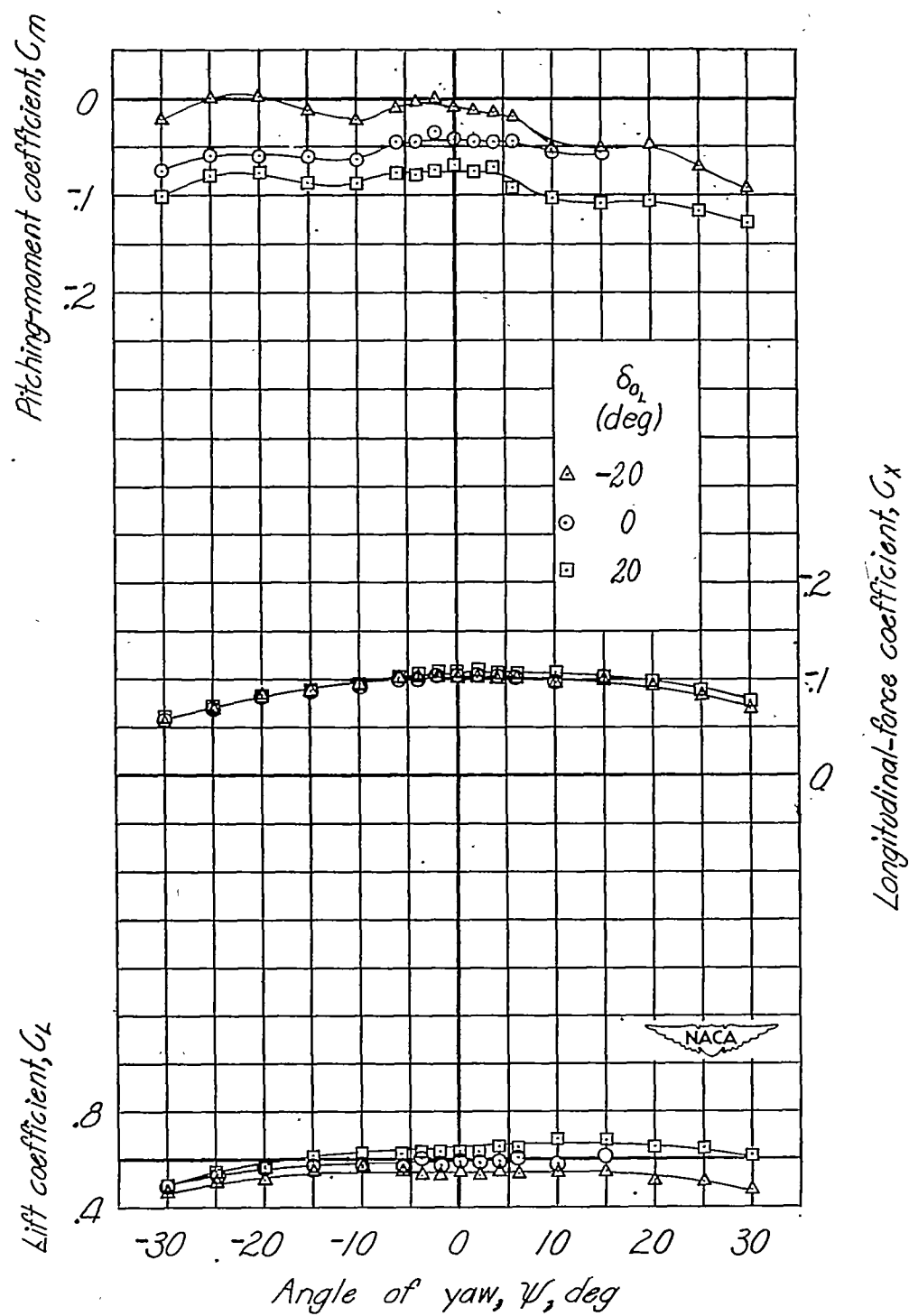
(a) Concluded.

Figure 61.- Continued.

(b) $\delta_f = 45^\circ$; $\alpha = 4.9^\circ$.

Figure 61.- Continued.

(b) Concluded.

Figure 61.- Concluded.
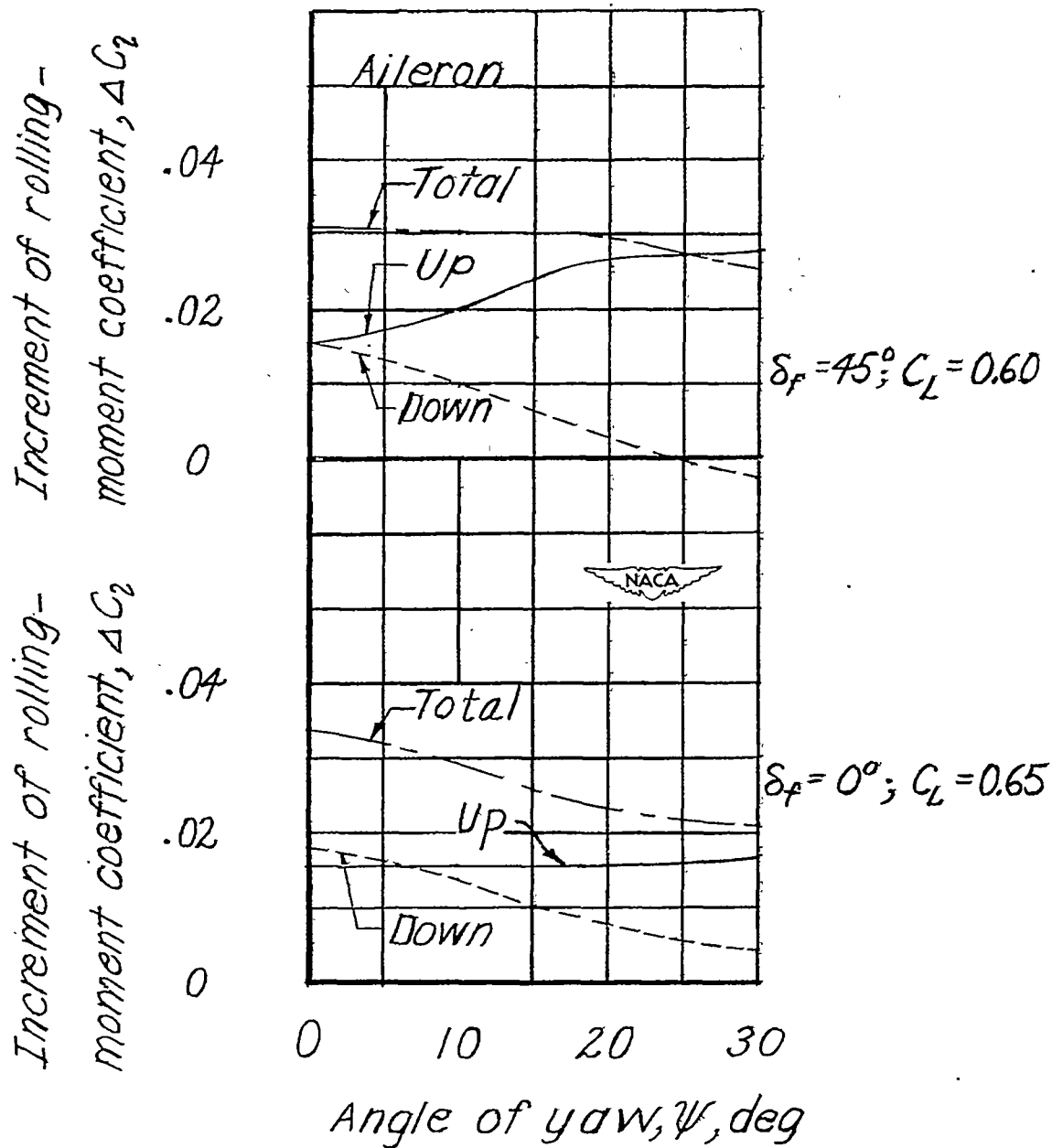
Figure 62.- Variation of aileron effectiveness with angle of yaw, as determined
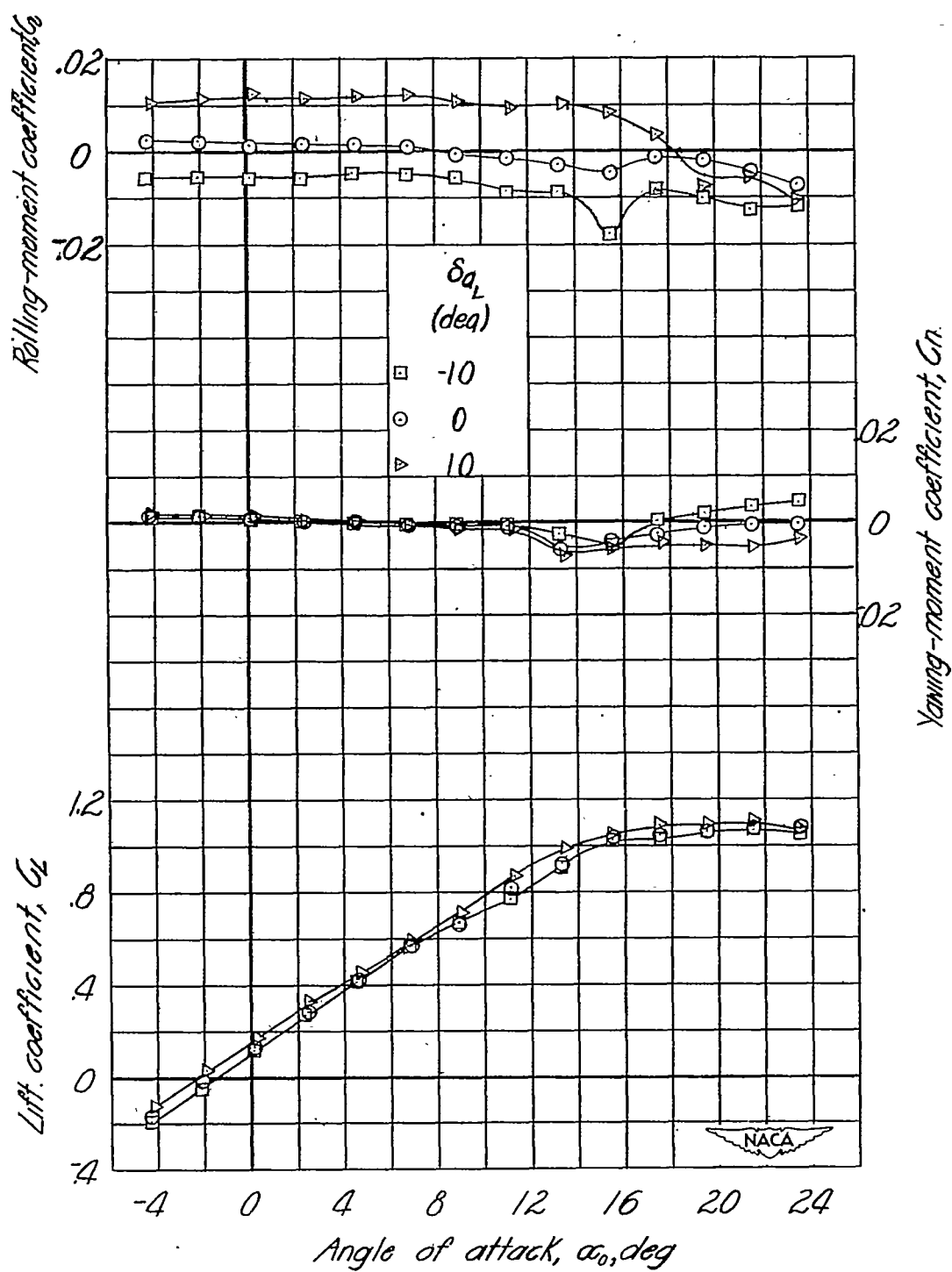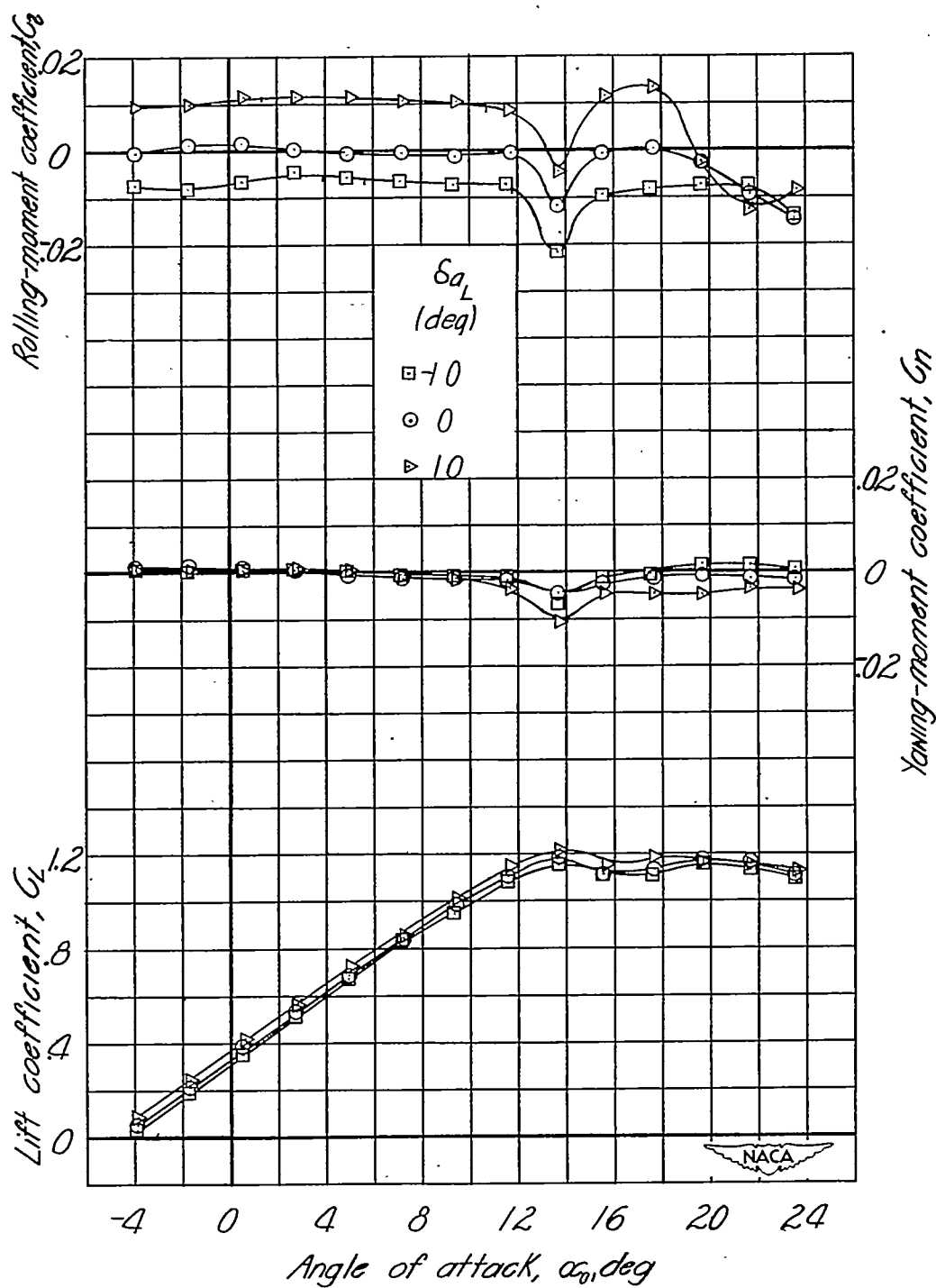from characteristics of the left aileron deflected ±20° (fig. 61).

(a) $\delta_f = 0^\circ$.

Figure 63.- Effect of aileron deflection on aerodynamic characteristics in pitch. Windmilling propeller; ventral fin 3; 0-percent-span slots; $i_t = -3.03^\circ$; $R = 2.05 \times 10^6$.
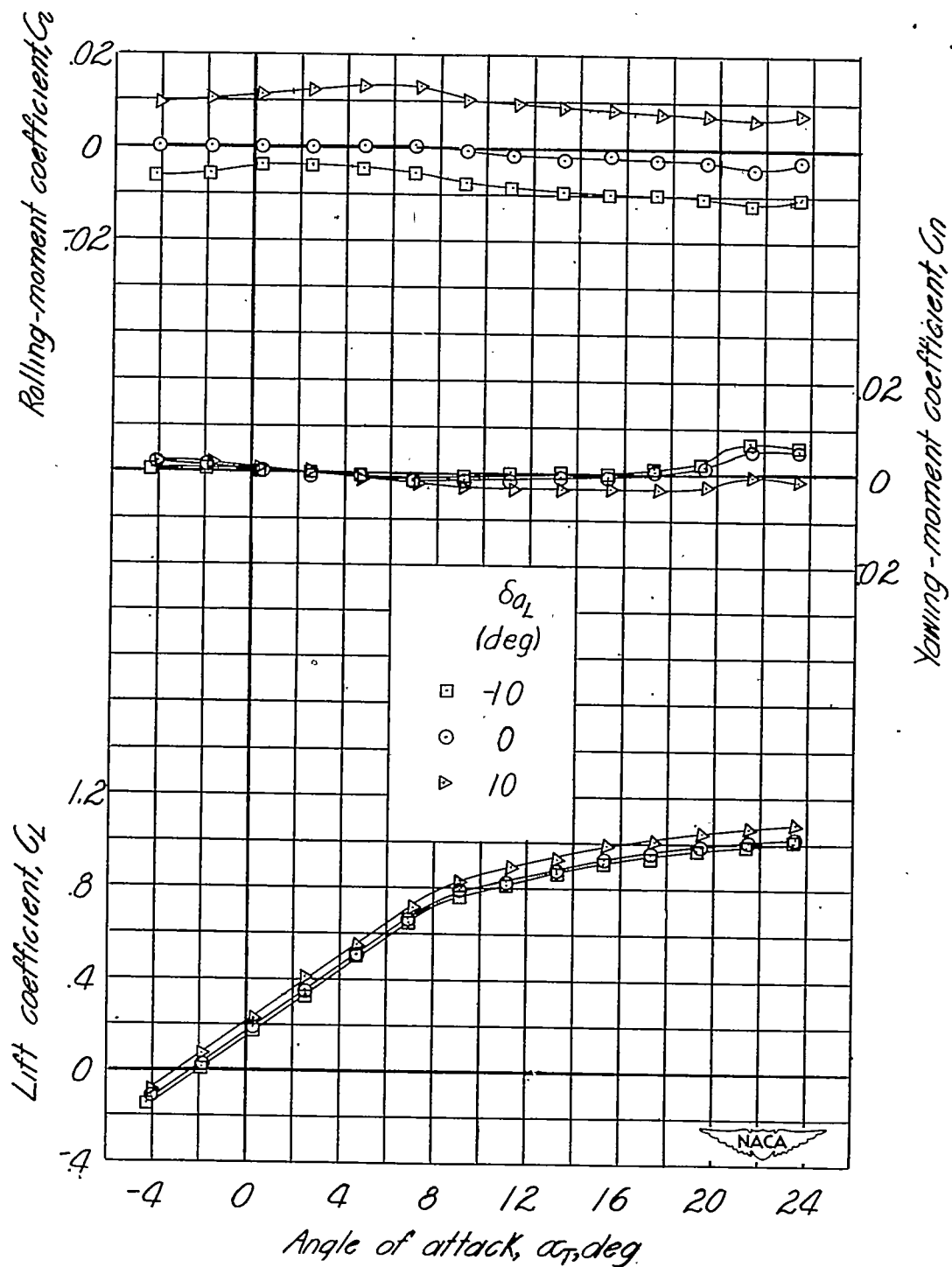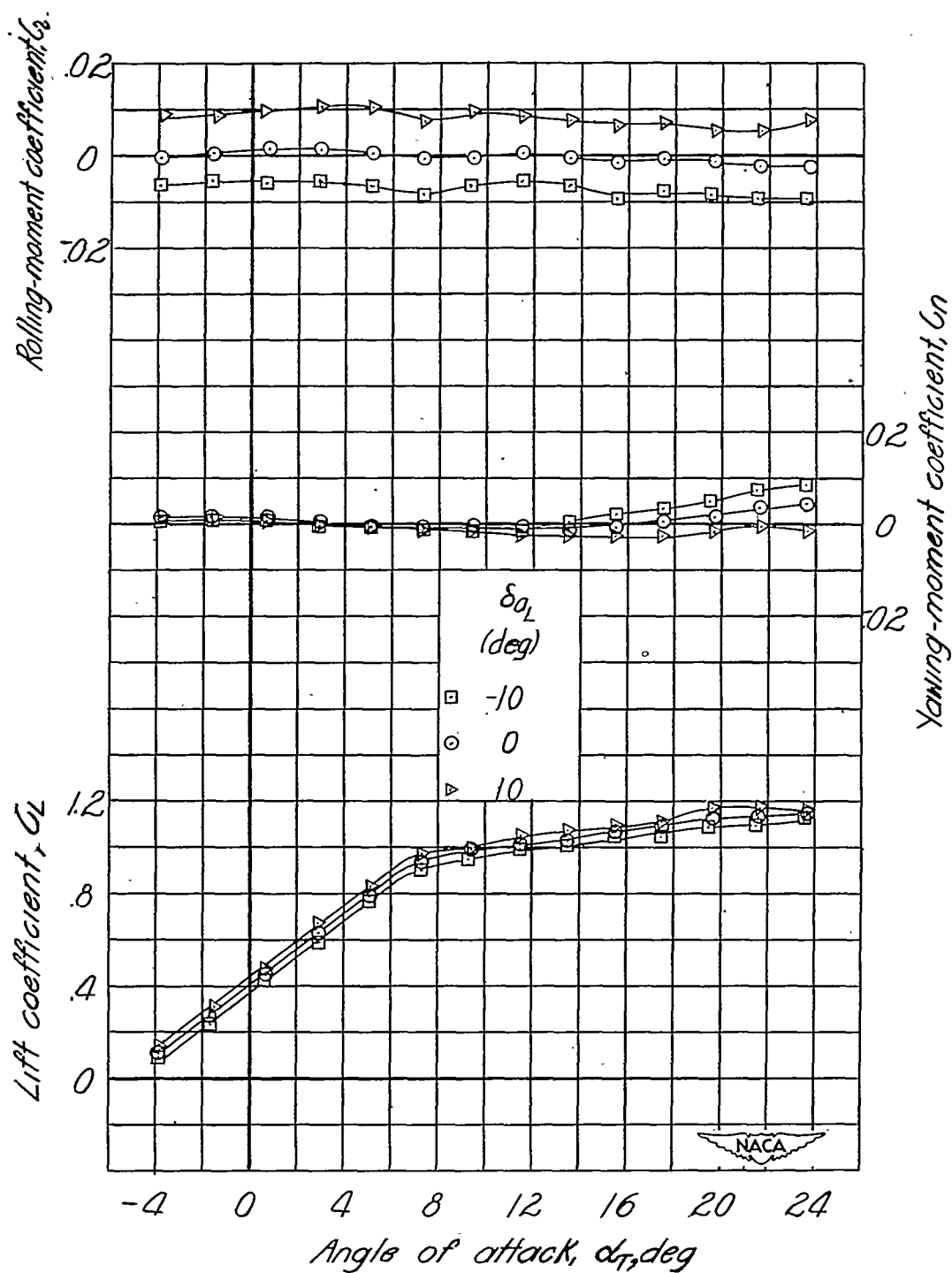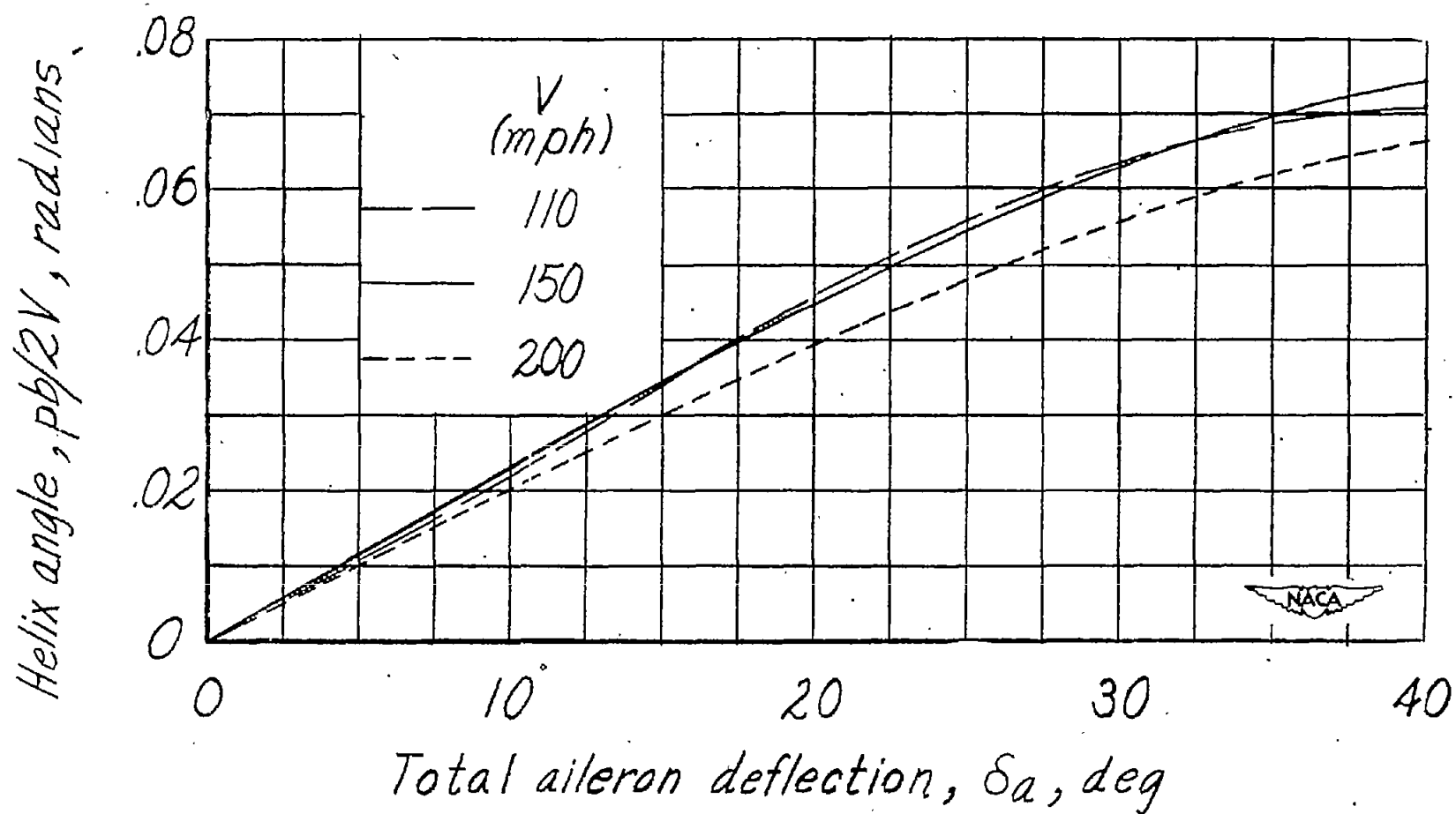
(b) $\delta_f = 45°$.

Figure 63.- Concluded.

(a) $\delta_f = 0^o$.

Figure 64.-   Effect of aileron deflection on aerodynamic characteristics in pitch
of model with circular-arc wing.   Windmilling propeller; extended fuselage;
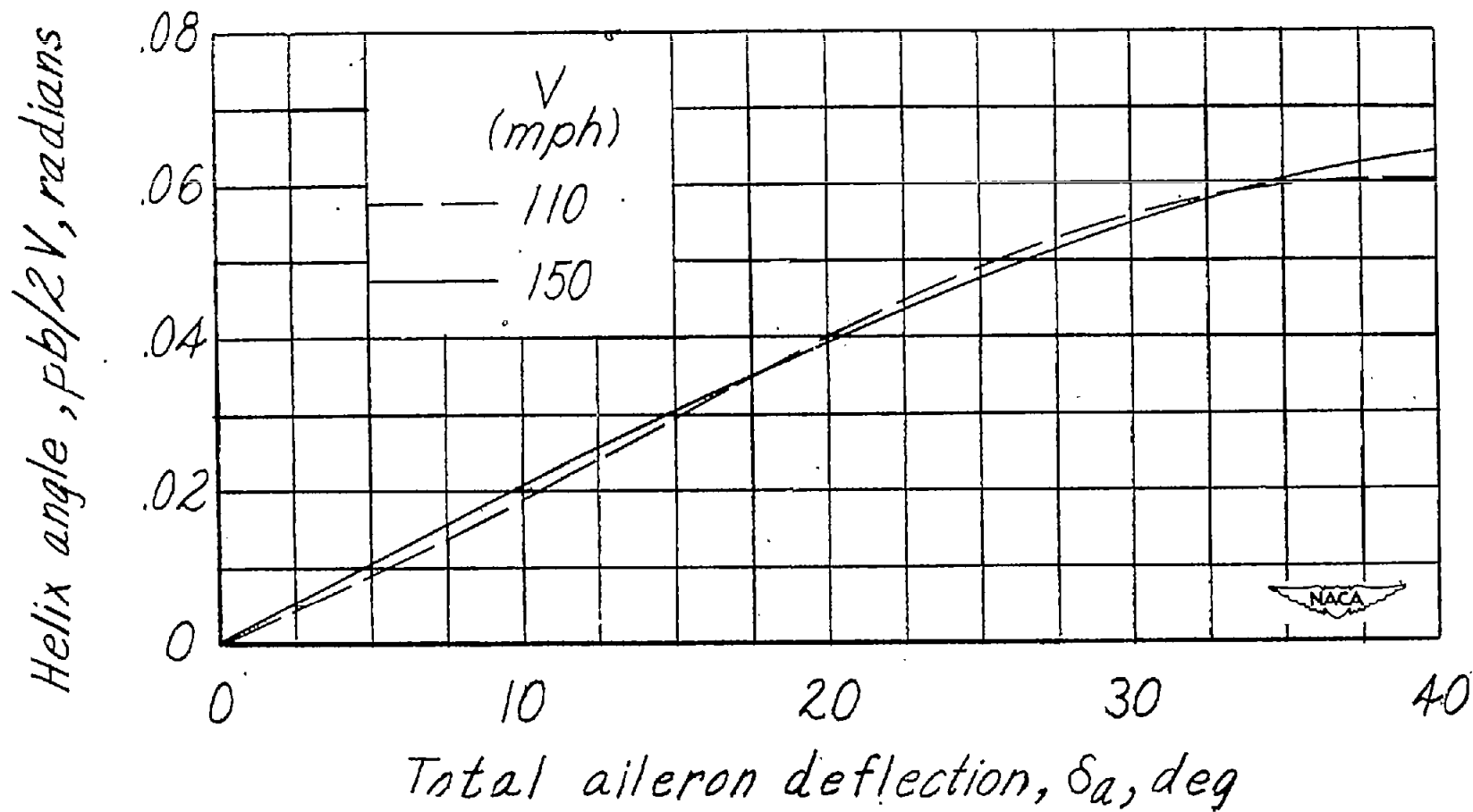ventral fin 3; $i_t = 2.8^o$; R = 2.35 $\times 10^6$.

(b) $\delta_f = 45°$.

Figure 64.- Concluded.

(a) $\delta_f = 0^\circ$.

Figure 65.- Variation of wing-tip helix angle pb/2V with aileron deflection. Windmilling propeller; ventral fin 1; 80-percent-span slots.

(b) $\delta_f = 45°$.
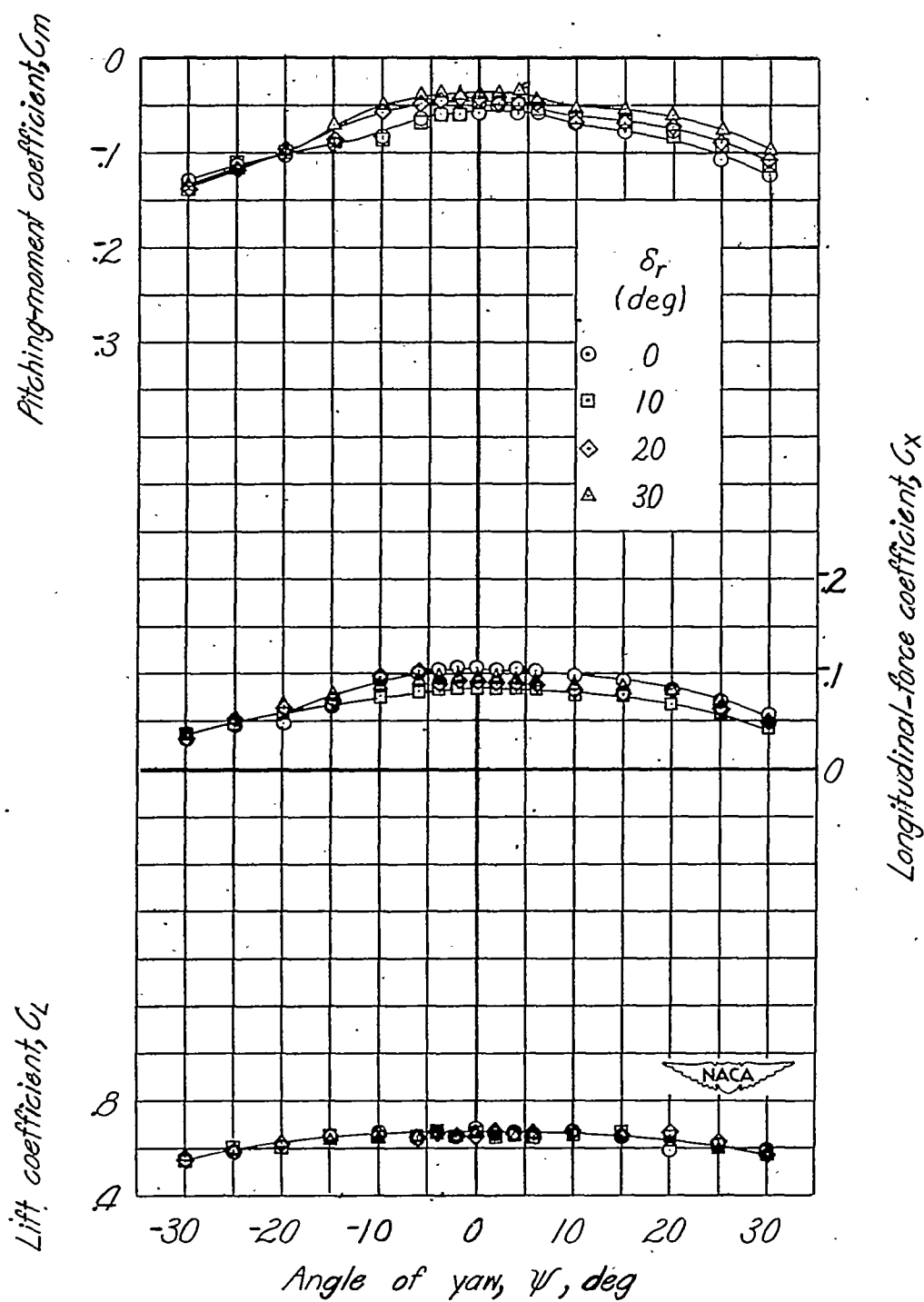
Figure 65.- Concluded.
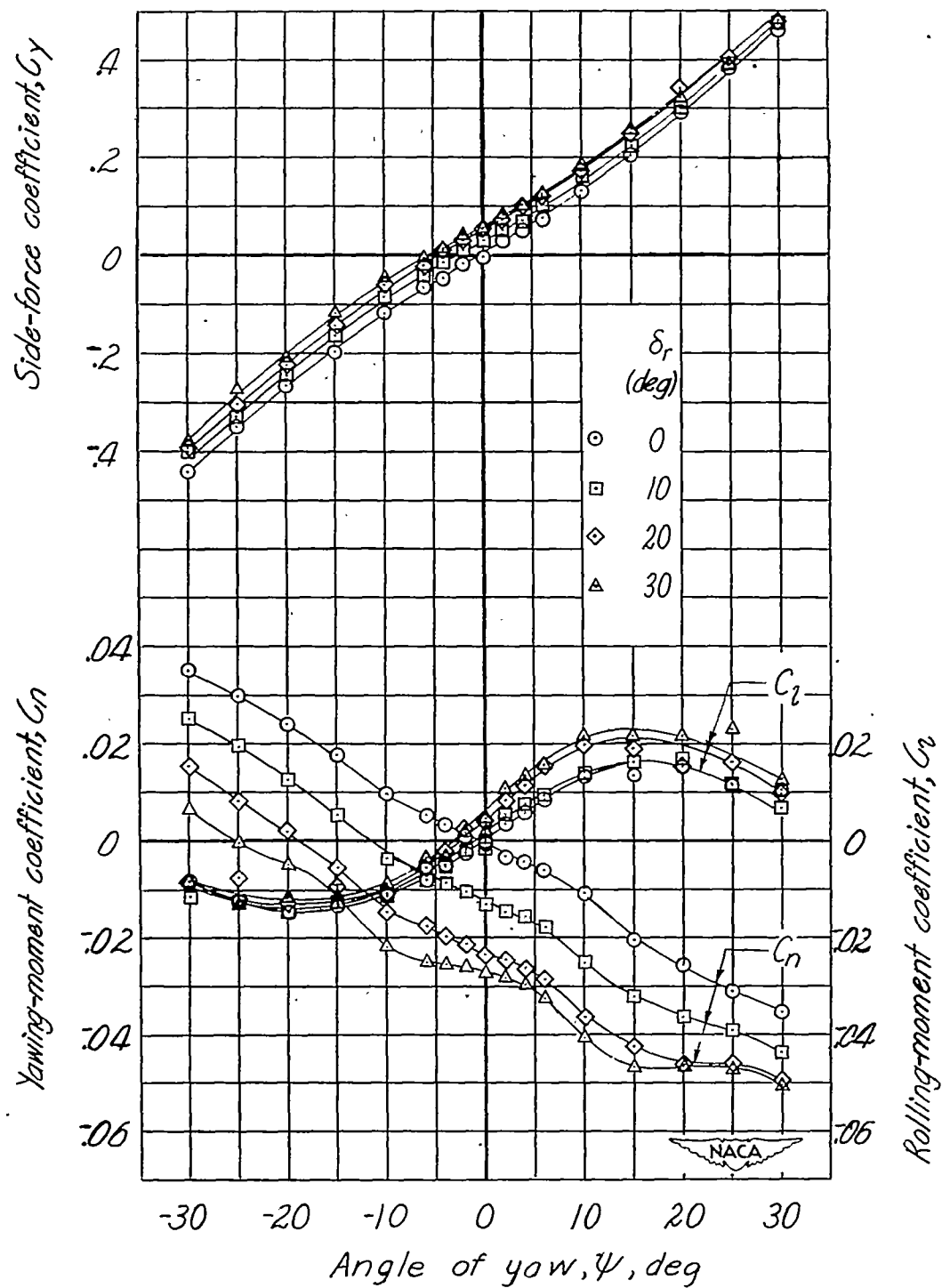
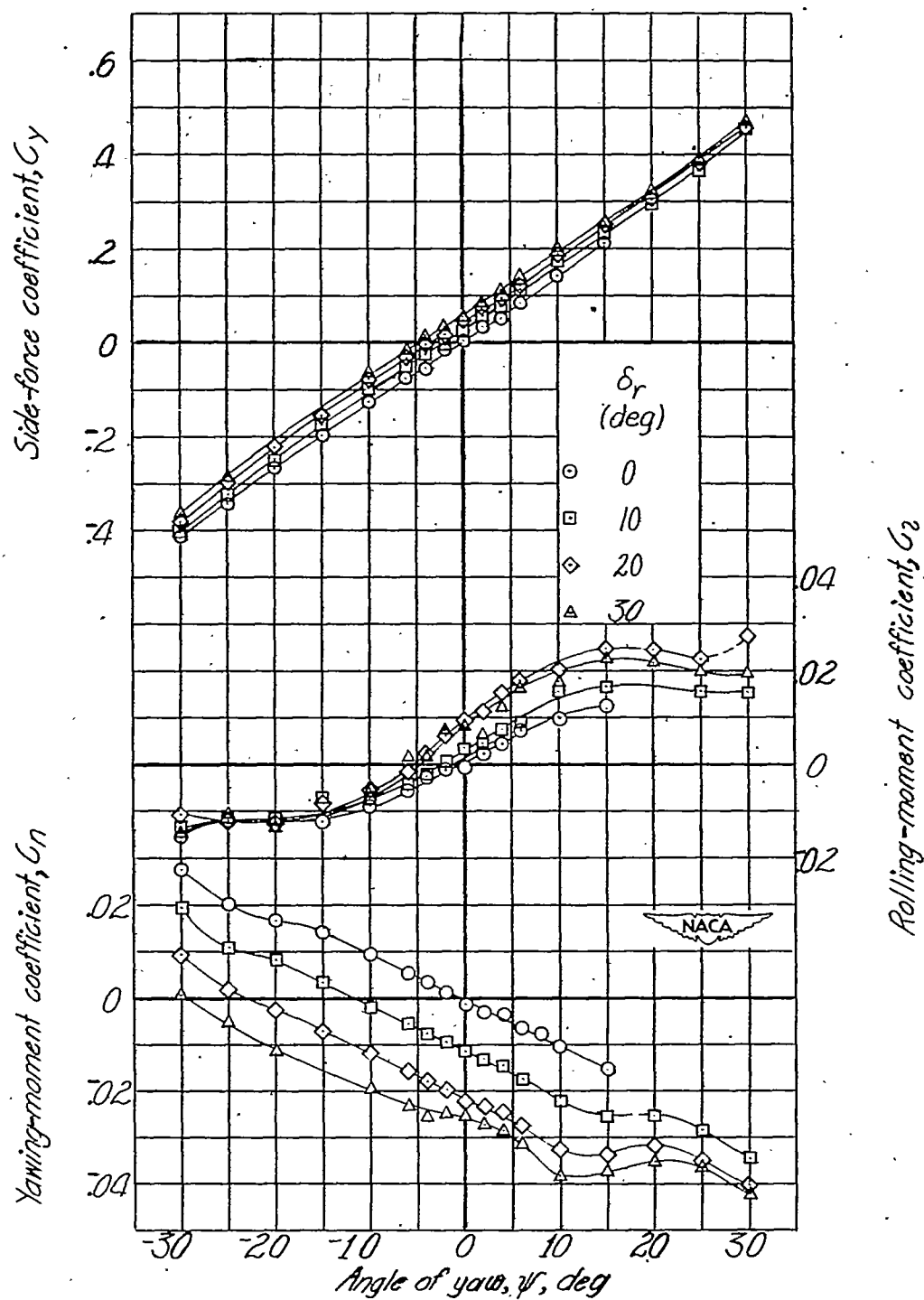(a) $\delta_f = 0°$: $\alpha = 8.9°$.

Figure 66.- Effect of rudder deflection on aerodynamic characteristics in yaw. Windmilling propeller; ventral fin 1; 80-percent-span slots; $i_t = -0.8°$; R = 2.05 × 10⁶.
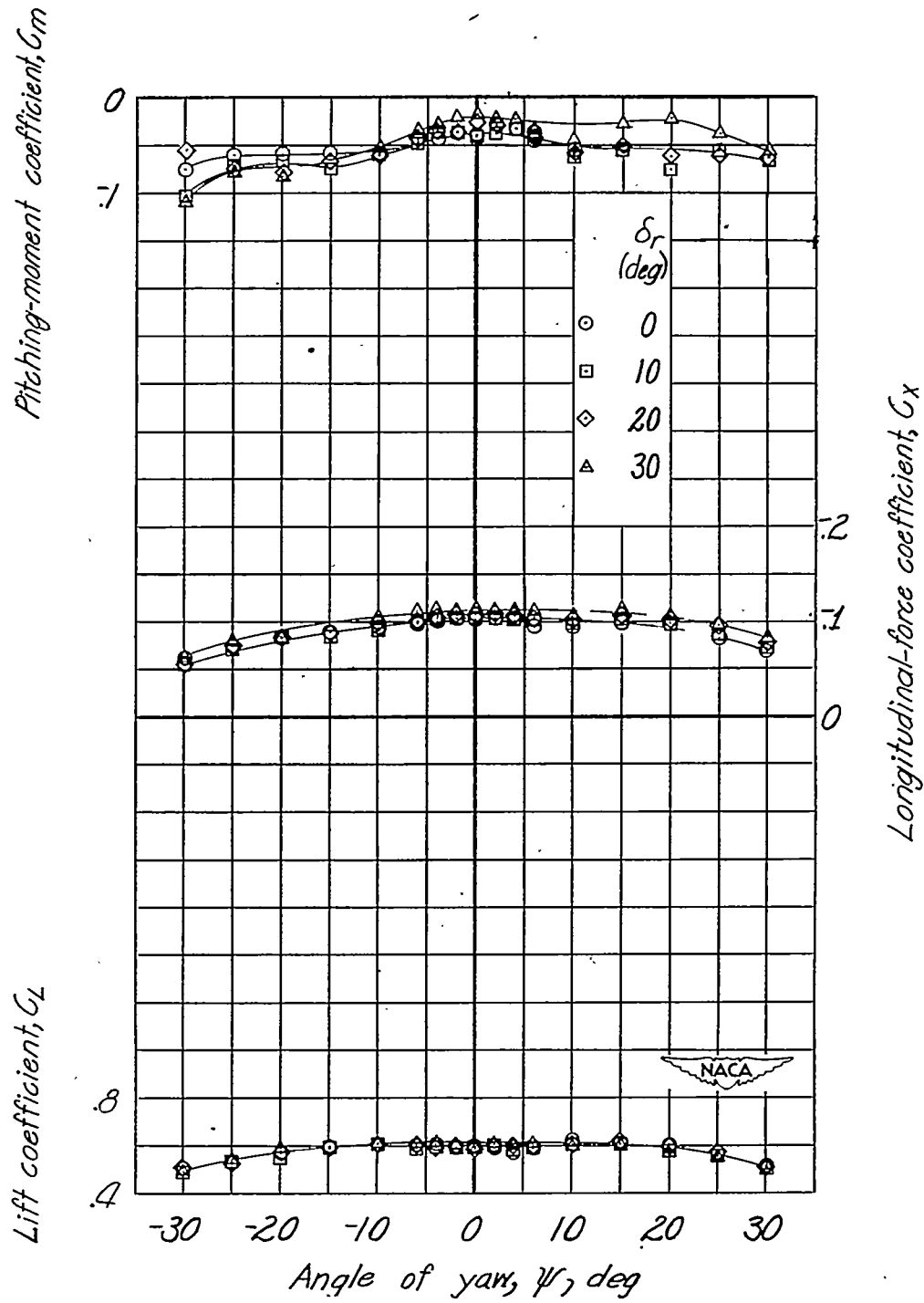
(a) Concluded.

Figure 66.- Continued.

(b) $\delta_f = 45^\circ$; $\alpha = 4.9^\circ$.

Figure 66.- Continued.

(b) Concluded.

Figure 66.- Concluded.

Figure 34 indicates that the elevator is capable of trimming the airplane at either the design center of gravity (18-percent M.A.C.) or the center of gravity at which the airplane was flown (22.5-percent M.A.C.). Near stalling speed, a large upward movement of the elevator is indicated with no change in speed, as a result of the very large increase in stability or loss in elevator effectiveness.

The difference in elevator required for trim between the original model and the extended-fuselage model is small. The data indicate that the original model will require about 3° less up elevator near maximum lift coefficient and slightly less down elevator at high speed than the extended-fuselage model.

Lateral Stability

The $\frac{1}{4.5}$-scale model of the test airplane shows the same general variation of effective dihedral parameter with lift coefficient as do other sweptback-wing models, that is, increased values of C_{l_ψ} with C_L.

The amount of effective dihedral obtained with this model and the exact variation with lift coefficient depend upon the leading-edge and tail configurations (figs. 35 to 59).

Scale effect.— Before the effect of any model changes on the lateral stability is analyzed, the variation of Reynolds number during the test program should be considered. The data of figures 35, 36, and 49 indicate that the slots were an effective means of delaying tip stall as indicated by the large values of C_{l_ψ} near maximum lift. Without slots the values of C_{l_ψ} decreased sharply at the relatively low Reynolds number of 2.05×10^6. When the effective Reynolds number was increased to 4.59×10^6 with the aid of a turbulence net, (figs. 40 and 52) the unslotted wing showed no significant loss in effective dihedral other than that directly associated with stall. Figures 40 and 52 also serve to illustrate the Reynolds number effect at high angles of attack. (Although the tail configuration is different for the two Reynolds numbers, figures 38, and 40(b), and 41 show that the tail has little effect on effective dihedral at $C_L \approx 1.0$.) Data obtained in the Langley 19-foot pressure tunnel on a wing of similar airfoil section showed a corresponding effect of Reynolds number on the effective dihedral of a swept wing.

Wing-fuselage interference.— The term "wing-fuselage interference" as used herein is defined as the difference in the effective dihedral of the wing alone and the effective dihedral of the wing-fuselage combination.

The effect of the various airplane components on the effective dihedral parameter is shown for the original model with 80–percent–span slots (fig. 38). The increase in C_{l_ψ} at large values of C_L for the complete model and the model with the tail off is associated with flow breakdown at the root of the trailing wing which nullifies the primary negative dihedral effect due to wing–fuselage interference. Note that the primary interference effect is a ΔC_{l_ψ} which varies from −0.0010 at $C_L = 0$ to −0.0013 at $C_L = 0.9$ for the flap–neutral condition and a somewhat smaller contribution which varies with C_L with the flaps down (fig. 38(a)). The effect of the windmilling propeller is included in these increments but is small, about 0.0002 at a lift coefficient of 0.68, as is indicated by figure 54.

The effect of the wing–fuselage interference on effective dihedral has been noted before for unswept wings (reference 7) and has been investigated in Germany for sweptback wings (reference 8). Some of the data from these sources are replotted in figures 47 and 48. Shown in figure 47 are sample incremental values ΔC_{l_ψ} of effective dihedral caused by wing–fuselage interference for an unswept wing in various positions $\frac{z}{c}$ on a circular fuselage. The discrepancy between the data of references 7 and 8 for the low wing position points to the importance of the wing–fuselage juncture filleting in influencing the effective dihedral. The tests of reference 7 were made without fillets. The effect of filleting is to reduce the variation of ΔC_{l_ψ} with C_L. For the well–filleted model of reference 8, there is little variation of ΔC_{l_ψ} with C_L up to $C_L = 0.9$, at which point the previously mentioned flow breakdown occurs, and the action is somewhat similar to the action of the unfilleted wing of figure 47.

Figure 48 indicates that variation of fuselage shape or sweepback angle has only a secondary effect on the variation of ΔC_{l_ψ} with vertical position $\frac{z}{d}$ of the wing on the fuselage. The value $\Delta C_{l_\psi} = -0.0010$ mentioned previously for the airplane model is spotted on the graph, and the correlation is good.

For the complete model, an effective dihedral of about 10° $\left(C_{l_\psi} = 0.0020 \right)$ was obtained at $C_L = 1.0$ for most of the conditions investigated. The dihedral effect obtained with the wing alone was appreciably increased, inasmuch as the negative dihedral effect of the wing–fuselage interference is absent (figs. 38 and 50). The rate of
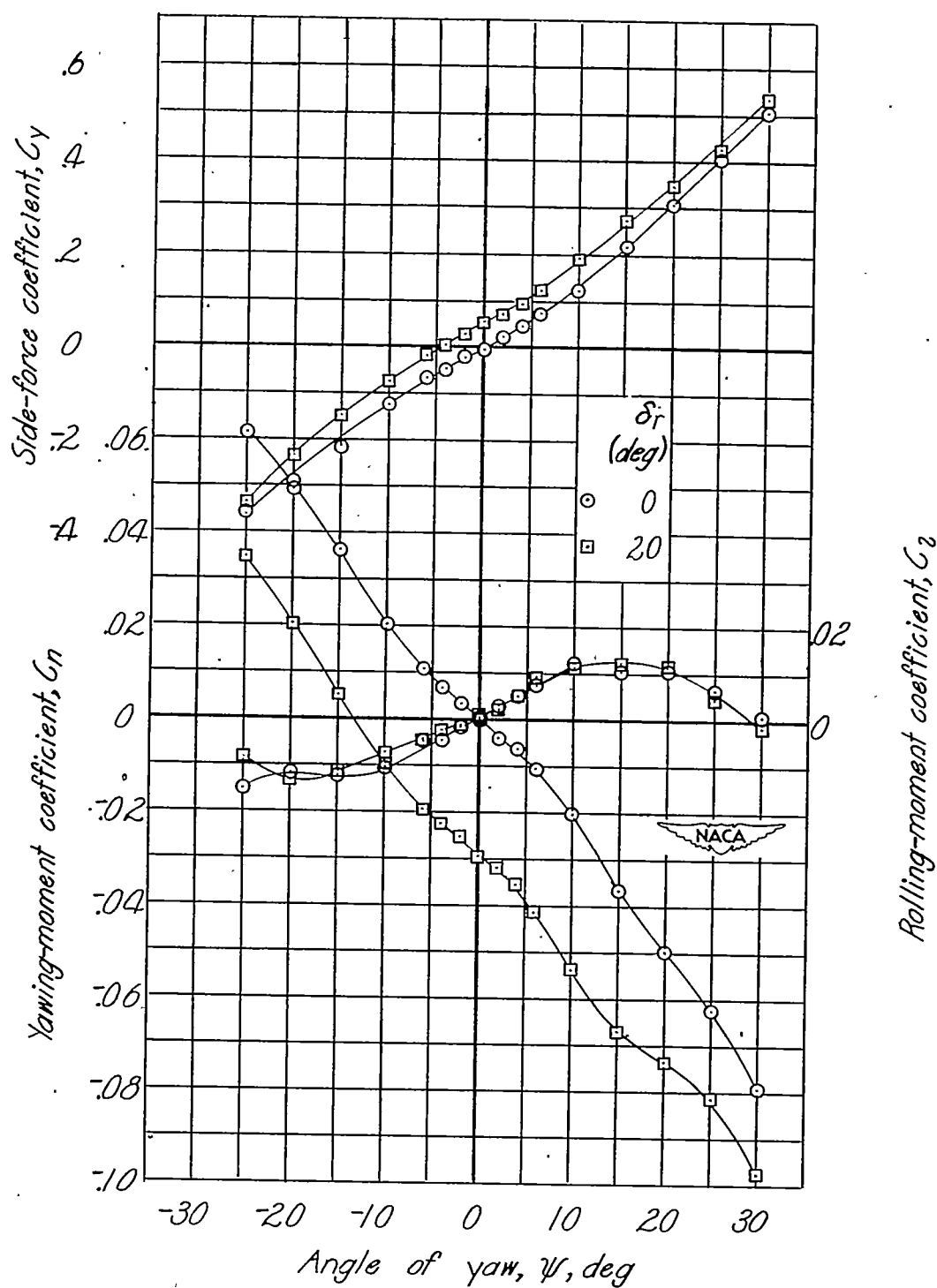
Figure 67.- Effect of rudder deflection on aerodynamic characteristics in yaw.
Windmilling propeller: extended fuselage; ventral fin 2; 80-percent-span
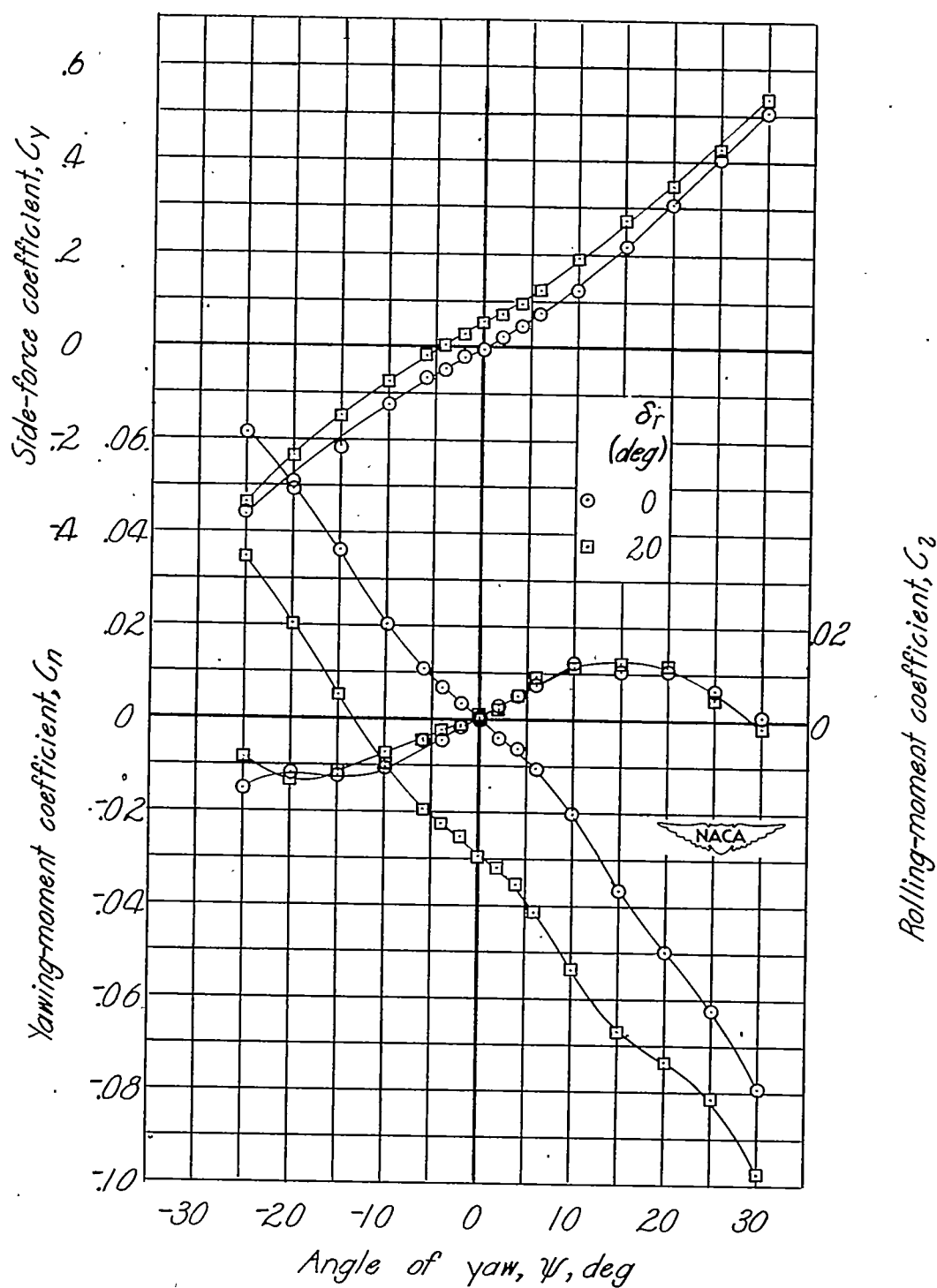slots; $\delta_f = 0^0$; $\alpha = 9.0^0$; $i_t = 1.0^0$; R = 2.05 × 10^6.

Figure 67.- Effect of rudder deflection on aerodynamic characteristics in yaw. Windmilling propeller: extended fuselage; ventral fin 2; 80-percent-span slots; $\delta_f = 0^o$; $\alpha = 9.0^o$; $i_t = 1.0^o$; $R = 2.05 \times 10^6$.
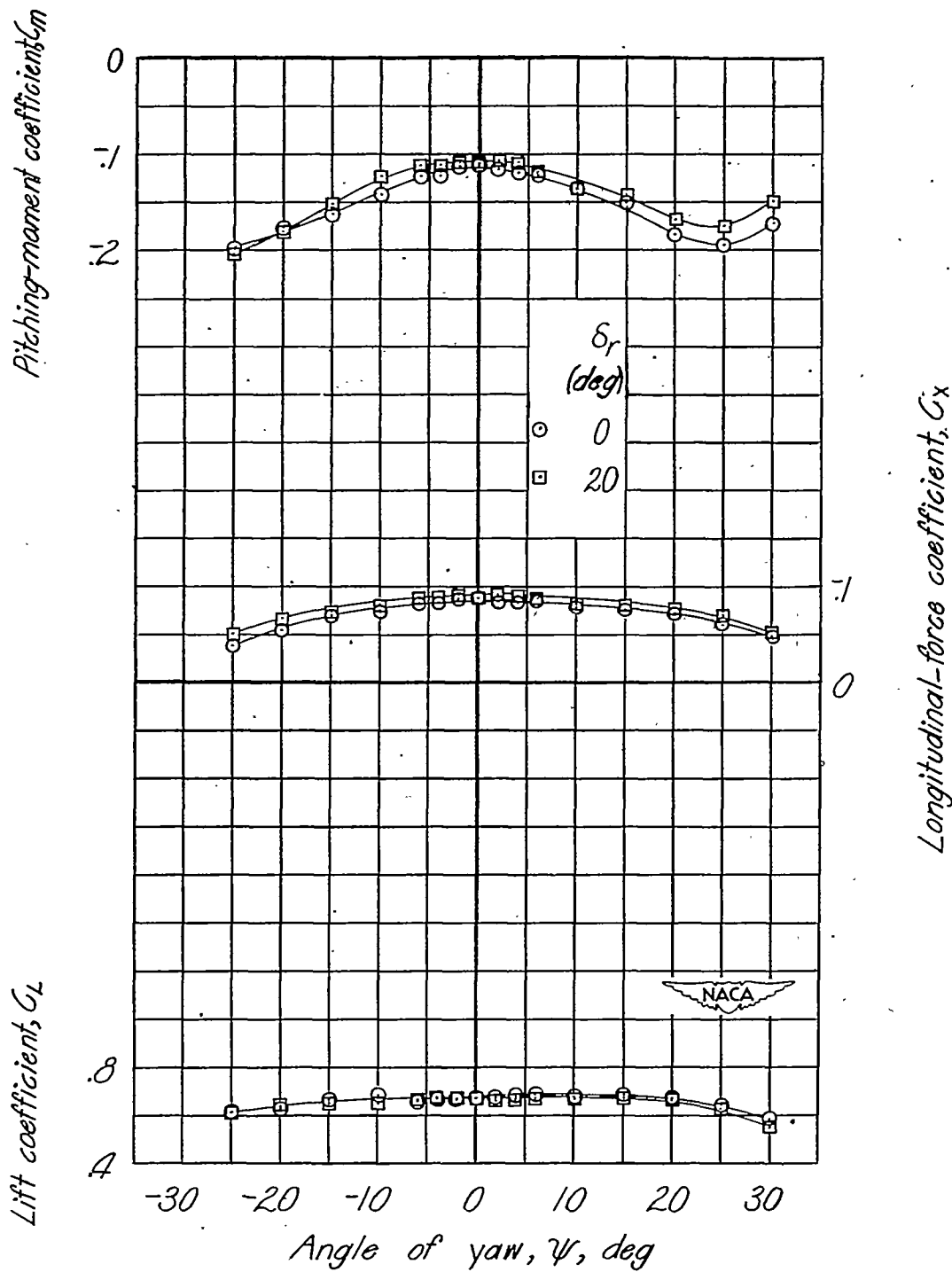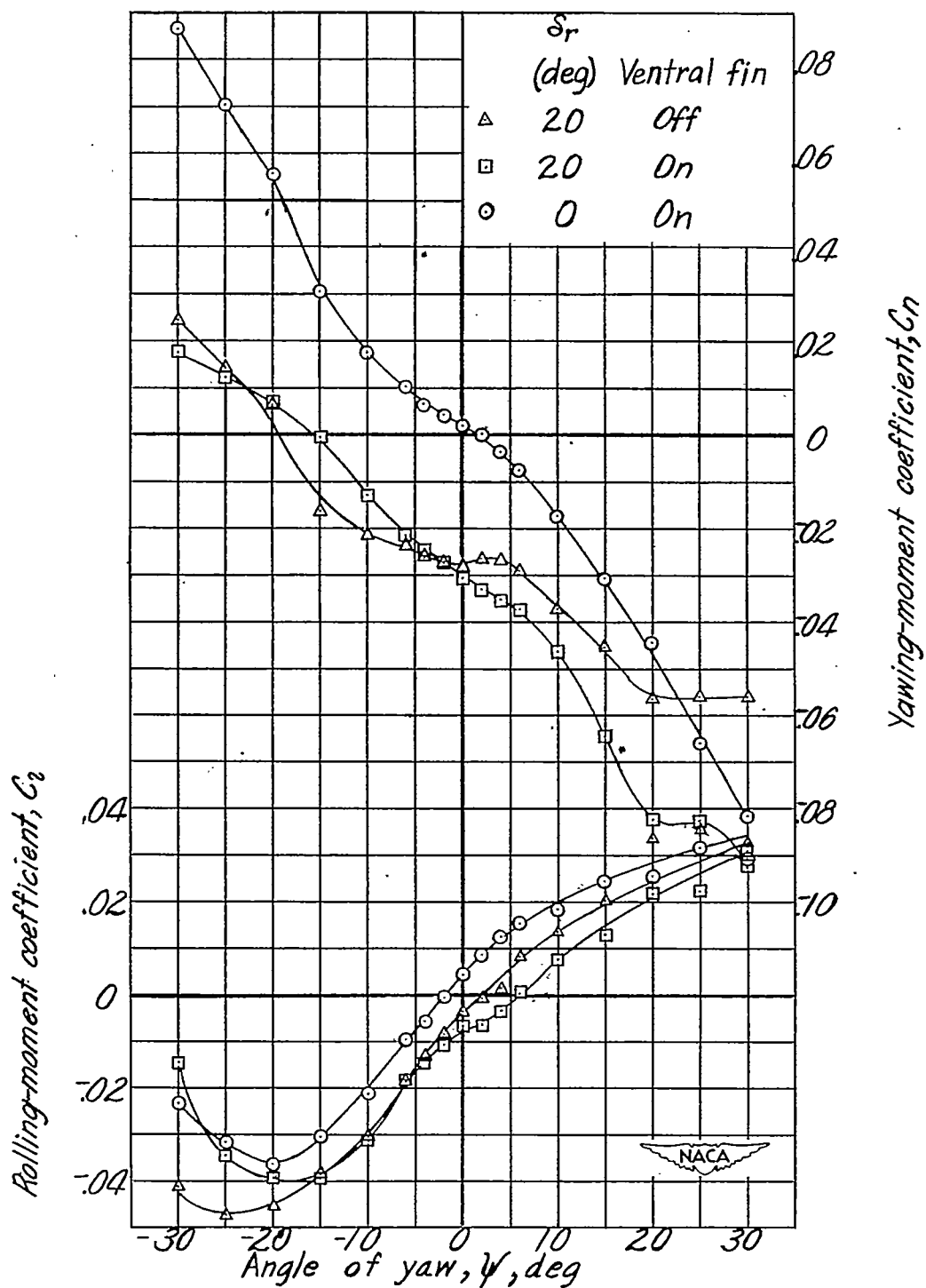
Figure 67.- Concluded.

Figure 68.- Effect of rudder deflection on aerodynamic characteristics in yaw. Windmilling propeller; extended fuselage; ventral fin 3; 40-percent-span slots: $\delta_f = 0°$; $\alpha = 18°$; $i_t = -3.7°$; $R = 4.59 \times 10^6$.
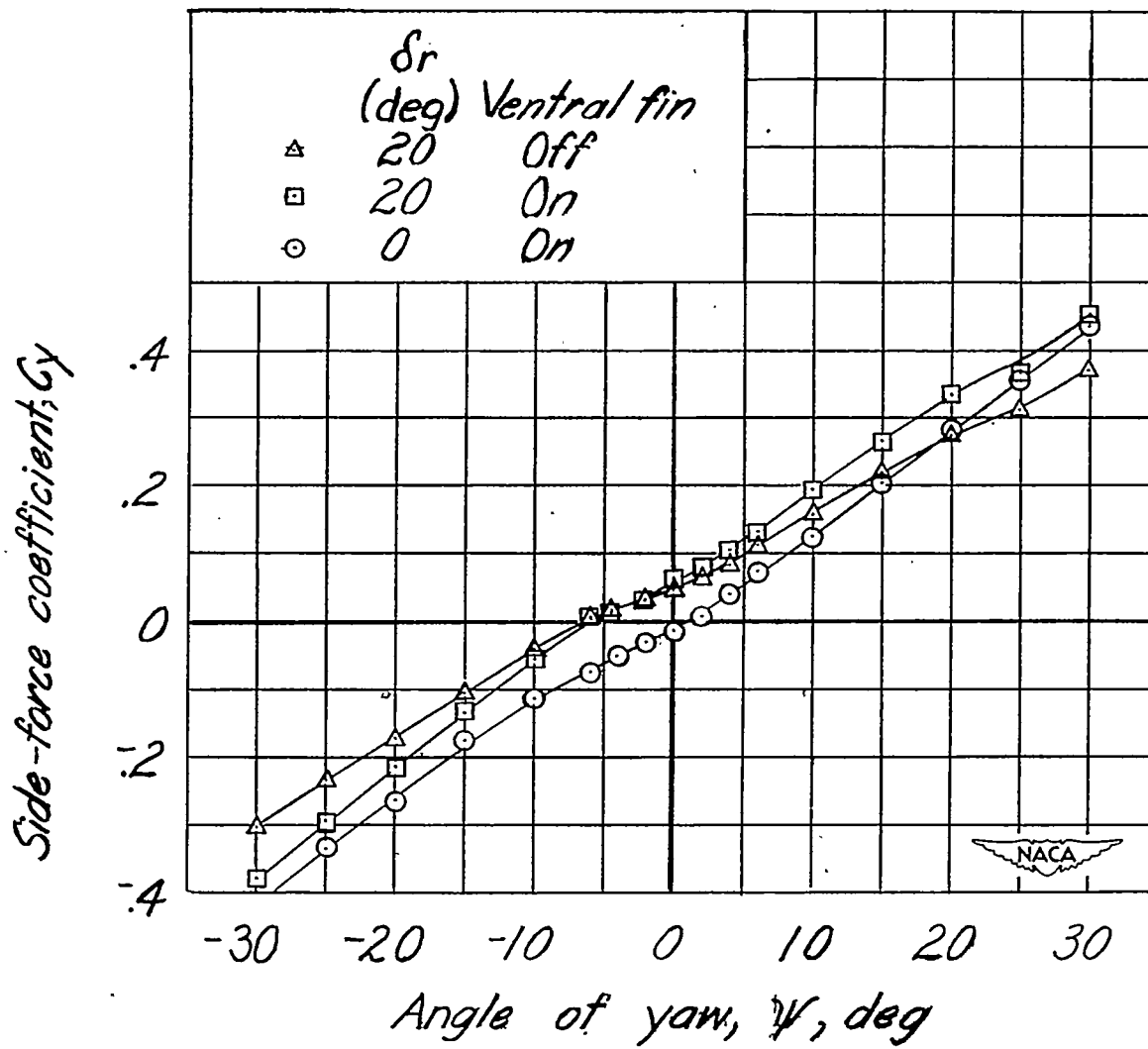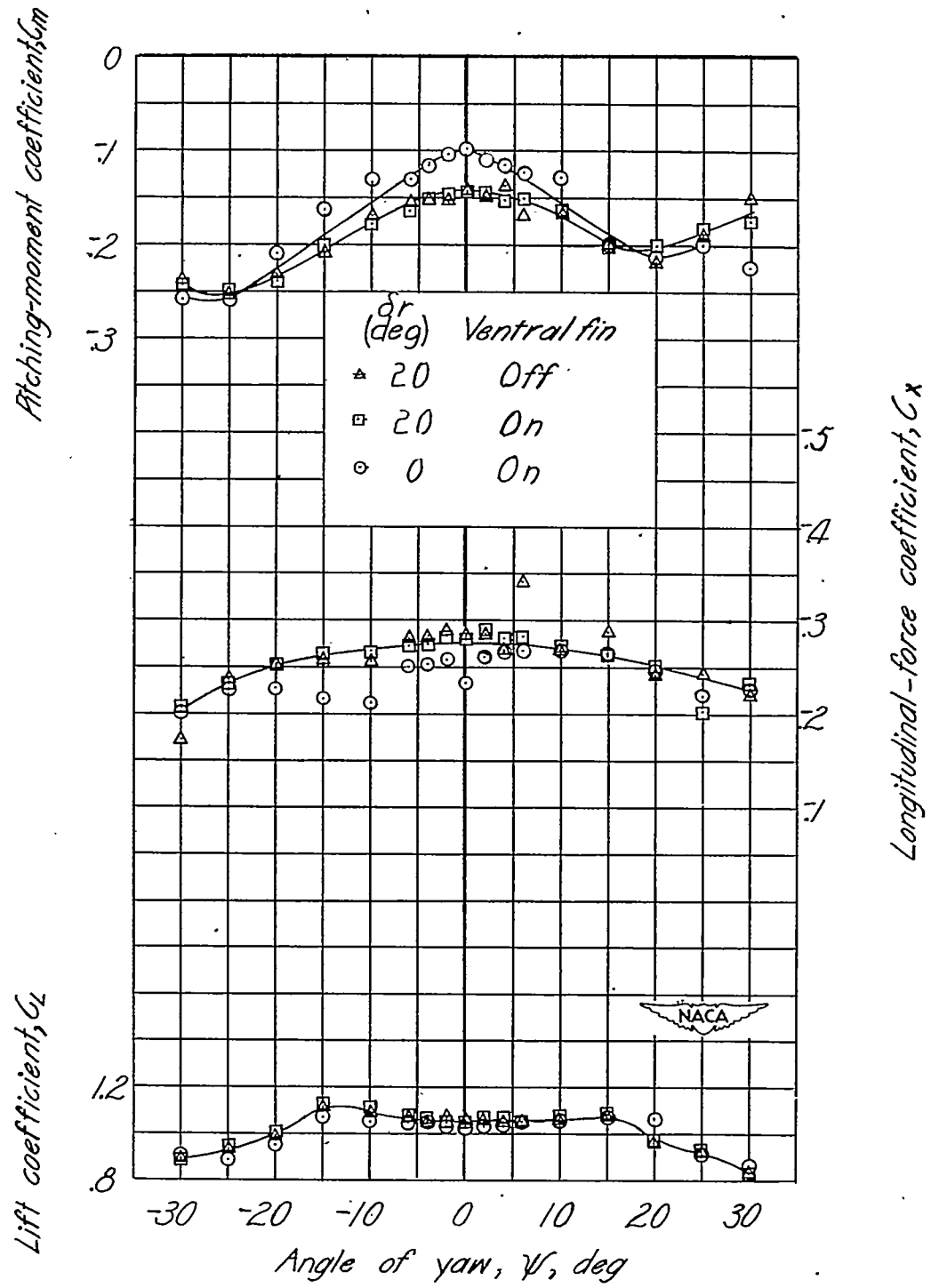
Figure 68.- Continued.

Figure 68.- Concluded.

The effect of the various airplane components on the effective dihedral parameter is shown for the original model with 80-percent-span slots (fig. 38). The increase in C_{l_ψ} at large values of C_L for the complete model and the model with the tail off is associated with flow breakdown at the root of the trailing wing which nullifies the primary negative dihedral effect due to wing-fuselage interference. Note that the primary interference effect is a ΔC_{l_ψ} which varies from -0.0010 at $C_L = 0$ to -0.0013 at $C_L = 0.9$ for the flap-neutral condition and a somewhat smaller contribution which varies with C_L with the flaps down (fig. 38(a)). The effect of the windmilling propeller is included in these increments but is small, about 0.0002 at a lift coefficient of 0.68, as is indicated by figure 54.

The effect of the wing-fuselage interference on effective dihedral has been noted before for unswept wings (reference 7) and has been investigated in Germany for sweptback wings (reference 8). Some of the data from these sources are replotted in figures 47 and 48. Shown in figure 47 are sample incremental values ΔC_{l_ψ} of effective dihedral caused by wing-fuselage interference for an unswept wing in various positions $\frac{z}{c}$ on a circular fuselage. The discrepancy between the data of references 7 and 8 for the low wing position points to the importance of the wing-fuselage juncture filleting in influencing the effective dihedral. The tests of reference 7 were made without fillets. The effect of filleting is to reduce the variation of ΔC_{l_ψ} with C_L. For the well-filleted model of reference 8, there is little variation of ΔC_{l_ψ} with C_L up to $C_L = 0.9$, at which point the previously mentioned flow breakdown occurs, and the action is somewhat similar to the action of the unfilleted wing of figure 47.

Figure 48 indicates that variation of fuselage shape or sweepback angle has only a secondary effect on the variation of ΔC_{l_ψ} with vertical position $\frac{z}{d}$ of the wing on the fuselage. The value $\Delta C_{l_\psi} = -0.0010$ mentioned previously for the airplane model is spotted on the graph, and the correlation is good.

For the complete model, an effective dihedral of about $10°$ $\left(C_{l_\psi} = 0.0020 \right)$ was obtained at $C_L = 1.0$ for most of the conditions investigated. The dihedral effect obtained with the wing alone was appreciably increased, inasmuch as the negative dihedral effect of the wing-fuselage interference is absent (figs. 38 and 50). The rate of